

CHARACTERIZING DISEASE WITH CONTRAST-ENHANCED ULTRASOUND:
APPLICATIONS IN ONCOLOGY AND THE KIDNEY

Rachel W. Walmer

A dissertation submitted to the faculty at the University of North Carolina at Chapel Hill in partial fulfillment of the requirements for the degree of Doctor of Philosophy in the Department of Biomedical Engineering in the School of Medicine.

Chapel Hill
2021

Approved by:

Paul A. Dayton

Kennita A. Johnson

Emily H. Chang

Caterina M. Gallippi

Gabriela S. Seiler

© 2021
Rachel W. Walmer
ALL RIGHTS RESERVED

ABSTRACT

Rachel W. Walmer: Characterizing Disease with Contrast-Enhanced Ultrasound:
Applications in Oncology and the Kidney
(Under the direction of Paul A. Dayton)

Early assessment of disease progression and response to therapy play an important role in patient health and contribute positively towards desired treatment outcomes. For cancer patients, imaging techniques that provide rapid feedback detailing therapeutic efficacy, particularly in the case of non-responsive or recurring tumors, allow clinicians to appropriately modify treatment regimens on a faster timescale. Current standards rely on changes in tumor volume, measured using computed tomography, to determine treatment response, an effective strategy against cytotoxic therapies. However, for targeted therapies, tumor volume may inadequately classify response while changes in molecular expression occur quite rapidly after treatment and may provide faster feedback regarding therapeutic response.

Similarly, early detection strategies capable of identifying the presence and progression of kidney disease faster than current clinical markers could facilitate faster intervention and more effectively mitigate long-term tissue damage. With chronic kidney disease (CKD) progression, changes in renal perfusion in response to structural and functional kidney has potential as a strategy for early detection. Contrast-enhanced ultrasound (CEUS) imaging offers a portable, widely accessible, inexpensive, and safe method for quantifying vascular changes. Ultrasound contrast agent (microbubble) destruction imaging techniques used to measure changes in disease biomarkers such as blood perfusion or vascular endothelial receptor expression are widely-

available and easily implemented on clinical systems. This dissertation focuses on the clinical adaptation of CEUS for disease detection and monitoring.

The first hypothesis is that CEUS can monitor response to different cancer therapies more accurately than tumor volume, both *in vivo* and in clinically relevant populations. Enhancements such as acoustic radiation force, buried ligand architecture, and microbubble size-selection were applied to improve the sensitivity of ultrasound molecular imaging and aid in the clinical translation of this imaging technique.

The second hypothesis is that CEUS can be used to diagnose kidney health through the early detection of kidney disease and can diagnose subsequent complications that arise from CKD. Here, flash-replenishment perfusion imaging was evaluated as a method for identifying kidney disease and characterizing kidney lesions in the presence of CKD. Together, the results presented in this work aid in the clinical advancement of CEUS imaging techniques for disease characterization.

To Christ, from whom all blessings flow.

To my husband, Evan, who has provided unwavering support and encouragement throughout this season.

To my parents, whose love and guidance has built a firm foundation for me stand on, which has helped me get where I am today.

ACKNOWLEDGEMENTS

I would like to thank my advisor, Dr. Paul Dayton, for his mentorship and support during my time in his lab. Your guidance has been the launching point for my career in clinical research. To Dr. Kennita Johnson, words cannot fully express how much your mentorship has meant to me. Our many conversations about life and research have been an inspiration to me and your constant encouragement has reminded me that although research involves failure, perseverance and dedication eventually lead to triumph. To the rest of my committee, Drs. Emily Chang, Caterina Gallippi, and Gabriela Seiler, thank you for the pleasure it has been working with each of you on various projects and for allowing me to benefit from your expertise.

Next, to my wonderful coworkers in the Dayton lab, both past and present, I am so grateful for the advice, the laughs, and the adventures we've had together. In the words of the Doctor: You (all) were fantastic, absolutely fantastic! To my friends, all of whom are a constant source of joy, thank you. Especially Rachael, for always asking about my research and wanting to know all of the details. And to Bretta, for commiserating with me, for your positivity, and for retreating into nature with me on our hiking trips. To my church family at Love Chapel Hill, thank you for the amazing community. It is by the grace of God that I have completed this work.

Finally, to my family, thank you for your love, dedication, and unwavering support throughout this journey. To my parents and siblings – Dan, Michele, and Sam – for your strong sense of character and perfect blend of wisdom and humor. Our time spent together always refreshes my soul. And most importantly, thank you to Evan, for being my biggest supporter and believing in my ability to succeed; your love empowers me.

TABLE OF CONTENTS

LIST OF FIGURES	xv
LIST OF TABLES	xix
LIST OF ABBREVIATIONS AND SYMBOLS	xxiv
CHAPTER 1: OVERVIEW OF CANCER AND KIDNEY DISEASE.....	1
1.1 Burden of Cancer.....	1
1.2 Angiogenesis: An Important Cancer Biomarker	2
1.3 Assessing Response to Therapy	3
1.4 Overview of Kidney Disease.....	6
1.5 Kidney Function and Mechanisms for Disease	7
1.6 Strategies for Characterizing Kidney Disease	9
CHAPTER 2: ULTRASOUND IN MEDICINE	11
2.1 Medical Ultrasound	11
2.2 Contrast-Enhanced Ultrasound.....	12
2.3 Ultrasound Molecular Imaging.....	17
2.3.1 Detection Methods for Targeted Microbubbles	17
2.3.2 Applications of Ultrasound Molecular Imaging	20
2.3.3 Improvements to Ultrasound Molecular Imaging	21

2.3.3.1	Acoustic Radiation Force	21
2.3.3.2	Buried Ligand Architecture	23
2.3.3.3	Tailoring Microbubble Size	24
2.3.3.4	Volumetric Imaging	25
2.4	Perfusion Imaging	27
2.4.1	Indicator-Dilution Bolus Imaging	27
2.4.2	Flash-Replenishment Imaging	29
2.4.3	Evaluation of Perfusion Imaging Methods	30
CHAPTER 3: ASSESSING EARLY RESPONSE TO RADIATION THERAPY USING ULTRASOUND MOLECULAR IMAGING		35
3.1	Overview	35
3.2	Materials and Methods	36
3.2.1	Assessing <i>in vivo</i> Targeted Microbubble Kinetics	36
3.2.1.1	Experimental Preparation	36
3.2.1.2	Ultrasound Image Acquisition	37
3.2.1.3	Data Analysis	38
3.2.2	Monitoring Response to Fractionated Radiation Therapy	39
3.2.2.1	Tumor Monitoring	39
3.2.2.2	Dosing Study Experimental Groups	39
3.2.2.3	Doubling Times and Response to Treatment	40
3.2.2.4	Treatment Study Experimental Groups	42

3.2.2.5	Classifying Tumor Response to Radiation Treatment.....	43
3.2.2.6	Imaging Protocol	43
3.2.2.7	Microbubble Preparation	45
3.2.2.8	Ultrasound Image Analysis	46
3.3	Results	47
3.3.1	Microbubble Kinetics.....	47
3.3.1.1	Area Under the Curve.....	47
3.3.1.2	Elimination Rate and Half-life	49
3.3.2	Monitoring Response to Radiation Therapy	53
3.3.2.1	Dosing Study: Tumor Volume	53
3.3.2.2	Treatment Cohort: Tumor Volume.....	58
3.3.2.3	Ultrasound Microbubble Targeting	61
3.4	Discussion.....	65
3.4.1	BLA Targeted Microbubble Kinetics	65
3.4.2	Response to Radiation Therapy	69
CHAPTER 4: CLINICAL TRANSLATION OF ACOUSTIC RADIATION FORCE ENHANCED ULTRASOUND MOLECULAR IMAGING.....		75
4.1	Introduction	75
4.2	Materials and Methods	75
4.2.1	<i>In vitro</i> Optimization of Acoustic Radiation Force	75
4.2.1.1	Acoustic Radiation Force Settings	75

4.2.1.2	Optical Microscope Setup	76
4.2.1.3	Data Acquisition	78
4.2.1.4	Data Analysis	79
4.2.2	Clinical Translation of Radiation Force Enhanced Ultrasound Molecular Imaging	81
4.2.2.1	Patient Recruitment and Enrollment Criteria	81
4.2.2.2	Study Protocol	82
4.2.2.3	Dynamic Contrast-Enhanced CT Image Acquisition	84
4.2.2.4	Ultrasound Equipment and Image Acquisition	84
4.2.2.5	Microbubble Formulation and Preparation.....	87
4.2.2.6	Data Analysis.....	88
4.2.2.7	DCE-CT and IHC Analysis	90
4.3	Results	90
4.3.1	<i>In vitro</i> Acoustic Radiation Force Trials	90
4.3.1.1	Pressure Calibrations	90
4.3.1.2	Microbubble displacement	92
4.3.2	Clinical Translation of Radiation Force Enhanced Ultrasound Molecular Imaging	98
4.3.2.1	Patient Recruitment and Enrollment.....	98
4.3.2.2	Monitoring Tumor Response to Treatment	100
4.3.2.3	Single Session Parameter Correlations.....	103
4.3.2.4	Correlations between DCE-CT, IHC, and Ultrasound Data.....	107

4.4	Discussion.....	112
4.4.1	Optimizing Acoustic Radiation Force	113
4.4.2	Evaluation in a Clinical Population	117
4.4.3	Canine Patient Enrollment	117
4.4.4	Longitudinal and Single Session Metrics	119
4.4.5	Regression Analysis for USMI, DCE-CT, and IHC Metrics.....	121
CHAPTER 5: THE PERFORMANCE OF FLASH-REPLENISHMENT CONTRAST ULTRASOUND IMAGING FOR EVALUATING KIDNEY HEALTH IN DIABETIC KIDNEY DISEASE		123
5.1	Overview	123
5.2	Materials and Methods	124
5.2.1	<i>Chlorocebus aethiops sabaeus</i> Diabetic Model.....	124
5.2.2	Ultrasound Data Acquisition.....	125
5.2.3	Data Processing and Analysis.....	126
5.2.3.1	Kidney Contouring	127
5.2.3.2	Kidney Segmentation	127
5.2.3.3	Signal Extraction	128
5.2.3.4	Fitting Reperfusion Data	129
5.2.3.5	Estimated Parameters	130
5.2.3.6	Feature Extraction and Linear Regression Model	132
5.3	Results	133
5.3.1	<i>Chlorocebus aethiops sabaeus</i> Clinical Measures.....	133

5.3.2	Monoexponential Model Fit Performance	134
5.3.3	Perfusion Model Parameter Estimation	135
5.3.4	Linear Regression Model Fitting	136
5.4	Discussion.....	137
5.4.1	Potential Confounding Factors	138
5.4.2	Kidney Segmentation and Concentric Layers.....	140
5.4.3	Model Performance.....	142
CHAPTER 6: QUALITATIVE ASSESSMENT OF FLASH REPLENISHMENT CONTRAST ULTRASOUND IMAGING FOR CHARACTERIZING KIDNEY LESIONS IN PATIENTS WITH CHRONIC KIDNEY DISEASE		146
6.1	Overview	146
6.2	Materials and Methods	147
6.2.1	Patient Recruitment.....	147
6.2.2	Imaging Protocol.....	148
6.2.3	Case Preparation and Interpretation.....	150
6.2.4	Reference Standards for Lesion Characterization.....	152
6.2.5	Performance Measures and Statistical Analysis	153
6.2.5.1	Assessing Malignant Diagnoses	153
6.2.5.2	Assessing Benign Diagnoses	154
6.3	Results	155
6.3.1	Patient Enrollment, Disease Severity, and Lesion Diagnoses	155

6.3.2	Malignant Lesion Classification	159
6.3.3	Benign Lesion Classification	160
6.3.4	Reader Agreement	160
6.4	Discussion.....	162
6.4.1	Lesion Classification.....	162
6.4.2	Classification Criteria for CEUS	164
6.4.3	Reader Agreement and Experience.....	165
6.4.4	Characterizing Lesions in the Presence of Kidney Disease.....	167
CHAPTER 7: DISCUSSION AND CONCLUSIONS		170
7.1	Overview	170
7.2	Early Assessment of Response to Cancer Therapy	170
7.3	Early Detection of Kidney Disease and Characterization of Related Complications	173
APPENDIX A: CONTRAST ULTRASOUND IMAGING CAPTURES LIGHT-FACILITATED DRUG RELEASE.....		176
A.1	Overview	176
A.2	Methods	177
A.3	Results and Summary	178
APPENDIX B: SUPPLEMENTAL FIGURES		180
B.1	Supplemental Figure for Chapter 3	180
B.2	Supplemental Figures for Chapter 4.....	180
APPENDIX C: SUPPLEMENTAL TABLES.....		182

C.1	Supplemental Tables for Chapter 3	182
C.2	Supplemental Tables for Chapter 4	197
C.3	Supplemental Tables for Chapter 5	199
C.4	Supplemental Tables for Chapter 6	210
REFERENCES.....		212

LIST OF FIGURES

Figure 1.1 Changes in angiogenic signaling in response to a tumor.....	3
Figure 2.1 Transducer design and applicaton.	11
Figure 2.2 Broadband microbubble response.....	15
Figure 2.3 Pulse-inversion imaging scheme.	16
Figure 2.4 Microbubble kinetics for differential targeted enhancement.....	18
Figure 2.5 Example of differential targeted enhancement image acquisition.	19
Figure 2.6 Lognormal fit (gray) of bolus time-intensity curve data (blue).....	29
Figure 2.7 Monoexponential fit (orange) of flash-replenishment time- intensity curve reperfusion data (blue).....	30
Figure 3.1 Timeline for radiation therapy dosing study.....	41
Figure 3.2 Timeline for monitoring response to radiation therapy.	43
Figure 3.3 Area under the curve by imaging day for A7R, cRGD, cRAD, and DBCO BLA bubbles	48
Figure 3.4 Elimination rate by imaging day for A7R, cRGD, cRAD, and DBCO BLA bubbles	50
Figure 3.5 Half-life by imaging day for A7R, cRGD, cRAD, and DBCO BLA bubbles	51
Figure 3.6 Distribution of tumor volumes in each dosing cohort	54
Figure 3.7 Tumor doubling time before and after fractionated radiation therapy.....	55
Figure 3.8 Tumor growth in the 0 Gy treatment cohort.....	55
Figure 3.9 Tumor growth in the 2 Gy treatment cohort.....	56

Figure 3.10 Tumor growth in the 5 Gy treatment group.....	57
Figure 3.11 Tumor growth in the 8 Gy treatment group.....	57
Figure 3.12 Halving times in tumors responsive to radiation treatment.	58
Figure 3.13 Distribution of tumor volumes in each cohort before baseline imaging and at the start of treatment.....	59
Figure 3.14 Tumor volume doubling time before and after radiation treatment in each cohort.	60
Figure 3.15 Tumor volume halving times in partially and completely responsive tumors.	61
Figure 3.16 Tumor growth curves (a) and molecular targeting (b) in untreated (n = 6) and non-responsive (n = 1) tumors.....	62
Figure 3.17 Tumor growth curves (a) and molecular targeting (b) in partially responsive tumors treated with 3.5 Gy fractionated radiation therapy.....	63
Figure 3.18 Tumor growth curves (a) and molecular targeting (b) in tumors that completely responded to 3.5 Gy fractionated radiation therapy	64
Figure 3.19 Tumor growth curves (a) and molecular targeting (b) in tumors that completely responded to 5 Gy fractionated radiation therapy	65
Figure 4.1 Experimental set-up for <i>in vitro</i> acoustic radiation force tests.	77
Figure 4.2 Quantifying microbubbles displaced by acoustic radiation force.....	80
Figure 4.3 Study timeline for canine patients enrolled in the longitudinal study.	82
Figure 4.4 Ultrasound imaging equipment and setup.	85
Figure 4.5 Process of signal extraction from tumor.	89
Figure 4.6 Recorded pressure from the 9L4 transducer.	91

Figure 4.7 Number of displaced bubbles for decreasing power outputs at depths from 2-5 cm.	92
Figure 4.8 Average number of displaced bubbles for power outputs ranging from 0 dB to -15 dB.	95
Figure 4.9 Streak images of bubbles in the presence and absence of a powerful acoustic radiation force push.	97
Figure 4.10 Streak images of bubbles in the presence and absence of an ideal acoustic radiation force push.	97
Figure 4.11 Canine recruitment and enrollment during study period.	100
Figure 4.12 Changes in dTE from UCAs targeted to $\alpha_v\beta_3$ integrin (cRGD-MBs) compared to tumor volume over the multi-week study.	102
Figure 4.13 Changes in dTE from UCAs targeted to VEGFR2 (A7R-MBs) compared to tumor volume over the multi-week study.	103
Figure 4.14 Tumor targeting and linear correlation between USMI and tumor parameters.	106
Figure 4.15 Relationship between CD31 expression and DCE-CT metrics.	107
Figure 4.16 Correlation between VEGFR2 expression and DCE-CT metrics.	108
Figure 4.17 Relationship between DCE-CT parameters.	109
Figure 4.18 Association between tumor volume and DCE-CT parameters.	110
Figure 4.19 Linear correlation between vascular markers and tumor volume.	110
Figure 4.20 Relationship between DCE-CT parameters and VEGFR2-targeted microbubble enhancement.	111
Figure 4.21 Relationship between DCE-CT parameters and $\alpha_v\beta_3$ -targeted microbubble enhancement.	112
Figure 5.1 Proposed flow for flash-replenishment data analysis.	127

Figure 5.2 Signal extraction process.	128
Figure 5.3 Time-intensity curve fitting process.	129
Figure 5.4 Time-intensity curve fitting of $Il(K)$ reperfusion data per kidney concentric layer.	130
Figure 5.5 Polynomial curve fitting of the normalized and non-normalized KCL estimated parameters in a control group vervet.	132
Figure 5.6 KCL curves normalized by the middle (5 th) layer for representative NHPs.....	136
Figure 6.1 Dual mode visualization of a kidney lesion in CPS mode (left) and B-mode (right).....	150
Figure 6.2 Graphical user interface layout.	151
Figure 6.3 Dichotomization of reader diagnoses and true reference standards.....	155
Figure 6.4 Flow diagram of patient and lesion retention from imaging through final analysis.	157
Figure 6.5 Lesion malignancy classification for each reader (R1-4) and reference standard of either imaging or pathology.	159
Figure A.1 Maximum intensity projection contrast ultrasound images.....	177
Figure A.2 Quantitative assessment of microbubble retention in the tumors of each experimental cohort normalized to baseline retention values.	178
Supplemental Figure B.1 Tumor growth in the 5 Gy dosing study cohort for tumors that responded to treatment (n = 4).	180
Supplemental Figure B.2 Microbubble targeting compared to available measures of CD31 and VEGFR2 expression.	180
Supplemental Figure B.3 Correlation between VEGFR2 expression and DCE-CT metrics after removing outlier case; n = 11.	181

LIST OF TABLES

Table 2.1 Formulations for different ultrasound contrast agents	13
Table 2.2 Solubility and diffusivity in water for common microbubble filling gases	14
Table 2.3 Definitions and notations for bolus imaging perfusion parameters	32
Table 4.1 Average pressure recorded for power outputs between 0 and -15 dB	91
Table 4.2 Linear regression parameters with goodness of fit for each depth	93
Table 4.3 Average number of displaced bubbles for power outputs between 0 and -15 dB.....	96
Table 4.4 Number of client-owned canine patients recruited and enrolled	99
Table 4.5 Tumor volume and ultrasound metrics for single session patients	104
Table 5.1 Average demographic and clinical measures for control, IR, and diabetic cohorts	134
Table 5.2 Monoexponential model performance by cohort per KCL	135
Table 5.3 Regression model <i>P</i> -values determined from blood pressure measurements and either non-normalized or normalized estimated parameter statistics	137
Table 5.4 Model term coefficient <i>P</i> -values from the normalized PI perfusion data for each regression test case	144
Table 5.5 Model term coefficient <i>P</i> -values from the non-normalized PI perfusion data for each regression test case	145
Table 6.1 Comparison of Modified CEUS Cystic Mass Classification to CT Bosniak Criteria	152
Table 6.2 Details on patients included in final analysis.....	156

Table 6.3 Number, diagnosis, laterality, and size of analyzed lesions.....	158
Table 6.4 Performance analysis of CEUS for diagnosing malignant kidney lesions.....	161
Table 6.5 Performance analysis of CEUS for diagnosing benign kidney lesions.....	161
Supplemental Table C.1 Pairwise comparisons (<i>P</i> -values) of background tissue AUC between imaging days for each bubble.....	182
Supplemental Table C.2 Pairwise comparisons (<i>P</i> -values) of kidney cortical AUC between imaging days for each bubble.....	183
Supplemental Table C.3 Pairwise comparisons (<i>P</i> -values) of kidney medullary AUC between imaging days for each bubble	184
Supplemental Table C.4 Pairwise comparisons (<i>P</i> -values) of liver AUC between imaging days for each bubble	185
Supplemental Table C.5 Pairwise comparisons (<i>P</i> -values) of elimination rate in background tissue between imaging days for each bubble	186
Supplemental Table C.6 Pairwise comparisons (<i>P</i> -values) of elimination rate in background tissue between bubbles on each imaging day.....	187
Supplemental Table C.7 Pairwise comparisons (<i>P</i> -values) of half-life in background tissue between imaging days for each bubble	187
Supplemental Table C.8 Pairwise comparisons (<i>P</i> -values) of half-life in background tissue between bubbles on each imaging day.....	188
Supplemental Table C.9 Pairwise comparisons (<i>P</i> -values) of elimination rate in the cortex between imaging days for each bubble	189
Supplemental Table C.10 Pairwise comparisons (<i>P</i> -values) of elimination rate in cortical tissue between bubbles on each imaging day.....	190
Supplemental Table C.11 Pairwise comparisons (<i>P</i> -values) of half-life in the kidney cortex between imaging days for each bubble	190
Supplemental Table C.12 Pairwise comparisons (<i>P</i> -values) of half-life in cortical tissue between bubbles on each imaging day.....	191

Supplemental Table C.13 Pairwise comparisons (<i>P</i> -values) of medullary elimination rate between imaging days for each bubble	191
Supplemental Table C.14 Pairwise comparisons (<i>P</i> -values) of elimination rate in the medulla between bubbles on each imaging day	192
Supplemental Table C.15 Pairwise comparisons (<i>P</i> -values) of half-life in the medulla between imaging days for each bubble	193
Supplemental Table C.16 Pairwise comparisons (<i>P</i> -values) of medullary half-life between bubbles on each imaging day	194
Supplemental Table C.17 Pairwise comparisons (<i>P</i> -values) of elimination rate in the liver between imaging days for each bubble	194
Supplemental Table C.18 Pairwise comparisons (<i>P</i> -values) of elimination rate in the liver between bubbles on each imaging day	195
Supplemental Table C.19 Pairwise comparisons (<i>P</i> -values) of half-life in liver tissue between imaging days for each bubble	195
Supplemental Table C.20 Pairwise comparisons of (<i>P</i> -values) half-life in liver tissue between bubbles on each imaging day	196
Supplemental Table C.21 Multiplicity adjusted <i>P</i> -values comparing displacement results between different depths within each power output	197
Supplemental Table C.22 Multiplicity adjusted <i>P</i> -values comparing differences in bubble displacement results across power output	198
Supplemental Table C.23 Corresponding targeted MB, CD31, and VEGFR expression	199
Supplemental Table C.24 Non-normalized estimated parameter, A, by KCL for each session and the average for a representative control NHP	199
Supplemental Table C.25 Normalized estimated parameter, A, by KCL for each session and the average for a representative control NHP	200
Supplemental Table C.26 Average non-normalized estimated parameters A, β , and PI per KCL for every NHP in the control cohort	201

Supplemental Table C.27 Average non-normalized estimated parameters A, β , and PI per KCL for every NHP in the IR cohort.....	201
Supplemental Table C.28 Average non-normalized estimated parameters A, β , and PI per KCL for every NHP in the diabetic cohort.....	202
Supplemental Table C.29 Average normalized estimated parameters A, β , and PI per KCL for every NHP in the control cohort	202
Supplemental Table C.30 Average normalized estimated parameters A, β , and PI per KCL for every NHP in the IR cohort	203
Supplemental Table C.31 Average normalized estimated parameters A, β , and PI per KCL for every NHP in the diabetic cohort.....	203
Supplemental Table C.32 Monoexponential model performance (MSE) in the control NHP cohort for each session per KCL.....	204
Supplemental Table C.33 Monoexponential model performance (MSE) in the IR NHPs for each session per KCL.....	205
Supplemental Table C.34 Monoexponential model performance (MSE) in the diabetic NHP cohort for each session per KCL	206
Supplemental Table C.35 Regression model input features from the non-normalized A, β , and PI per KCL for control NHPs.....	207
Supplemental Table C.36 Regression model input features from the non-normalized A, β , and PI per KCL for NHPs in the IR cohort.....	207
Supplemental Table C.37 Regression model input features from the non-normalized A, β , and PI per KCL for diabetic NHPs	208
Supplemental Table C.38 Regression model input features from the normalized A, β , and PI per KCL for NHPs in the control cohort.....	208
Supplemental Table C.39 Regression model input features from the normalized A, β , and PI per KCL for NHPs in the IR cohort.....	209
Supplemental Table C.40 Regression model input features from the normalized A, β , and PI per KCL for NHPs in the diabetic cohort	209

Supplemental Table C.41 Details for all enrolled patients	210
Supplemental Table C.42 Inter-reader agreement between reader 1 and readers 2-4 regarding lesion characterization	211
Supplemental Table C.43 Inter-reader agreement between reader 2 and readers 3-4 regarding lesion characterization	211
Supplemental Table C.44 Inter-reader agreement between reader 3 and reader 4 regarding lesion characterization	211

LIST OF ABBREVIATIONS AND SYMBOLS

2D	Two-Dimensional
3D	Three-Dimensional
A	Amplitude, Steady-State Plateau
A.U.	Arbitrary Units
A7R	Heptapeptide Alanine-Threonine-Tryptophan-Leucine-Proline-Proline-Arginine (ATWLPPR)
ABC	Accelerated Blood Clearance
ANOVA	Analysis of Variance
ARF	Acoustic Radiation Force
AUC	Area Under the Curve
$\alpha_v\beta_3$	Alpha-v-beta-3-integrin
β	Beta, reperfusion rate
BLA	Buried Ligand Architecture
BMI	Body Mass index
B-mode	Brightness Mode
BP	Blood Pressure
BV	Blood Volume
C3/C3b	Complement Component 3
CD	Color Doppler
CD31	Cluster of Differentiation 31, Platelet Endothelial Cell Adhesion Molecule

CEUS	Contrast-Enhanced Ultrasound
CKD	Chronic Kidney Disease
CPS	Contrast Pulse Sequencing
cRAD	Peptide cyclic-Arginine-Alanine-Aspartic Acid
cRGD	Peptide cyclic-Arginine-Glycine-Aspartic Acid
CT	Computed Tomography
CV	Coefficient of Variation
δ	Delta, Effect Size
D_t	Doubling Time
dB	Decibel
DBCO	Dibenzocyclooctyl
DCE-CT	Dynamic Contrast-Enhanced Computed Tomography
DCM	Division of Comparative Medicine
DFB	Decafluorobutane
DICOM	Digital Imaging and Communications in Medicine
DKD	Diabetic Kidney Disease
dTE	Differential Targeted Enhancement
eGFR	Estimated Glomerular Filtration Rate
ESKD	End-Stage Kidney Disease
FBG	Fasting Blood Glucose

FOV	Field of View
FPS	Frames Per Second
FSA	Fibrosarcoma
G	Gauge
GOF	Goodness of Fit
GUI	Graphical User Interface
Gy	Gray (Unit of Radiation Therapy Dose)
H_t	Halving Time
HbA1c	Hemoglobin A1c, Glycated Hemoglobin
HPF	High-Powered Field
Hz	Hertz (Unit of Frequency)
$I_l(K)$	Intensity for layer (l) and frame (K)
IACUC	Institutional Animal Care and Use Committee
IHC	Immunohistochemistry
IR	Insulin-Resistant
K	Frame Number
K	Rate Constant, Elimination Rate
KCL	Kidney Concentric Layer
kHz	Kilohertz (Unit of Frequency)
kPa	Kilopascal (Unit of Pressure)

kV	Kilovolt (Unit of Electric Potential)
l	Layer
M_l	Mask for layer (l)
mA	Milliampere (Unit of Electric Current)
MATLAB	MathWorks Programming Language
MB	Microbubble
MBD	Microbubble Destruction
MHz	Megahertz (Unit of Frequency)
MI	Mechanical Index
MRI	Magnetic Resonance Imaging
MSE	Mean Squared Error
NHP	Nonhuman Primate
NPV	Negative Predictive Value
p_{xx}	Polynomial Coefficient (i.e. p_{10})
PE	Peak Enhancement
PEG	Polyethylene Glycol
PET	Positron Emission Tomography
PI	Perfusion Index
PNP	Peak Negative Pressure
PPV	Positive Predictive Value

PW	Pulsed Wave
ρ	Rho, Correlation Coefficient
R^2	R-Squared, Coefficient of Determination
RECIST	Response Evaluation Criteria in Solid Tumors
RBC	Red Blood Cell
RCC	Renal Cell Carcinoma
ROI	Region of Interest
RT	Radiation Therapy
SD	Standard Deviation
STS	Soft Tissue Sarcoma
Tx	Transmit
T1D	Type 1 Diabetes
T2D	Type 2 Diabetes
TIC	Time Intensity Curve
TTP	Time to Peak
UCA	Ultrasound Contrast Agent
USMI	Ultrasound Molecular Imaging
V	Volume
VEGF	Vascular Endothelial Growth Factor
VEGFR2	Vascular Endothelial Growth Factor Receptor 2

CHAPTER 1: OVERVIEW OF CANCER AND KIDNEY DISEASE

1.1 Burden of Cancer

Globally and in the United States, cancer places a huge burden on patients and the healthcare system. Worldwide, there were 19.29 million new cancer cases and 9.96 million deaths from cancer in 2020 [1]. In the United States, it is estimated that there will be 1.9 million new cases in 2021 and currently cancer is the second leading cause of death [2,3]. Fortunately, since 1991 cancer mortality has decreased continuously [4], which is due to a variety of factors such as implementing preventative measures (lifestyle changes) [5,6], making improvements to early detection [7,8], and advances in cancer treatment and technologies [9]. Despite this, costs associated with cancer care continue to increase [10], particularly as a wider variety and more expensive treatment options become available [11]. Early detection and effective treatment regimens not only help mitigate the rising costs associated with cancer, but are also extremely beneficial to the patient by reducing treatment time, lessening disruptions to daily life, and contributing to a favorable prognosis [12]. These patient care strategies have helped pave the way for precision medicine and targeted therapies (immunotherapy, gene therapy, anti-angiogenic therapy), where treatment regimens are tailored according to molecular traits expressed by the tumor in order to directly target cancer cells or pathways involved in tumor maintenance, growth, and metastasis. Many targeted therapies have focused on angiogenesis, due to the crucial role it plays in supporting a tumor.

1.2 Angiogenesis: An Important Cancer Biomarker

Angiogenesis, the formation of new blood vessels, is a key contributor to the growth and development of tumors. Typically, angiogenesis is a tightly regulated process, relying on a balanced expression of pro-angiogenic and anti-angiogenic factors (Figure 1.1a) to maintain a normal, structured vascular environment [13]. However, in the presence of a tumor this balance is disrupted, resulting in the formation of a chaotic and unregulated environment. Tumor-induced signaling influences angiogenesis and results in both morphological and molecular alterations to vascular expression. Previously hierarchical vasculature becomes disorganized, tortuous, and leaky (Figure 1.1b) in an attempt to support rapid growth and the high demand for oxygen and nutrients [13,14]. Further, vascular molecular markers become overexpressed (Figure 1.1b) due to aberrant pro-angiogenic signaling instigated by the tumor [15,16]. Overexpression of tumor biomarkers presents a unique opportunity to assess the molecular signature of cancer. This work focuses on two different cancer biomarkers: $\alpha_v\beta_3$ integrin, a protein that mediates endothelial cell attachment and migration [16,17], and vascular endothelial growth factor (VEGF) and its receptor family, which serve as the main mechanism for the development of new blood vessels [18,19]. Specifically, VEGF receptor 2 (VEGFR2), which promotes endothelial cell proliferation and survival to support vascular growth [15,20]. The information gained by measuring these biomarkers is particularly useful when considering how susceptible a tumor will be to specific treatments and for monitoring treatment response over time. For example, VEGF inhibitors serve as a common targeted therapy in cancer treatment. Their use has contributed to improved outcomes in cancer patients when combined with conventional therapies [21]. Similar to conventional therapies, tumors may respond poorly either initially or by developing resistance to anti-VEGF therapy over time. As such, measures of molecular expression can assist in providing

timely feedback on patient response to therapy.

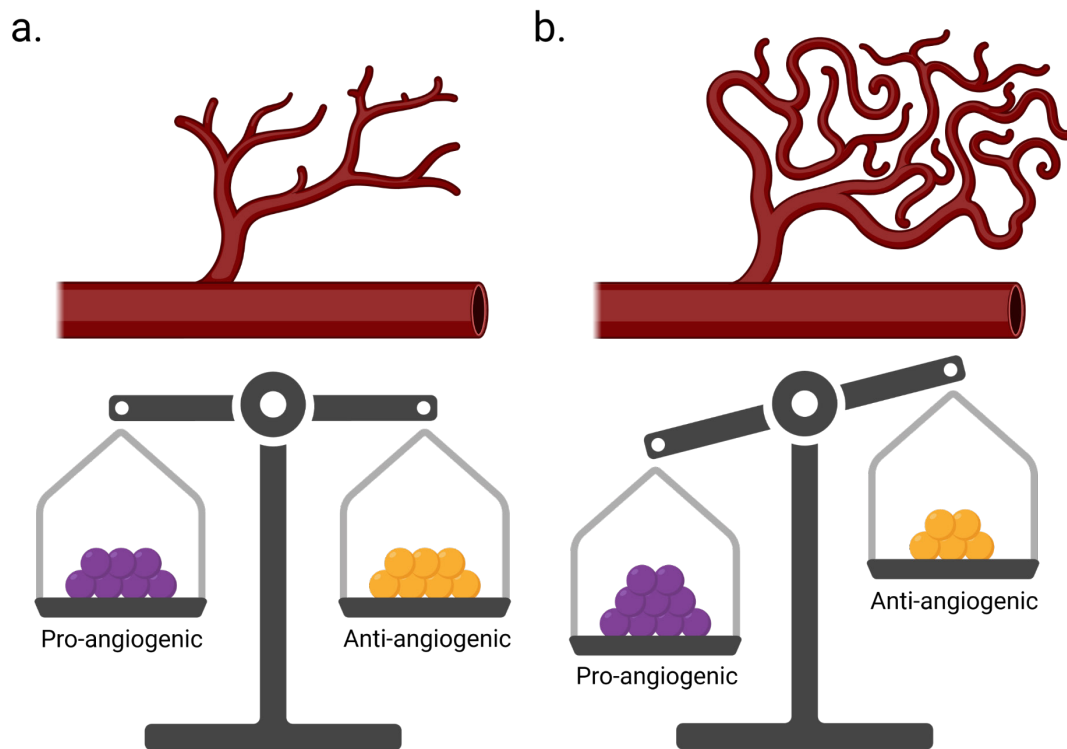


Figure 1.1 Changes in angiogenic signaling in response to a tumor. a) Normal regulation of pro-angiogenic and anti-angiogenic factors results in hierarchical well-formed vascular networks. b) Unregulated expression of pro-angiogenic factors results in a chaotic network of poorly formed vessels. Created with BioRender.com.

1.3 Assessing Response to Therapy

The current gold standard for monitoring response to therapy relies on changes in tumor size and volume, based on the Response Evaluation Criteria in Solid Tumors (RECIST). The RECIST guidelines were developed for anatomical imaging modalities, primarily computed tomography (CT), but are also used with magnetic resonance imaging (MRI) [22]. The first step in applying RECIST guidelines involves delineating between measurable and non-measurable lesions, following which treatment outcomes are classified as complete response, partial response, stable disease, or progressive disease. Measurable lesions have a largest diameter > 10

mm per CT or in the case of lung tumors > 20 mm per chest x-ray [22]. The response categories are based on tumor disappearance, no change, or a given percent size increase or decrease over the course of treatment. Complete response occurs when the treated lesion completely disappears, compared to partial response, which is classified as a 30% decrease in the largest diameter relative to the initial largest diameter measurement. On the other hand, progressive disease occurs when there is at least a 20% increase in the largest diameter compared to the minimum largest diameter value. Finally, stable disease considers the case where the lesion neither classifies as partially responding nor progressive disease. These criteria are used to label both measurable and non-measurable lesions. RECIST performs well at identifying tumor response to classic cytotoxic chemotherapy and radiotherapy treatments. Even in this context, there are some limitations to RECIST, such as partial volume averaging, measurement discrepancies, or inter-observer variability. However, with the rise of targeted therapies, novel methods for establishing tumor response are necessary. For example, disrupting tumor signaling pathways through immunotherapy or anti-angiogenic therapy may result in overall tumor control without a corresponding reduction in tumor size [23,24]. Prior studies determined that RECIST severely underestimated the response of anti-angiogenic therapies (Sorafenib and Sunitinib) in renal cell carcinoma (RCC) and could identify progression-free survival in only 15-17%% of patients [25,26], highlighting the need for alternate markers of tumor response.

Many imaging modalities are capable of assessing molecular and functional changes in the tumor. Positron emission tomography (PET) imaging is commonly used with a fluorodeoxyglucose radionuclide to assess glucose uptake, providing a physiological measure of tumor activity [27]. Anatomical imaging modalities, such as CT and MRI, also serve a role in assessing functional changes in response to treatment. The addition of a contrast agent allows CT

or MRI to measure tissue perfusion, a potential marker of therapeutic response [27]. Combining anatomical modalities with those that assess tumor physiology, such as PET/CT or PET/MRI, has provided a way to map functional information over anatomical features to further aid in tumor assessment. Alterations to tumor metabolism or blood flow are just two possible methods for evaluating tumor response to treatment that are independent of changes in tumor volume. In fact, these biomarkers have been shown to be more sensitive to tumor response than morphological changes, providing faster and more accurate feedback. It has been shown that PET [28–30], contrast-enhanced CT [31,32], and contrast-enhanced MRI [33,34] all have the ability to monitor and even predict tumor response to treatment earlier than conventional tumor size metrics. This is an important consideration due to the rising cost of treatment, negative side effects of cancer therapies, and the potential for tumors to develop resistance to treatment over time. Tumor resistance can cause the tumor to become more aggressive even when there was an initially positive response [35]. Therefore, the use of more sensitive biomarkers will lead to better treatment efficacy and patient prognosis. While CT, MRI, and PET can effectively identify early response to treatment, these modalities are expensive, not always well tolerated by patients, involve the use of ionizing radiation (PET, CT) and contrast agent use is contraindicated in certain patient populations (MRI, CT) [36–38]. As such, these modalities are used intermittently, approximately once every few months. To accurately pinpoint positive or negative changes in response to therapy more frequent tumor monitoring is preferred. In comparison to CT, MRI, and PET, ultrasound imaging offers a less expensive, well tolerated, accessible, and safe (no ionizing radiation) method that enables frequent assessment of treatment response [39]. This modality will be addressed in more detail in Chapter 2.

1.4 Overview of Kidney Disease

Another major contributor to disease burden in the United States comes from kidney disease. From 2002 to 2016 the burden from chronic kidney disease (CKD) increased at an alarming rate, while overall the burden from cardiovascular disease and other non-communicable disease decreased [40]. Mortality and morbidity associated with CKD are also high [41]. Factors associated with the increase in CKD include population growth and aging, and dietary and metabolic risk factors [40], with diabetes considered to be the leading cause of CKD [42–44]. In the United States, as of 2018, an estimated 34 million people currently have diabetes and another 88 million are pre-diabetic [45]. Diabetic patients have an increased risk of developing kidney complications [46], with approximately 40% of diabetic patients eventually developing diabetic kidney disease (DKD) [47,48]. Currently, DKD is the leading cause of end-stage kidney disease (ESKD) and the risk of ESKD increases when considering factors such as socioeconomic status and race [46,49]. Prevention and treatment strategies for CKD typically target lifestyle modifications, regulating controllable risk factors, and addressing underlying disease processes in an attempt to reduce further loss of kidney function [41,47,50,51]. However, for these interventions to be truly effective, they need to be implemented as early as possible, ideally at a stage where they can prevent disease onset or help mitigate progression [41,50]. Current clinical diagnosis of CKD depends on the persistence of elevated albuminuria or decreased estimated glomerular filtration rate (eGFR) among other markers [43,52]. This creates an environment where diagnosis lags behind actual disease progression. As kidney disease progresses, remodeling and fibrosis occurs, which if left untreated leads to irreversible alterations in structure and function. With this knowledge, the challenge then becomes the ability to effectively characterize structural and functional alterations in the kidney in the early stages of disease.

1.5 Kidney Function and Mechanisms for Disease

The kidney has developed as a highly efficient and adaptable organ in order to fulfill its core function of removing metabolic waste from the bloodstream. To accomplish this, the kidney is composed of a tightly regulated system that balances nutrient reabsorption with waste excretion. Metabolic byproducts are brought to the kidney via the renal artery, which branches until reaching the afferent glomerular arterioles, at which point molecules, depending on their size and charge, pass through fenestrations in the glomerular capillary network to cross into Bowman's capsule [53]. From here, the filtrate travels through the renal tubules and the loop of Henle, where reabsorption and secretion take place, resulting in waste generation and return of valuable solutes back to body. This entire process is supported by intricate communication across multiple channels to ensure proper kidney function.

Prior to the onset of and in the presence of disease, alterations in microvascular, glomerular, and tubular components occur, which, if left uncorrected may persist and create a cascade effect resulting in decline and eventually permanent loss of kidney function [54,55]. There are multiple pathways to CKD, but in this work we consider disease pathogenesis through the lens of diabetes, since it is currently the main mechanism for CKD onset and progression. Initial disruption to kidney function results from hyperglycemia in insulin-resistant and diabetic patients. Increased oxygen demand coupled with decreased oxygen delivery in diabetic patients also plays a key role by worsening the already naturally occurring hypoxic state of the kidney, which further degrades and impairs kidney function [56,57].

The mechanisms by which kidney injury occur are interwoven across the vascular, glomerular, and tubular systems. Under normal conditions, glomerular capillary pressure is tightly regulated to maintain a stable and efficient glomerular filtration rate. This is accomplished

through vasoregulation of the afferent and efferent glomerular arterioles, which is partially influenced by tubuloglomerular feedback. In a hyperglycemic environment, protective mechanisms that shield glomerular capillary pressure from alterations in systemic pressure are impacted, exposing glomerular capillaries to unexpected changes in pressure [58].

Hyperfiltration further subjects the glomerulus to unsustainable changes in capillary pressure, which lead to glomerular hypertrophy. One mechanism for hyperfiltration results from a salt imbalance in the tubules, which prompts tubuloglomerular feedback mechanisms to influence vasoregulation in an attempt to restore the sodium balance. Increased sodium reabsorption in the proximal tubules, due to higher levels of glucose in the filtrate, causes subsequent vasodilation and increased glomerular filtration until the salt balance is restored in the distal tubules [59].

Changes in morphology linked to these irregularities include glomerular and tubular hypertrophy. Tubular thickening further exacerbates the issue by increasing the distance oxygen must travel when crossing the capillary bed, worsening hypoxia. Resulting tubular atrophy reduces VEGF expression, which impedes capillary regeneration [56]. This causes endothelial cell loss and capillary rarefaction, the latter of which is categorized as either a reduction in the total number of capillaries or a reduction in the total number of perfused capillaries [55,60,61].

Schoina et al. demonstrated that the presence of diabetes worsens capillary loss, further degrading kidney function in CKD [60]. Capillary rarefaction causes a reduction in renal blood flow and perfusion, increasing the demand for oxygen, worsening the hypoxic state, and inviting further injury. As conditions deteriorate and nephrons lose functionality, single nephrons increase glomerular filtration rate to compensate, beginning the destructive cycle all over again.

1.6 Strategies for Characterizing Kidney Disease

Alterations within a subsection of the nephron, influence surrounding interconnected systems to create a negative feedback loop that slowly degrades kidney health over time. While current standards for diagnosing kidney disease rely on sustained decreases in eGFR or increases in albuminuria [62], this approach fails to capture the structural integrity of the kidney and is unsuitable for early disease detection [63]. A few of the consequences of hyperglycemia, hyperfiltration, and hypertension include changes in hemodynamics, decreases in microvascular density, tubular thickening and atrophy, glomerular hypertrophy, glomerulosclerosis, and kidney fibrosis [54,64,65]. Kidney biopsies provide definitive evidence of tubular atrophy, fibrosis, and glomerular scarring, but are invasive and the risks may outweigh the benefits in CKD patients [43,66]. Novel strategies for early identification of kidney disease have focused on detecting biomarkers for these morphological and functional changes in the glomerulus, tubules, and microvasculature.

Different serum and urine markers with the potential to identify and predict CKD progression have been studied for the early diagnosis of kidney disease. Gohda et al. and Niewczas et al. evaluated the ability of tumor necrosis factor receptors (TNFRs) to predict CKD in T1D and ESKD in T2D, respectively [67,68]. The results from Gohda et al. demonstrated that levels of circulating TNFR1 and TNFR2 strongly associated with risk of GFR loss, and Niewczas et al. determined that circulating TNFR1 strongly associated with ESKD risk [67,68]. Neutrophil gelatinase-associated lipocalin (NGAL) was also studied as a possible early predictor of diabetic nephropathy and was found to increase in T1D patients prior to elevations in microalbuminuria [69]. Kidney Injury Molecule-1 (KIM-1) expression has been shown to correlate with tubular injury and fibrosis and has the potential to serve as a non-invasive test for

CKD [70,71]. In addition to serum and urine markers, imaging may provide a more comprehensive approach to characterizing kidney disease. A plethora of different functional MRI techniques have been developed to assess kidney fibrosis [72,73], hypoxia [74–76], and microstructure [77,78]. Molecular MRI using cationized ferritin to determine glomerular size and number has arisen as another possible marker predictive of kidney disease [79,80]. In addition to MR, ultrasound imaging has been explored as a tool for characterizing kidney disease, focusing on assessing changes in kidney perfusion. Certain ultrasound imaging techniques have the potential to pick up on subtle microvascular changes and may prove useful for early disease detection and prevention. The merits of ultrasound imaging for classifying kidney disease will be discussed further in the following chapter.

CHAPTER 2: ULTRASOUND IN MEDICINE

2.1 Medical Ultrasound

Ultrasound is characterized by acoustic frequencies beyond the range of human hearing (> 20 kHz) with medical ultrasound transducers typically operating between 1-15 MHz [81–83]. Ultrasound probes are designed with a specific transmit frequency bandwidth, geometry, and footprint size depending on the intended application (Figure 2.1).

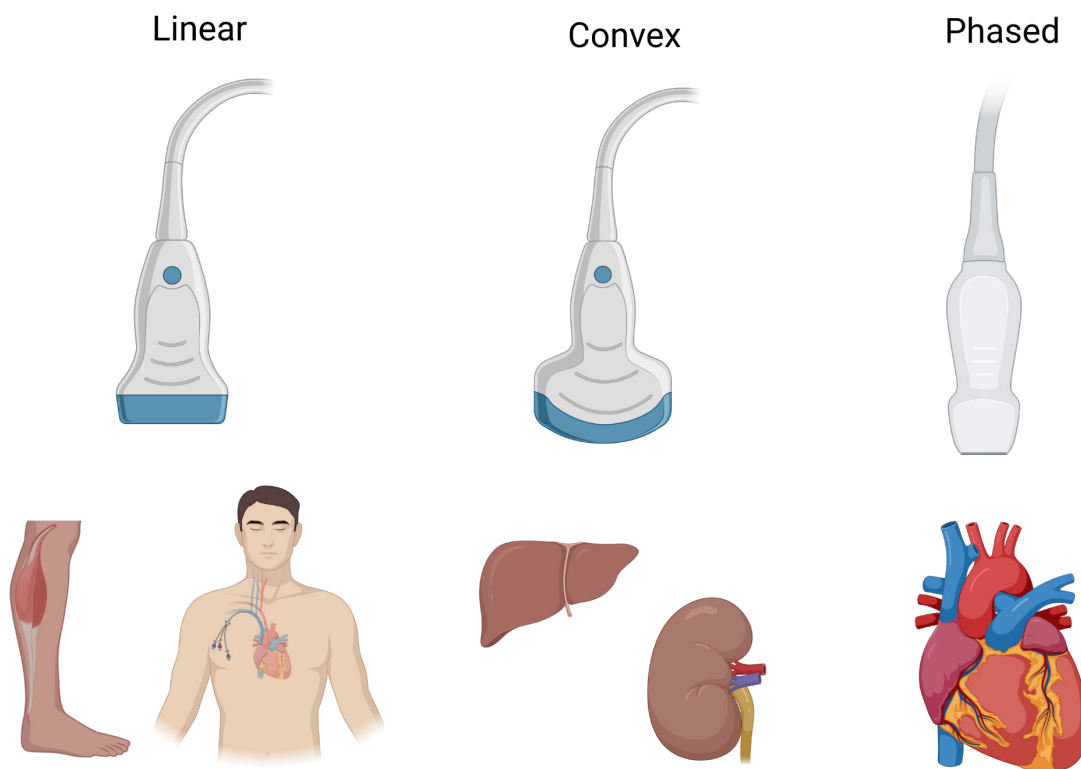


Figure 2.1 Transducer design and application. Uses of linear arrays include superficial imaging of muscle and aid in venous catheter placement, convex arrays facilitate imaging of larger organs at depth, and phased arrays enable imaging through a narrow acoustic window, such as cardiac imaging through the rib cage. Created with BioRender.com.

To generate an image, an acoustic pressure wave is transmitted into the tissue of interest and the returned signal recorded, where the amount of reflection, scattering, and tissue absorption dictate how much energy reaches the receiver. The received signal is then used to construct an image by summing the individual amplitude (A-mode) lines from each transducer element to form a two-dimensional brightness mode (B-mode) image. This type of conventional ultrasound imaging is frequently used in the clinic for a variety of diagnostic purposes such as cardiac [84], breast [85], and abdominal [86] imaging. B-mode ultrasound is well suited for soft tissue imaging, but performs poorly when imaging blood due to the low scattering of red blood cells (RBCs) relative to tissue [82,87]. To address this limitation, Doppler imaging was developed in the late 1950s, initially as a way to visualize blood flow in peripheral arteries and to detect motion in the heart [88]. Advances in Doppler imaging technology have improved its capabilities to include visualization of complex velocity maps [89] and even monitoring tumor perfusion in response to anti-angiogenic treatment [90]. Although Doppler ultrasound excels at imaging larger blood vessels, it cannot adequately capture slower flow in microvasculature [85,91,92]. With other imaging modalities, such as CT and MRI, contrast agents are added to improve sensitivity to both tissue and vascular features [93,94]. Similarly, the addition of ultrasound contrast agents combined with contrast-specific imaging techniques can improve ultrasound sensitivity to smaller vessels.

2.2 Contrast-Enhanced Ultrasound

One of the first uses for ultrasound contrast agents (UCAs), or microbubbles, was vascular illumination during ultrasound examinations. Over the course of their development, microbubbles have now come to serve a variety of functional and therapeutic purposes.

Microbubbles (MB) are true blood pool agents, on the order of 1-10 μm [95,96], with a size and

rheology similar to that of red blood cells [87,97]. These properties help make UCAs well suited for vascular imaging. Exact microbubble formulations vary, but in general UCAs are composed of an elastic shell surrounding a dense, inert gaseous core [98]. Commonly used shell materials include lipids, proteins, or polymers [99], and typically low solubility gases such as sulfur hexafluoride (SF_6), decafluorobutane (DFB, C_4F_{10}), or octofluoropropane (OFP, C_3F_8) are incorporated as the gaseous core (Table 2.1).

Table 2.1 Formulations for different ultrasound contrast agents

Microbubble Agents	Shell Type	Filling Gas	Concentration (mL^{-1})
SonoVue®	Lipid	SF_6	5×10^8
Definity®	Lipid	C_3F_8	1.0×10^{10}
Sonazoid™	Lipid	C_4F_{10}	1.2×10^9
BR55	Lipid	$\text{C}_4\text{F}_{10}/\text{N}_2$	2×10^9
Optison™	Albumin	C_3F_8	$5\text{-}8 \times 10^8$

DFB, although not commonly used in commercial agents, is frequently used in research settings as an ideal agent due to its lower solubility and diffusivity relative to SF_6 or OFP (Table 2.2). Differences in microbubble compressibility and density in relation to the surrounding medium generate a strong acoustic signal, the magnitude of which is dependent on intrinsic properties of the bubble [96]. For instance, exciting a bubble on resonance greatly improves the backscattered echo, contributing to better signal to noise ratio and contrast sensitivity [100]. Fortuitously, clinically relevant transmit frequencies (1-10 MHz) align with typical microbubble size distributions such that microbubbles are excited on resonance.

Table 2.2 Solubility and diffusivity in water for common microbubble filling gases

Filling Gas	Solubility in water (Ostwald coefficient)	Diffusivity in water (m^2/s)
SF_6	5.4×10^{-3}	1.20×10^{-9}
C_3F_8	5.2×10^{-3}	7.45×10^{-10}
C_4F_{10}	2.02×10^{-4}	6.9×10^{-10}

Several imaging techniques have been developed to delineate microbubble signal from tissue signal. These techniques rely primarily on the nonlinear behavior of microbubbles in an acoustic field, which results from asymmetric oscillation between microbubble compression and rarefaction [92,101]. When insonified, microbubbles produce a broadband response, emitting frequencies both above (second harmonic and super harmonics) and below (subharmonics) the fundamental frequency (Figure 2.2). In comparison, tissue has a primarily linear response to a propagating wave, although does enter the nonlinear regime when exposed to higher acoustic energies [102].

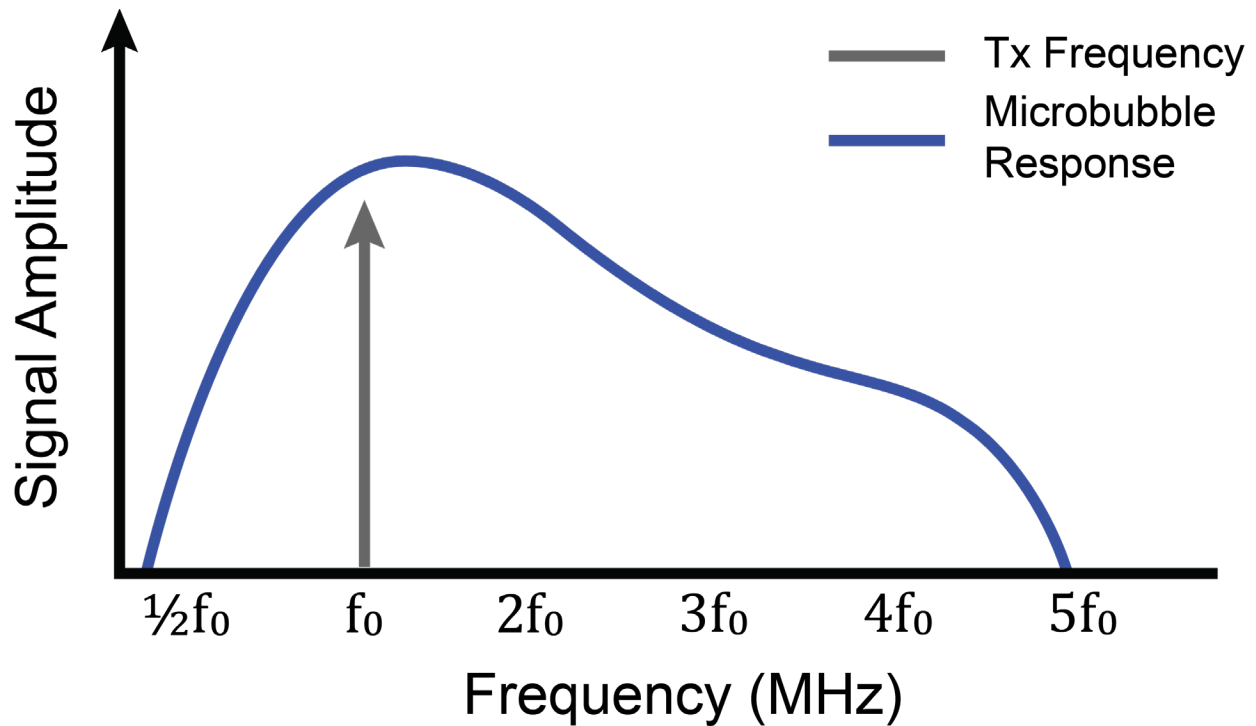


Figure 2.2 Broadband microbubble response. In response to an acoustic waveform transmitted at the fundamental frequency (f_0), a microbubble emits frequencies across the spectrum, at subharmonics as well as second harmonics and higher. Microbubble detection techniques take advantage of this harmonic content to isolate microbubble signal.

Tissue harmonic imaging takes advantage of this phenomenon to reduce side lobe interference and improve image contrast [82,85]. When restricted to lower acoustic pressures, harmonic imaging can be used to selectively detect microbubble signal, however this method limits receive frequencies to a narrow bandwidth. Pulse-inversion is an alternate technique for bubble detection that utilizes the full receive bandwidth when measuring the response from microbubbles. Two waveforms of opposite phase are transmitted in succession and the receive patterns summed to form the final image [82,101,102]. The linear response from tissue cancels out, while the nonlinear response from bubbles is retained (Figure 2.3).

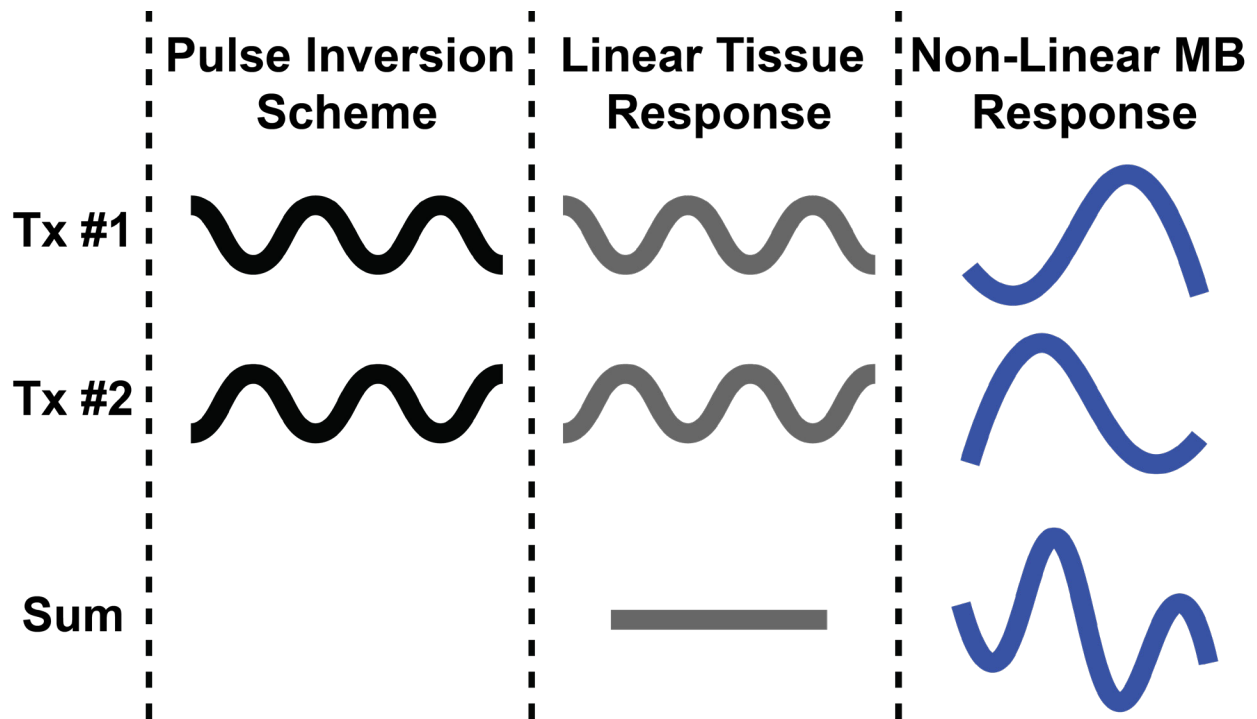


Figure 2.3 Pulse-inversion imaging scheme. Two separate waveforms (Tx #1, Tx #2) are transmitted sequentially, with the phase of the second inverted relative to the first. Summing the linear tissue response from both waveforms leads to signal cancellation, while the non-linear microbubble response is retained.

To increase sensitivity to microbubbles, amplitude modulation can also be incorporated into the transmit sequence. A combination of phase-inversion and amplitude modulation is often used in clinical ultrasound systems [92]. These microbubble-specific techniques combined with the powerful echo response generated by UCAs excited on resonance are sensitive enough to detect single bubbles [87,99]. Superharmonic imaging, receiving only the higher microbubble harmonics, can further improve image quality and produces impressive vascular maps, but requires specialized equipment (dual frequency arrays), which are not yet widely available.

In addition to microbubble-specific imaging modes, various data acquisition techniques have been developed that use contrast-enhanced ultrasound (CEUS) imaging to detect disease and monitor disease progression. Typically, data is collected using low mechanical index (MI)

imaging to preserve microbubble signal. At higher pressures, microbubble oscillation becomes increasingly unstable leading to fragmentation and rupture [99,103,104]. This effect is usually avoided, however, there are specific applications and imaging sequences that briefly utilize microbubble destruction pulses during data collection. For example, such methods have been implemented to aid in the quantification of tissue and tumor perfusion or with targeted microbubble imaging.

2.3 Ultrasound Molecular Imaging

Ultrasound imaging can be performed with targeted microbubbles, which behave differently than non-targeted bubbles used for contrast enhanced ultrasound perfusion imaging. Microbubbles are modified by incorporating a targeting ligand on the outer shell of the bubble. Surface modification lets the bubble bind selectively to vascular markers, allowing the bubble to facilitate site-specific delivery of a therapeutic payload or to serve as a molecular imaging probe. The use of targeted MBs to gain insight into the molecular activity of a specific site has been termed ultrasound molecular imaging (USMI).

2.3.1 Detection Methods for Targeted Microbubbles

Ultrasound molecular imaging relies on the ability to distinguish targeted MBs that have attached to the vascular endothelium from unbound, freely flowing bubbles. In the absence of a targeting ligand, MBs will flow uninterrupted through the vasculature, with signal loss largely attributed to clearance by the lungs and the reticuloendothelial system. However, when a targeted MB attaches to the vessel lumen, the main mechanism for signal decay results from gas dissolution. These differences in signal deterioration and targeted microbubble retention can be taken advantage of to differentiate bound and free flowing bubbles. Briefly, an injection of

targeted MBs is followed by a wait period between 5-10 minutes to simultaneously allow bubble accumulation at the site of interest and clearance of freely circulating bubbles (Figure 2.4).

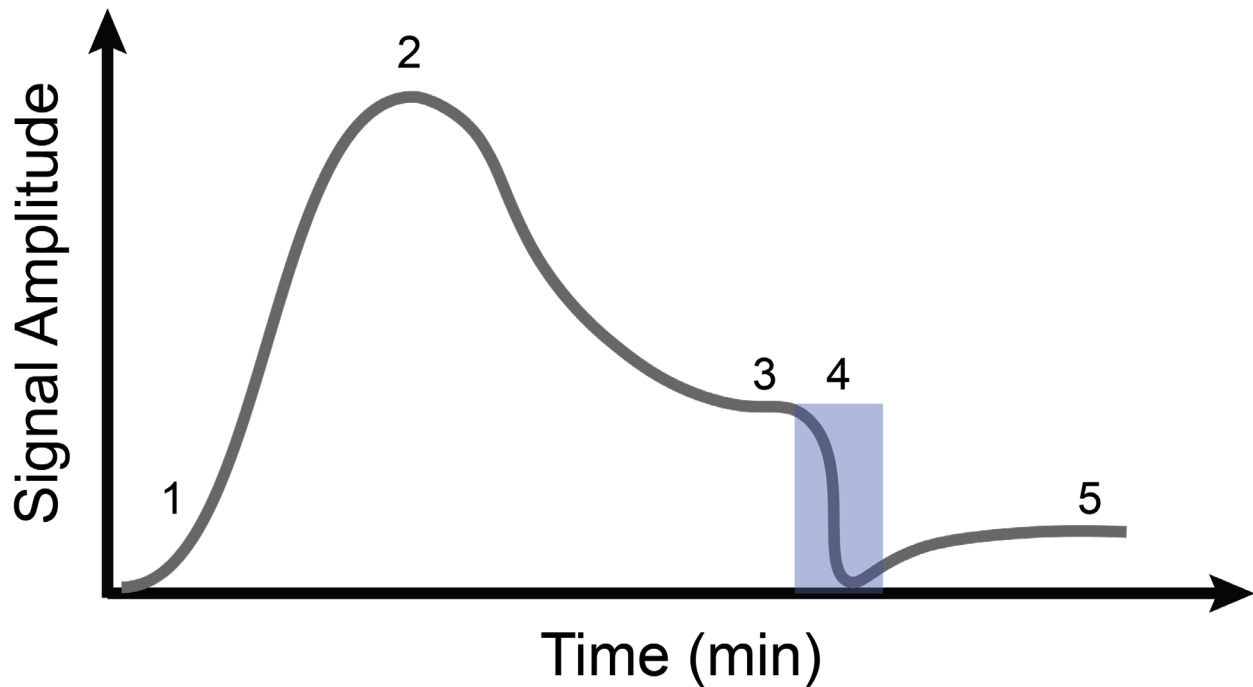


Figure 2.4 Microbubble kinetics for differential targeted enhancement. Targeted microbubbles injected intravenously enter the FOV at the site of interest (1) and increase in concentration until reaching peak enhancement (2). Freely flowing bubbles circulate and begin to clear over time, while adhered bubbles accumulate at the site of interest (2 → 3). After a sufficient wait period, an image of the total signal (free and attached) in the region of interest is acquired (3). Immediately following, a short high energy burst pulse is introduced to silence all bubbles in the FOV (4, purple rectangle). Any remaining unattached freely circulating bubbles are allowed to re-enter the FOV prior to acquiring an image containing signal from only free bubbles (5).

Intermittent imaging may also be performed during this time, but should be minimized to avoid disrupting adhered bubbles. At the end of the dwell time, an image of the region of interest (ROI) is acquired, which contains signal from bound and unbound MBs (Figure 2.5a). Immediately following, a high MI pulse is implemented to silence all bubbles in the field of view (FOV), both free flowing and adhered. Next, a post-break image is collected to capture signal from any remaining freely circulating bubbles (Figure 2.5b). The result of this post-break image

is subtracted from the pre-break image to produce a measure of bound microbubble signal, a technique called differential targeted enhancement (dTE).

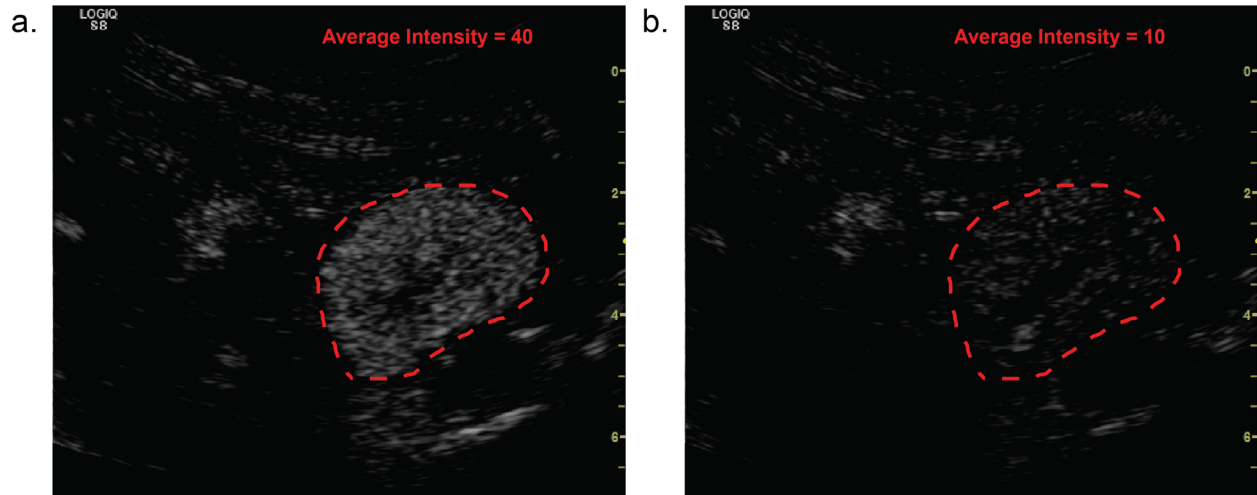


Figure 2.5 Example of differential targeted enhancement image acquisition. a) Image acquired prior to microbubble destruction (MBD) with an average intensity in the kidney (red dashed line) measuring 40 A.U., representing signal from both bound and freely flowing bubbles. b) Image acquired post MBD with an average intensity of 10 A.U., representing only signal from freely flowing bubbles. The signal difference (30 A.U.) reflects the bound bubble intensity.

Other methods besides the classic image-destroy-image technique have been developed to differentiate adherent from free flowing bubbles. Pharmacokinetic modeling may offer real-time analysis of targeted MB behavior. Sirsi et al. used a two-compartment pharmacokinetic model to distinguish bound from unbound MBs by comparing the time-intensity and time-fluctuation curves [105]. A modified random-walk algorithm has also been proposed, incorporating a ramp function, where the slope represents MB accumulation due to attachment at the site of interest [106]. The unique non-linear behavior of MBs and distinct temporal characteristics of attached, stationary bubbles has enabled additional methods for bound bubble detection. One technique uses harmonic imaging to isolate MB signal from tissue signal, followed by inter-frame low pass filtering through slow time to distinguish adhered and non-adhered bubbles [107–109]. Another method takes advantage of the differences in the temporal

echo characteristics of bound compared to free flowing bubbles, using decorrelation to distinguish between bubbles in an attached or unattached state [110,111].

2.3.2 Applications of Ultrasound Molecular Imaging

Various vascular targeting ligands have been explored for USMI, with notable applications including the detection of inflammation, thrombus, and tumor angiogenesis. Inflammation coincides with many disease processes, including ischemia-reperfusion injury, transplant rejection, and inflammatory diseases in the gastrointestinal tract, heart, liver and kidneys [112]. Cell adhesion molecule expression is upregulated with the onset of inflammation and MBs targeted to these molecules (ICAM-1, VCAM-1, E-selectin, and P-selectin) can be used to monitor inflammatory processes. For example, selectin-targeted MBs have been used to assess ischemia-reperfusion injury, and have shown the ability to identify previously ischemic tissue [113–115]. Weller et al. used MBs targeted to ICAM-1 to assess post-operative myocardial tissue acceptance and rejection, where increased signal intensity indicated graft rejection [116]. Single, dual, and even triple-targeted agents have been successful at monitoring response to anti-inflammatory treatment *in vivo* [117–119]. Evaluating tumor angiogenesis is another major focus for USMI. As mentioned previously, new vascular growth is a hallmark of cancer, with many tumors overexpressing vascular markers. VEGFR2 and $\alpha_v\beta_3$ integrin are two key components of oncogenic signaling that have received much attention in USMI research. USMI targeted signal intensity can be used to differentiate benign and malignant breast tissue with high sensitivity and specificity [120]. Studies by Ellegala et al., Grouls et al., and Pysz et al. have shown that measuring $\alpha_v\beta_3$ integrin and VEGFR2 expression on tumor and dysplastic endothelial cells supports earlier cancer detection and intervention [121–123]. In preclinical cancer models, USMI can successfully monitor and even predict tumor angiogenic activity in response to treatment

[124–127]. In fact, tumor responsiveness to bevacizumab, an anti-angiogenic drug, was determined by $\alpha_v\beta_3$ integrin-targeted MBs after just three days, much earlier than tumor volume or tumor perfusion measurements [125]. In a study by Zhou et al., observable decreases in USMI signal from VEGFR2-targeted MBs occurred as early as one day following tumor treatment with bevacizumab [126]. Tumor response to sunitinib malate was identified by VEGFR2-specific MBs just one week after treatment, but significant tumor volume changes were not observed until three weeks following treatment [127]. Many advances have been made to strengthen the preclinical applications of USMI. These improvements have helped address current challenges and limitations to aid in the clinical translation of this technique.

2.3.3 Improvements to Ultrasound Molecular Imaging

One limitation faced by ultrasound molecular imaging is the low numbers of bubbles that initially adhere and then remain bound to the target site. Lack of ideal targeting may provide an underestimate of the actual molecular expression, hindering accurate diagnosis of current disease state. To address this issue, techniques have been adopted to mitigate the causes behind low bubble adherence. Two factors that influence bubble binding include ligand exposure to the targeting site and microbubble persistence in circulation.

2.3.3.1 Acoustic Radiation Force

Sufficient time and proximity is required to facilitate lasting ligand interaction with the desired receptor [128,129]. Microbubbles flowing through circulation present a two-fold problem for the successful attachment of ligands to the target receptor: 1) a microbubble flowing through the center of a vessel exists far from the vessel wall, and 2) with non-zero velocity spends less time exposed to the target vascular receptors. The implementation of acoustic radiation force (ARF) alongside USMI has helped to mitigate this issue. Applications of ARF extend beyond

USMI, however for this work, ARF pulses that support microbubble translation are considered. Radiation force used in this manner is characterized by low pressure, long pulse duration, high pulse repetition frequency transmit sequences [128,130,131]. The time-varying pressure gradient from an acoustic wave coupled with an oscillating bubble cause a net force to be experienced by the bubble [132,133]. This resultant force on a microbubble from a traveling acoustic wave causes bubble displacement in the direction of wave propagation, referred to as primary acoustic radiation force [130]. Secondary forces arise from the exertion of a radiating pressure field from one oscillating bubble acting on another, where bubbles oscillating in phase experience an attractive force that results in bubble aggregation [130]. The magnitude of this force is inversely proportional to the bubble separation distance squared and can exert an influence across a distance of 100 microns [134]. The aggregation behavior from secondary ARF is transient and subsides shortly after the conclusion of the transmit sequence [134]. Studies by Dayton et al. have demonstrated that ARF pulses can result in bubble displacement across hundreds of microns [130,134]. Further, bubble displacement across multiple microns can be achieved at velocities upwards of 0.5 m/s [135]. The magnitude and speed of this displacement is ideal for increasing targeted UCA interaction with the blood vessel wall, particularly in microvasculature, with diameters between 10 to 100 microns. Studies evaluating targeting enhancement using ARF have demonstrated over 60-fold increases in bubble adhesion *in vitro* and up to 20-fold increases *in vivo* between the treated (ARF) and untreated (no ARF) conditions [129,136,137]. When applied to volumetric imaging, an almost 80% increase in targeting was achieved in the presence of ARF compared to the absence of ARF [138]. Radiation force-assisted targeting may also decrease the MB dose required to achieve measurable bound bubble signal, increasing the ratio of specific to non-specific binding (reducing the amount of off target binding) and reducing

imaging time [131]. Faster circulating bubble clearance from a lower initial MB dose is advantageous since conventional USMI detection methods implement a dwell time between 5-10 minutes to allow sufficient targeted bubble accumulation in relation to freely circulating bubble clearance. Other approaches have been developed to improve the circulation time of targeted microbubbles.

2.3.3.2 Buried Ligand Architecture

In the absence of a targeting ligand, unmodified freely flowing microbubbles will persist in circulation for multiple minutes. The main mechanism for their removal is uptake by the reticuloendothelial system primarily in the lungs, liver, and spleen [139,140]. These organs have capillary beds with large populations of phagocytic cells, such as the Kupffer cells in the liver, which can remove MBs from circulation. Similarly, circulating white blood cells, such as neutrophils, can also bind to MBs and facilitate their removal from the blood stream. Although the materials used to fabricate microbubbles are biocompatible, the attachment of a targeting ligand to the surface of a microbubble for targeted imaging exposes the microbubble to the mononuclear phagocyte system. Subsequently opsonization occurs, whereby the complement protein C3b binds to the MB surface and tags the bubble for immune clearance. The addition of C3b also changes the ligand binding properties. Complement activation is detrimental to USMI by expediting targeted MB clearance and interfering with binding dynamics [141]. To offset targeted bubble immunogenicity, Borden et al. and Chen et al. have developed a fabrication method that shields the targeting ligand using a polyethylene glycol (PEG) overbrush [142–144]. A 5000 Da PEG chain is incorporated onto the bubble surface and covers the targeted ligand attached via a shorter (2000 Da) PEG tether [142]. This surface modification, termed buried ligand architecture (BLA), conceals the ligand to prevent interaction with not only the immune

system, but also the desired vascular markers. However, ligand availability can be modulated by inducing radial oscillations via ARF to transiently expose the ligand to its vascular target, resulting in adhesion at a comparable level to MBs with exposed ligand architecture [144,145]. Borden et al. demonstrated 30-50% improvement in detectable circulation time in a rodent kidney [144] and a three-fold increase in persistence in tumor vasculature with the use of BLA MBs compared to exposed-ligand MBs [146]. Further, with the application of ultrasound radiation force BLA MBs achieved higher binding specificity compared to their exposed ligand counterparts [146]. These studies demonstrate that BLA UCAs facilitate localized adhesion mediated by ultrasound radiation force, increase agent specificity, reduce off target adhesion, and successfully bypass complement activation to improve contrast persistence. These results strongly support the implementation of BLA UCAs as a method to improve USMI.

2.3.3.3 Tailoring Microbubble Size

The aforementioned techniques aim to enhance USMI by improving contrast agent adhesion and binding specificity by taking advantage of microbubble behavior in an acoustic field and modifying surface architecture. Another option for improving USMI is to increase contrast sensitivity by tailoring the microbubble distribution to isolate bubbles of a certain size [100,147,148]. Most transducers operate with a limited bandwidth and are less sensitive to polydisperse microbubble populations [147]. For molecular imaging, where low numbers of bubbles are retained at the target site, detection of only a small percentage of the overall microbubble population presents a significant limitation for the accurate depiction of disease pathology. Thus, it becomes important to tailor microbubble size distribution to optimize detection by the ultrasound system. This can be achieved by tuning microbubble size to generate stronger echo amplitudes. Kaya et al. demonstrated that backscattered echo amplitude increased

by exciting bubbles at their natural resonance frequency and by selecting microbubbles with a larger radius [100]. Further, Streeter et al. found that bubbles with a larger diameter (3 μm) resulted in an almost twentyfold increase in measured targeted signal intensity compared to polydisperse bubbles and showed increased persistence in circulation [148]. The increase in circulation time can be explained by the microbubble dissolution behavior, which is influenced by the initial bubble radius [149,150]. As such, selecting larger monodisperse bubbles improves the sensitivity of USMI by increasing microbubble persistence to allow more time for targeted bubble interaction with the vascular endothelium and by producing greater echo amplitudes.

2.3.3.4 Volumetric Imaging

Lastly, volumetric imaging has been explored as a method of increasing the accuracy of USMI. The majority of available clinical and preclinical transducers are designed to capture data in 2D, which often limits acquired information to a single imaging plane. Taking into consideration the oftentimes complex and heterogeneous vascular environment present in disease, such as within a tumor, gathering information from only a single slice may misrepresent molecular activity in the tissue. On the other hand, acquiring three dimensional (3D) data should provide a comprehensive, and therefore more accurate, evaluation of molecular expression within a tumor or other tissue of interest. Volumetric scanning can be achieved with a linear array transducer by mounting the probe on a linear actuator or stage to translate it across the tissue volume, collecting images for each step in the volume. Streeter et al. collected volumetric data in this manner and compared targeting as determined by the 3D data to that determined by 2D data from the center slice of the tumor [148]. The results from Streeter et al. revealed that volumetric signal intensity from targeted bubbles could have been overestimated or underestimated by 16% and 28%, respectively, when considering only the center slice of the

tumor volume [148]. This work also demonstrated the spatial heterogeneity in molecular expression present across a tumor volume and the possibility of introducing significant measurement error due to slight deviations in transducer placement or a minor shifting of position over the course of a study. Three-dimensional data acquired by stepping the transducer across a tissue volume can be difficult to implement in practice without specialized equipment. An alternate approach utilizes 2D matrix arrays to acquire 3D data. Wang et al. demonstrated the feasibility and reproducibility of using a clinical matrix array to monitor response to treatment in a colon cancer model [151]. Similar to Streeter et al., the results from Wang et al. confirmed the spatial heterogeneity of tumor vasculature and quantified error introduced by using only 2D imaging. In their study, on average, tumor response to treatment was overestimated by 27% using a single slice compared to the volumetric data [151]. Potential under- and oversampling of molecular expression in the tumor from 2D imaging provides an inaccurate depiction of tumor response to treatment advocating for the use of 3D imaging. When implemented, these methods for acquiring 3D data show improvements in the overall accuracy of USMI for characterizing disease.

In summary, much of the progress pertaining to USMI has revolved around preclinical imaging in small animal models with a focus on evaluating response to anti-angiogenic therapy. Very little work assessing the feasibility of monitoring response to other forms of treatment (i.e. radiation therapy) has been completed. Additionally, although the value of longitudinal USMI to monitor and predict tumor response to treatment using *in vivo* models has been clearly demonstrated, implementation in a clinically relevant population has not been well studied. This is due in part to lack of widely available clinically approved targeted agents as well as the need to address key limitations such as low numbers of bound bubbles present at the target site and

activation of the immune system resulting in rapid clearance of targeted UCAs over time. Techniques discussed above, including the use of acoustic radiation force, buried ligand architecture, volumetric imaging, and size-isolated bubble distributions have proven useful for mitigating some of the limitations faced by USMI. Their successful application in preclinical models resulting in remarkable improvements to USMI has paved the way for the clinical translation of USMI. In this work, these strategies to enhance USMI will be implemented in a novel manner to assess tumor response to radiation therapy using longitudinal USMI in a rodent model (Chapter 3), and to validate the use of longitudinal USMI for monitoring response to therapy in a clinically relevant canine population (Chapter 4).

2.4 Perfusion Imaging

Ultrasound contrast agents were originally conceived as a freely circulating blood tracer [136]. With a size and rheology similar to RBCs, microbubble contrast agents serve as a marker for measuring vascular perfusion. Microbubbles remain confined to the vascular space [91] and monitoring microbubble transit through an organ provides a method for extracting parameters related to blood velocity, flow, and volume. Indeed, contrast-enhanced ultrasound can characterize blood flow with high temporal and spatial resolution, which proves useful for assessing microcirculation and providing quantitative measures of tissue perfusion [91]. Notable uses of CEUS perfusion imaging include the evaluation of blood flow in tumors, the liver, and kidneys [152].

2.4.1 Indicator-Dilution Bolus Imaging

Perfusion data is typically acquired by introducing UCAs in one of two ways, either through an instantaneous bolus injection or by delivering a constant infusion. An advantage of bolus imaging is that a small dose of the agent can be administered to capture the entire influx

and efflux of the UCA through an organ of interest over the course of multiple minutes. The kinetics of the bolus UCA dose follow that of a tracer diluted over time as it is distributed throughout the system (circulation), allowing indicator-dilution principles to be applied to estimate blood flow and volume [153–155]. A number of appropriate distributions are available for fitting the extracted time-intensity curve (TIC) data to derive parameters that describe the microcirculation. Most commonly, the lognormal, gamma variate, local density random walk (LDRW), and lagged normal models are utilized given that the basis for these models fits expected flow distribution, mixing, and vascular branching throughout different tissue types [156–158]. The solutions to these models provide estimates of mean transit time (mTT) – the time it takes the UCA to pass through the region – and time to peak enhancement (TTP). Additional parameters such as area under the curve (AUC), wash-in rate (WiR), wash-out rate (WoR), rise time, fall time, and other features can be derived based on the model (Figure 2.6). The fitted curves provide many advantages over the raw data, by reducing noise in the image, extracting just the first pass behavior of the bubbles, and providing an analytical solution for specific perfusion parameters.

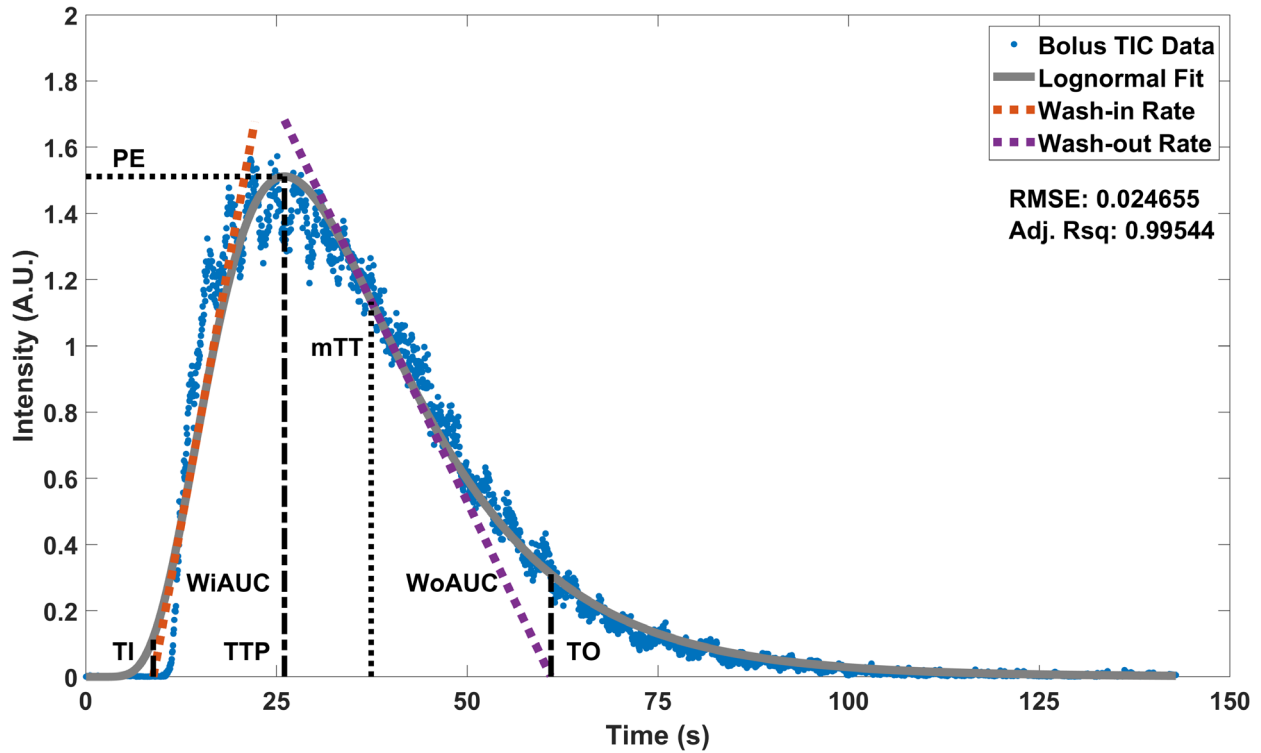


Figure 2.6 Lognormal fit (gray) of bolus time-intensity curve data (blue). Analytical solutions are provided for mTT and TTP, while other time, area, and intensity-based parameters are derived from the model (PE = maximum intensity, WiR (dashed orange) = maximum slope, WoR (dashed purple) = minimum slope, WiAUC = integral from TI (WiR zero-crossing) to TTP, WoAUC = integral from TTP to TO (WoR zero-crossing).

2.4.2 Flash-Replenishment Imaging

Flash-replenishment imaging uses a constant infusion delivery method to collect data on tissue perfusion. Continuous UCA administration is required in order to achieve steady state concentration in the tissue. The steady state intensity is recorded prior to introducing a high-powered burst that disrupts all microbubbles in the field of view. Following the burst, the ultrasound system reverts to low pressure imaging to capture MB replenishment throughout the region until steady state levels are re-established. The reperfusion data from the time-intensity curve is isolated and fit with a model to estimate parameters related to blood flow (Figure 2.7). The extracted parameters are related to blood velocity, blood volume, and flow rate in the region of interest. Sigmoidal and exponential models are most often used to fit flash-replenishment

reperfusion data given that refilling in the presence of a steady influx of the tracer results in a rapid increase in measured signal followed by reaching an eventual plateau [159–162].

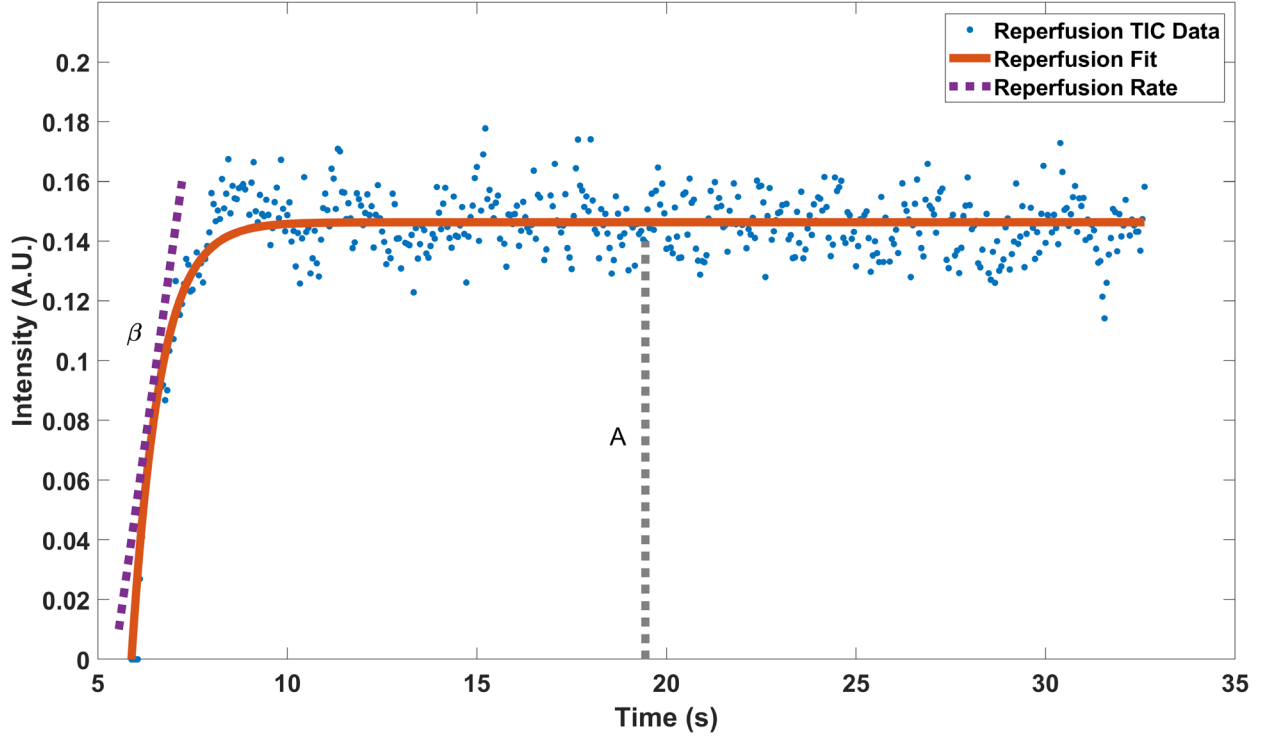


Figure 2.7 Monoexponential fit (orange) of flash-replenishment time-intensity curve reperfusion data (blue). Reperfusion rate (dashed purple, β) and steady state (dashed gray, A) are the coefficients of the model solution and represent relative blood velocity and blood volume, respectively.

2.4.3 Evaluation of Perfusion Imaging Methods

Bolus imaging and flash-replenishment imaging both provide relative measures of microvascular blood volume, velocity, and flow, in addition to other available time/rate-based, enhancement, and combined parameters [163,164]. Both techniques have been evaluated for their repeatability and reproducibility when considering factors such as acquisition settings, patient variability, and operator variability. Reported bolus parameters with the least amount of variance include rise time and mTT [165,166], AUC [167,168], and TTP [169] depending on the study design and organ of interest. However, large variances (>50%) within bolus parameters

have also been reported [165–169]. Standardizing study protocols [170] and the availability of commercial software packages such as VueBox® (Bracco Suisse, Geneva, Switzerland), which provide consistency in data analysis [171], have helped improve parameter reproducibility. Unfortunately, variations in parameter definition, notation, and number reported still exist among studies using bolus imaging for CEUS perfusion analysis (Table 2.3) [164]. In comparison, Williams et al. 2011 demonstrated that the reproducibility of flash-replenishment imaging parameters was higher than for bolus parameters [172]. The repeatability of flash-replenishment imaging parameters has been reported primarily for preclinical imaging as flash-replenishment imaging has not reached the same frequency of use in the clinic as bolus imaging.

Table 2.3 Definitions and notations for bolus imaging perfusion parameters

Parameter	Abbreviation	VueBox Definition and Uses [173–175]	Alternate Forms or Definitions
Peak enhancement	PE	Maximum intensity in the region of interest	Peak intensity (I_p or PI) [165–168,176,177]
Rise time	RT	Time from the point where the maximum slope tangent intersects with the x-axis (TI) to peak enhancement	Wash-in time (WIT) or RT: time from 5% to 95% of I_p [166,176], time from 10% to 90% of PE [170], time from zero to PI [165]
Local mean transit time	mTTI	Average time (local) for bubbles to pass through the ROI determined by subtracting TI from the time span of the curve full-width half maximum (FWHM)	mTT: the first mathematical moment [166,176] MTT: the time span of the FWHM [167,168,170]
Time to peak	TTP	Time from the initial bolus dose injection to PE [170]	time from contrast arrival to PI (t_p or T_{pi}) [167,168,176,177]
Fall time	FT	Time from peak enhancement to the point where the minimum slope tangent intersects with the x-axis (TO)	Wash-out time (WOT): time from PI to zero intensity [176]
Wash-in rate	WiR	Maximum slope	Upslope determined from data points 10% above baseline to 85% of PE [178]
Wash-out rate	WoR	Minimum slope	Not reported
Wash-in area under the curve	WiAUC	AUC from the arrival of contrast (TI) to PE	Area under the wash-in (AUWI) [167,168]
Wash-out area under the curve	WoAUC	AUC from PE to TO	Area under the wash-out (AUWO) [167,168]
Wash-in and wash-out area under the curve	WiWoAUC	Combined AUC for wash-in and wash-out	AUC: first appearance of UCA in the ROI to a predefined end time [176] or until the last point on the curve [170]

Xie et al. evaluated the repeatability of flash-replenishment imaging for assessing hepatic microvascular perfusion in a rabbit model, specifically addressing infusion rate, parameter consistency across depth, and operator consistency [179]. The perfusion estimate A (steady state, referenced here as perfusion peak intensity) was significantly different ($P < 0.05$) for the lowest infusion rate (2×10^8 MB/min) compared to the two higher infusion rates (3×10^8 MB/min, 4×10^8 MB/min), but was stable across the upper two infusion rates ($P > 0.05$). Variations in steady state across depth were also observed, with coefficients of variation (CVs) ranging from 3.9-30.3%. Lastly, intra-operator and inter-operator intraclass correlation coefficients were reported as 0.985 and 0.948, respectively, demonstrating strong agreement within and between operators [179]. Variability in flash-replenishment parameters has also been reported based on ROI size, with a small ROI (50 pixels) resulting in large variation followed by substantial reductions in variation with increasingly larger ROIs (100-500 pixels) [162]. Lastly, one study found that repeated measurements of cortical renal blood flow resulted in a CV of 11.9% and 24.5% for two different flash-replenishment models [180]. Flash-replenishment parameters are reported with consistent definitions, where steady state/signal plateau (A), reperfusion rate (β), and the cross product perfusion index ($A\beta$, denoted PI), are related to blood volume, blood velocity, and flow rate, respectively [162]. Less discrepancy regarding the definitions of these parameters may be attributed to the fact that much of the current work using the flash-replenishment technique incorporates the same base mathematical model to describe reperfusion behavior [163]. The most general form is provided as (2.1):

$$y = A(1 - e^{-\beta t}) \quad (2.1)$$

where coefficients A and β equate to steady state and reperfusion rate, respectively. Other models have been proposed, such as Krix's multivessel model and the Arditi-Hudson model,

based on the physiological bubble behavior and physical principles [159,160,180–182]. Despite differences in the derivations of these models, the resultant parameters still provide descriptions of blood volume, velocity, and flow in a similar manner as the monoexponential model, based on the maximum intensity (plateau) and refill slope. Krix et al. found that the multivessel model parameters were highly correlated (0.99 between each model plateau, 0.94 between each model slope) to the monoexponential model parameters [159].

In short, although flash-replenishment imaging is influenced by parameter variability, the consistency among reported parameters and ability to reduce variation by careful selection of ROIs and fine-tuning imaging parameters support its use as an accurate and repeatable tool for measuring tissue perfusion [162,179]. New models based on a physical description of the replenishment process have also helped reduce parameter variability [180,182]. Additional advantages of flash-replenishment imaging include rapid image acquisition (10-30s), the ability to collect repeated measures and data in multiple sections of the tissue volume to better account for heterogeneity, and less susceptibility to external influences resulting from the use of a replenishment method as opposed to a tracer dilution method [165,172,182]. Despite these benefits, flash-replenishment imaging is not often utilized in a clinical setting. However, the exploration of CEUS flash-replenishment perfusion imaging, particularly for characterizing kidney disease, has slowly begun to gain traction. Here, the role that flash-replenishment CEUS imaging plays in characterizing kidney disease will be evaluated to identify perfusion parameters able to differentiate healthy and diseased kidneys (Chapter 5) and to assess the performance of flash-replenishment CEUS imaging for differentiating benign and malignant kidney lesions in the presence of CKD (Chapter 6).

CHAPTER 3: ASSESSING EARLY RESPONSE TO RADIATION THERAPY USING ULTRASOUND MOLECULAR IMAGING

3.1 Overview

Radiation therapy is one of the most common treatment strategies for managing tumor burden in cancer patients [183–185]. However, tumor response is often assessed months after the end of treatment, which in the case of non-responsive tumors introduces a significant delay in receiving effective treatment. Endothelial cell damage induced by radiation treatment [186] means vascular metrics may serve as an early marker of tumor response. Perfusion parameters extracted from dynamic contrast-enhanced CT scans decreased significantly one day after therapy, faster than tumor volume, and were well correlated with microvascular density [187]. Similarly, contrast ultrasound imaging has demonstrated the potential to assess early response to radiation therapy through pharmacokinetic analysis [188] and measures of vascular density [189]. Molecular imaging with targeted microbubbles has been widely studied and successfully implemented as a method of evaluating tumor response to anti-angiogenic therapy, providing faster feedback than conventional measures. This technique takes advantage of changes in vascular expression in response to treatment, providing a measure of the molecular signature of cancer. The information gained by imaging these cancer biomarkers, and assessing receptor density, provides important information on tumor susceptibility to therapy and tumor response to treatment over time. However, ultrasound molecular imaging has not yet been tested as a method for early assessment of response to radiation therapy.

To effectively monitor response to therapy, USMI requires that unbound, freely flowing bubbles exhibit stable circulatory kinetics. Decreases in targeted microbubble circulation time impede accurate data acquisition and decrease the sensitivity of USMI. The technique relies on bubble accumulation over time, however most targeting ligands attached to the microbubble surface illicit an immune response, resulting in accelerated particle clearance over time. Surface modifications that shield the tethered ligand (buried-ligand architecture) have improved the circulation time of targeted UCAs [141,146]. However, it has also been demonstrated that MB removal can be expedited by an adaptive immune response, which results from antibody generation against PEG itself, a common component of the MB lipid shell. In a preclinical study observing repeated dosing with PEGylated microbubbles over the course of 28 days, a four-fold reduction in non-targeted MB half-life was observed in the kidney and surrounding tissue [190]. In this chapter, repeated dosing using BLA targeted microbubbles will be performed *in vivo* to characterize targeted microbubble kinetics in normal rodent tissues before applying targeted kinetic information to assess the ability of USMI to evaluate early response to fractionated radiation therapy (RT).

3.2 Materials and Methods

3.2.1 Assessing *in vivo* Targeted Microbubble Kinetics

3.2.1.1 Experimental Preparation

Fischer 344 rats (Charles River Laboratories, Durham, NC, USA) were housed in a Division of Comparative Medicine (DCM) facility until use. All animal procedures were approved by the Institutional Animal Care and Use Committee (IACUC) at the University of North Carolina at Chapel Hill. To prepare for imaging, rats were put under anesthesia using 5% isoflurane delivered via O₂ at a rate of 1 L/min (Vevo Compact Anesthesia System,

VisualSonics, Toronto, ON, Canada). Upon induction, the amount of isoflurane delivered was reduced to 2.5% for the duration of the experiment. To regulate internal body temperature, rats were placed on a heating pad (37°C) and a heat lamp was used to provide additional warmth. The right flank was depilated to enable ultrasound transmission to the tissues of interest. A 24G SurFlash® polyurethane I.V. catheter (Terumo Medical Corporation, Somerset, NJ, USA) was inserted into the tail vein to provide an access point for microbubble injections.

3.2.1.2 Ultrasound Image Acquisition

Ultrasound cines were collected using Contrast Pulse Sequencing (CPS) mode on the Acuson Sequoia (Siemens, Mountain View, CA, USA). A linear array (15L8) was placed over the right flank with the transducer orientated such that kidney, liver, and background tissue were all included in the FOV. Degassed ultrasound gel was used to couple the skin and the face of the transducer. Scanner settings – frequency (7 MHz), MI (0.18), CPS gain (-5 dB), dynamic range (80 dB), focus (15 mm), image depth (30 mm), capture rate (1 Hz), and acquisition length (20 min) – were kept the same between animals and for each imaging session. Buried-ligand architecture microbubbles (3 μm) were provided by the Borden Lab from the University of Colorado at Boulder. Four different BLA microbubbles were provided that included unlabeled DBCO, and DBCO labeled with A7R, cRAD, and cRGD ligands. MB size and concentration were recorded using an Accusizer 780 (Particle Sizing Systems, Santa Barbara, CA, USA). A 100 μL bolus containing 5×10^7 MBs was administered sequentially for each bubble type. The circulation kinetics of each bubble were observed at a capture rate of 1 Hz for 20 minutes. Both MB injection order and animal order were randomized for each day. Ultrasound cines were stored as DICOMs and analyzed offline.

3.2.1.3 Data Analysis

Ultrasound DICOMs were loaded into ImageJ where liver, kidney cortex, kidney medulla, and background tissue were isolated as separate regions of interest. ROIs were manually drawn around each tissue in such a manner that avoided shadowing to the greatest extent possible. Average intensity in the ROI was evaluated for all frames in the image set, resulting in time-intensity curves describing microbubble kinetics in the tissue of interest. This process was repeated to extract TIC data in liver, kidney cortex, kidney medulla, and background tissue for each of the four BLA microbubble formulations (A7R, cRGD, cRAD, DBCO), at every time point in the repeated dosing study. TICs were imported into Prism 6 (GraphPad Software, San Diego, CA, USA) and the wash-out portion (downslope) of the TIC fit with a one phase exponential decay model (3.1) of the following form:

$$Y = (Y_0 - A) * e^{-Kt} + A \quad (3.1)$$

where Y_0 is the intensity value at the first point on the wash-out curve, A is the plateau of the exponential decay as time approaches infinity, K is the rate constant (min^{-1}), and t is time (min). The half-life (min) was calculated from the rate constant using Eq (3.2).

$$t_{1/2} = \frac{\ln(2)}{K} \quad (3.2)$$

Differences in area under the TIC curve (AUC), microbubble elimination rate (K), and microbubble half-life based on bubble type and imaging day were evaluated by performing two-way ANOVA followed by Tukey's post-hoc testing. Two types of multiple comparisons were performed to evaluate the effect of repeated dosing (imaging day) within a specific bubble on TIC parameters, and the effect of using different bubbles within a specific imaging day on TIC parameters. Differences between comparisons were considered significant for P -values < 0.05 .

3.2.2 Monitoring Response to Fractionated Radiation Therapy

3.2.2.1 Tumor Monitoring

Fischer 344 rats (Charles River Laboratories, Durham, NC, USA) were housed in a DCM facility until use. All animal procedures were performed using an IACUC approved protocol. A section of rat fibrosarcoma (FSA) tumor tissue (1 mm³) was subcutaneously implanted into the right flank of 20 female rats using an established method [191]. This FSA tumor is non-metastasizing, highly vascularized, and oxygen dependent. These traits make it a suitable model for monitoring response to radiation therapy using USMI. Animal welfare and tumor growth after implantation were monitored and recorded throughout the study. Animals were euthanized when the tumor burden reached humane limits. The study protocol was developed primarily to assess appropriate fractionated radiation therapy doses with a secondary aim of testing the USMI data acquisition protocol and was initiated once the majority of the tumors reached a size between 5-8 mm in the longest dimension. To place animals in experimental cohorts, tumor volumes were ordered from smallest to largest in groups of four. For each size threshold, animals were randomly sorted into one of four experimental groups (n = 5 per group). The tumor size distributions for each group were tested for significant differences ($P < 0.05$) both at the point of cohort randomization and prior to the start of radiation therapy. Group tumor distributions were evaluated using one-way ANOVA followed by Tukey's multiple comparison. P -values for post hoc testing are reported as multiplicity adjusted values [192,193].

3.2.2.2 Dosing Study Experimental Groups

Each cohort received a different fractionated radiation dose: 0 Gy (control), 2 Gy, 5 Gy, or 8 Gy delivered daily for five consecutive days. Prior to radiation therapy, rodents were anesthetized on 5% isoflurane using O₂ as the carrier gas. Rodents were placed in an irradiation

chamber (XRAD 320, Precision X-Ray, North Branford, CT, USA) and maintained under anesthesia at 2.5% isoflurane for the duration of radiation treatment. The average dose rate was 1 Gy/min, for a total treatment time that varied between 2-8 minutes, depending on the treatment cohort. The radiation beam width was modified using an adjustable collimator to encompass the entire tumor while minimizing exposure to surrounding tissue. Lead shielding, with a cutout for the tumor, was positioned over the rodent to further protect all non-tumor tissue from radiation exposure. The XRAD 320 irradiator was operated using a predefined program with the following settings: tube voltage of 320 kV, tube current of 12.50 mA, source to specimen distance (SSD) of 48 cm, variable dose mode, and x-ray beam conditioning filter composed of 1.5 mm aluminum, 0.25 mm copper, and 0.75 mm tin. Variable dose mode utilized a set voltage, current, and dose rate to produce x-rays, ending exposure once the specified dose was reached. The beam hardening filter removed low energy photons unable to penetrate beneath the skin to reduce unnecessary superficial irradiation and ensure the tumor volume was exposed to the proper dose. To assist with radiation therapy recovery, rodents were provided with a modified diet, consisting of a hydration gel (HydroGel®) and a high-energy nutritional supplement (DietGel® Boost, ClearH₂O, Westbrook, ME, USA) in addition to normal free access to food and water, starting after the first day of treatment through the last day of treatment.

3.2.2.3 Doubling Times and Response to Treatment

Tumor growth prior to radiation therapy and tumor response to radiation therapy was monitored over 37 days, starting from the tumor implant date (day 0) (Figure 3.1).

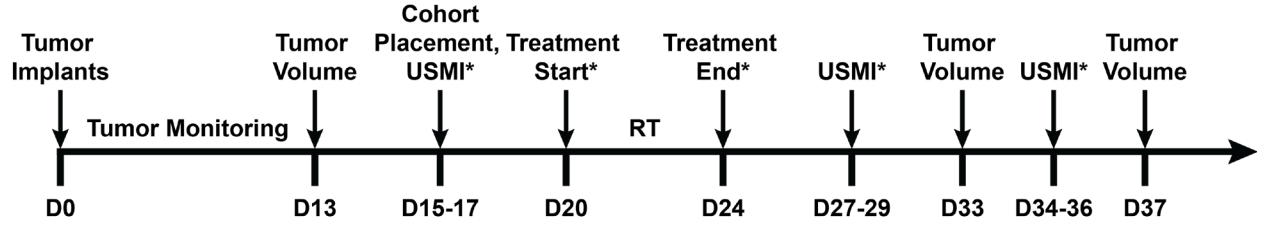


Figure 3.1 Timeline for radiation therapy dosing study. *Additional tumor volume measurements.

Initial doubling time, doubling time after beginning treatment, recurrence doubling time, and halving times for tumors responsive to treatment were (3.3-3.5) [194,195]:

$$K_v = \frac{\ln\left(\frac{V_2}{V_1}\right)}{t_2 - t_1} \quad (3.3)$$

$$D_t = \frac{\ln(2)}{K_v} \quad (3.4)$$

$$H_t = \frac{\ln(0.5)}{K_v} \quad (3.5)$$

where K_v is either the doubling or halving rate (day^{-1}) for the tumor based on volume (V_1 , V_2) changes at two different times (t_1 , t_2). Doubling (D_t) and halving times (H_t) (days) were determined from K_v . Initial doubling time was calculated as the time from the first tumor volume measurement (day 13) to the beginning of radiation treatment (day 20). Doubling time after beginning treatment was calculated from the start of RT until the tumor reached the volume limit or began to decrease in size. Halving time was determined for responsive tumors starting from the largest measurement after beginning RT until the study end point or regrowth occurred. Recurrence doubling time was calculated from the minimum volume achieved in response to treatment until the study end point (day 37). The effect of dose (0 Gy, 5 Gy, 8 Gy) and radiation therapy (before, after) on doubling time were compared using two-way ANOVA followed by multiple comparisons using Tukey's method. Post-hoc testing evaluated potential differences in doubling time for the same dose before and after RT as well as differences between doses before

treatment and differences between doses after treatment. Comparisons were considered significant for $P < 0.05$.

3.2.2.4 Treatment Study Experimental Groups

Eighteen Fischer 344 rats (Charles River Laboratories, Durham, NC, USA) were purchased and housed in an approved DCM facility during the study. Animals were temporarily removed from the facility for imaging and therapeutic procedures that were performed in accordance with an approved IACUC protocol. FSA tumors were implanted and rodents monitored as described in section 3.2.2.1 above. Animals were randomly placed into three experimental groups ($n = 6$ per group). Each cohort received a different fractionated radiation dose: 0 Gy (untreated), 3.5 Gy, or 5 Gy, delivered daily for five consecutive days. Two dose levels, 3.5 and 5 Gy, were selected to assess tumor volume and microvascular expression for complete and partially responsive tumors. Prior to radiation therapy, rodents were anesthetized on 5% isoflurane delivered via O₂. Rodents were placed in an irradiation chamber (XRAD 320, Precision X-Ray, North Branford, CT, USA) and maintained under anesthesia at 2.5% isoflurane during treatment. The average dose rate was 1 Gy/min, for a total treatment time that varied between 3.5-5 minutes, depending on the treatment cohort. The therapy protocol and XRAD pre-programmed settings described in section 3.2.2.2 were applied to irradiate the rodent tumors. A modified diet was provided during treatment days to assist with animal recovery.

3.2.2.5 Classifying Tumor Response to Radiation Treatment

Tumor growth prior to radiation therapy and tumor response to radiation therapy was monitored over 45 days, starting from the tumor implant date (day 0) (Figure 3.2).

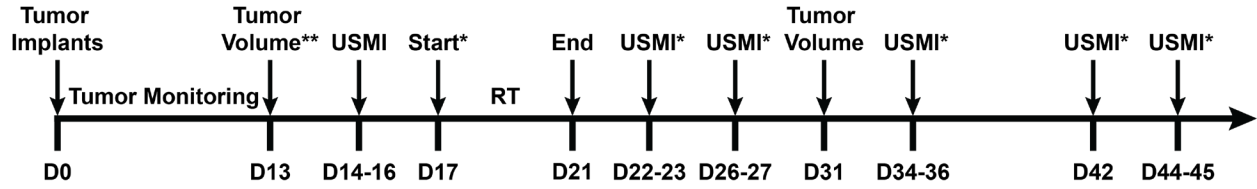


Figure 3.2 Timeline for monitoring response to radiation therapy. *Additional tumor volume measurements; **Cohort randomization.

Initial doubling time, doubling time after starting treatment, recurrence doubling time, and halving times for tumors that responded to treatment were calculated as described in section 3.2.2.3 above. Tumors were individually classified as non-responders, partial responders, and complete responders using established criteria [196,197] based on relative changes in tumor volume. Non-responders demonstrated clear progression (≥ 73 % increase in tumor volume), while partial responders exhibited at least 65% decrease in tumor volume prior to progression. Typically, complete responders are characterized by total disappearance, but for the purposes of this study, criteria were modified to include any tumors that achieved at least a 90% decrease in volume by day 42, that was sustained between day 42 and the final imaging session (days 44-45). Group analysis of untreated/non-responders, partial responders, and complete responders was performed using one-way repeated measures ANOVA followed by Tukey's multiple comparisons between measurement time points. For each response category, changes in tumor size over time were considered significant for $P < 0.05$.

3.2.2.6 Imaging Protocol

Ultrasound images were acquired before and after radiation therapy to monitor tumor response to treatment. An Acuson Sequoia 512 (Siemens, Mountain View, CA, USA) system

was used to record ultrasound images and cines. Volumetric data across the tumor was collected in B-mode and CPS mode. Pulsed Wave (PW) Doppler mode was utilized to apply radiation force in 3D, which served a dual purpose of enhancing MB interaction with the vascular endothelium while also exposing the targeting ligands shielded from the immune system. To apply ARF in 3D and to acquire volumetric data, the ultrasound probe was mounted on a 3-axis motion stage. A LabVIEW program (National Instruments, Austin, TX, USA) was constructed to synchronize stage movement and image acquisition. A general purpose interface bus (GPIB) was used to facilitate communication between LabVIEW and the 3-axis motion controller (ESP300 Universal Motion Controller, Newport Corporation, Irvine, CA, USA). The motion controller supplied an input trigger to the Sequoia by wiring a general purpose input/output (GPIO) pin to a phono plug inserted into the Sequoia DC A input port. In this manner, clip capture was first initiated using a relay circuit connecting the LabVIEW program to the Sequoia footswitch, and was then gated according to stage movement identified by the motion controller output. Volumetric data was acquired using a 0.8 mm step size, at 1 frame per step, and scan length was modified according to tumor length. B-mode volumes were first acquired prior to MB injection as a reference for later analysis. Scanner settings in B-mode were programmed to acquired data at a set frequency (14 MHz), power output (-30 dB), MI (0.03), dynamic range (70 dB), gain (-5 dB), image depth (30 mm), and focus (15 mm). The transducer (15L8) was orientated such that the focal point aligned with tumor depth and position. Following B-mode acquisition but prior to MB administration, a baseline contrast scan in CPS mode was collected with a set frequency (7 MHz), power output (-21 dB), MI (0.18), dynamic range (80 dB), gain (-5 dB), image depth (30 mm), and focus (15 mm). Next, microbubbles were injected as described below and ARF pushes applied across the tumor volume using PW Doppler scanner settings, previously determined to

optimize microbubble displacement during *in vivo* imaging [138]. Parameters used a set Color Doppler (CD) frequency (7 MHz), image depth (80 mm), focus (65 mm), PW gate (18 mm), PW cursor depth (65 mm), cursor position (centered laterally), scale (1 m/s, HPRF), gain (-30 dB), and power output (-3 dB). After applying ARF, scanner setting were reverted to CPS mode to acquire 3D targeting data. Volumetric data was acquired every 2 minutes to observe targeted microbubble accumulation in the tumor and freely circulating bubble clearance. Microbubble targeting was assessed using an image-destroy-image technique, where volumetric data was acquired at a targeted time point, followed by bubble destruction in 3D to clear all (bound and free) bubbles from the tumor, and finally volumetric data was acquired post-destruction to assess remaining freely-circulating bubble signal. Targeted time points were adjusted over the course of the study to account for accelerated clearance with repeated dosing.

3.2.2.7 Microbubble Preparation

Microbubbles used in these experiments were provided by the Borden lab at the University of Colorado in Boulder. Microbubbles were size-selected (3 μm diameter) by differential centrifugation [198] and prepared at a concentration of 1×10^9 MB/mL. Functionalized ligands cyclo[Arg-Gly-Asp-D-Phe-Lys-(Azide)] (cRGD) or Lys(Azide)-Ala-Thr-Trp-Leu-Pro-Pro-Arg (A7R) were conjugated to the microbubble surface using strain-promoted [3 + 2] azide-alkyne cycloaddition (SPAAC) click chemistry by reacting 1,2-distearoyl-*sn*-glycero-3-phosphoethanolamine-*N*-[dibenzocyclooctyl(polyethylene glycol)-2000] (DSPE-PEG2000-DBCO) with the ligand of choice [199,200]. Targeting ligands were shielded by incorporating 1,2-distearoyl-*sn*-glycero-3-phosphoethanolamine-*N*-[methoxy(polyethylene glycol)-5000] (DSPE-PEG5000) into the lipid solution. Buried-ligand architecture has been previously described by Borden and Chen [142–144]. Control BLA microbubbles were

synthesized and labeled with cyclo Arg-Ala-Asp (cRAD) to serve as a comparison to targeted bubbles (cRGD, A7R). Prior to use, MB size and concentration were measured using an Accusizer 780 (Particle Sizing Systems, Santa Barbara, CA, USA). Stock solutions were diluted to form a 100 μ L solution containing 5×10^7 MBs. After preparation, microbubbles were administered according to the imaging protocol outlined above, which was repeated in each animal for every targeted and control bubble.

3.2.2.8 Ultrasound Image Analysis

A custom MATLAB® program was developed to analyze targeted bubble signal across the tumor volume. First, B-mode scans were used to draw separate ROIs around the tumor and non-tumor background tissue for each slice in the data set. The two ROI sets were applied to all 3D contrast scans acquired following ARF, with the first scan used to measure initial tumor perfusion and identify unenhanced (necrotic) portions of the tumor. Tumor ROIs were updated to exclude necrotic regions and identify MB signal in each slice by quantizing the images based on a single level threshold that separated contrast signal from background noise. This binary data was multiplied by the original tumor ROI to generate a new image that only included perfused regions of the tumor. Perfused pixels were extracted from the data set to calculate the average bubble signal in the tumor. Average tissue signal from non-tumor tissue ROIs was also calculated and subtracted from signal in the tumor. Then, the difference between the average bubble signal in the targeted scan (pre-destruction) and the post-destruction scan was used to calculate tissue-subtracted differential targeted enhancement (dTE) and determine the signal magnitude from adhered bubbles. Changes in microbubble targeting were evaluated using two-way ANOVA assessing both imaging day and targeted bubble (A7R, cRGD, cRAD), followed

by Tukey's post-hoc testing comparing differences in dTE over the course of the study within each bubble. Results with P -values < 0.05 were considered significant.

3.3 Results

3.3.1 Microbubble Kinetics

3.3.1.1 Area Under the Curve

The elimination rate, half-life, and AUC were calculated from the microbubble TIC curve data from each imaging day in background tissue, kidney cortex, kidney medulla, and liver. For all bubbles, the background tissue AUC decreased from day 0 to day 3, but began to increase from day 17 to day 28 (Figure 3.3a). Similar behavior was observed for cortical AUC, where AUC decreased from day 0 to day 7, and then began to slowly increase for each bubble until day 28 (Figure 3.3c). In the medulla, AUC decreased from day 0 to day 3, remained fairly stable until day 17 for all bubbles except DBCO (which began to increase), and then slowly increased until day 28 (Figure 3.3d). In comparison, liver AUC remained stable for the duration of the study, with only a slight dip from days 10-17 (Figure 3.3b).

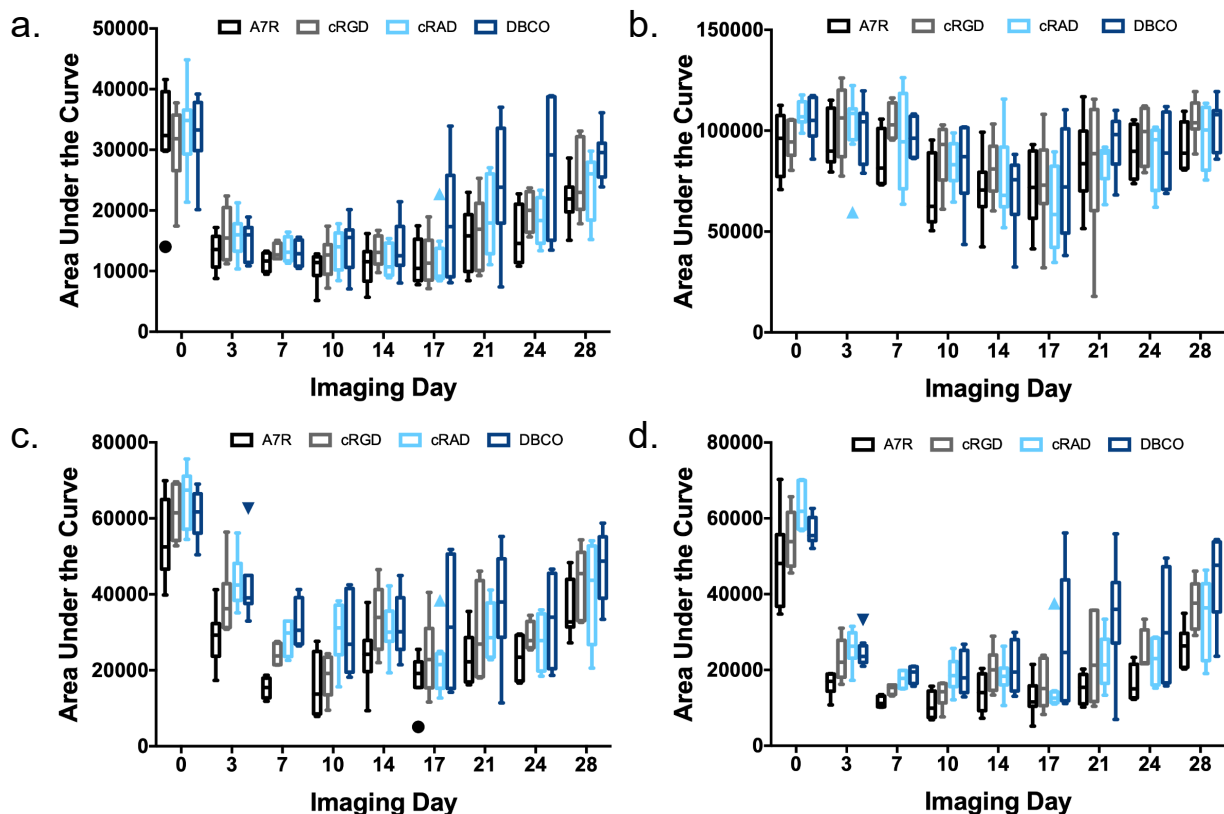


Figure 3.3 Area under the curve by imaging day for A7R, cRGD, cRAD, and DBCO BLA bubbles in a) background tissue, b) liver tissue, c) kidney cortical tissue, and d) kidney medullary tissue.

Background tissue, cortical, and medullary AUCs were all significantly different when considering imaging day and bubble type ($P < 0.0001$ for each), while liver AUCs were only significant when comparing imaging day ($P < 0.0001$). Within an imaging day and tissue type, AUCs between bubble formulations were fairly consistent, with DBCO-MBs behavior deviating the most. The background tissue AUCs for A7R vs DBCO on day 21 ($P = 0.0187$), day 24 ($P = 0.0088$), and day 28 ($P = 0.0419$), were all significantly different, but all other comparisons between AUCs for each bubble were non-significant ($P > 0.05$). In the cortex, AUCs for A7R vs cRAD on day 3 ($P = 0.0066$) and day 10 ($P = 0.0382$), as well as AUCs for A7R vs DBCO on day 3 ($P = 0.0146$), day 7 ($P = 0.0445$), day 17 ($P = 0.01$), and day 21 ($P = 0.0366$) were significantly different, but all other comparisons between AUCs for each bubble were non-

significant ($P > 0.05$). In the medulla, A7R vs cRAD (day 0: $P = 0.0009$), A7R vs DBCO (day 17: $P = 0.0004$, day 21: $P = 0.0001$, day 24: $P = 0.0353$, day 28: $P = 0.0003$), cRGD vs DBCO (day 17: $P = 0.0102$, day 21: $P = 0.0422$), cRAD vs DBCO (day 17: $P = 0.0056$, day 21: $P = 0.0303$), and A7R vs cRGD (day 28: $P = 0.0473$) AUCs were significantly different, while all other comparisons between AUCs for each bubble were non-significant ($P > 0.05$). In the liver, no significant differences in the AUCs between bubble formulations were found ($P > 0.05$).

In background tissue, AUCs were significantly different ($P < 0.05$) between day 0 and all other imaging days with A7R and cRAD MBs, for all days except day 28 with cRGD MBs, and for days 3-17 with DBCO MBs (Supplemental Table C. 1). In the cortex, AUCs were significantly different ($P < 0.05$) between day 0 and all other imaging days with A7R, cRGD, and cRAD MBs, and for all days except day 28 with DBCO MBs (Supplemental Table C. 2). In the medulla, AUCs were significantly different ($P < 0.05$) between day 0 and all other imaging days with A7R, cRGD, cRAD, and DBCO MBs (Supplemental Table C. 3). In the liver, AUCs were significantly different ($P < 0.05$) on day 0 vs. 14 and 0 vs. 17 for cRAD MBs and DBCO MBs (Supplemental Table C. 4). There were no significant differences ($P > 0.05$) in AUC between any imaging days for A7R MBs, and no significant differences ($P > 0.05$) between day 0 and days 3-28 for cRGD MBs (Supplemental Table C. 4). P -values for all comparisons in each tissue have been provided in Appendix C: Supplemental Tables.

3.3.1.2 Elimination Rate and Half-life

Microbubble elimination rate (Figure 3.4) and half-life (Figure 3.5) in background tissue, cortical tissue, and medullary tissue were significantly different when considering both imaging day and bubble type ($P < 0.0001$ for each). In liver tissue, elimination rate was only significant for imaging day ($P = 0.0024$) and half-life was significant for both imaging day ($P <$

0.0001) and between different bubbles ($P = 0.0007$). Elimination rate in background tissue for A7R MBs was significantly different ($P < 0.05$) for day 0 vs. 3, 7, 10, 14, 17, 21, and 28, day 3 vs. 24, and 28, day 7 vs. 14, 17, 21, 24, and 28, day 10 vs. 14, 17, 21, 24, and 28, and day 14 vs. 24, and 28 (Supplemental Table C. 5). Significant differences in elimination rate between bubble types occurred on days 3, 7, 10, 14, 17, 21, and 28 (Supplemental Table C. 6).

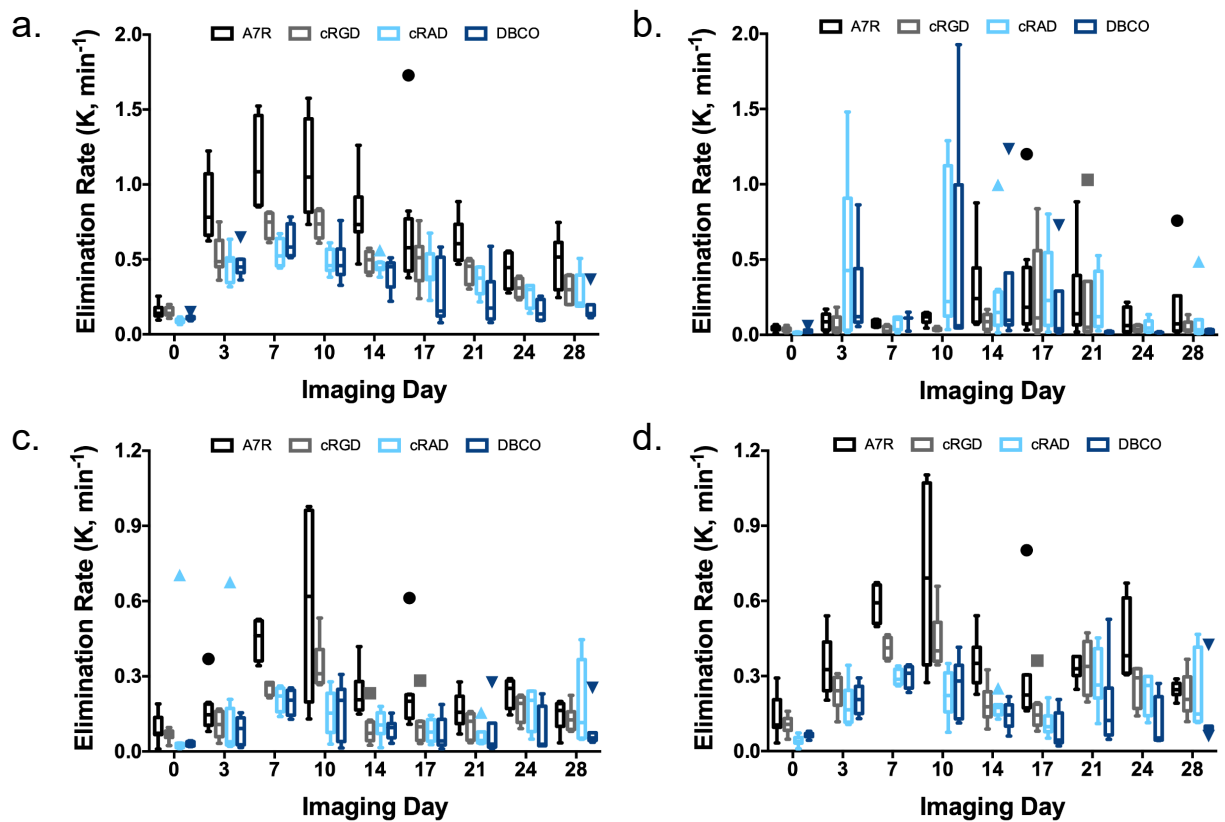


Figure 3.4 Elimination rate by imaging day for A7R, cRGD, cRAD, and DBCO BLA bubbles in a) background tissue, b) the liver, c) kidney cortical tissue, and d) kidney medullary tissue.

Bubble half-life in background tissue was significantly different ($P < 0.05$) on day 0 compared to every other day for A7R, cRGD, and cRAD, but was not significantly different for comparisons between any other days. DBCO half-life was significantly different ($P < 0.05$) on day 0 vs. 3, 7, 10, 14, 17, 21, and 28, day 3 vs. 17, 21, 24, and 28, day 7 vs. 17, 21, 24, and 28, day 10 vs. 17, 21, 24, and 28, and day 14 vs. 17, 21, 24, and 28 (Supplemental Table C. 7).

Significant differences in half-life between individual bubble types occurred on days 0, 17, 21, 24, and 28 (Supplemental Table C. 8).

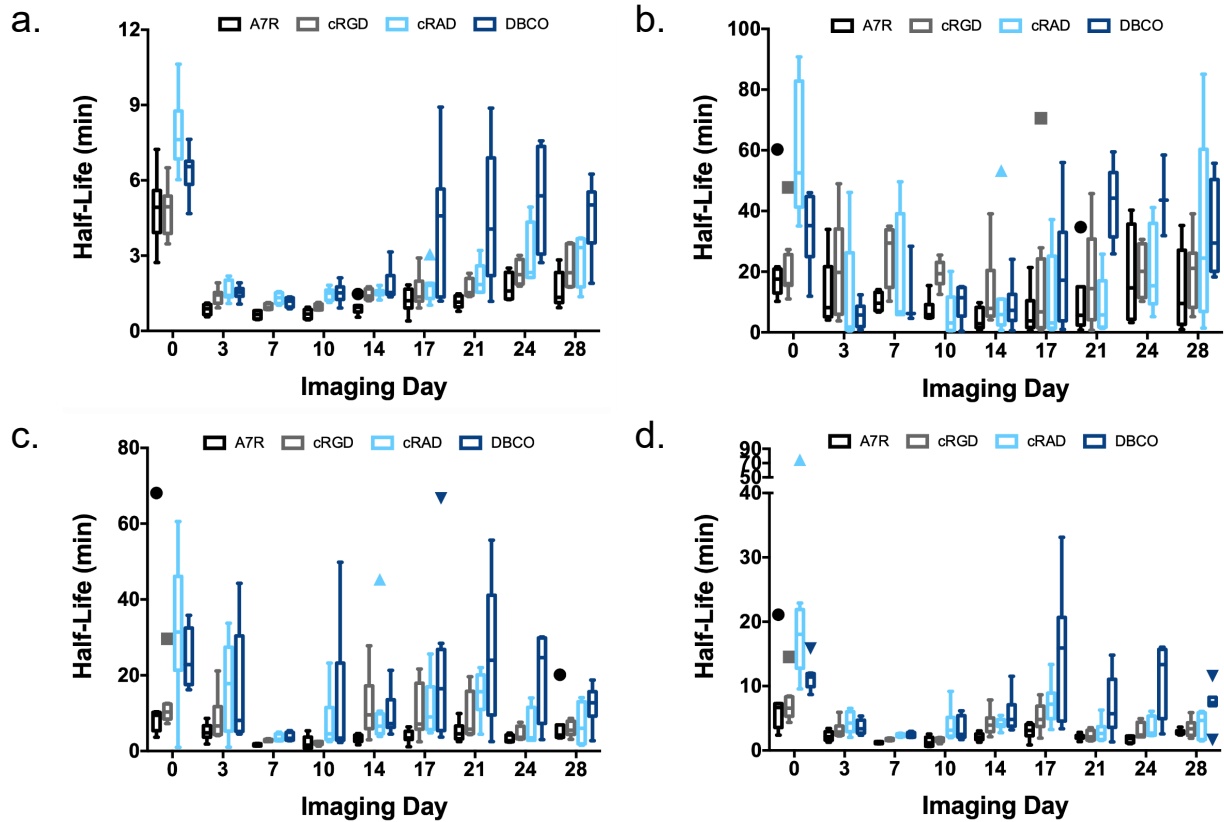


Figure 3.5 Half-life by imaging day for A7R, cRGD, cRAD, and DBCO BLA bubbles in a) background tissue, b) the liver, c) kidney cortical tissue, and d) kidney medullary tissue.

In the cortex, elimination rate between imaging days was significantly different ($P < 0.05$) in A7R bubbles on day 0 vs. 3, day 7 vs. 3, 21 and 28, and day 10 vs. 0, 3, 14, 17, 21, 24 and 28 and cRGD bubbles on day 10 vs. 0, 3, 14, 17, 21, and 28 (Supplemental Table C. 9). No significant differences in elimination rate were found between imaging days for cRAD or DBCO MBs. Elimination rate was significantly different between bubble types on days 7, 10, and 17 (Supplemental Table C. 10). Half-life in the cortex was significantly different ($P < 0.05$) for cRAD MBs on day 0 compared to every other imaging day except day 3, and for DBCO on day 7 vs. 0 and 21 (Supplemental Table C. 11). No significant differences in cortical half-life were

found between imaging days for A7R or cRGD MBs. Significant differences in half-life between individual bubble types occurred on days 0, 17, and 21 (Supplemental Table C. 12).

Medullary elimination rate between imaging days was significantly different ($P < 0.05$) within A7R bubbles on day 0 vs. 3, 7, 10, 14, 21, and 24, day 3 vs. 7 and 10, day 7 vs. 14, 17, 21 and 28, and day 10 vs. 14, 17, 21, 24 and 28; within cRGD bubbles on day 0 vs. 21, day 7 vs. 0, 14, and 17, and day 10 vs. 0, 3, 14, 17, and 28; within cRAD bubbles on day 0 vs. 7, 21, and 28; and in DBCO bubbles on day 0 vs. 7 and 10 (Supplemental Table C. 13). Elimination rate was significantly different between bubble types on days 3, 7, 10, 14, 17, 21, and 24 (Supplemental Table C. 14). Half-life in the medulla was significantly different ($P < 0.05$) for cRAD MBs on day 0 compared to every other day, and for DBCO on day 0 vs. 3, and day 17 vs. 3, 7, 10, and 14 (Supplemental Table C. 15). No significant differences in medullary half-life were found between imaging days for A7R or cRGD MBs. Significant differences in half-life between individual bubble types occurred on days 0, 17, and 24 (Supplemental Table C. 16).

In the liver, elimination rate between imaging days was only significant for cRAD on day 0 vs 3 ($P = 0.0249$) and day 0 vs. 10 ($P = 0.0248$). For all other imaging days, differences in elimination rate were non-significant (Supplemental Table C. 17). Although the group difference between bubble type was not significant ($P = 0.0679$), post-hoc multiple comparisons found that on day 3 and day 10 elimination rates between A7R vs. cRAD (day 3: $P = 0.0175$, day 10: $P = 0.0426$) and cRGD vs. cRAD (day 3: $P = 0.0122$, day 10: $P = 0.0115$) were significantly different (Supplemental Table C. 18). Half-life in the liver was significantly different ($P < 0.05$) for cRAD MBs on day 0 compared to every other imaging day, and on day 10 vs. 28 (Supplemental Table C. 19). For DBCO MBs, half-life in the liver was significantly different ($P < 0.05$) for day 3 vs. 0, 21, 24, and 28, day 10 vs. 21 and 24, and day 14 vs. 21 and 24

(Supplemental Table C. 19). Significant differences in half-life between individual bubble types occurred on days 0, 21, and 28 (Supplemental Table C. 20).

3.3.2 Monitoring Response to Radiation Therapy

3.3.2.1 Dosing Study: Tumor Volume

Tumors were randomly assigned to a treatment cohort (0, 2, 5, or 8 Gy fractionated radiation therapy) prior to the first day of baseline USMI. Average tumor volume at the start of baseline imaging was $140.3 \pm 65.12 \text{ mm}^3$, $151.8 \pm 85.59 \text{ mm}^3$, $134.3 \pm 73.91 \text{ mm}^3$, and $177.9 \pm 128.2 \text{ mm}^3$ for the 0 Gy, 2 Gy, 5 Gy, and 8 Gy experimental groups. The range of tumor volumes for each cohort was 64.53-218.1 mm^3 , 69.78-285.5 mm^3 , 45.01-227.0 mm^3 , and 75.21-397.5 mm^3 , respectively. The largest spread in tumor volume occurred in the 8 Gy group, but the distribution of tumor volumes for this group was not statistically different from the 0 Gy, 2 Gy, and 5 Gy groups (Figure 3.6). In fact, analysis of tumor volume distribution confirmed that no treatment group had significantly different tumor volumes at the point of randomization ($P \gg 0.05$). Possible differences in tumor size distribution between the four treatment groups were also assessed at the start of radiation therapy. Average tumor volume increased to $320.0 \pm 107.5 \text{ mm}^3$, $362.0 \pm 217.6 \text{ mm}^3$, $267.8 \pm 129.8 \text{ mm}^3$, and $465.8 \pm 384.0 \text{ mm}^3$, for the 0 Gy, 2 Gy, 5 Gy, and 8 Gy groups. The range also increased to 173.4-477.0 mm^3 , 135.4-650.1 mm^3 , 162.7-496.7 mm^3 , and 96.42-1100 mm^3 , for each dose respectively. Again, the 8 Gy group had the widest distribution of tumor sizes, but was not statistically different from the other cohorts (Figure 3.6). As with the randomization point, none of the group means were statistically significant at the start of radiation therapy ($P \gg 0.05$).

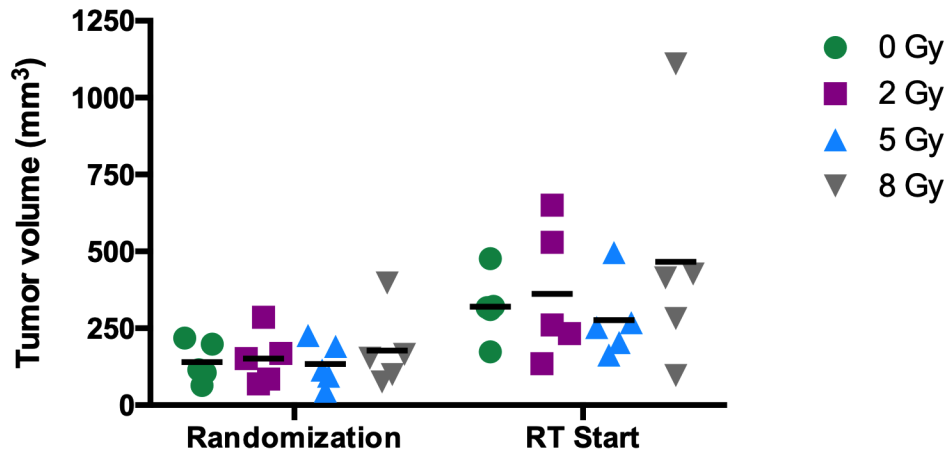


Figure 3.6 Distribution of tumor volumes in each dosing cohort at the time of randomization and at the start of radiation therapy; $n = 5$ per group.

Changes in tumor volume were recorded for each animal in the different treatment cohorts. The first measurement was recorded 13 days after tumors were implanted and the last measurement was recorded 37 days after tumor implants (17 days after the start the RT). Average tumor doubling time (\pm SD) prior to radiation therapy was 1.987 ± 0.331 days, 1.813 ± 0.425 days, 2.046 ± 0.430 days, and 1.588 ± 0.319 days for the 0 Gy, 2 Gy, 5 Gy, and 8 Gy groups. After radiation therapy, average doubling time was 2.854 ± 0.448 days, 5.367 ± 1.813 days, 6.198 ± 1.357 days, and 8.906 ± 9.928 days for the same respective cohorts. Results from a two-way ANOVA indicated that there were significant differences in doubling time before and after treatment ($P = 0.0002$). Post-hoc testing within RT cohorts revealed that only the 8 Gy group had a significant difference in doubling time before and after treatment ($P = 0.0041$) (Figure 3.7). Although doubling times for the 0 Gy, 2 Gy, and 5 Gy group were slower after RT compared to before RT, these differences were not significant ($P > 0.05$). The doubling time prior to RT was not significantly different for any RT cohort ($P > 0.05$). After RT, the doubling time steadily increased with increasing RT fractionated dose (Figure 3.7), however the only significant increase occurred between the 0 Gy and 8 Gy groups ($P = 0.0257$).

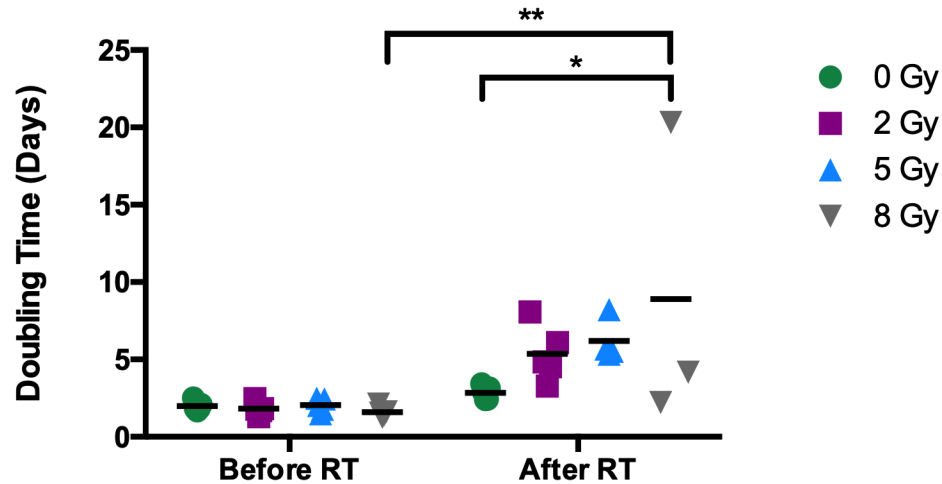


Figure 3.7 Tumor doubling time before and after fractionated radiation therapy; * $P < 0.05$, ** $P < 0.01$.

Tumors in the 0 Gy group experienced uninhibited growth throughout the course of the dosing study (Figure 3.8), steadily increasing in size until reaching volume limits or the end of the study.

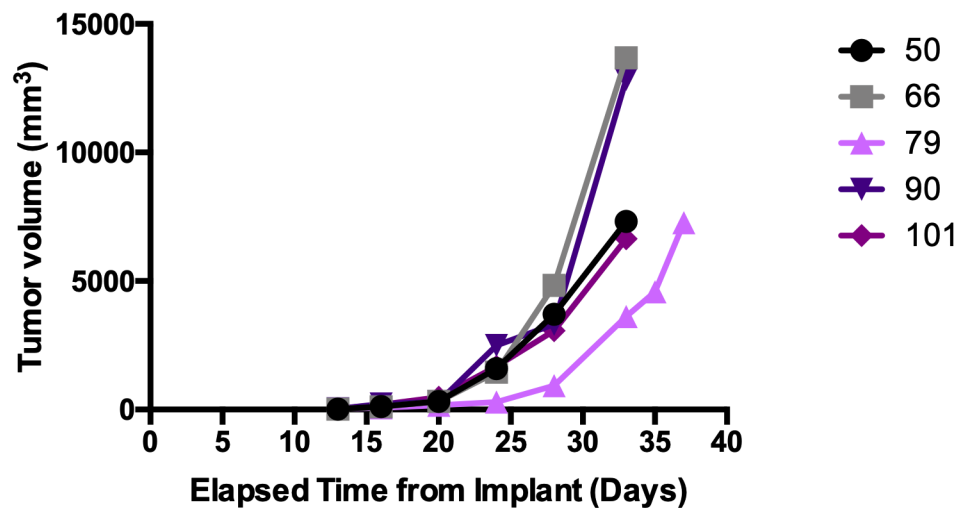


Figure 3.8 Tumor growth in the 0 Gy treatment cohort from implant (day 0) to study completion (day 37); $n = 5$.

Three tumors in the 2 Gy treatment group continued to grow during the course of the study, although the growth rate slowed in each after receiving fractionated RT (Figure 3.9).

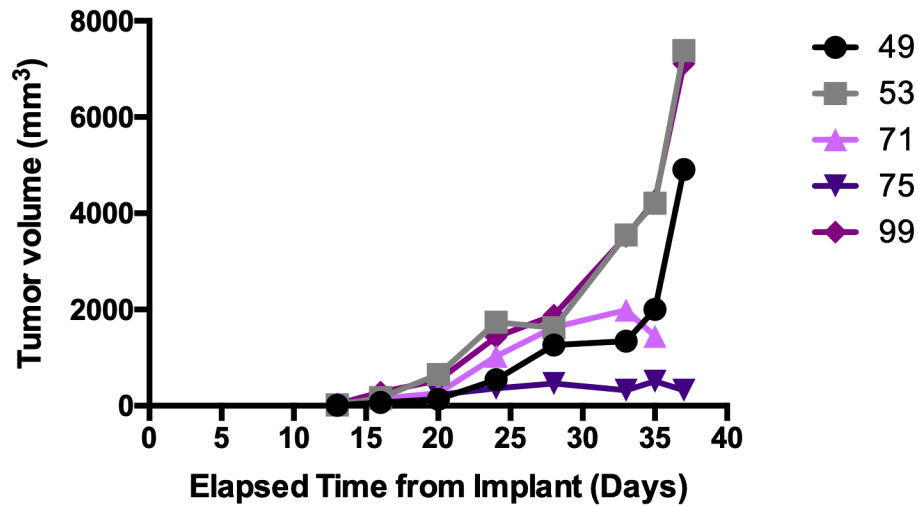


Figure 3.9 Tumor growth in the 2 Gy treatment cohort from implant (day 0) to study completion (day 37); n = 5.

For these tumors, initial doubling times were 1.692 days, 1.293 days, and 1.785 days prior to RT, and slowed to 3.282 days, 4.849 days, and 4.539 days after RT. One tumor in the 2 Gy increased in size until day 28, following which tumor volume fluctuated until the end of the study. The last tumor grew until day 33 and then began to decrease in size. One tumor that received 5 Gy fractionated RT continue to grow for the duration of the study, but the remaining four tumors responded to treatment and began to shrink after RT (Figure 3.10, Supplemental Figure B.1).

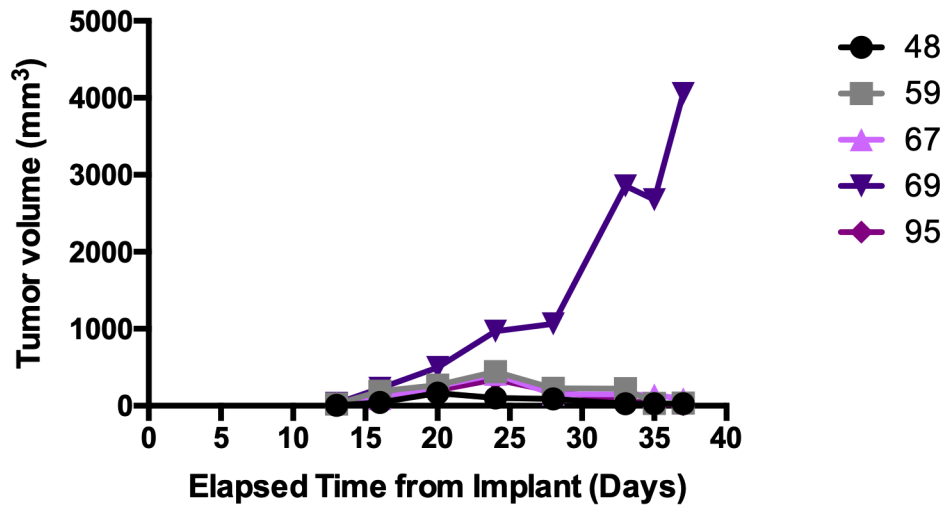


Figure 3.10 Tumor growth in the 5 Gy treatment group from implant (day 0) to study completion (day 37); n = 5.

One tumor began to shrink after day 20, while the remaining three began to decrease in size after day 24. Lastly, all tumors that received 8 Gy fractionated RT initially responded to treatment, beginning to decrease in size after day 20 or 24 (Figure 3.11). However, one tumor rebounded and began to increase in size again after day 33. The doubling time after recurrence was 3.514 days compared to an initial pre-treatment doubling time of 1.615 days.

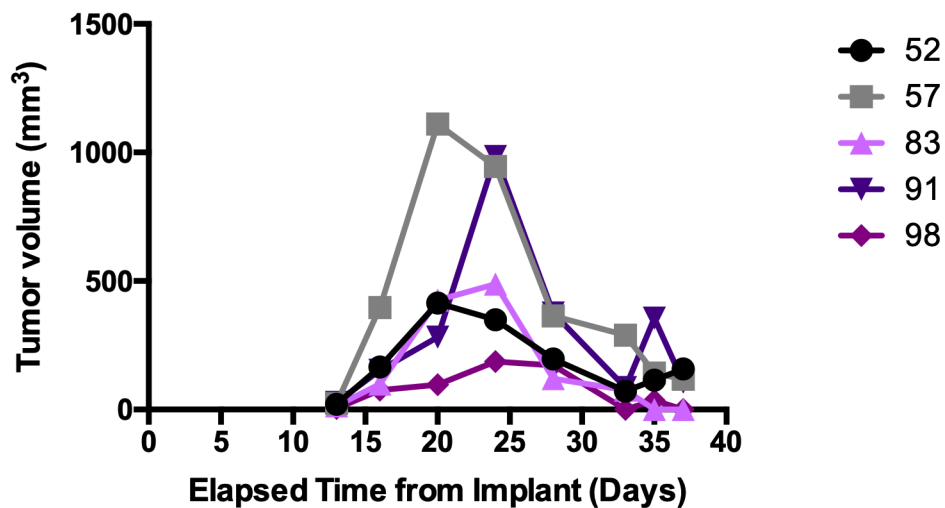


Figure 3.11 Tumor growth in the 8 Gy treatment group from implant (day 0) to study completion (day 37); n = 5.

Tumor halving times were calculated for tumors that experienced a decrease in volume in response to RT during the study. Average halving times for the 2 Gy cohort ($n = 2$), 5 Gy cohort ($n = 4$), and 8 Gy cohort ($n = 5$) were 3.899 ± 9.485 days, 4.747 ± 1.761 days, and 4.486 ± 0.792 days respectively (Figure 3.12).

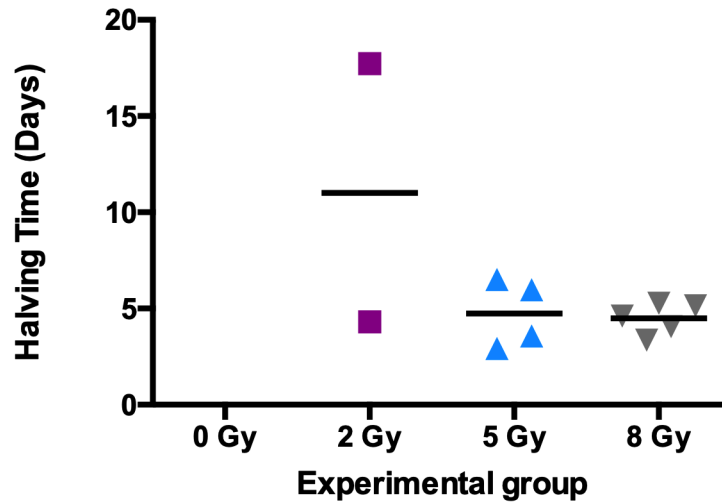


Figure 3.12 Halving times in tumors responsive to radiation treatment.

3.3.2.2 Treatment Cohort: Tumor Volume

Tumors were randomly assigned to a treatment cohort (0, 3.5, or 5 Gy fractionated radiation therapy) prior to the first day of baseline USMI. Average tumor volume at the start of baseline imaging was $268.4 \pm 182.8 \text{ mm}^3$, $300.9 \pm 144.7 \text{ mm}^3$, and $307.5 \pm 158.4 \text{ mm}^3$ for the 0 Gy, 3.5 Gy, and 5 Gy experimental groups. The range of tumor volumes for each cohort was $26.15\text{-}519.7 \text{ mm}^3$, $134.8\text{-}539.3 \text{ mm}^3$, and $85.61\text{-}504.7 \text{ mm}^3$, respectively (Figure 3.13). Analysis of tumor volume distribution confirmed that no treatment group had significantly different tumor volumes at the baseline imaging time point ($P \gg 0.05$). At the start of radiation therapy, potential differences in volume resulting from tumor growth were evaluated. Average tumor volume increased to $664.7 \pm 505.7 \text{ mm}^3$, $703.7 \pm 456.6 \text{ mm}^3$, and $792.1 \pm 482.6 \text{ mm}^3$, for the 0 Gy, 3.5 Gy, and 5 Gy cohorts. The range also increased to $87.18\text{-}1337.3 \text{ mm}^3$, $168.5\text{-}1466.9$

mm³, and 133.5-1417.5 mm³, for each dose respectively (Figure 3.13). Again, the distribution of tumor volumes was determined to be non-significant between treatment cohorts ($P \gg 0.05$).

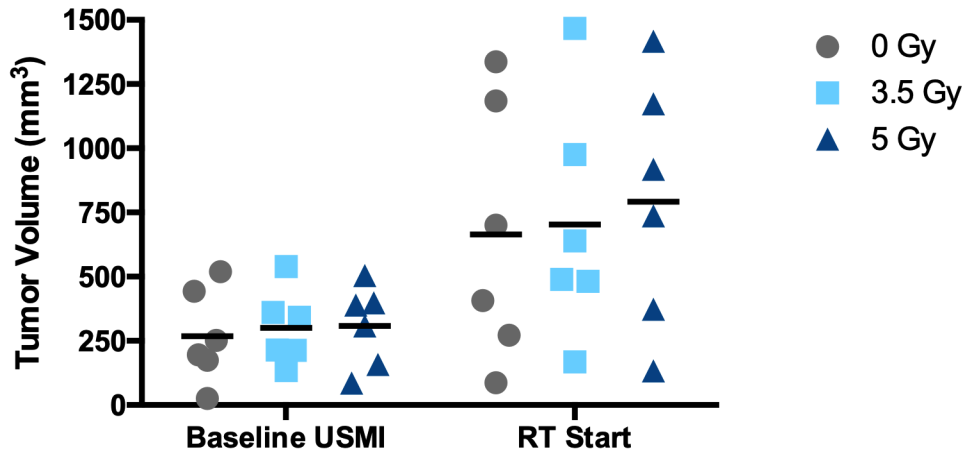


Figure 3.13 Distribution of tumor volumes in each cohort before baseline imaging and at the start of treatment.

Changes in tumor volume were recorded for each animal in the three treatment cohorts.

The first measurement was recorded 13 days after tumors were implanted and the last measurement was recorded 45 days after tumor implants (Figure 3.2). Average tumor doubling time (\pm SD) prior to radiation therapy was 3.48 ± 1.45 days, 4.87 ± 3.75 days, and 3.66 ± 1.51 days, for 0 Gy, 3.5 Gy, and 5 Gy cohorts. After radiation therapy, average doubling time was 2.75 ± 0.477 days, 8.07 ± 7.39 days, and 16.57 ± 8.43 days for the same respective groups. Two-way ANOVA revealed significant differences in doubling time before and after treatment ($P = 0.0024$) and between dosing groups ($P = 0.0042$). Multiple comparisons found that the 5 Gy cohort had significantly longer doubling times after vs. before RT ($P = 0.0005$). Average doubling time also increased in the 3.5 Gy group, but differences before and after RT were not significant ($P = 0.519$). Doubling time between cohorts was similar before RT, but was significantly different in both the 0 Gy ($P = 0.0002$) and 3.5 Gy ($P = 0.0259$) cohorts compared to 5 Gy (Figure 3.14).

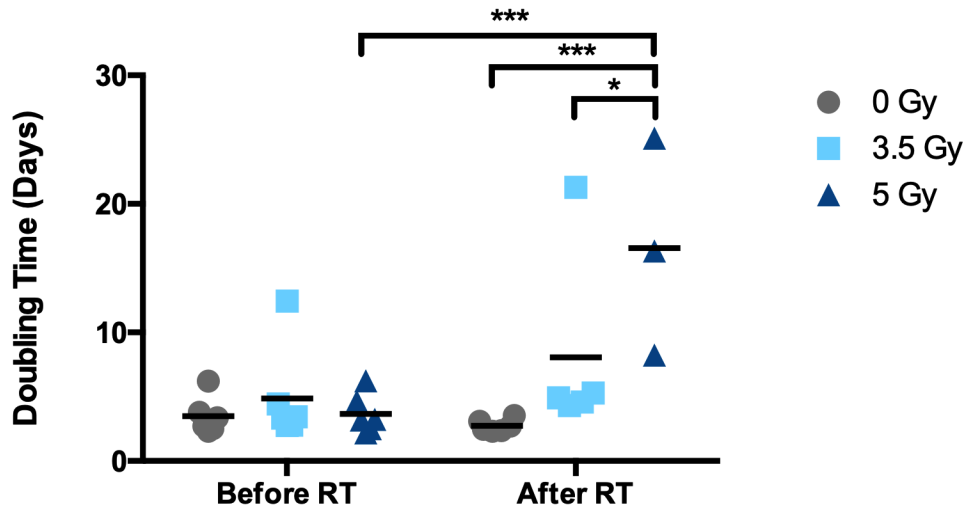


Figure 3.14 Tumor volume doubling time before and after radiation treatment in each cohort. Significant differences are noted with an asterisk (* $P < 0.05$, ** $P < 0.01$, *** $P < 0.001$).

Untreated tumors in the 0 Gy group experienced uninhibited growth throughout the course of the study. In the 3.5 Gy cohort, one tumor did not respond to treatment, showing clear progression from the first day of RT until reaching the tumor burden; two tumors partially responded to treatment but then progressed; and three tumors completely responded to RT. In the 5 Gy cohort all tumors completely responded to treatment. For the tumors that responded (either partial or complete), halving times were calculated. Average halving times were 4.28 ± 1.53 days for the 3.5 Gy tumors, and 5.45 ± 1.50 days for the 5 Gy tumors (Figure 3.15). In the two 3.5 Gy tumors that partially responded before progressing, recurrence doubling times were 5.94 days and 3.12 days.

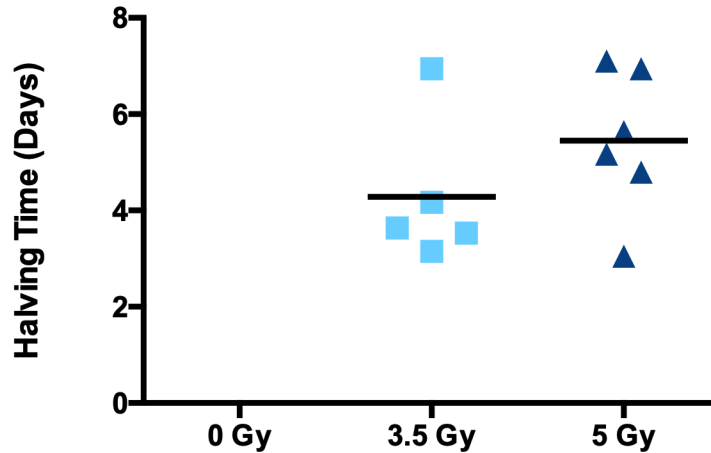


Figure 3.15 Tumor volume halving times in partially and completely responsive tumors.

3.3.2.3 Ultrasound Microbubble Targeting

Tumors were categorized according to response (untreated/non-responders (0 Gy: n = 6, 3.5 Gy: n = 1), partial responders (3.5 Gy: n = 2), and complete responders (3.5 Gy: n = 3, 5 Gy: n = 6)) and compared to ultrasound molecular imaging data. Molecular expression, measured by targeted microbubble binding, remained relatively unchanged in the untreated/no response tumors (Figure 3.16). Baseline (day 13) average microbubble targeting was 16.02 ± 5.97 A.U., 10.61 ± 7.49 A.U., and 18.70 ± 3.07 A.U. using cRGD, A7R, and cRAD BLA microbubbles, respectively. Microbubble targeting was lowest with A7R, a ligand that interacts with VEGFR2, and highest in cRAD, a ligand that typically interacts non-specifically with vasculature. Lastly, cRGD signal was similar to cRAD signal. After RT, all microbubbles experienced a slight, non-significant ($P = 0.0891$) decrease in signal intensity (Figure 3.16). At the last available imaging time point for untreated/non-responding tumors, targeting was 13.98 ± 7.41 A.U., 6.69 ± 7.97 A.U., and 12.24 ± 6.13 A.U. using cRGD, A7R, and cRAD BLA microbubbles, respectively (Figure 3.16).

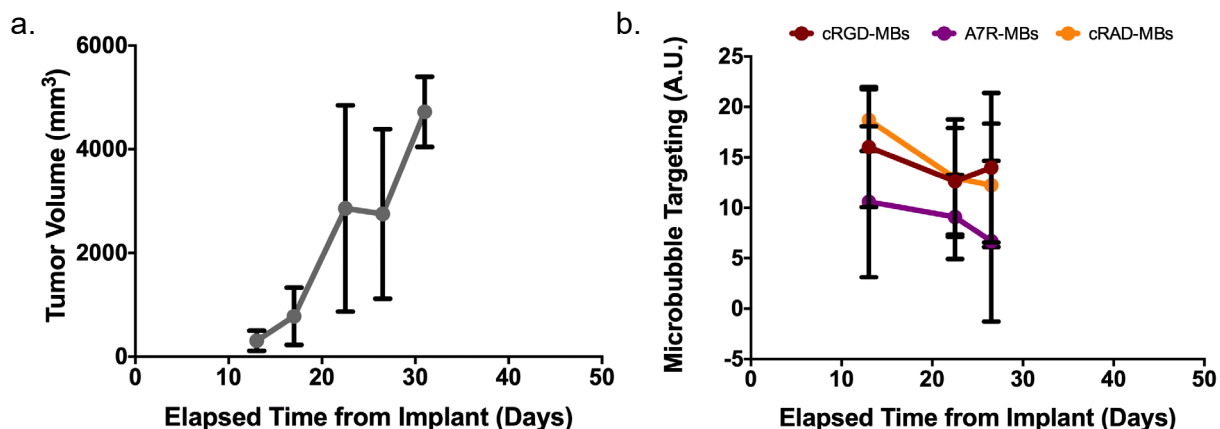


Figure 3.16 Tumor growth curves (a) and molecular targeting (b) in untreated ($n = 6$) and non-responsive ($n = 1$) tumors.

For the two tumors that exhibited a partial response, followed by progression, both decreased in size after the end of RT (day 22) until days 34-36, at which point tumor size increased until study completion (Figure 3.17). In comparison, microbubble targeting displayed different behavior. Bubbles targeted to VEGFR2 (A7R) saw no change in signal enhancement between baseline imaging (days 14-16) and the end of RT (days 22-23), while bubbles targeted to $\alpha_v\beta_3$ integrin (cRGD) had a non-significant ($P = 0.893$) drop in signal between baseline and post-RT imaging session 1 (days 22-23). cRAD bubble signal also decreased between days 14-16 and 22-23 ($P = 0.939$). The largest decrease in targeting occurred from post-RT session 2 (days 26-27) to post-RT session 3 (days 34-36) for both A7R-MBs ($P = 0.102$) and cRAD-MBs ($P = 0.189$), dropping from 18.03 ± 1.42 A.U. to 1.66 ± 1.68 A.U. using the VEGFR2-targeted UCAs and from 15.12 ± 1.44 A.U. to 0.981 ± 1.42 A.U. for non-specific cRAD. The decrease in cRGD-MB signal ($P = 0.982$) was much smaller, decreasing from 10.72 ± 1.01 A.U. to 7.47 ± 1.76 A.U. Following the drop in signal, microbubble targeting immediately increased from day 35 to day 42, to 14.50 A.U. (no SD, $n=1$), 17.53 ± 20.82 A.U., and 9.42 ± 1.95 A.U. for cRGD, A7R, and cRAD (Figure 3.17).

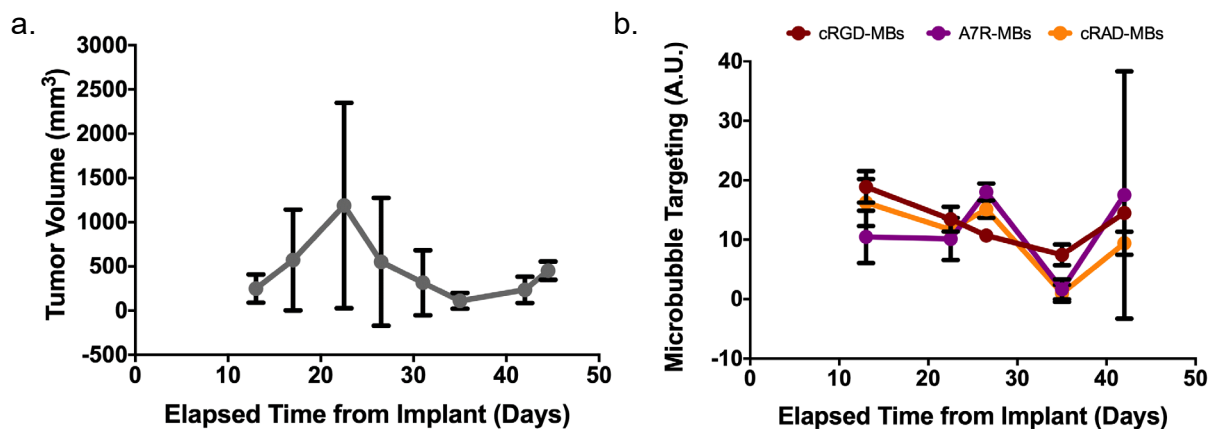


Figure 3.17 Tumor growth curves (a) and molecular targeting (b) in partially responsive tumors treated with 3.5 Gy fractionated radiation therapy; $n = 2$.

Three tumors in the 3.5 Gy cohort completely responded to the fractionated radiation therapy. On average, tumors grew until the end of radiation therapy and then shrank until they were no longer measureable (Figure 3.18). Microbubble targeting to $\alpha_v\beta_3$ integrin (cRGD) decreased ($P = 0.150$) from baseline imaging (19.37 ± 5.51 A.U.) to the end of radiation therapy (9.36 ± 5.26 A.U.), while targeting to VEGFR2 (A7R) remained the same before (7.01 ± 2.45 A.U.) and after (7.03 ± 4.50 A.U.) radiation therapy (Figure 3.18). Control cRAD bubble signal also decreased ($P = 0.153$) before (17.37 ± 1.90 A.U.) and after (7.42 ± 1.20 A.U.) RT. From day 26-27 (13.54 ± 4.33 A.U.) until day 42 (-6.45 A.U., $n = 1$), cRGD signal steadily decreased and was significantly different between the two days ($P = 0.0058$). Signal from A7R MBs also steadily decreased from 9.16 ± 3.85 A.U. to -3.53 A.U. ($n = 1$), but was not significant ($P = 0.148$). Signal from cRAD MBs dropped slightly from 6.38 ± 3.14 to 1.23 A.U. ($P = 0.901$). On the last imaging day, signal remained low from cRGD (4.87 ± 2.05 A.U.), A7R (0.153 ± 3.39 A.U.), and cRAD (5.46 ± 0.599 A.U.) bubbles (Figure 3.18).

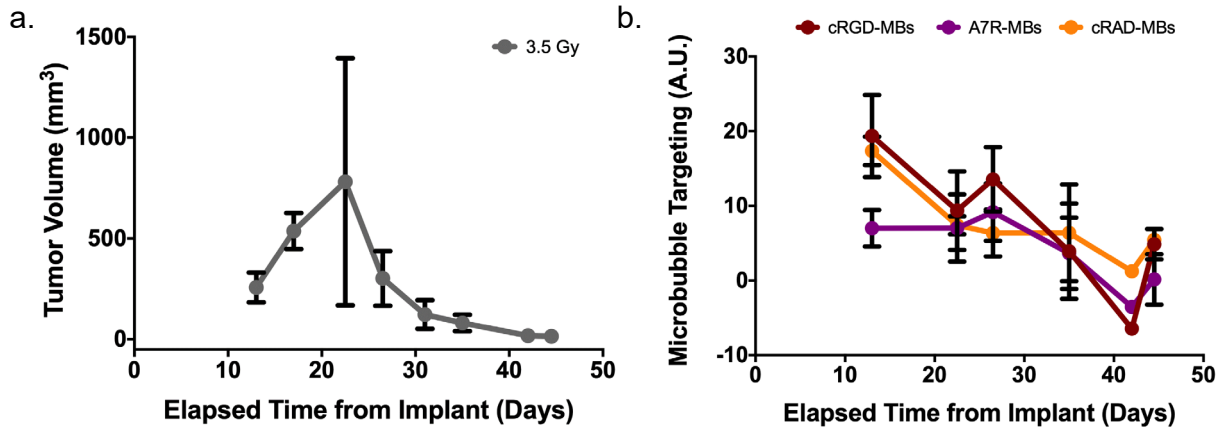


Figure 3.18 Tumor growth curves (a) and molecular targeting (b) in tumors that completely responded to 3.5 Gy fractionated radiation therapy; $n = 3$.

Lastly, all tumors ($n = 6$) from the 5 Gy cohort were classified as complete responders.

On average, tumors grew until the start of radiation therapy and by the end of treatment were already responding, steadily decreasing in size until they were no longer measureable (Figure 3.19). Microbubble targeting to $\alpha_v\beta_3$ integrin (cRGD) between baseline imaging (16.69 ± 1.90 A.U.) and the end of radiation therapy (18.23 ± 5.82 A.U.) remained stable, as did targeting to VEGFR2 (A7R) before (10.63 ± 3.79 A.U.) and after (12.49 ± 7.18 A.U.) radiation therapy (Figure 3.19). Following RT, cRGD MB signal decreased, reaching a minimum value on imaging days 34-36 (1.38 ± 5.28 A.U.), and remaining low until the last day (3.09 ± 0.255 A.U.). cRGD signal was significantly different from baseline and post-RT values by days 34-36 ($P < 0.0001$ for both comparisons) and remained so for the duration of the study ($P < 0.05$). Signal from A7R MBs steadily decreased from the end of RT to the study endpoint (-2.88 ± 6.45 A.U.). By imaging on days 34-36, signal from A7R MBs was significantly different from baseline ($P = 0.0124$) and post-RT ($P = 0.0017$) values. Control cRAD signal steadily decreased from baseline imaging (18.27 ± 5.78 A.U.) to the study endpoint (1.13 ± 5.68 A.U.) (Figure 3.19). Signal drop-off became significant from baseline imaging (days 14-16) by days 34-36 ($P = 0.0006$).

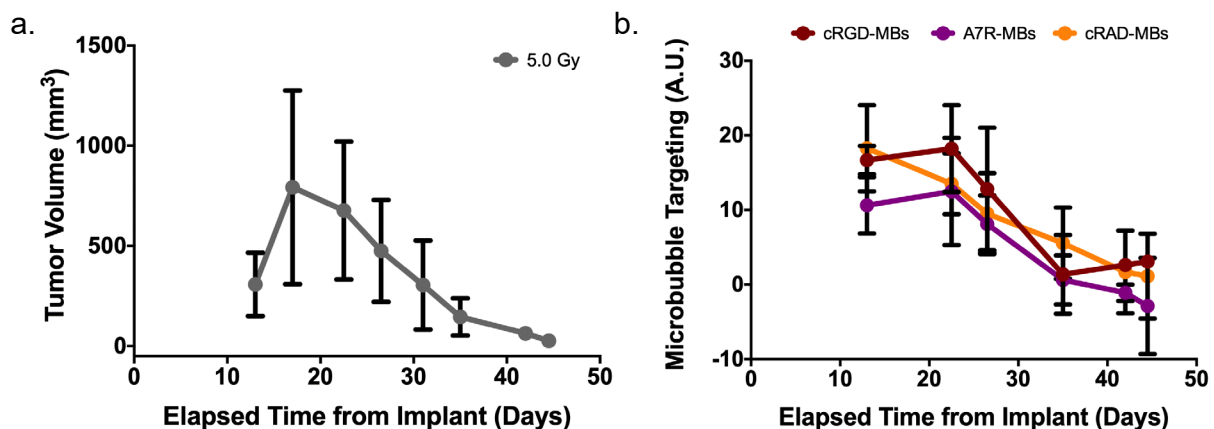


Figure 3.19 Tumor growth curves (a) and molecular targeting (b) in tumors that completely responded to 5 Gy fractionated radiation therapy; n = 6.

3.4 Discussion

3.4.1 BLA Targeted Microbubble Kinetics

Differences in microbubble half-life, elimination rate, and AUC with repeated dosing have been demonstrated using non-targeted bubbles. Fix et al. found reductions in half-life and increases in elimination rate as early as day 2 after initial dosing, with the largest change occurring on day 14 of the study [190]. Accelerated blood clearance caused by repeated dosing has not previously been explored for targeted microbubbles, but could significantly impact longitudinal USMI, by reducing bubble accumulation and resulting in low signal at later time points regardless of actual receptor expression. To characterize potential differences in targeted microbubble circulation over time and implement solutions to preserve targeted signal for USMI, the circulation kinetics of four different shielded microbubbles (BLA A7R, BLA cRGD, BLA cRAD, and BLA DBCO) were evaluated in rodent liver, kidney, and background tissue over the course of a month long repeated dosing imaging study. Regions of interest in the liver, kidney cortex, kidney medulla, and background tissue were isolated and average intensity over time calculated for each frame acquired during the 20 minute observation period. Changes in

microbubble AUC, elimination rate, and half-life were evaluated for differences between imaging day and bubble formulation.

Background tissue had the smallest AUCs for each bubble at every imaging day compared to calculated AUCs in cortical tissue, medullary tissue, and liver tissue. Background tissue, cortical tissue, and kidney tissue MB AUCs exhibited similar behavior over the 28 day imaging study. AUC initially decreased from day 0 to day 7, remained stable until ~ days 14/17 and then slowly rebounded until the last imaging time point (day 28). In comparison, liver AUC remained stable in each bubble for the duration of the 28 day study. Liver AUCs had the highest values and on day 0 were 1.8-3.1x larger than medullary, cortical, and background tissue AUC. Medullary and cortical AUC were only 1.7-1.9x larger than background tissue AUC on day 0. On day 7, when AUC reached a minimum, liver AUC was 3.8-7.5x greater than medullary, cortical, and background tissue AUCs, while cortical and medullary AUCs were only 1.2-2.0x greater than background tissue AUCs. Finally, on day 28, liver AUC was 2.4-4.0x greater than medullary, cortical, and background tissue AUCs. Medullary and cortical AUCs were 1.4-1.7x greater than background tissue. Sustained MB enhancement in the liver, resulting in large and stable AUCs was expected since one mechanism for microbubble clearance from circulation involves phagocytosis by Kupffer cells, resulting in sustained uptake and contrast enhancement in the liver [201]. The fact that microbubble AUC in the kidney was higher than background tissue was likely due to microbubble entrapment. Liu et al. demonstrated that microbubbles were retained in rodent and human kidneys and hypothesized that complement activation facilitated renal entrapment [202]. This argument was strengthened by the 90% decrease in signal enhancement in C3 deficient mice. The authors considered possible microbubble lodging and compared two microbubble populations, $2.2 \pm 1.5 \mu\text{m}$ and $1.7 \pm 0.7 \mu\text{m}$ to evaluate this

possibility, but found no difference in retention with the smaller bubbles, suggesting an alternate mechanism for entrapment.

Overall patterns in microbubble half-life across tissue types were similar to AUC, while elimination rate displayed inverse behavior compared to half-life and AUC. On day 0, elimination rate in background tissue was 1.5-4.3x faster than elimination rate in the medulla, cortex, and liver. Elimination rate in the cortex and medulla were 2.5-2.9x faster than the liver, and the medulla was 1.2x faster than the cortex. By day 7, difference in elimination rate had increased and background tissue microbubble elimination rate was 1.9-10.5x faster than elimination in the medulla, cortex, and liver. Cortical and medullary elimination rate were 3.9-5.5x faster than the liver, and medullary elimination rate was 1.4x faster than cortical elimination rate. Lastly, on day 28, differences in elimination rate returned to initial values (day 0) and was only 1.5-3.4x faster in background tissue compared to medullary, cortical, and liver tissue. Cortical and medullary tissue elimination rate decreased to only 1.5-2.3x faster than liver elimination rate, while medullary elimination rate was 1.6x faster than cortical elimination rate on average. Lastly, average liver MB half-life was the longest on any given imaging day, followed by cortical half-life, medullary half-life, and finally MB half-life in background tissue. On day 0, MB half-life in the liver was 1.6-5.7x longer than half-life in cortical, medullary, and background tissue. Half-life in the cortex was 1.7-3.5x longer than background tissue or medullary half-life, and medullary half-life was 2.1x longer than half-life in background tissue. Differences in tissue half-life increased by day 7 and MB half-life in the liver was 5.8-16.3x longer than MB half-life in cortical, medullary, and background tissue. In the cortex and medulla, half-life was 1.9-2.8x longer than in background tissue. Cortical half-life was 1.5x longer than medullary MB half-life. On day 28, differences in MB half-life had decreased, but

were larger than day 0. MB half-life in the liver was 3.2-8.8x longer than in kidney cortex, kidney medulla, and background tissue. Half-life on day 28 in the cortex and medulla was 1.5-2.8x longer than in background tissue, and was 1.8x longer in the cortex compared to the medulla. Due to the sustained enhancement in the liver, average half-life ranged from 9.55 ± 3.84 min to 34.19 ± 18.23 min over the 28 day study. In the cortex average half-life ranged from 6.16 ± 5.07 min to 21.15 ± 9.09 min, while in the medulla, average half-life ranged from 1.91 ± 0.57 min to 12.47 ± 7.63 min. Average half-life was shortest in background tissue and ranged from 1.02 ± 0.287 min to 5.99 ± 1.44 min.

Unlike the study by Fix et al. where there were sustained decreases in microbubble half-life, increases in elimination rate, and decreases in AUC from day 2 to day 28, in this study, after days 14/17, parameters began to shift back towards day 0 values. Since molecular imaging utilizes frequent monitoring (every few days), more evenly spaced dosing time points were incorporated compared to the study by Fix et al. We administered microbubbles on days 0, 3, 7, 10, 14, 17, 21, 24, and 28, whereas the study by Fix et al. looked at TIC behavior on days 0, 1, 2, 3, 7, 14, and 28 [190]. The consistent administration of microbubbles every 3-4 days may have resulted in a different interaction with the immune system. Fix et al. saw considerable decreases in anti-PEG IgG values from day 14 (maximum) to day 28, although microbubble kinetics on day 28 still resembled kinetics on day 14. Since day 28 was the study endpoint, no further measures were acquired to confirm whether the decrease in anti-PEG IgG would have been sustained. However, it could offer a possible explanation for the rebound effect observed in this study, if after a certain point anti-PEG antibody production decreases and eventually results in some recovery of microbubble persistence. Here, we administered microbubble doses at more evenly spaced intervals across the 28 day study, which may explain why minimum half-life,

maximum elimination rates, and minimum AUC values began to shift towards day 0 values after ~ days 14/17. We hypothesize that with consistent repeated dosing, after reaching a certain threshold some circulation persistence could possibly be recovered at later time points, although the mechanism by which this might occur is currently unknown. Future work should explore this possibility to help preserve or recover microbubble signal for longitudinal imaging.

Characterizing changes in targeted microbubble AUC, elimination rate, and half-life helps elucidate targeted microbubble kinetics in non-tumor tissue to devise strategies to offset accelerated particle clearance with repeat dosing. This is particularly important for USMI, where longitudinal monitoring of tumor response relies on the ability to accurately detect changes in targeted microbubble signal due to increases or decreases in receptor expression. With further study and classification of targeted microbubble kinetics, imaging time points to assess MB targeting could be modified over the course of a longitudinal study to preserve microbubble signal and more accurately isolate changes in targeting due to therapeutic response instead of accelerated clearance.

3.4.2 Response to Radiation Therapy

In studies assessing early response to anti-angiogenic treatment, ultrasound molecular imaging metrics have been able to clearly identify tumor response based on rapid changes in molecular expression that precede changes in tumor volume [127,203,204]. We hypothesized that similar changes in molecular expression could be observed in response to fractionated radiation treatment. Microbubbles targeted to $\alpha_v\beta_3$ integrin and VEGFR2 were administered before and after fractionated RT to assess tumor response using changes in molecular expression compared to tumor volume changes. Clear changes to tumor doubling times occurred before and after radiation therapy, indicating the influence of RT on tumor growth. Increases in tumor

doubling time (slower growth) were observed using both 3.5 Gy and 5 Gy doses, but were only significant in the 5 Gy cohort ($P = 0.0005$). Untreated tumors ($P = 0.0002$) and tumors treated with 3.5 Gy fractionated RT ($P = 0.0259$) both had significantly faster doubling times compared to the 5 Gy group after RT, whereas before RT there were no significant differences ($P < 0.05$) in doubling time between any of the treatment cohorts. Untreated tumors ($n = 6$) experienced uninhibited growth and reached tumor volume limits by day 31 of the study at the latest. Three reached the study endpoint after the first post-RT imaging session (days 22-23), one tumor reached the endpoint after the second post-RT imaging session (days 26-27), and the last two on the measurement day between post-RT imaging sessions two and three (day 31). The one non-responsive tumor in the 3.5 Gy cohort reached the study endpoint after the first post-RT imaging session (days 22-23). Doubling time slowed in the non-responsive tumor after RT, increasing from 2.77 days to 4.31 days, but was not enough to arrest tumor growth. Evaluating group changes in tumor volume throughout the study in the untreated/non-responders cohort, resulted in significant growth ($P = 0.0003$) over time. By days 22-23 the average volume in the untreated/non-responder group was significantly higher than the average volume on day 13 ($P = 0.0068$) and on day 17 ($P = 0.0335$). Days 13 vs. 31 ($P = 0.0017$) and days 17 vs. 22-23 ($P = 0.0052$) also showed statistically significant differences in average tumor volume. By comparison, there were no significant changes in average MB targeting over the course of treatment ($P = 0.0891$). Multiple comparisons of targeting for each bubble across the three imaging sessions (baseline, and two post-RT) also confirmed that there were no significant differences in tumor targeting. Average targeting was initially high for all three bubbles (16.02 ± 5.97 A.U., 10.61 ± 7.49 A.U., and 18.70 ± 3.07 A.U. for cRGD, A7R, and cRAD) and signal was retained with non-significant average losses until the final imaging session (days 26-27) for the

untreated/non-responsive tumors. This behavior followed expected patterns for the cRGD and A7R bubbles, since we anticipated that $\alpha_v\beta_3$ integrin and VEGFR2 expression would remain elevated to contribute to continued tumor progression. Slight signal loss over time was likely due to the development of a necrotic core resulting from rapid growth, leading to only peripheral targeting in the larger tumors.

For partially responsive tumors ($n = 2$), two-way ANOVA evaluating group differences in MB targeting for both bubble type and imaging day was significant for imaging day ($P = 0.0259$) but not between bubble types ($P = 0.7198$). However, multiple comparisons within each bubble across imaging days found non-significant differences when comparing each time point ($P > 0.05$). Although changes in average targeting from cRGD and A7R MBs were determined to be statistically non-significant there was a clear decrease in average VEGFR2-targeting (A7R), between days 34-36 and day 42. Average VEGFR2-targeting dropped from 18.03 ± 1.42 A.U. to 1.66 ± 1.68 A.U., but was not determined to be a significant change ($P = 0.1024$). In a similar manner, although average tumor volume increased prior to RT and decreased after RT before recurrence, group tumor volume changes were only considered significant between days 34-36 and 44-45 ($P = 0.0298$), time points that had small variance. Given, the small number of partial responders ($n = 2$), an extremely large effect size ($\delta = 2.5$) would be necessary to achieve significant results. This was clearly not achieved given the large variance in relation to differences between the means. In order to accurately detect true significant changes in targeting for the whole group, there should be a minimum of six tumors per response category. The uneven distribution of tumors across response categories was a limitation of the study. There were six tumors per cohort (0 Gy, 3.5 Gy, and 5 Gy) and we expected these treatment regimens to result in a significant number of complete responders, partial responders, and non-responders.

However, only one treated tumor in the 3.5 Gy group failed to respond, two tumors in the 3.5 Gy group partially responded, and the remaining treated tumors all completely responded. These results suggest that the 3.5 Gy fractionated dose alone would likely provide a more even distribution across response categories as opposed to including both the 3.5 Gy and 5 Gy cohorts.

The best group molecular imaging results were found in the complete responders using both 3.5 Gy and 5 Gy. Changes in $\alpha_v\beta_3$ integrin expression (cRGD MBs) were significant in the 3.5 Gy cohort by days 34-36 compared to baseline imaging on days 14-16 ($P = 0.0024$) and remained significantly different for imaging sessions on day 42 ($P = 0.0003$) and days 44-45 ($P = 0.0129$). Similarly, for the 5 Gy cohort, changes in cRGD MB targeting were first significantly different from baseline (days 14-16) measures by days 34-36 ($P < 0.0001$) and remained significant for the final two imaging sessions (day 42: $P = 0.0133$, days 44-45: $P = 0.0039$). Average tumor volume changes in the 3.5 Gy complete responders were first significantly different from the start of RT (day 17) by days 34-36 ($P = 0.0161$) and remained significant for the remaining two measures (day 42: $P = 0.0467$, days 44-45: $P = 0.044$). In the 3.5 Gy complete responders, significant changes in tumor volume and molecular targeting were identified at the same time. Average tumor volume changes in the 5 Gy cohort were first significantly different from baseline measures (day 13) by days 34-36 ($P = 0.0465$) and remained significant for the remaining two imaging sessions (day 42: $P = 0.0419$, days 44-45: $P = 0.0418$). Again, in the 5 Gy cohort tumor volume changes compared to baseline were identified on the same time scale as changes in cRGD microbubble targeting. The results from group analysis of tumors by response category did not quickly identify significant changes in average tumor volume or average microbubble targeting indicative of tumor response. In comparison to the overall group response, individual tumor response based on tumor volume was easily detected. By the second post-RT

imaging session (days 26-27) two tumors had already shown a partial response to treatment and four more achieved a partial response by the following tumor measurement (day 31). The remaining five initially responsive tumors all achieved at least a partial response by the third post-RT imaging session (days 34-36). By the fourth post-RT imaging session (day 42), all tumors had either achieved complete response ($n = 9$) or recurred ($n = 2$). The majority of the molecular imaging results in individual tumors displayed the same behavior as tumor volume for characterizing response to a lesser extent and did not provide faster feedback.

One limitation of the study was the time between imaging sessions. Molecular changes can occur with 24-48 hours following treatment, however the first imaging session after baseline measures did not occur until after the last fractionated dose, 5 days after treatment began. In fact, four tumors had already begun to respond by the end of treatment, but molecular expression was not assessed until after the end of treatment. The study was designed in this manner to avoid influencing tumor response with the use UCAs that included MB destruction imaging techniques (dTE) during the treatment period. Ultrasound-mediated microbubble therapy has been shown to increase tumor radiosensitivity and contribute to therapeutic outcomes [185,205]. Klein et al. evaluated the effect of delivery sequence, either MBs followed by RT or the reverse, for separation times ranging from 0 to 24 hours [205]. The authors determined that the optimal separation time between treatment methods (MB and RT) was 6 hours, but that there was no significant difference in therapeutic effect when changing treatment order and even MBs administered up to 24 hours before or after RT had a noticeable impact on endothelial cell death. McNabb et al. studied the effect of single dose vs. fractionated dose therapy combined with ultrasound-stimulated MB therapy and found that the combination of fractionated RT with MB therapy had the greatest impact on tumor response [185]. To avoid a confounding effect due to

MB delivery and destruction during USMI acquisition, baseline imaging and post-RT session 1 were performed at least 24 hours before and after fractionated therapy. However, as this limited the ability to accurately capture rapid changes in molecular expression, future studies should consider accounting for the radioenhancing properties of MB destruction imaging to enable earlier detection of changes in molecular expression. Characterizing the effect of repeated imaging during consecutive radiation therapy sessions on tumor growth and response to treatment should help identify the appropriate fractionated dose that results in non-responders, partial responders, and complete responders. Prior studies have demonstrated that single large doses (> 8 Gy) cause immediate damage to surrounding microvasculature, aiding in the overall tumor response to treatment [184]. Endothelial cell disruption resulting in apoptosis should correspond to a decrease in endothelial cell markers measurable by ultrasound molecular imaging. We hypothesized this vascular effect would be retained when switching to fractionated therapy and could be assessed using ultrasound molecular imaging. Here, molecular imaging results were not significant, but further optimization could improve study outcomes. Radiation therapy is a widely-used strategy for tumor management and the ability to identify early response or lack of response through changes in molecular expression would contributed to improving patient outcomes.

CHAPTER 4: CLINICAL TRANSLATION OF ACOUSTIC RADIATION FORCE ENHANCED ULTRASOUND MOLECULAR IMAGING

4.1 Introduction

The ability of USMI to accurately monitor and predict tumor response to treatment has been well-established using *in vivo* models, but has not been validated in clinically relevant populations. Prior work by Gessner et al. demonstrated that ARF could be successfully implemented on a clinical scanner and used to enhance targeting across a tumor volume [138]. Radiation force assisted targeting was 78% higher compared to passive targeting, in their work. Further, Streeter et al. and Borden et al. have demonstrated that larger bubbles and surface modifications (shielding), respectively, improve contrast sensitivity, contrast persistence, and modulate ligand availability on targeted bubbles, enhancing localized targeting [144,146,148]. In this chapter, we assess the efficacy of ultrasound molecular imaging to monitor treatment response in a canine patient population. We expect that the improvements to USMI gained by optimizing ARF, tailoring microbubble size, and reducing bubble immunogenicity, should enable the successful translation of USMI into the clinic.

4.2 Materials and Methods

4.2.1 *In vitro* Optimization of Acoustic Radiation Force

4.2.1.1 Acoustic Radiation Force Settings

A Siemens Acuson Sequoia 512 clinical ultrasound system (Siemens, Mountain View, CA, USA) was used with a 9L4 linear array to generate and test acoustic radiation force parameters. Parameters established for preclinical imaging were modified for deeper imaging

with the 9L4. Acoustic radiation force pushes were generated using PW Doppler mode, with the following settings: CD frequency of 3.5 MHz, image depth of 140 mm, image focus at 120 mm, PW gate of 18 mm, PW cursor depth of 128 mm, PW cursor centered laterally, scale of 1 m/s with HPRF displayed on screen, and a gain of -30 dB. Power outputs between 0 dB and -15 dB were tested at depths ranging from 2 cm to 5 cm. A hydrophone (HNA-0400-1050, Onda Corporation, Sunnvale, CA, USA) was used to map the corresponding pressure for each power output at depth. Voltage measurements recorded by the hydrophone were converted to pressure using a calibration curve. Pressures were evaluated along the centerline of the transducer face with distances of 2-5 cm between the transducer and hydrophone. To account for ultrasound wave attenuation in tissue, derated pressures were calculated using the following equation:

$$P(z) = P_0 * e^{-\alpha f z} \quad (4.1)$$

where $P(z)$ represents pressure values derated for depth dependent tissue attenuation, P_0 is the pressure measured in water at depth, α is the attenuation coefficient (Np/MHz/cm), f is the transmit frequency (MHz), and z is the depth (cm). These pressures were applied across different depths to determine the optimal ARF push.

4.2.1.2 Optical Microscope Setup

Acoustic radiation force pushes generated by the 9L4 transducer were observed using an optical set-up with a high-speed camera (Figure 4.1). A 200 μ m cellulose tube was mounted on a three-axis motion stage, submerged in a water tank and placed in the FOV of an inverted brightfield microscope (IX71, Olympus, Tokyo, Japan). Fine adjustments to the tube alignment were made using three-axis water hydraulic micromanipulators (Narishige International, Amityville, NY, USA). A 60x water immersion objective (LUMPlanFL N/w, Olympus

Corporation, Center Valley, PA, USA) with an additional 1.6x magnification factor applied, was inserted through a latex seal in the water tank and was used to observe microbubble response to ARF pulses.

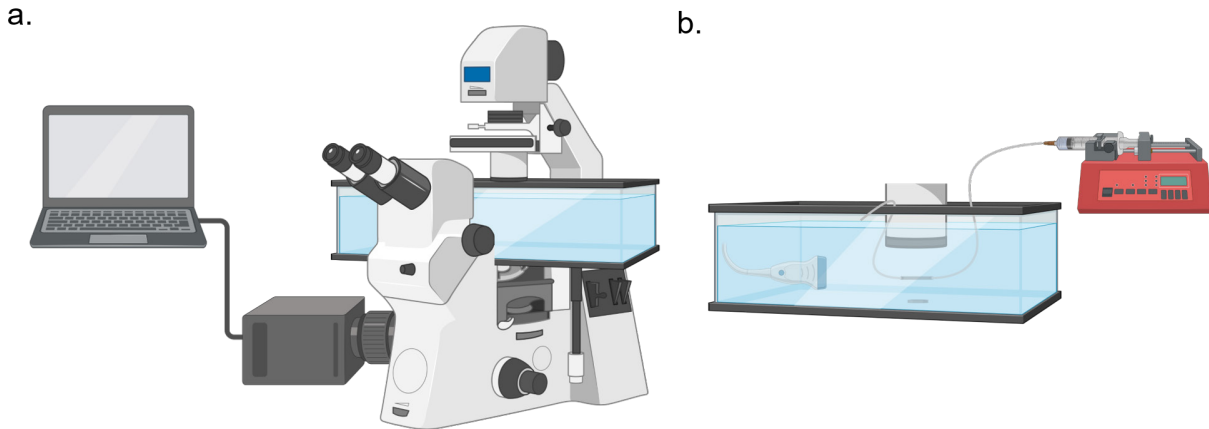


Figure 4.1 Experimental set-up for *in vitro* acoustic radiation force tests. a) An inverted microscope fit with a water tank was used to observe microbubble displacement in response to acoustic radiation force pushes. A high-speed camera captured the microscope field of view and recordings were stored on a laptop for offline analysis. b) View from inside the water tank, showing a submerged clinical transducer parallel to a microtube aligned to the microscope focus. A syringe pump delivers flowing microbubbles through the tubing at a set rate. Created using BioRender.com.

Prior to submerging the ultrasound transducer in the water tank, gel was placed on the face of the transducer and a CIV-Flex general purpose ultrasound probe cover (CIVCO Medical Solutions, Coralville, IA, USA) pulled over the transducer to protect it while in the water bath. The transducer was aligned parallel to the microtube, configured such that the transmitted ARF pulses were perpendicular to the direction of both microbubble flow and buoyancy. In house microbubbles, filled with a gas core surrounded by a lipid monolayer, were synthesized by first preparing a lipid solution composed of 1,2-distearoyl-sn-glycero-3-phosphocholine (DSPC) (Avanti Polar Lipids, Alabaster, AL, USA) stabilized by 1,2-distearoyl-sn-glycero-3-phosphoethanolamine-N-methoxy (polyethylene-glycol)-2000 (DSPE-PEG2000) (Avanti Polar Lipids, Alabaster, AL, USA) in a 9 to 1 molar ratio. Next, the lipid solution was emulsified in a

phosphate buffered saline solution containing 15% propylene glycol (v/v) and 5% glycerol (v/v). Following, 1.5 mL aliquots of the lipid solution were placed in 3 mL vials and sealed shut. The air in the vial headspace was exchanged for DFB gas and the vial was mechanically agitated for 45 seconds using a high-speed mixer (VialMix™, Lantheus Medical Imaging, North Billerica, MA, USA) to form the final microbubble suspension. MB size and concentration were measured using an Accusizer 780 (Particle Sizing Systems, Santa Barbara, CA, USA). Following, a 3 mL MB solution was prepared by injecting 100 µL of the MB stock solution (1×10^{10} #/mL) into distilled water. A blunt 27G ½ inch needle was connected to the 3 mL syringe and inserted into the tubing to enable MB delivery to the microtube. Microbubbles were delivered to the tube at a flow rate of 0.2 µL/s using a syringe pump (Pump 11 Elite, Harvard Apparatus, Holliston, MA, USA). This rate was selected to reflect microcirculatory blood flow. Data was collected to observe MB flow and direction in the absence and presence of ARF pushes. Between trials, MB debris was cleared from the tubing by flushing it with water followed by air three times in a row.

4.2.1.3 Data Acquisition

Video clips of microbubble response to ARF pushes were recorded using a high-speed camera (FASTCAM-APX RS, Photron, Tokyo, Japan) that was connected to the left side port of the IX71 to capture the view from the microscope objective. Data was collected at 250 frames per second (fps) using the full 1024 x 1024 pixel grid, which generated a total of 2048 frames (approximately 8 seconds of data). The read-out resolution (pixel grid) can be reduced to record images at a faster frame rate or for a longer duration, however the selected settings were ideal for observing bubble displacement across the entire width of the 200 µm tube. Photron FASTCAM Viewer (PFV) software was used to complete the initial calibration, to configure the camera settings, to control data capture, and to store acquired data. Before each use, the camera was

calibrated to correct for non-uniform pixel sensitivity across the sensor array. This was accomplished with a shading correction function, internal to the APX RS camera, which requires a completely dark reference image (all black, no light exposure) in order to provide a uniform output for each pixel proportional to the level of light exposure. To sync data capture with the onset of ARF pulses the manual trigger mode recording setting was utilized. This mode allows the user to determine how many frames will be captured before the trigger input and how many will be captured after the trigger input. This setup was configured to capture 100 frames prior to and the remaining 1948 frames after receiving the input trigger, with ARF pulses synced to start with the input trigger. In this mode the camera endlessly loops through the available memory, until an input is received that begins the process of recording the data. Recorded data were stored with a playback rate of 30 fps and were transferred offline for analysis.

4.2.1.4 Data Analysis

A custom-designed MATLAB® program was developed to analyze the video data. Video files were loaded into the program and the first frame displayed on a set of axes. The frame prior to the start of acoustic radiation force was used to determine the baseline number of bubbles at the tube wall (Figure 4.2a). The final frame in the video data, at the end of acoustic radiation force, was used to quantify the number of bubbles displaced to the tube wall (Figure 4.2b). The difference between the baseline bubble count and the final bubble count represented the number of displaced bubbles.

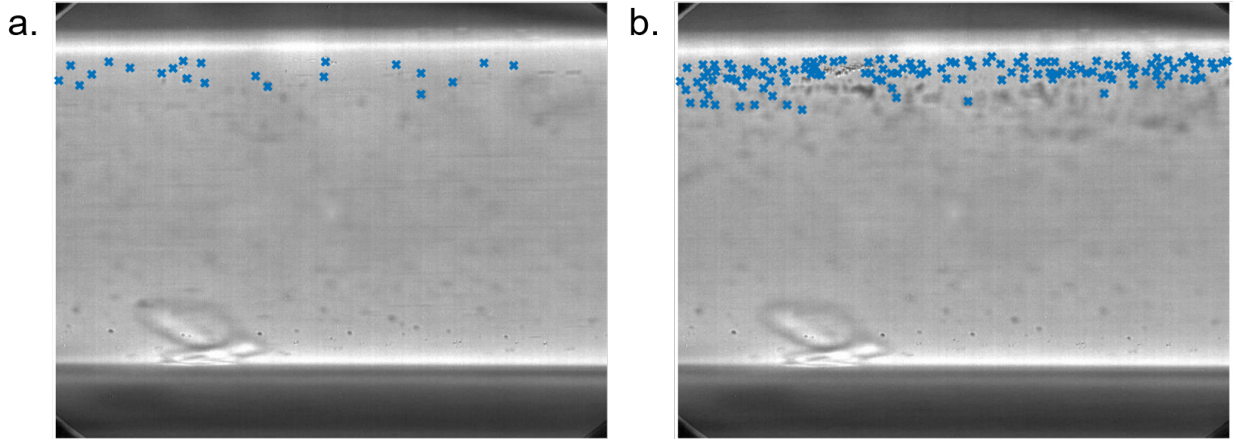


Figure 4.2 Quantifying microbubbles displaced by acoustic radiation force. a) Immediately prior to the start of ARF, the number of background bubbles in the vicinity of the distal tube wall were counted. b) After applying ARF, the number of bubbles pushed to the distal tube wall were counted, excluding bubble aggregates or bubbles in motion. Total number of displaced bubbles was calculated by subtracting the baseline value from the final value. Bubbles counted are marked by a blue x.

Large bubble aggregates or bubbles determined to be in motion were excluded from the final count. Data was collected in triplicate for each pressure and depth. To assess the relationship between the magnitude of bubble displacement in response to changes in pressure a linear regression model was fit to the data, with the form:

$$y = m * x + b \quad (4.2)$$

where y represents the number of displaced bubbles for a given pressure, x , m is the slope of the line and b the model intercept. The regression model was individually fit to the data for each depth from 2-5 cm. Goodness of fit (GOF) was evaluated by calculating adjusted R^2 values and testing to see if the slope of the line was significantly non-zero ($P < 0.05$). The linear model generated for each depth was compared to see if the slopes and intercepts were significantly different ($P < 0.05$). To test for an interaction between pressure and depth in relation to microbubble displacement, a two-way ANOVA was performed followed by post-hoc multiple comparisons using Tukey's method, testing for both overall differences in bubble displacement

across pressure regardless of depth, and differences in displaced bubbles based on depth for a given pressure. Reported *P*-values were adjusted to account for multiple comparisons using an α level of 0.05 [192,193]. The adjusted *P*-value calculates the smallest level where the comparison would be considered significant in relation to the entire family of comparisons. Statistics were computed using Prism 6 (GraphPad Software, San Diego, CA, USA). Multiple comparisons were considered significant for $P < 0.05$.

4.2.2 Clinical Translation of Radiation Force Enhanced Ultrasound Molecular Imaging

4.2.2.1 Patient Recruitment and Enrollment Criteria

This study was designed to validate ultrasound molecular imaging for the detection of tumor microvascular changes in response to anti-angiogenic treatment and was performed with the approval of the Institutional Animal Care and Use Committee at North Carolina State University. Imaging took place on site at the College of Veterinary Medicine Teaching Hospital. All animal care was provided by trained veterinary radiologists and technicians. Canine patients were recruited from veterinary clinics across the state of North Carolina. Owners were invited to have their dog participate in the study, if the dog met the study criteria. Inclusion criteria were: 1) canines at least 1 year old; 2) minimum weight of at least 3.5 kg; 3) presence of biopsy accessible, histologically confirmed soft tissue sarcoma (STS) of any stage or grade in a location accessible to ultrasound imaging; 4) tumor size of at least 4 cm and no greater than 17.5 cm; 5) adequate organ function determined by an absolute neutrophil count > 2000 cells/ μ L, hemotacrit $> 30\%$, platelets $> 75,000/\mu$ L, creatinine $< 2\times$ the upper limit of normal, bilirubin $< 2.5\times$ the upper limit of normal; 6) performance status of either 0 or 1 confirmed on the study start date, according to the modified ECOG Performance Scheme; and 7) signed informed consent by the owner. Exclusion criteria were: 1) any prior radiation to the tumor; 2) previous surgery, except in

the case where gross disease is present and the surgical site is well-healed; 3) received chemotherapy within 2 weeks or planning to receive concurrent chemotherapy during the enrollment period; 4) ulceration of the skin overlying the tumor; 5) the presence of metastatic disease; 6) any pre-existing immune-mediated disease; 7) diagnosis of diabetes mellitus; 8) STS located orally or located behind bone; 9) concurrent malignancy or other serious systemic disorder limiting life expectancy to < 1 year; and 10) received or taking homeopathic or alternative therapies within 1 day of the study start date, with the exception of supplements such as chondroitin sulfate, vitamins, essential fatty acids and glucosamine. Informed, written consent from the owner was received for all canine patients that participated in this study. The Colorado State University (CSU) Flint Cancer Center served as a secondary enrollment site for this study, with the same criteria as outlined above.

4.2.2.2 Study Protocol

Canine patients who enrolled in the longitudinal study participated in an 8-week imaging series (Figure 4.3). Prior to the start of treatment, baseline measurements were collected in all canines.

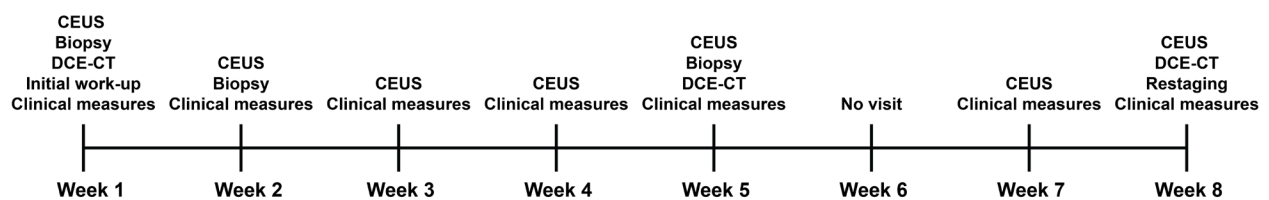


Figure 4.3 Study timeline for canine patients enrolled in the longitudinal study.

Initial study work-up during week 1 consisted of thoracic radiographs, abdominal ultrasound, and a coagulation panel. Clinical measures, which included a complete blood count, chemistry panel, urinalysis, urine protein to creatinine ratio, blood pressure, body weight, and tumor size, were collected at baseline and each subsequent session. Dynamic contrast-enhanced

CT (DCE-CT) scans, CEUS imaging, and a biopsy of the tumor were also completed at baseline. After baseline (week 1), patients returned once per week, except during week 6, for follow-up CEUS imaging and collection of clinical data. Follow-up DCE-CT scans were performed during weeks 5 and 8. Additional tumor biopsy samples (5-8 mm) were collected during weeks 2 and 5 using either a punch or tru-cut method. Finally, at the conclusion of the study, the tumor was restaged. Canine patients were placed under general anesthesia in order to perform DCE-CT and CEUS imaging examinations and to collect tissue samples. After completing baseline imaging (week 1), client-owned patients began a treatment regimen that consisted of toceranib phosphate (Palladia™, Pfizer, New York, NY, USA), a tyrosine kinase receptor inhibitor, and cyclophosphamide (Cytosan®, Bristol-Myers Squibb, New York, NY, USA), an anti-neoplastic agent. Owners were instructed to give their dog a weight-based dose of toceranib phosphate (2.75 mg/kg), taken by mouth, every other day. Cyclophosphamide was taken orally every day using a dose of 15-17.5 mg/m²/day. In the event that an adverse reaction to either treatment arose, veterinarians implemented a treatment break alongside the following approved concurrent medications: Famotidine or Omeprazole in the case that melena developed, Metronidazole or Loperamide if diarrhea occurred, and Maropitant or Ondansetron if vomiting occurred. Treatment regimen, dosing, and all other decisions regarding patient welfare were determined by the veterinarian providing care. After the first 15 months that the study was open, participation criteria were modified in an attempt to offset low enrollment numbers. The option to enroll for a single imaging session in lieu of the multi-week study was discussed with interested patients. Canine patients that enrolled in the single session underwent the same imaging protocol used for the first session of the multi-week study.

4.2.2.3 Dynamic Contrast-Enhanced CT Image Acquisition

DCE-CT scans were acquired using a SOMATOM Perspective 64 multi-slice helical scanner (Siemens Medical Solutions, Malvern, PA, USA). Iodinated contrast, nonionic iohexol (Omnipaque™, GE Healthcare, Chicago, IL, USA), was injected intravenously at a standard rate (3-5 mL/sec) using a controlled pressure injector (EnVision CT Injector, Medrad, Warrendale, PA, USA). The concentration of Omnipaque was 350 mg/mL and the contrast dose, 2.2 mL/kg, was determined based on canine body weight. DCE-CT image acquisition began immediately following the start of the contrast agent injection. Repeated multislice scans were acquired through a 24 mm cross section of the tumor at 1 rotation per second, with the following scanner settings: 90 kVp and 50-100 mA, which varied based on the thickness of the body region. The tumor cross section selected for imaging included the portion of the tumor that was found to be most hyper-attenuating on pre-contrast images, as determined by the veterinary radiologist who performed the DCE-CT data collection. After data was acquired, the tumor volume was reconstructed with a slice thickness of 1.5 mm. A standard post-contrast CT scan was collected at the end of the DCE-CT image acquisition.

4.2.2.4 Ultrasound Equipment and Image Acquisition

Ultrasound images were collected using the Acuson Sequoia 512 (Siemens, Mountain View, CA, USA) with the 9L4 linear array transducer. Volumetric data was acquired to account for tumor vascular heterogeneity, using an imaging setup designed to facilitate 3D data collection (Figure 4.4). The US probe was mounted onto a linear actuator (XSlide, Velmex, Bloomfield, NY, USA) set in the transducer housing, which was attached to a camera arm that allowed for imaging in any orientation. Probe translation via the linear actuator was directed by a VXM-1 stepper motor controller (Velmex, Bloomfield, NY, USA). A LabVIEW program (National

Instruments, Austin, TX, USA) was developed to synchronize probe translation with video capture.

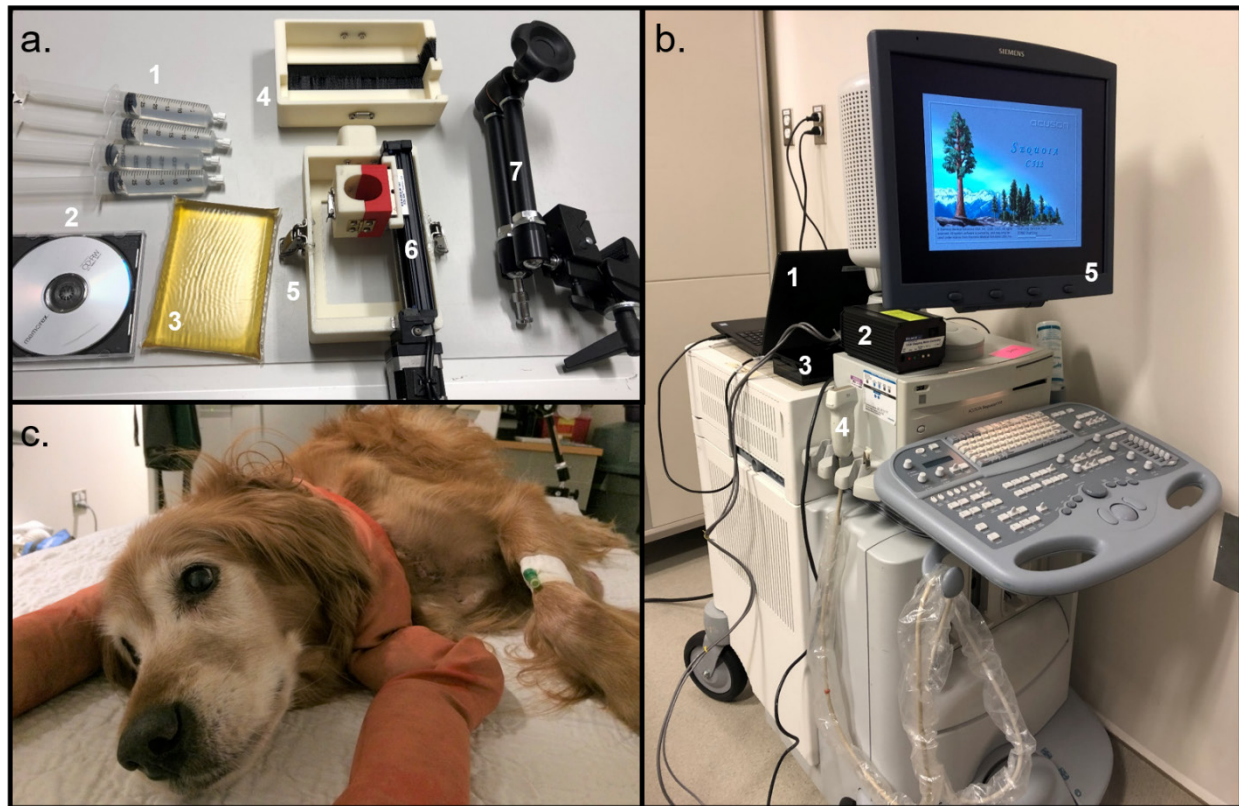


Figure 4.4 Ultrasound imaging equipment and setup. a) Equipment that enables 3D data acquisition and retrieval. 1. Degassed ultrasound gel, 2. CD for data retrieval, 3. Acoustic standoff pad, 4. 3D printed top casing with black brushing that houses ultrasound probe and linear actuator, 5. 3D printed bottom casing with side piece for camera arm attachment, notched cutouts to secure placement of the linear actuator, and window for probe translation across the tumor volume, 6. XSlide 4" single axis linear actuator with stepper motor and 3D printed transducer holder mounted on axis stage, and 7. Camera arm used to maneuver enclosed system for placement over tumor volume. b) Ultrasound system and master control setup. 1. Laptop with LabVIEW program to control and sync clip capture with probe translation, 2. VXM stepping motor controller, 3. NI-DAQmx and relay circuit encased in black 3D printed housing, 4. Ultrasound probe (9L4), and 5. Siemens Acuson Sequoia 512 ultrasound system used to collect CEUS data. c) Enrolled canine patient awaiting CEUS imaging.

The start and end of the US video clip was triggered by relaying LabVIEW commands through a NI-DAQmx driver (National Instruments, Austin, TX, USA) to the Sequoia footswitch, while the VXM simultaneously relayed commands to sweep the transducer across the

tumor volume. The scan speed for CEUS data acquisition was 2 mm/s, which corresponded to 2.5 frames per mm step.

Four scanning modes were utilized during data acquisition: B-mode, CPS, PW Doppler, and Color Doppler. Prior to imaging, hair was removed from the tumor region using electric shavers in addition to a depilation cream. The transducer was coupled to the tumor by covering the tumor with a thin layer of degassed ultrasound gel, followed by placing a reusable acoustic standoff pad (AliMed, Dedham, MA, USA) over the tumor, and then applying a final layer of gel to the face of the transducer. In combination with the ultrasound gel, the standoff pad minimized bright reflections resulting from the unintentional introduction of air at each interface during volumetric data acquisition. B-mode imaging was initially performed to scan the tumor volume. For each patient, image depth and focus were determined based on tumor size and location. B-mode frequency (7 MHz), power output (0 dB), dynamic range (68 dB), and frame rate (5 Hz) were kept consistent for each patient. Gain was adjusted to optimize tumor visualization. B-mode data acquisition was followed by a 3D ARF-enhanced USMI protocol. Briefly, targeted microbubbles (5×10^7 MB/kg) were injected intravenously through a catheter placed in a peripheral vein, followed by a 3 mL saline flush. ARF sweeps across the tumor volume were initiated synchronously with bubble injection and applied continuously for three minutes. ARF sweep speed varied slightly based on tumor size to ensure that the transducer traversed the tumor volume 10 times over a consistent timeframe. ARF pushes were generated using PW Doppler with the following settings: 3.5 MHz frequency, 0 dB power output, image focus placed at 120 mm, image depth of 140 mm, 18 mm PW gate, 128 mm PW cursor depth with the cursor centered laterally, 1 m/s scale with HPRF displayed on-screen, and -30 dB gain. Following ARF sweeps, volumetric scans in CPS mode were collected using a set transmit frequency (4 MHz),

MI (0.18), dynamic range (50 dB), and frame rate (5 Hz). CPS gain varied between patients, but was kept constant across imaging sessions (day 0 to day 56) within individual patients. CEUS videos were collected intermittently between 3 and 6 minute after MB injection. The volumetric scan collected at 3 minutes was used to assess initial tumor perfusion and MB targeting was assessed at 6 minutes. A pre-destruction clip of MB signal throughout the tumor volume was acquired, then, using Color Doppler, high pressure pulses (MI = 1.9) were applied across the tumor volume to disrupt all bubbles in the tumor volume. Remaining freely-circulating bubbles were allowed to repopulate the tumor before a post-destruction volumetric scan in CPS mode was acquired. MB signal in the tumor prior to and following disruption was calculated in order to extract signal from bubbles bound to the tumor vasculature. Molecular expression measured by two different targeted microbubbles compared to a control bubble was evaluated using this imaging protocol. The above protocol was repeated for each separate microbubble injection, with down time between acquisitions to allow remaining freely circulating MBs to clear from tissue.

4.2.2.5 Microbubble Formulation and Preparation

Microbubbles were synthesized at the University of Colorado in Boulder and shipped to North Carolina for use in the study. Microbubbles were size-selected (3 μm diameter) by differential centrifugation [198] and prepared at a concentration of 1×10^9 MB/mL. Functionalized ligands cyclo[Arg-Gly-Asp-D-Phe-Lys-(Azide)] (cRGD) or Lys(Azide)-Ala-Thr-Trp-Leu-Pro-Pro-Arg (A7R) were conjugated to the microbubble surface using strain-promoted [3 + 2] azide-alkyne cycloaddition (SPAAC) click chemistry by reacting 1,2-distearoyl-*sn*-glycero-3-phosphoethanolamine-*N*-[dibenzocyclooctyl(polyethylene glycol)-2000] (DSPE-PEG2000-DBCO) with the ligand of choice [199,200]. Targeting ligands were shielded by incorporating 1,2-distearoyl-*sn*-glycero-3-phosphoethanolamine-*N*-[methoxy(polyethylene

glycol)-5000] (DSPE-PEG5000) into the lipid solution. Buried-ligand architecture has been previously described by Borden and Chen [142–144]. Control BLA microbubbles were synthesized and labeled with cyclo Arg-Ala-Asp (cRAD) to serve as a comparison to targeted bubbles (cRGD, A7R). Following fabrication, microbubbles were packaged on ice and shipped to either the University of North Carolina at Chapel Hill or the Colorado State University Flint Animal Cancer Center, based on the site where the patient was enrolled. Upon receipt, MB size and concentration were measured using an Accusizer 780 (Particle Sizing Systems, Santa Barbara, CA, USA). Three replicates were averaged to determine the concentration of each bubble type, which was used to calculate the appropriate dose to be administered to the patient. Microbubbles were administered by hand as a bolus injection using a weight-based dosing scheme of 5×10^7 MB/kg, which corresponds to 50 $\mu\text{L/kg}$. Prior to use in client-owned canine patients, the safety and tolerability of these targeted bubbles using three different doses, 0.1 $\mu\text{L/kg}$, 10 $\mu\text{L/kg}$, and 100 $\mu\text{L/kg}$, was established [200].

4.2.2.6 Data Analysis

A MATLAB® program was developed to analyze targeted bubble signal across the tumor volume. First, B-mode scans were used to draw ROIs around the tumor for each slice in the data set. The ROI set was applied to the 3D contrast scans acquired post-ARF between 3 and 6 minutes (Figure 4.5). The first contrast scan following ARF was used as a measure of the initial tumor perfusion. ROIs were updated based on initial tumor perfusion to exclude non-perfused regions.

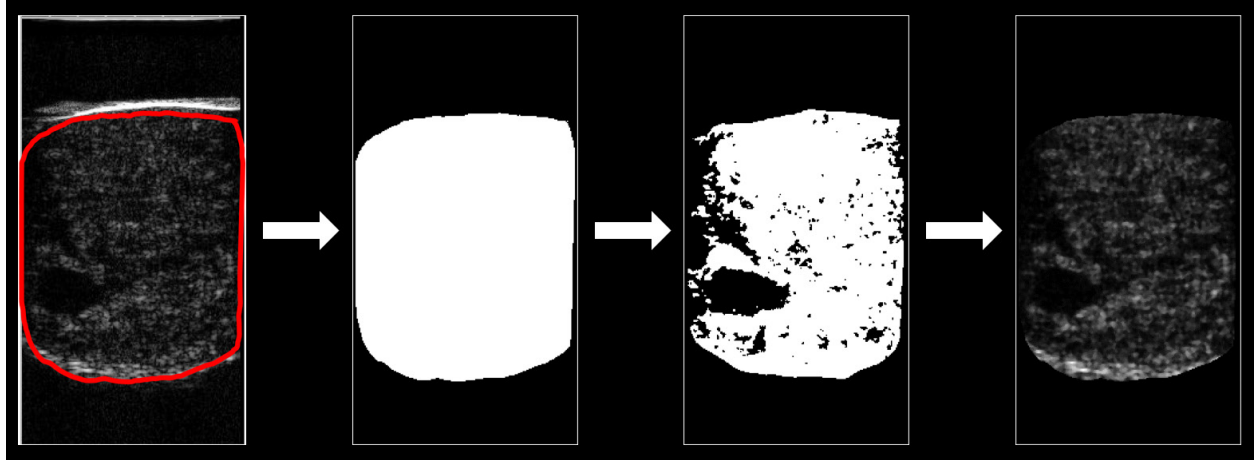


Figure 4.5 Process of signal extraction from tumor. An ROI (red outline) originally drawn on the B-mode data set is applied to the contrast frame. A binary mask of the tumor ROI is generated and a binary mask of perfused tumor regions is generated by applying a threshold to the first contrast scan after ARF (at 3 minutes). The product of the tumor mask and the perfusion mask is used to extract signal from only perfused regions of the tumor volume.

Perfused regions were isolated from background signal by quantizing the images based on a single level threshold that separated contrast signal from background noise. The perfused ROI set was multiplied by the original tumor ROI to generate a new ROI that only included perfused regions of the tumor (Figure 4.5). The updated ROI set was applied across the tumor volume to extract all perfused pixels and calculate the average bubble signal in the tumor. The difference between the average bubble signal in the targeted scan at 6 minutes and the post-destruction scan at 9 minutes was used to calculate dTE and determine the signal magnitude from adhered bubbles. This metric was calculated for each bubble type across each imaging session and compared to tumor volume. For patients enrolled in the single session, the same process was used for data extraction. In addition to dTE, other metrics were calculated for the single session patients, which included percent tumor perfusion immediately following ARF (at 3 minutes), average MB signal across the tumor volume at 3 minutes, and percent tumor perfusion during the targeted scan (6 minutes). Pearson's pairwise linear correlation was computed to test for a relationship between specific parameters using an α level of 0.05. The

correlation coefficients (ρ) and corresponding P -values were provided, where associations between 0-0.19 were regarded as very weak, 0.20-0.39 as weak, 0.40-0.59 as moderate, 0.60-0.79 as strong, and 0.80-1 as very strong.

4.2.2.7 DCE-CT and IHC Analysis

DCE-CT scans and tissue samples were processed at the CSU Flint Cancer Center. DCE-CT data was analyzed by a veterinary radiologist and tissue samples were stained and assessed by the Molecular Pathology laboratory. Perfusion parameters were extracted from the DCE-CT images by drawing ROIs slice-by-slice across the tumor volume. Average perfusion, peak enhancement (PE), time to peak (TTP), and blood volume (BV) were calculated using the DCE-CT data. Immunohistochemistry (IHC) analysis was completed on the tissue samples collected from each patient. Tissue sections were stained to assess either CD31, VEGFR2, or $\alpha v \beta_3$ integrin expression and results were reported as average vessel density per high-powered field (HPF). Pearson's pairwise linear correlation was computed to test for a relationship between ultrasound, DCE-CT, IHC, and tumor volume measures ($\alpha = 0.05$). The correlation coefficients (ρ) and corresponding P -values were provided for each comparison.

4.3 Results

4.3.1 *In vitro* Acoustic Radiation Force Trials

4.3.1.1 Pressure Calibrations

Transducer center pressure was measured for tested power outputs between 0 and -15 dB. Pressures were recorded with the hydrophone at a distance of 2, 3, 4, and 5 cm from the transducer face. The highest peak negative pressure (PNP) was 178.15 kPa, recorded at a depth of 5 cm and the lowest PNP was 15.02 kPa, recorded at a depth of 4 cm (Figure 4.6a). The corresponding derated pressure measurements were 97.35 kPa and 9.26 kPa, respectively (Figure

4.6b). Average PNP pressure and average derated pressure values were calculated and reported in Table 4.1. The microbubble displacement resulting from utilizing different pressures at depths ranging from 2-5 cm were assessed to determine the optimal acoustic radiation force settings across a range of tumor sizes larger than 1 cm.

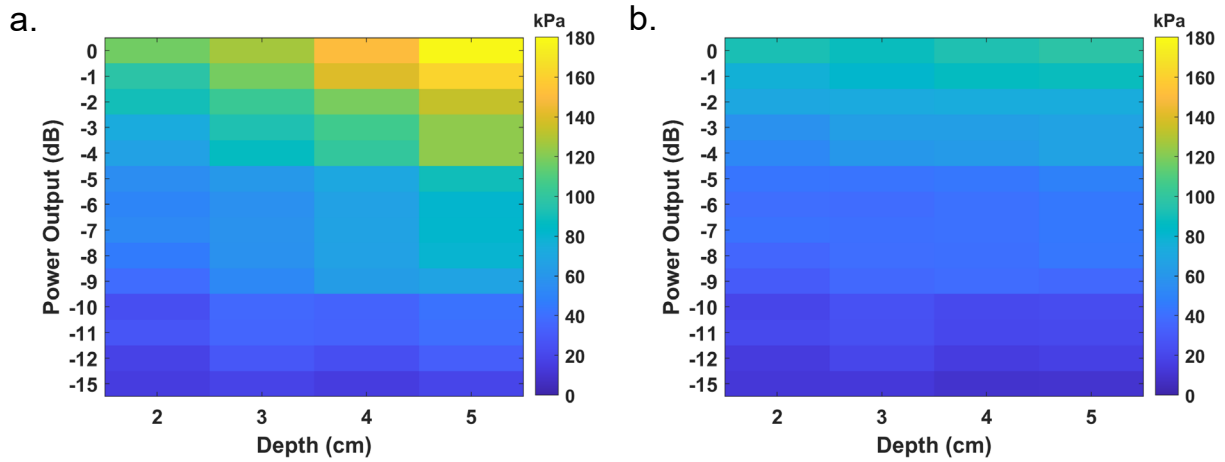


Figure 4.6 Recorded pressure from the 9L4 transducer. a) PNP recorded at depths of 2, 3, 4, and 5 cm for power outputs between 0 and -15 dB. b) Derated pressure from (a).

Table 4.1 Average pressure recorded for power outputs between 0 and -15 dB

Power Output (dB)	Average Pressure (kPa) \pm SD	Average Derated Pressure (kPa) \pm SD
0	143.39 \pm 27.17	92.76 \pm 3.67
-1	129.54 \pm 27.77	83.50 \pm 5.24
-2	111.72 \pm 18.88	72.40 \pm 1.09
-3	98.46 \pm 20.92	63.48 \pm 4.32
-4	94.28 \pm 23.56	60.52 \pm 6.13
-5	69.26 \pm 14.93	44.68 \pm 2.82
-6	63.72 \pm 13.50	41.12 \pm 2.40
-7	64.91 \pm 12.67	41.98 \pm 1.93
-8	62.32 \pm 14.31	40.10 \pm 3.13
-9	55.93 \pm 12.84	36.00 \pm 3.59
-10	34.47 \pm 7.35	22.28 \pm 2.77
-11	34.24 \pm 4.90	22.30 \pm 1.74
-12	25.67 \pm 5.83	16.60 \pm 2.45
-15	16.98 \pm 2.14	11.15 \pm 1.65

4.3.1.2 Microbubble displacement

For each depth, total microbubble displacement decreased as transmit pressure decreased, with a relationship between the two variables following a moderate linear regression (Figure 4.7).

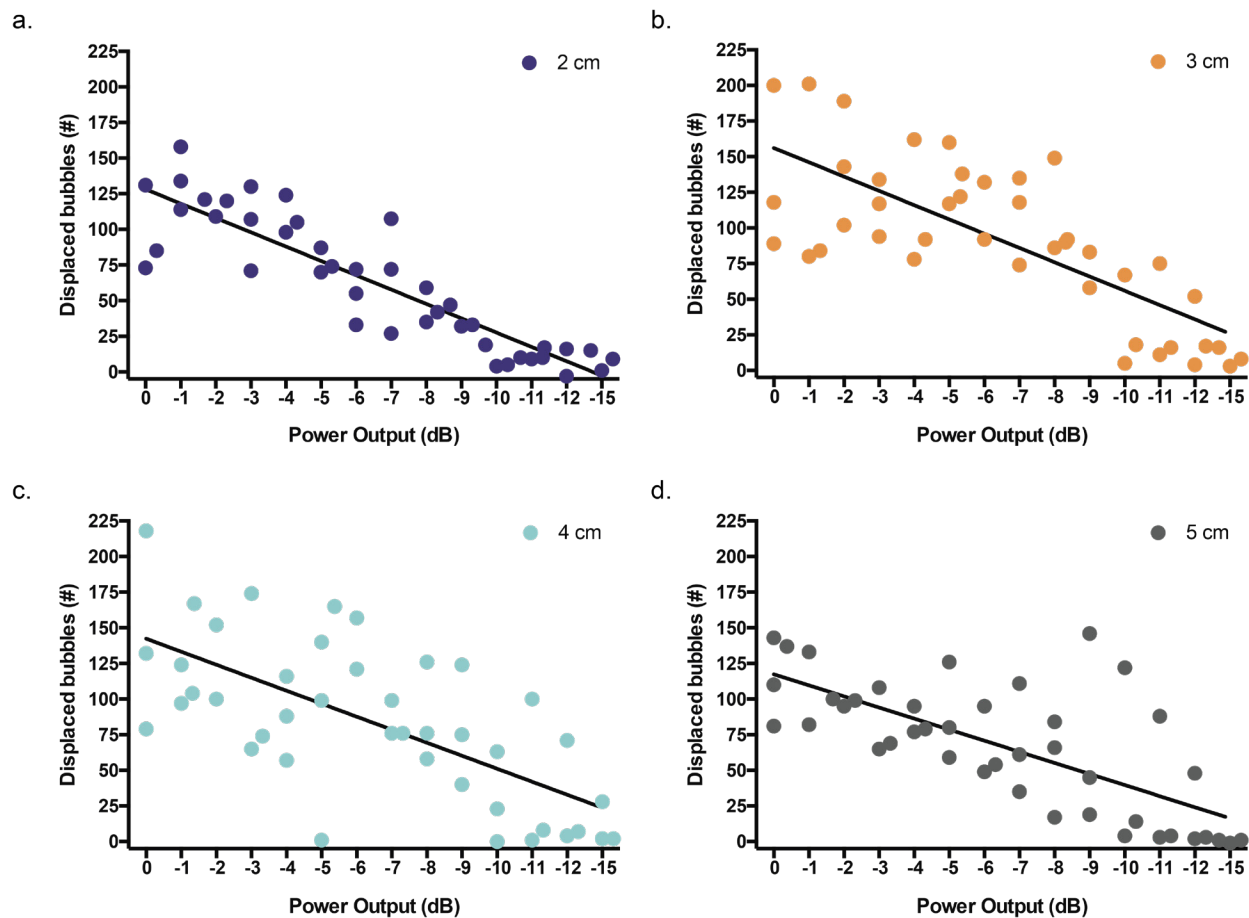


Figure 4.7 Number of displaced bubbles for decreasing power outputs at depths from 2-5 cm. Power outputs tested ranged from 0 to -15 dB (high to low) with the tube placed at a distance of a) 2 cm, b) 3 cm, c) 4 cm, and d) 5 cm from the face of the transducer. Each data set ($n = 3$ per power output) was fit with a linear regression model.

The strength of the regression was highest for a distance of 2 cm ($R^2 = 0.7852$) and lower for distances of 3-5 cm ($R^2 = 0.5448, 0.431$, and 0.4842). Larger variance in the number of displaced bubbles for each power output was observed when the transducer was 3-5cm from the

microtube, which likely contributed to the decreased GOF for these groups. The model parameters with standard error (SE) for each depth from 2-5 cm are displayed in Table 4.2.

Table 4.2 Linear regression parameters with goodness of fit for each depth

Depth (cm)	Slope (\pm SE)	Intercept (\pm SE)	Adjusted R^2	Non-zero slope
2	-10.06 ± 0.819	128.2 ± 6.264	0.7852	$P < 0.0001$
3	-10.02 ± 1.416	156.1 ± 10.83	0.5448	$P < 0.0001$
4	-9.125 ± 1.612	142.4 ± 12.33	0.431	$P < 0.0001$
5	-7.775 ± 1.237	117.4 ± 9.463	0.4842	$P < 0.0001$

For each depth, the slope of the regression line was significantly non-zero ($P < 0.0001$). Testing to determine if a pooled slope and intercept best described the data revealed no significant differences between the slopes ($P = 0.5693$), but significant differences between the intercepts ($P = 0.0004$). This resulted in a best fit model with a shared slope of -9.245 ± 0.6501 and individual intercepts for each depth from 2-5 cm of 122.9 ± 6.733 , 151.1 ± 6.733 , 143.2 ± 6.733 , and 127 ± 6.733 , respectively. Using a shared slope, the rate of decrease for displaced bubbles can be considered similar across all depths, although the amount of displaced bubbles at each pressure may vary for each depth. Two-way ANOVA evaluating potential effects of pressure and depth on bubble displacement revealed significant differences in displacement when considering pressure ($P < 0.0001$) and depth ($P = 0.0007$) individually, but not when considering the interaction between the two parameters ($P = 0.8988$). Post-hoc multiple comparisons assessed the influence of different depths at each power output on bubble displacement (Supplemental Table C. 21) and the overall influence of varying pressure on bubble displacement (Supplemental Table C. 22). The only significant differences in bubble displacement due to varying depth occurred when comparing 2 cm vs. 4 cm ($P = 0.007$) and 4 cm vs. 5 cm ($P = 0.0258$) at a power output of -6 dB. Any variations in bubble displacement

comparing all other depths at each pressure were not significant ($P > 0.05$). When evaluating differences in bubble displacement by varying power output, without grouping by depth, significant differences were found primarily between pressure outputs separated by at least three levels (i.e. -7 dB and -10 dB) after a certain threshold. Displacement using power outputs from 0 to -7 dB were all significantly greater than displacement using power outputs from -10 to -15 dB ($P < 0.05$). Additionally, displacement for power outputs from 0 to -2 dB were significantly greater than displacements using -8 and -9 dB ($P < 0.05$), while displacements using -8 dB were greater than -12 or -15 dB ($P < 0.05$), and displacements using an output of -9 dB were greater than -15 dB ($P < 0.05$). Finally, to select the optimal ARF power output, the calculated displacements at each depth were combined to assess which output resulted in the least amount of variance in displaced bubbles (Figure 4.8). Given that displacement using all power outputs from 0 to -7 dB were significantly greater than displacement from all power outputs between -10 and -15 dB, -7 dB was selected as the lower threshold for determining the output with minimal variance.

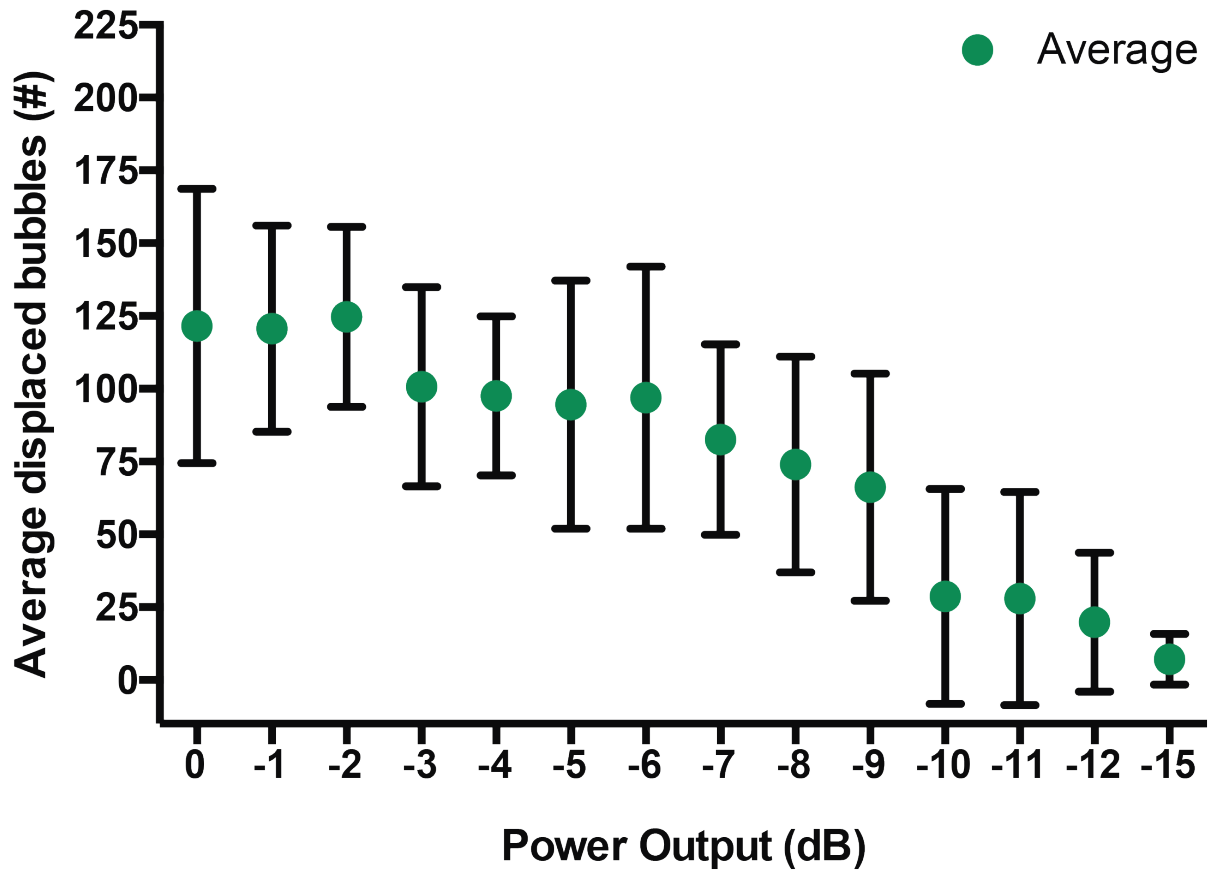


Figure 4.8 Average number of displaced bubbles for power outputs ranging from 0 dB to -15 dB. Results from bubble pushing trials at depths of 2, 3, 4, and 5 cm were combined to determine the average number of bubbles pushed to the tube wall for each power output. Error bars denote standard deviation.

As a result, it was determined that an output of -4 dB generated the most stable push, with a minimum variance of 27.25 (Table 4.3). Lower outputs (-12, -15 dB) had smaller variance in bubble displacement, but these were not considered for optimal push settings given the significantly greater amount of displaced bubbles for outputs above -7 dB. The corresponding average derated pressure closest to the average pressure measured at -4 dB was found for an output of 0 dB.

Table 4.3 Average number of displaced bubbles for power outputs between 0 and -15 dB

Power output (dB)	Average Displacement	Standard deviation
0	121.58	47.16
-1	120.67	35.46
-2	124.75	30.99
-3	100.67	34.24
-4	97.58	27.25
-5	94.58	42.56
-6	96.92	45.10
-7	82.63	32.74
-8	74.00	37.14
-9	66.17	39.09
-10	28.67	36.89
-11	27.92	36.64
-12	19.83	23.87
-15	7.08	8.68

These data were corroborated by visual observations of ARF push parameters. Ideal push parameters create a gentle force that causes bubble translation towards the tube wall. At higher acoustic outputs (0 to -2 dB), it was observed that the magnitude of the force felt by the bubbles resulted in the formation of large bubble aggregates that were rapidly displaced towards the tube wall and continued moving along the wall after impact (Figure 4.9). In comparison, at lower acoustic outputs (-3 to -8 dB), the magnitude of ARF was such that bubbles in the acoustic field experienced a steady push, were less prone to aggregation, and accumulated at the boundary of the distal tube wall (Figure 4.10).

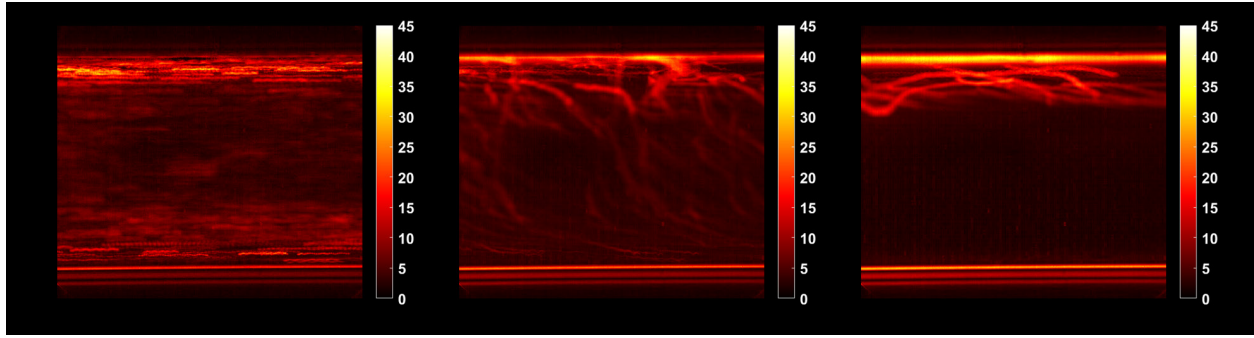


Figure 4.9 Streak images of bubbles in the presence and absence of a powerful acoustic radiation force push. Left image: Freely flowing bubbles (no ARF) moving through a microtube in the direction of flow from right to left. A typical parabolic velocity profile can be observed where flow is slower near the tube walls (brighter streaks) compared to the center (darker streaks). Streak standard deviation image generated represents 120 ms of data. Center image: Initialization of ARF causes bubbles to be pushed towards the distal tube wall in the direction of wave propagation (bottom to top). The formation of bubble aggregates from secondary radiation force causes thicker streaks. Streak image represents 1 s of data. Right image: Too forceful of a push will cause bubble translation along the distal wall, instead of facilitating interaction with the wall. Streak image represents 1 s of data. These panels provide an example where the transducer was placed 2 cm from the tube using a power output of 0 dB.

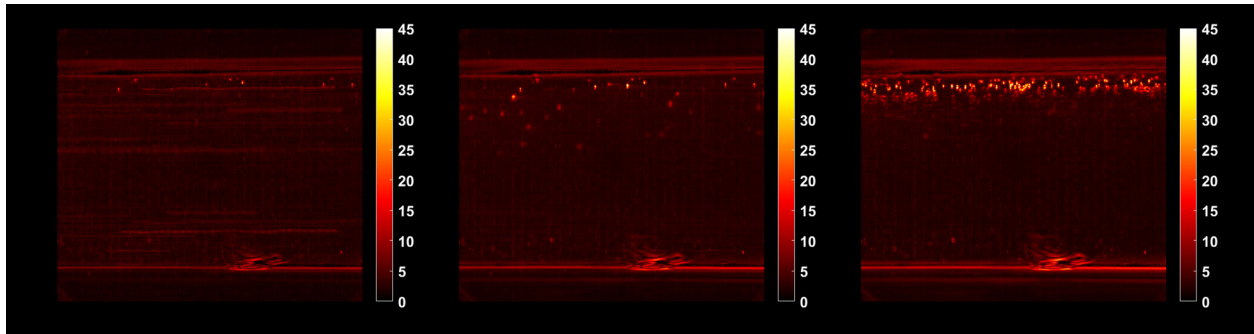


Figure 4.10 Streak images of bubbles in the presence and absence of an ideal acoustic radiation force push. Left image: Freely flowing bubbles (no ARF) moving through a microtube in the direction of flow from right to left. Streak standard deviation image generated represents 120 ms of data. Center image: Initialization of ARF causes bubble displacement towards the distal tube wall in the direction of wave propagation (bottom to top). Streak image represents 1 s of data. Right image: An ideal push allows for bubble accumulation along the wall (bright dots). Streak image represents 1 s of data. These panels provide an example where the transducer was placed 3 cm from the tube using a power output of -5 dB.

4.3.2 Clinical Translation of Radiation Force Enhanced Ultrasound Molecular Imaging

4.3.2.1 Patient Recruitment and Enrollment

The study was open for patient enrollment at the North Carolina State University (NCSU) College of Veterinary Medicine during two separate time spans, between July 2018-March 2020 and July 2020-March 2021. During the enrollment period, 85 clients expressed interest in or were recruited for the study. Forty-six clients expressed initial interest, but did not proceed to a consultation; 24 consulted with an oncologist, but did not enroll; 6 enrolled, but did not complete the study; and 9 enrolled and successfully completed the study (Table 4.4). The majority of the cases where owners were interested, but did not proceed to a consultation (46/85, 54.12%) was due to ineligibility as a result of the wrong tumor type (21/85, 24.71%) or the fact that the tumor had already been surgically removed (12/85, 14.12%). Following consultation, the most common cause for not enrolling was due to the client declining for undisclosed reasons (8/85, 9.41%), ineligibility from a non-healing wound (7/85, 8.24%), or the client elected for the patient to undergo surgery and possible follow-up RT (6/85, 7.06%). Less than a fifth of the patients recruited for the study decided to enroll (15/85, 17.65%), and further dropout occurred after enrollment. Six patients withdrew early, become ineligible to continue, or were unable to complete the study due to cancelation, while nine patients successfully completed the study. Recruitment was highest between January and March 2019, with 23 potential patients interested in the study during that period (Figure 4.11a). Of these patients, ultimately only two chose to enroll in the study (Figure 4.11b-c).

Table 4.4 Number of client-owned canine patients recruited and enrolled

Client-owned Patients	N (%)
Total number	85 (100%)
Initial contact (owner interest)	
Ineligible	
Tumor surgically removed	12 (14.12%)
Tumor type	21 (24.71%)
Tumor characteristic	4 (4.71%)
Other study criteria	4 (4.71%)
Declined to participate	4 (4.71%)
Elected for surgery	1 (1.18%)
After consultation	
Ineligible	
Ulcerated or non-healing wound	7 (8.24%)
Multiple masses or metastasis	2 (2.35%)
Tumor type	1 (1.18%)
Declined to participate or undisclosed reason	8 (9.41%)
Elected for surgery (with or without follow-up RT)	6 (7.06%)
Enrolled	
Did not complete	
Withdrew	3 (3.51%)
Became ineligible	2 (2.35%)
Study canceled ¹	1 (1.18%)
Multi-week imaging	2 (2.35%)
Single session imaging	7 (8.24%)

Between July 2018 and September 2019, 60 patients were recruited for the study, but only five patients enrolled (Figure 4.11). Given low enrollment numbers coupled with the fact that only two of the five successfully completed the 8-week protocol, the study was modified to allow patients to enroll for only a single session of imaging (DCE-CT, CEUS, biopsy). This boosted enrollment and from October 2019 – March 2020 and July 2020 – March 2021 (the study was closed from April 2020 – June 2020) an additional 25 patients were recruited, 10 of

¹Last minute cancellation in response to COVID-19.

which enrolled in the study (Figure 4.11). Three of the enrolled patients during this period either withdrew or became ineligible prior to imaging.

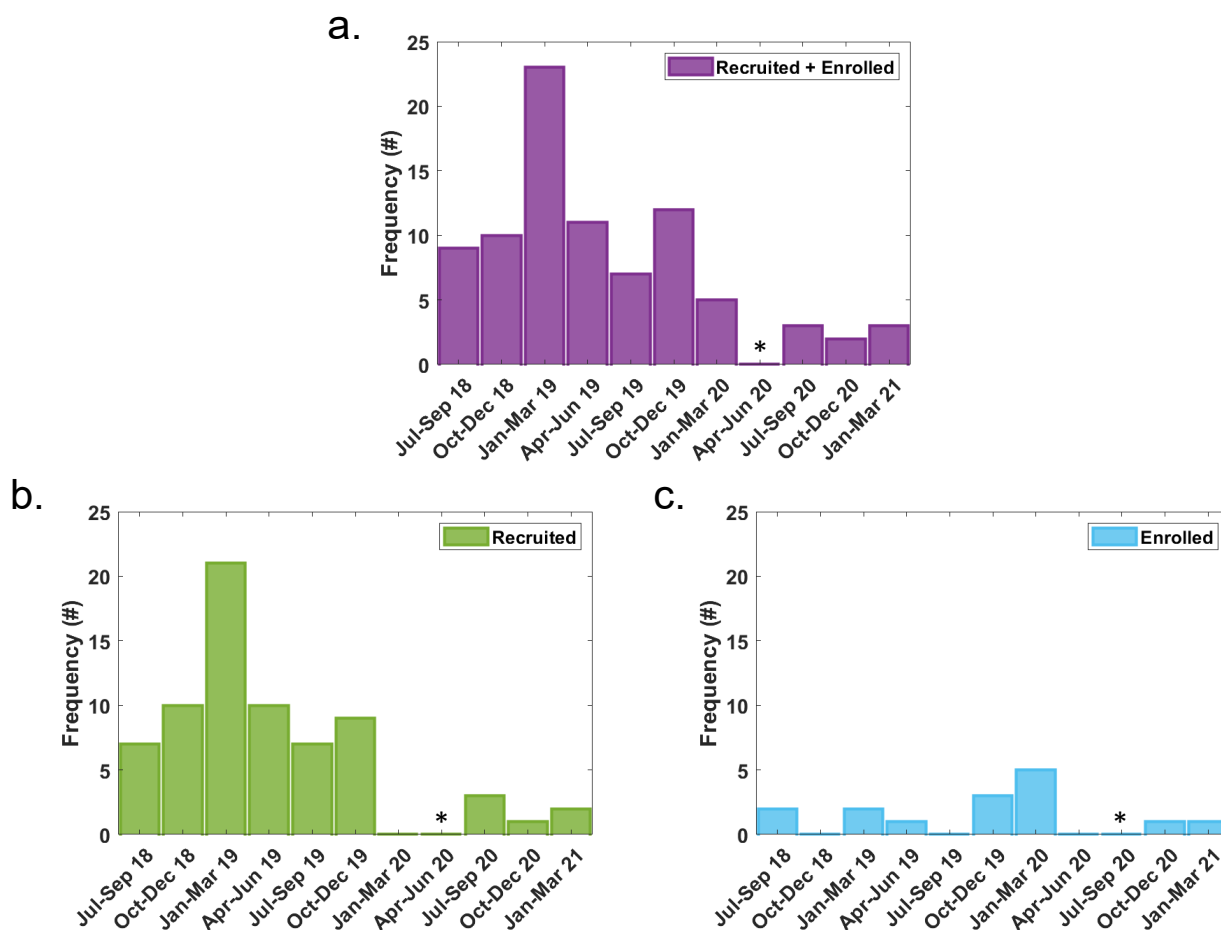


Figure 4.11 Canine recruitment and enrollment during study period. a) Total number of patients recruited and enrolled during each quarter that the study was open, b) Number of canine patients recruited that did not enroll during each quarter of the study period, and c) Number of patients that were recruited and enrolled during each quarter of the study period. *The study was not open for recruitment or enrollment during this quarter.

4.3.2.2 Monitoring Tumor Response to Treatment

Three canine patients enrolled in the multi-week imaging study and two completed the 8-week protocol. One patient withdrew from the study after week 3 due to a poor response to the chemotherapy (002). The imaging protocol and MB dosing scheme were modified during the first patient (001) to optimize imaging for remaining patients. The original protocol captured a

wash-in video to quantify initial tumor perfusion prior to initiating an ARF push. However, given the architecture of the targeted bubbles (BLA), this severely limited exposure of the targeting ligand during a critical stage of MB transit through the tumor. The wash-in followed by ARF sequence was substituted for a longer ARF push phase that sufficiently covered the first pass of the MBs through the tumor volume, to maximize targeting ligand exposure to tumor vasculature. Information lost by removing the wash-in clip acquisition was offset by the additional exposure time of the targeting ligand to the vascular endothelium with the lengthened ARF push. The MB dose was adjusted after the first patient and was increased from 2×10^7 MB/kg to 5×10^7 MB/kg, to ensure a sufficient concentration of targeted MBs was delivered to the tumor.

USMI data collected over the multi-week imaging study in the third patient (003) was compared to changes in tumor volume to assess patient response to treatment. Data from two sessions, the 2nd and 6th weeks, were excluded from analysis due to technical difficulties during data collection (2nd session) and an equipment malfunction during acquisition (6th session). All data suffered from technical difficulties encountered during the 2nd session, but only cRGD-MB data collection was impacted by the equipment malfunction during the 6th session. To accommodate the availability of patient 003, the imaging schedule for sessions six and seven were interchanged so that imaging occurred during the 6th week and the break occurred in the 7th week. Tumor volume fluctuated over the eight-week treatment regimen, remaining stable between the 1st and 2nd week, growing from the 2nd week to the 3rd week, then oscillating around the volume from the 3rd week before exhibiting a large increase in size between the 6th and 8th week (Figure 4.12). In comparison, cRGD-MBs dTE decreased from the 1st to the 3rd session, after which point dTE began increasing, surpassing baseline dTE (1st session) by the 5th session and remaining stable from the 5th session to the 8th session (Figure 4.12).

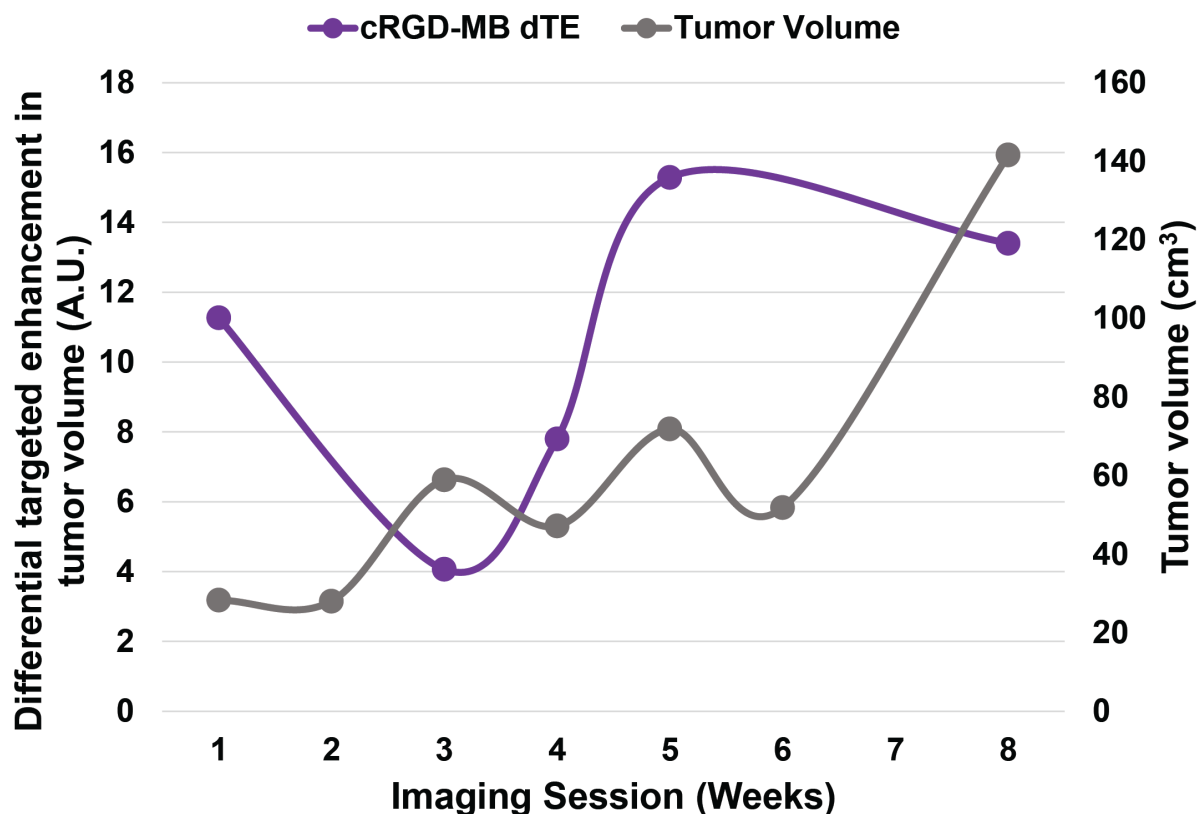


Figure 4.12 Changes in dTE from UCAs targeted to $\alpha_v\beta_3$ integrin (cRGD-MBs) compared to tumor volume over the multi-week study. The left y-axis marks dTE (A.U.) and the right y-axis marks tumor volume (cm³).

Differential targeted enhancement from A7R-MBs followed a similar trend as changes in tumor volume, starting at 2.90 A.U. for the 1st session, increasing slightly for the 3rd (5.26 A.U.) and 4th (4.38 A.U.) sessions, before exhibiting a larger increase between the 4th and 5th sessions (Figure 4.13). Unlike with the cRGD-MBs, A7R-MB dTE did not remain stable, but decreased from the 5th week to the 6th week, before increasing again at the 8th session (Figure 4.13).

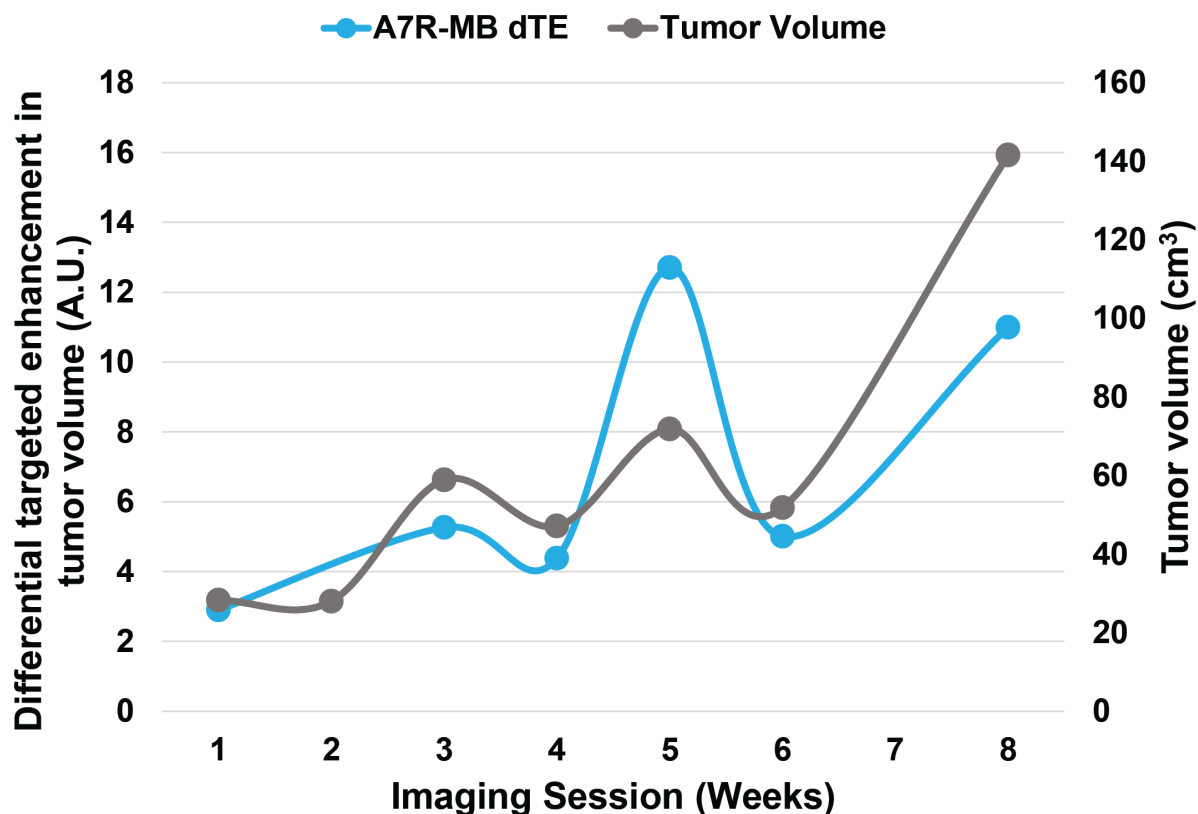


Figure 4.13 Changes in dTE from UCAs targeted to VEGFR2 (A7R-MBs) compared to tumor volume over the multi-week study. The left y-axis marks dTE (A.U.) and the right y-axis marks tumor volume (cm³).

4.3.2.3 Single Session Parameter Correlations

Seven client-owned, canine patients successfully completed a single imaging session. One patient was excluded from data analysis due to technical issues during image acquisition. Images collected from the remaining six patients were analyzed to assess bubble adherence to tumor vasculature using non-specific MBs (cRAD), $\alpha_v\beta_3$ -targeted MBs (cRGD), and VEGFR2-targeted MBs (A7R). Metrics extracted from single session data included tumor perfusion (%) and MB intensity in the tumor volume immediately following ARF (A.U.), tumor perfusion (%) immediately preceding bubble destruction (preMBD), and adherent MB signal using dTE (A.U.) (Table 4.5). Tumor volume was also recorded for each patient (Table 4.5).

Table 4.5 Tumor volume and ultrasound metrics for single session patients

Patient	Tumor Grade	Tumor Volume (cm ³)	Initial Perfusion (%)			Initial Intensity (A.U.)			PreMBD Perfusion (%)			dTE (A.U.)		
			<u>cRAD</u>	<u>cRGD</u>	<u>A7R</u>	<u>cRAD</u>	<u>cRGD</u>	<u>A7R</u>	<u>cRAD</u>	<u>cRGD</u>	<u>A7R</u>	<u>cRAD</u>	<u>cRGD</u>	<u>A7R</u>
004	STS 2	113.10	27.86	24.82	1.90	36.91	31.07	1.60	0.26	0.23	0.19	1.30	0.63	0.10
005	LPS ²	628.32	7.04	10.55	0.85	17.79	29.77	2.92	0.31	0.44	0.36	1.36	2.38	0.64
006	STS 1	7.24	79.09	92.35	69.74	53.60	83.98	41.70	17.61	14.34	3.92	26.95	24.38	4.43
007	STS 1	41.88	5.97	16.82	1.22	11.51	37.47	2.18	0.37	0.55	0.29	0.96	4.04	1.13
008	STS 2	213.90												
009	STS 1	321.20	3.25	9.22	1.39	1.43	7.36	1.09	0.51	1.22	0.69	-0.14	0.10	-0.01
010	STS 1	48.25	2.34	0.65	0.72	34.52	8.33	10.26	2.34	0.65	0.72	28.91	4.86	5.72

²Liposarcoma (LPS)

Pairwise linear correlation was computed to assess the relationship between parameters. Targeted MB adherence to vascular markers was low in many patients, with only one patient (006) displaying meaningful targeting (Figure 4.14a). In many cases, non-specific attachment (cRAD-MBs) matched or exceeded targeted attachment (cRGD-MBs and A7R-MBs). Follow-up *in vitro* experimentation to assess the validity of cRAD as a control revealed an interaction between cRAD and recombinant $\alpha_v\beta_3$ (results not shown). PreMBD tumor perfusion (%) and cRGD-MB attachment (dTE) revealed a very strong positive linear correlation (Figure 4.14b). This relationship was maintained to a lesser extent with cRAD-MBs (strong association) and A7R-MBs (moderate association). The correlation coefficients (ρ) corresponding to the aforementioned pairs were 0.97 ($P = 0.00094$), 0.68 ($P = 0.134$), and 0.55 ($P = 0.256$), respectively. Tumor volume had a moderate negative association with cRGD-MB dTE ($\rho = -0.43$, $P = 0.394$), but was very weakly associated with cRAD-MB dTE ($\rho = -0.16$, $P = 0.758$) and A7R-MB dTE ($\rho = -0.12$, $P = 0.827$) (Figure 4.14c). Percent tumor perfusion following ARF (initial perfusion) and A7R-MB intensity post-ARF (initial intensity) had a very strong positive linear correlation ($\rho = 0.97$, $P = 0.00094$), which was also reflected by initial perfusion and initial cRGD-MB enhancement ($\rho = 0.95$, $P = 0.004$) (Figure 4.14d). This strong association was sustained by initial perfusion and initial cRAD-MB intensity to a slightly lesser degree ($\rho = 0.80$, $P = 0.0584$). Lastly, moderate negative correlations were observed between tumor volume and initial perfusion using cRGD ($\rho = -0.55$, $P = 0.263$), cRAD ($\rho = -0.52$, $P = 0.293$), and A7R ($\rho = -0.46$, $P = 0.355$) MBs (Figure 4.14e).

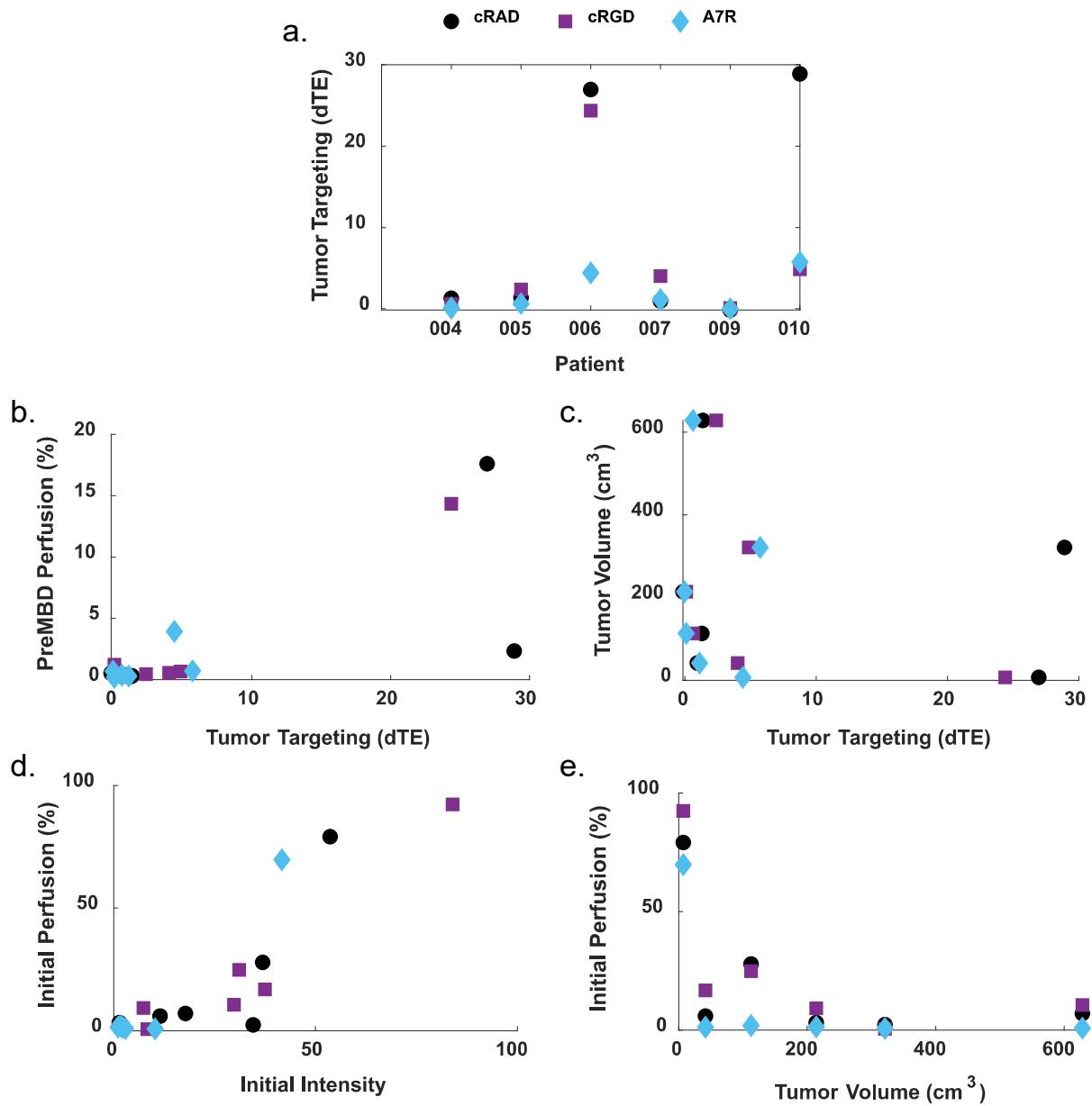


Figure 4.14 Tumor targeting and linear correlation between USMI and tumor parameters. a) Differential targeted enhancement (dTE) across the tumor volume for each single session patient using non-specific (cRAD), $\alpha_v\beta_3$ -targeted (cRGD), and VEGFR2-targeted (A7R) MBs, b) PreMBD perfusion (%) plotted against dTE for each MB, c) Tumor volume (cm³) versus dTE per MB, d) Initial perfusion (%) compared to initial MB intensity, and e) Initial perfusion (%) versus tumor volume (cm³). Data points are black circles (cRAD), purple squares (cRGD), and blue diamonds (A7R).

4.3.2.4 Correlations between DCE-CT, IHC, and Ultrasound Data

In addition to the patients enrolled at NCSU, at the secondary site (CSU) one patient enrolled in the multi-week study and 12 patients enrolled in the single session study. Due to issues with data integrity (noise corruption, beam artifacts, inclusion of tissue signal, image saturation), microbubble signal from the ultrasound data could not be extracted and analyzed. Those cases were excluded from US analysis, but were included in the DCE-CT and IHC datasets, where available. Issues with sample integrity precluded $\alpha_v\beta_3$ integrin from analysis, and remaining IHC metrics (CD31 and VEGFR2 vessel density) were limited due to poor staining. Correlations between ultrasound, DCE-CT, IHC, and tumor volume were evaluated, where data was available. The association between DCE-CT parameters and average CD31 vessel density was examined for 11 cases, which included one multi-session case that provided two separate data points ($n = 12$). All DCE-CT metrics, tumor perfusion ($\rho = 0.572$, $P = 0.052$), PE ($\rho = 0.477$, $P = 0.117$), TTP ($\rho = -0.427$, $P = 0.166$) and BV ($\rho = 0.515$, $P = 0.086$), demonstrated moderate correlation with CD31 vessel density, although no associations were statistically significant ($P < 0.05$). All associations were positive, except TTP, which had a negative linear correlation (Figure 4.15).

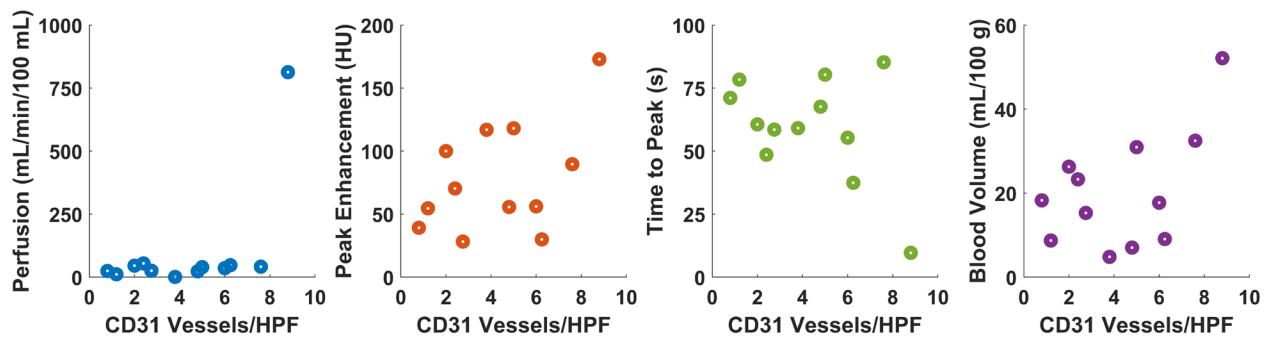


Figure 4.15 Relationship between CD31 expression and DCE-CT metrics. Moderate associations existed between tumor perfusion, PE, TTP, and BV compared to CD31 expression; $n = 12$.

The association between DCE-CT parameters and average VEGFR2 vessel density was tested for 12 cases ($n = 12$). DCE-CT tumor perfusion ($\rho = 0.622$, $P = 0.031$) revealed a strong positive association with VEGFR2 density, while TTP ($\rho = -0.599$, $P = 0.040$) revealed a moderate negative association with VEGFR2 density; both relationships were significant (Figure 4.16). DCE-CT PE ($\rho = 0.479$, $P = 0.115$) showed a moderate positive association that failed to achieve statistical significance, while BV ($\rho = 0.053$, $P = 0.870$) did not correlate with VEGFR2 vessel density. The lack of correlation between BV and VEGFR2 density was likely due to one case, which had a high BV measurement coupled with a low average number of VEGFR2 vessels/HPF (Figure 4.16).

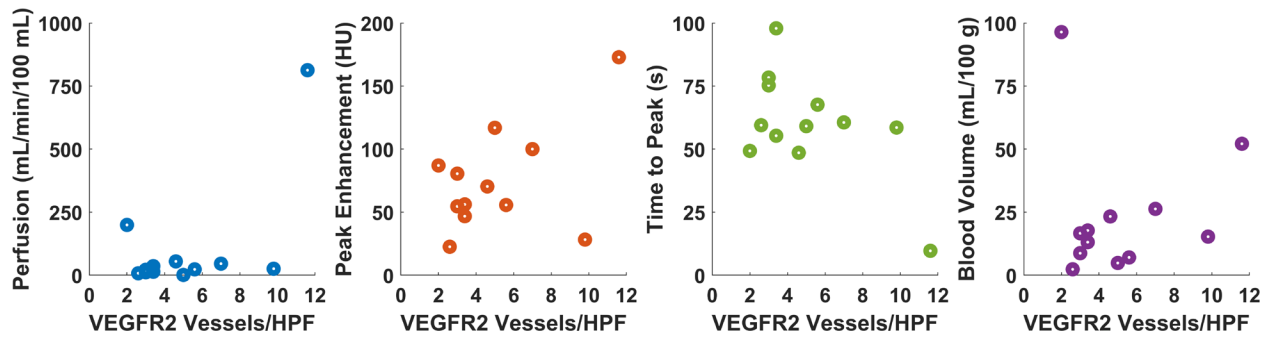


Figure 4.16 Correlation between VEGFR2 expression and DCE-CT metrics. A strong association was revealed between tumor perfusion and VEGFR2, while moderate associations existed between PE and TTP. BV did not correlate with measured VEGFR2 vessel density; $n = 12$.

DCE-CT data was available for 19 cases, which included two multi-session cases that each provided two separate data points ($n = 21$). Correlation analysis between DCE-CT metrics revealed that tumor perfusion had a strong positive association with PE ($\rho = 0.612$, $P = 0.0032$), a strong negative association with TTP ($\rho = -0.624$, $P = 0.0025$), and a moderate positive association with BV ($\rho = 0.487$, $P = 0.025$) (Figure 4.17). The linear relationship between tumor perfusion and all other DCE-CT parameters (PE, TTP, BV) was significant for each comparison ($P < 0.05$). In comparison, peak enhancement had a weak negative association with TTP ($\rho = -0.218$, $P = 0.342$), and a weak positive association with BV ($\rho = 0.335$, $P = 0.138$) (Figure 4.17).

Lastly, TTP and BV had a weak negative association ($\rho = -0.228$, $P = 0.321$) (Figure 4.17).

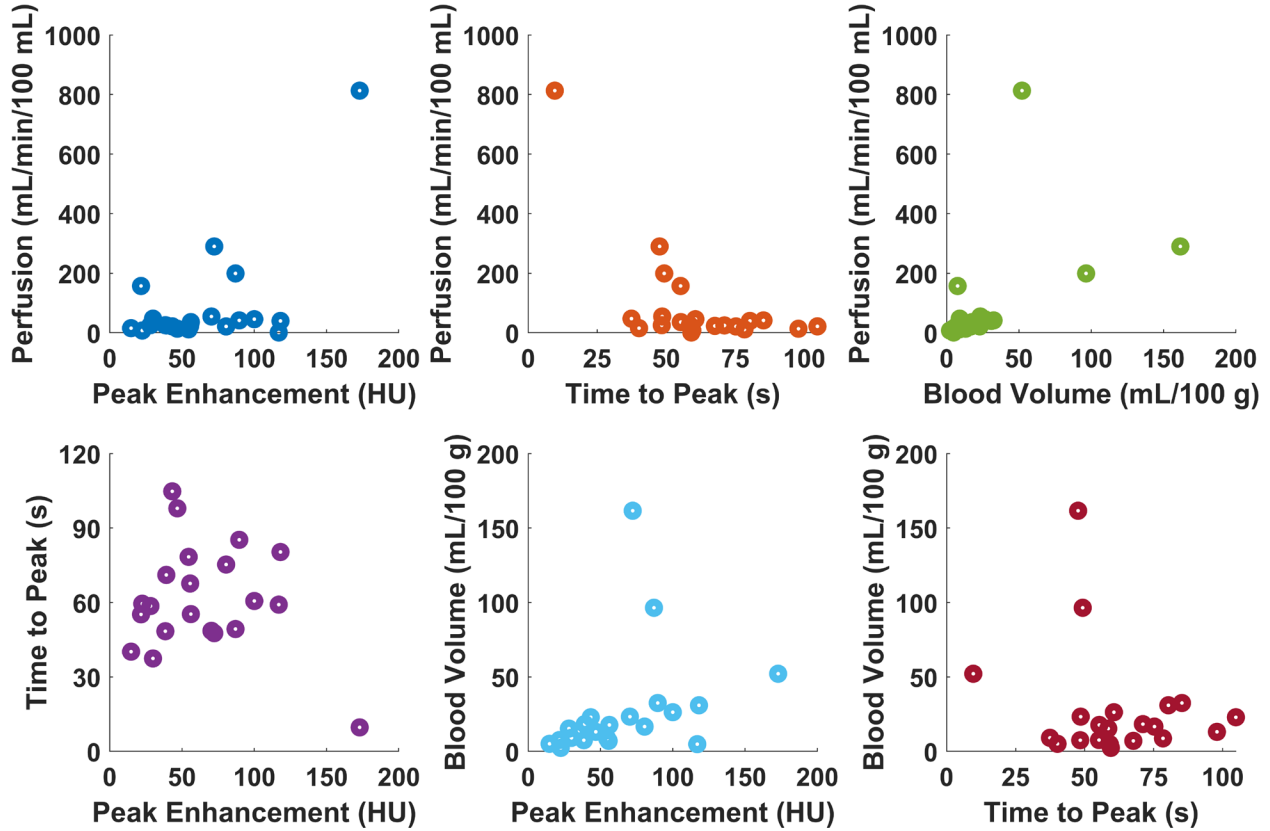


Figure 4.17 Relationship between DCE-CT parameters. Tumor perfusion was strongly associated with PE and TTP, and was moderately associated with BV. PE was weakly associated with both TTP and BV. TTP and BV were also weakly associated; $n = 21$.

DCE-CT metrics were compared to tumor volume measurements in seven canine patients, including one multi-session patient with two measurements at different time points ($n = 8$). All DCE-CT parameters displayed an inverse linear relationship with tumor volume (Figure 4.18). PE had the strongest relationship with tumor volume demonstrating a very strong significant negative association ($\rho = -0.818$, $P = 0.013$). TTP had the next best association with tumor volume and showed a strong negative correlation, but failed to reach significance ($\rho = -0.669$, $P = 0.070$). BV had a moderate negative association with tumor volume ($\rho = -0.420$, $P = 0.300$), and perfusion had the weakest association with tumor volume ($\rho = -0.371$, $P = 0.366$). In contrast, IHC metrics (CD31, VEGFR2) were both positively associated with tumor volume

(Figure 4.19). IHC data were available for five (CD31) and four (VEGFR2) canine patients.

Tumor volume and CD31 vessel density had a moderate positive association ($\rho = 0.450$, $P = 0.447$), while tumor volume and VEGFR2 density had a very strong positive association ($\rho = 0.892$, $P = 0.108$). However, neither association was statistically significant ($P > 0.05$).

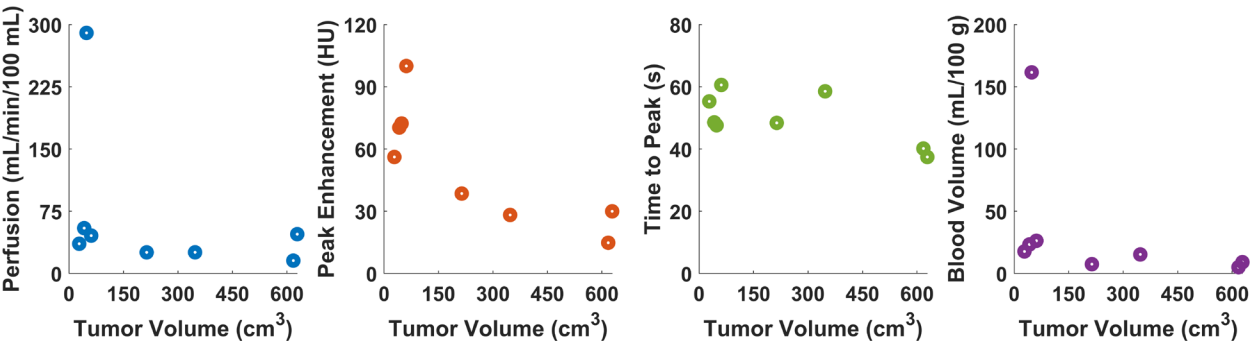


Figure 4.18 Association between tumor volume and DCE-CT parameters. Tumor perfusion was weakly associated with tumor volume, PE was very strongly associated with tumor volume, TTP was strongly associated with tumor volume, and BV was moderately associated with tumor volume; $n = 8$.

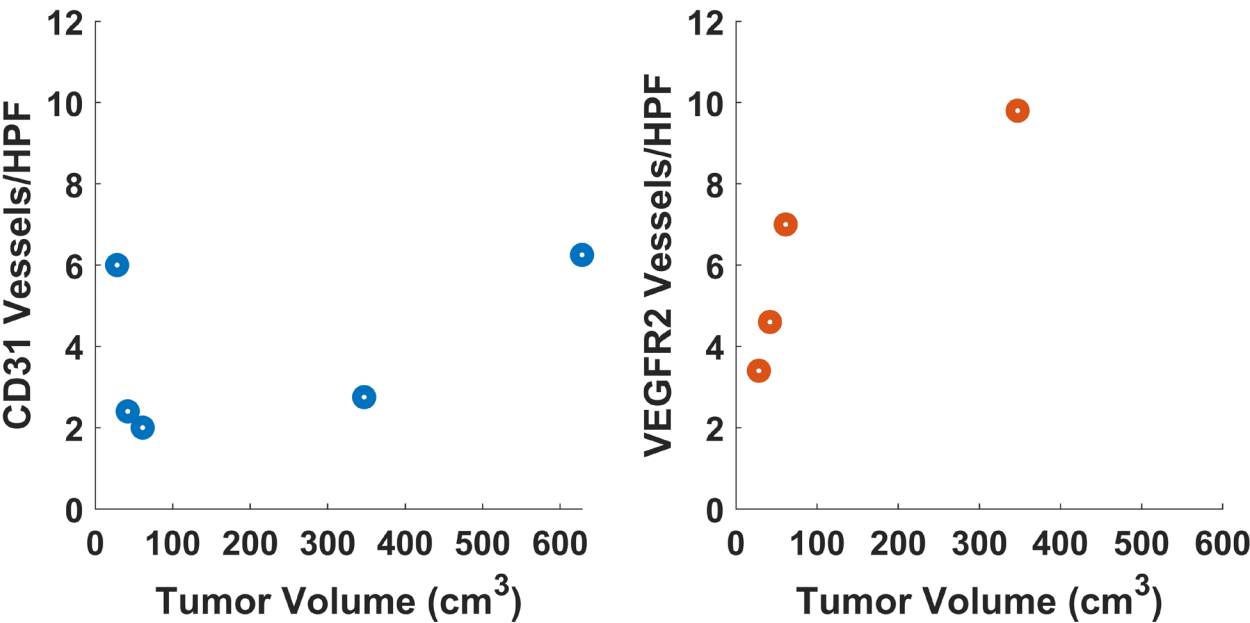


Figure 4.19 Linear correlation between vascular markers and tumor volume. CD31 staining was moderately associated with tumor volume ($n = 5$), while VEGFR2 staining was very strongly associated with tumor volume ($n = 4$).

Lastly, targeted MB enhancement was compared to DCE-CT metrics where available. VEGFR2-targeted MBs (A7R-MBs) were positively associated with all DCE-CT parameters, but no associations were significant (Figure 4.20). Tumor perfusion revealed the weakest association with A7R-MB targeted enhancement ($\rho = 0.112$, $P = 0.888$). PE ($\rho = 0.504$, $P = 0.496$) and BV ($\rho = 0.588$, $P = 0.412$) were both moderately correlated with A7R-MB targeted enhancement, while TTP ($\rho = 0.643$, $P = 0.357$) had the strongest association with A7R-MB targeted enhancement.

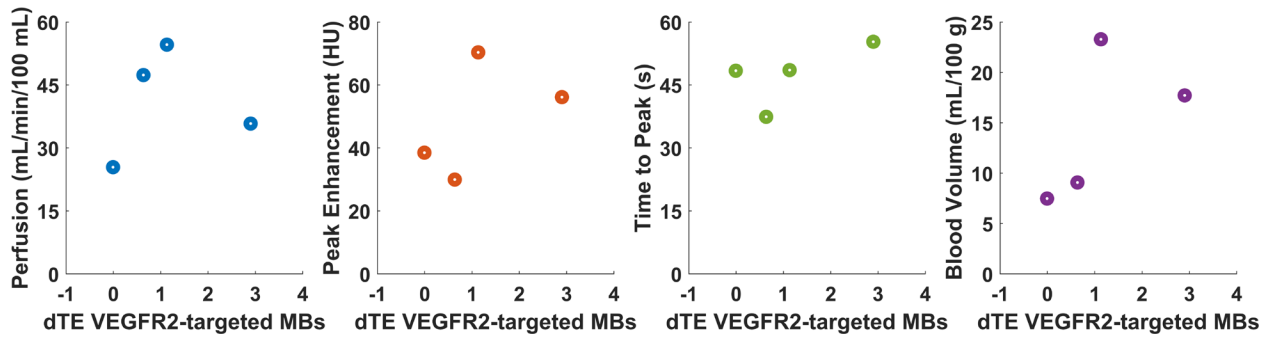


Figure 4.20 Relationship between DCE-CT parameters and VEGFR2-targeted microbubble enhancement. VEGFR2-targeted MBs (A7R-MBs) were very weakly associated with perfusion, were moderately associated with PE and BV, and were strongly associated with TTP; $n = 4$.

Microbubbles targeted to $\alpha_v\beta_3$ integrin (cRGD-MBs) exhibited similar behavior as VEGFR2-targeted MBs when compared to DCE-CT metrics (Figure 4.21). Tumor perfusion showed no association with cRGD-MB targeting ($\rho = 0.073$, $P = 0.927$). PE ($\rho = 0.478$, $P = 0.522$) and BV ($\rho = 0.558$, $P = 0.442$) were both moderately correlated with cRGD-MB targeting, while TTP ($\rho = 0.651$, $P = 0.349$) had the strongest association with cRGD-MB targeting. Associations between targeted MB enhancement and vascular markers (CD31, VEGFR2) were not evaluated due to the low number of data points available for these comparisons. Three patients had corresponding targeted MB data and tissue samples stained for CD31, while only two patients had corresponding targeted MB data and tissue stained for

VEGFR2 (Supplemental Figure B.2, Supplemental Table C. 23).

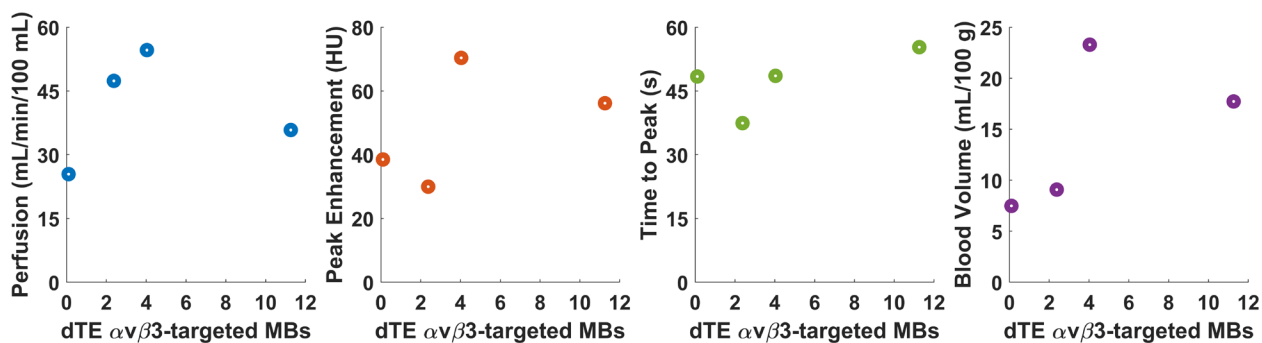


Figure 4.21 Relationship between DCE-CT parameters and $\alpha_v\beta_3$ -targeted microbubble enhancement. $\alpha_v\beta_3$ -targeted MBs (cRGD-MBs) were not associated with perfusion, were moderately associated with PE and BV, and were strongly associated with TTP; $n = 4$.

4.4 Discussion

The aim of this chapter was to validate the use of acoustic radiation force enhanced ultrasound molecular imaging in a clinical population. To date, two prominent studies have been published that assessed the feasibility of molecularly targeted contrast agents in patient populations. Both studies used a clinical grade UCA, BR55 (Bracco Suisse SA, Geneva, Switzerland), which targets VEGFR2. Smeenge et al. performed a safety and feasibility study for the use of BR55 in patients with prostate cancer [206]. Patients with biopsy-proven disease who were scheduled to receive a prostatectomy elected to undergo contrast ultrasound imaging to evaluate the use of a targeted UCA (BR55) for prostate cancer detection. Patients received up to two doses of BR55 and were monitored for any adverse reactions following contrast administration. No serious adverse events were reported and only 17% of the patients reported a non-serious adverse event, all of which resolved without the need for medical intervention. USMI using BR55 detected 50% of the malignant lesions identified by histopathology, with 29% identified during a variable protocol refinement period and 68% identified after modifying the imaging protocol. Results from this pilot study demonstrated the safety of BR55, but also noted the necessity of further optimizing USMI protocols to reliably detect prostate cancer.

Willmann et al. reported a first-in-human use of BR55 for patients with breast and ovarian lesions [207]. For this study, patients scheduled for surgery to remove either breast or ovarian lesions elected to undergo targeted contrast ultrasound imaging. Patients received one weight-based dose of BR55 followed by continuous data acquisition of bubble wash-in for 45 seconds and then intermittent acquisition from 5 minutes out to 29 minutes. Lesions were qualitatively assessed by two radiologists, using focal enhancement of remaining bound bubbles after sufficient clearance of circulating bubbles to identify lesion malignancy. USMI results were compared to tissue sections that had been obtained for IHC analysis to assess CD31 and VEGFR2 expression, revealing a diagnostic agreement between USMI and IHC for 86% of the ovarian lesions and 89% of breast lesions. The outcomes from this study demonstrated the utility of USMI for differentiating between benign and malignant lesions, paving the way for future studies to investigate the clinical feasibility of using USMI to diagnose disease state.

The studies discussed above relied on 2D imaging during a single imaging session to detect cancer and assess malignancy. Here, volumetric data of targeted UCA adherence to tumor vasculature was acquired and used in conjunction with a longitudinal imaging protocol to assess tumor response over the course of a multi-week treatment regimen in a canine patient population. Prior to implementation in the clinic, optimal acoustic radiation force transmit parameters to enhance molecularly targeted UCA signal were first determined.

4.4.1 Optimizing Acoustic Radiation Force

Acoustic radiation force has been shown to increase adhered bubble signal by 20-fold for *in vitro* experiments and up to 78% relative to passive targeting for *in vivo* applications [137,138]. Ideal parameters to enhance USMI for *in vivo* imaging in tumors with an average diameter of 1 cm were previously established using the Acuson Sequoia 512, a commercial

ultrasound system [138]. Here, microbubble displacement for distances 2-5 cm from the transducer were tested to determine an optimal ARF push sequence for imaging larger tumors. Two parameters, transmit pressure and distance from the transducer, were tested to select ideal ARF settings. Microbubble displacement behavior revealed a similar trend at each distance from the transducer, for decreasing pressure (Figure 4.7). Higher acoustic pressures produced larger numbers of displaced microbubbles, which aligns with prior simulated and experimental results [135,137,138]. For each power output level, from 0 to -15 dB, the effect of depth on microbubble displacement was evaluated. Microbubble displacement was not significantly different ($P > 0.05$) between depths at any given pressure level, except for two depths when transmitting at -6 dB. For a power output of -6 dB, microbubble displacement was significantly different at 2 cm vs 4 cm from the transducer and 4 cm vs 5 cm from the transducer. At this power level, a depth of 4 cm resulted in the largest number of displaced bubbles compared to shallower and deeper distances (Figure 4.7). However, when comparing differences in number of displaced bubbles based on changes in transmit pressure (without grouping by depth), significant differences were confined to power outputs less than -8 dB when compared to outputs at least three increments higher (Supplemental Table C. 22). Power outputs between -7dB and 0 dB (64.91 kPa to 143.39 kPa) did not demonstrate significantly different amounts of microbubble displacement ($P > 0.05$). The lack of significance when comparing depth at each transmit pressure, and for comparing average displacement for depth at different pressures may have been influenced by the small sample size ($n = 3$) and large variance in number of displaced bubbles for any given pressure. A large effect size was assumed, given the nonlinear relationship between acoustic radiation force and transmit pressure [129,130,133], however, using the acquired data, the effect size for bubble displacement between transmit pressures was determined for each depth, showing

that the general assumption of a large effect size did not hold for all pressures. In the future, to fully characterize differences in microbubble displacement between adjacent transmit pressures, the use of a smaller effect size and a larger sample size should be considered. Here, given the lack of significance between higher acoustic outputs (-7 dB to 0 dB), the output with the lowest variance (-4 dB) was selected as the pressure that would likely provide the most stable push over a set range of depths. The ability of this power output (-4 dB) to generate an ideal push, facilitating efficient bubble displacement while minimizing movement along the wall, was also visually confirmed. The pressure measured at this power output was 94.28 ± 23.56 kPa, and when derated to account for tissue attenuation, corresponded to the highest available power output (0 dB, 92.76 ± 3.67 kPa).

Although only transmit pressure and distance were evaluated, other parameters influence the magnitude of ARF. For example, transmit frequency is an important consideration when optimizing ARF. Bubbles insonified at their resonance frequency will experience greater displacement from ARF [135,208], therefore tuning the transmit frequency according to MB size, or vice versa, should improve the adhesion efficiency by way of a more effective push. However, clinical scanners, such as the Acuson Sequoia, offer a limited range of transmit frequencies for each transducer, and the number of available frequencies varies within each imaging mode. The Sequoia is able to achieve a high pulse repetition frequency in PW mode relative to other imaging modes (B-mode, CPS, Color Doppler), which makes it the ideal choice for optimizing acoustic radiation force, but this benefit comes at the cost of a single transmit frequency (3.5 MHz) with the 9L4 transducer. Alternatively, preclinical scanners offer greater flexibility for tuning ultrasound parameters, such as the ability to match transmit frequency with bubble size in addition to being able to modify other transmit settings. However, preclinical

systems are not as readily translatable or available in a clinical environment. As such, the use of a clinical system presents a tradeoff between transmit frequency and bubble size for USMI. Larger bubbles (3 μm) are better suited for USMI, maximizing contrast sensitivity and improving contrast persistence [148], but insonifying bubbles on resonance to maximize bubble displacement also helps to improve USMI by increasing the number of bound bubbles that interact with the vascular endothelium and more accurately depicts levels of molecular expression. Larger bubbles (3 μm) were used in this work to improve sensitivity to low numbers of accumulated bubbles. For this bubble size (resting radius of 1.5 μm) the corresponding resonance frequency is roughly 2.5 MHz in an unbounded field [209,210]. The resultant discrepancy between the bubble resonance frequency and transmit frequency utilized (3.5 MHz), meant that bubbles were insonified off-resonance, decreasing the magnitude of displacement. For the given transmit frequency, bubbles with a resting radius around 1 μm should theoretically experience maximum displacement, but this estimate [209], does not consider all the complexities of an *in vivo* environment. The dynamic viscosity of blood, bubble surface tension, and threshold for isothermal versus adiabatic behavior as well as changes in tissue and vessel stiffness in the tumor microenvironment during growth, all influence the expected resonance behavior of a bubble with a given resting radius. In fact, when bubbles were constrained by small vessels (5-20 μm) Qin et al. found that the resonance frequency decreased for rigid boundary conditions and increased for compliant boundary conditions [211]. Bubble simulations could be used to help determine the appropriate ARF parameters based on a complex set of input conditions representing the anticipated experimental environment, however, experimental data should still be collected to confirm simulated results. Frinking et al. evaluated how changes in MB concentration, duty cycle, and acoustic pressure influence ARF enhancement of targeted MB

binding. Their findings showed that binding increased linearly with dose and duty cycle, but did not follow expected theoretical behavior for acoustic pressure. At a dose of 8×10^7 MB/kg with a 95% duty cycle, an acoustic pressure of 38 kPa resulted in the highest amount of MB binding compared to 26 kPa and 51 kPa [131]. Deviation from theoretical bubble behavior, the complex nature of an *in vivo* environment, and the influence of different experimental parameters support the need to tune ultrasound and bubble parameters to determine ideal ARF settings according to the intended application. In this chapter, we demonstrated how bubble displacement from ARF was influenced by different acoustic pressures across depths of 2-5 cm in order to develop an ideal protocol for use in a clinical population with larger tumors.

4.4.2 Evaluation in a Clinical Population

After evaluating different ARF settings for larger tumors, the selected parameters were applied to enhance USMI in a clinical population. The original aim of this work was to enroll 16 canine patients with biopsy accessible, histologically confirmed STS of any stage/grade in a peripheral location with minimal respiratory motion. The goal was to detect early tumor response to anti-angiogenic therapy in patients using USMI. Here, dogs received a combination of anti-angiogenic and cytotoxic chemotherapies to treat STS and the tumor response was monitored over the course of eight weeks using USMI, DCE-CT, IHC, and tumor volume measures.

4.4.3 Canine Patient Enrollment

A significant barrier to this study was the ability to successfully enroll and retain patients. Enrollment numbers may have suffered because the treatment regimen for the study did not align with preferred treatment plans. The ideal treatment strategy consists of surgical removal of the tumor, with possible follow-up RT. However, the treatment approach used in this study consisted of 8 weeks of two different chemotherapeutics (toceranib phosphate,

cyclophosphamide). The necessity of waiting until study completion to remove the tumor coupled with the harsher side effects of chemotherapy may have presented a less desirable approach to treatment, which may have deterred some owners from participating. For example, patient 001 experienced harsh side effects from the chemotherapy that impeded their ability to participate in the study without interruptions. Patient 001 took a 14 day break from treatment and reduced the dose of toceranib phosphate when they resumed treatment. Modifying study criteria to allow patients to enroll for a single imaging session, boosted enrollment numbers. Offering the 8-week protocol resulted in only 5 patients (of 60 potential cases) that enrolled over the course of 15 months, while opening the single session protocol saw 10 patients (of 25 potential cases) enroll over the same time span. One possible explanation for this increase in enrollment could be that the single session allowed patients to circumnavigate chemotherapy and receive their preferred method of treatment after participating in the study. Determining the minimum number of weeks required to differentiate responding tumors from non-responding tumors based on USMI metrics, may allow for a reduction in the number of imaging sessions necessary for future multi-session studies. This could provide a way to improve enrollment for future longitudinal studies, or alternatively studies could be designed with a different form of treatment. All patients that completed the single session imaging ($n = 7$) went on to either receive RT or had the tumor surgically removed. This highlights the need to consider the impact that the treatment regimen may have on willingness to enroll and ability to complete the study. The negative side effects of chemotherapy (anti-angiogenic therapy) support shifting the focus towards radiation therapy. Demonstrating that USMI techniques have the ability to evaluate patient response to radiation therapy may better assist in the establishment of USMI as a clinical technique.

4.4.4 Longitudinal and Single Session Metrics

Although single session imaging saw an increase in patient enrollment over the 8-week protocol, participation in the multi-week imaging study holds more value as a predictive tool regarding patient response to treatment. In this study, only two NCSU patients (001, 003) successfully completed the multi-week protocol, making it difficult to draw significant conclusions about the predictive power of USMI to tumor response to treatment in a clinical population. The study protocol and dosing scheme were optimized using patient 001 and patient 002 withdrew early, resulting in analysis of only data from patient 003. Based on patient 003, changes in cRGD-MB differential targeted enhancement, an indirect measure of $\alpha_v\beta_3$ integrin expression, appeared to precede changes in tumor volume (Figure 4.12). The steady increase in cRGD-MB dTE from sessions 3 to 5, after the drop in dTE from session 1 to 3, may indicate the return of vascular markers ($\alpha_v\beta_3$ integrin) involved in tumor progression. The sharp increase in tumor volume from week 6 to week 8 seems to support this hypothesis. Unlike cRGD-MB dTE, changes in A7R-MB dTE, an indirect measure of VEGFR2 expression, did not precede, but rather fluctuated alongside changes in tumor volume (Figure 4.13). It was unclear from the data whether A7R-MBs have the ability to give an accurate indication of VEGFR2 expression. However, since USMI results were only available for one patient, and since neither DCE-CT nor IHC data were available beyond session 1 for patient 003 to validate the molecular expression measured by $\alpha_v\beta_3$ integrin- and VEGFR2-targeted MBs, it was challenging to draw meaningful conclusions from the data.

Switching to a single imaging session was more successful in terms of patient recruitment, with seven patients who enrolled in that portion of the study. However, results from USMI data were unable to provide much insight into the tumor microenvironment. One major

limitation was low signal intensity from targeted bubbles. There was negligible targeted intensity for single session patients 004, 005, and 009. In fact, patient 008 was excluded from analysis due to the inability to distinguish signal from background noise. The lack of targeted signal may be explained by lower initial tumor perfusion for these patients. For patient 006, who displayed the best targeted intensity, initial perfusion measured three minutes after injection (postARF) covered 92.35% of the tumor volume. In comparison, initial tumor perfusion for patients 004, 005, and 009 covered only 27.86%, 10.55%, and 9.22% of the tumor volume. Actual tumor perfusion during the wash-in phase was likely higher than perfusion measured three minutes after injection, however, the loss of a wash-in sequence was deemed a necessary and appropriate trade-off in order to effectively apply ARF pushes across the tumor volume during the initial (and peak) transit of the targeted MBs through the tumor. This was particularly important given the use of BLA to shield the targeting ligand from rapid clearance by the immune system. In this scenario, lack of sufficient ARF pulses results in poorly exposed targeting ligands, since in the absence of ARF, BLA targeted bubbles exhibit very little interaction with nearby vascular receptors [142,144]. While this is beneficial for shielding targeting ligands from unwanted clearance by the immune system and for localized targeting, failure to adequately expose the ligand could pose a significant barrier to USMI. This was a potential limitation for our study, given the range of tumor depths encountered. As such, the lower initial measured perfusion for patients 004, 005, and 009 may be attributed to increases in tumor size. ARF parameters were tested for depths between 2-5 cm, however tumor depth ranged from 2.5-10.8 cm. Optimizing ARF in such a dynamic environment, across a wide range of depths, presents a unique challenge for the translation of ARF-enhanced USMI into the clinic. Preclinical studies have involved the use of a relatively small range of tumor sizes, where the average diameter measures 1 cm and

typically does not exceed 2.5 cm. A small tumor size distribution enables the selection of a single set of parameters that maximize ARF enhancement of USMI, but this is unlikely to be the case in the clinic given the larger tumor size distributions. To address larger tumor sizes, ideal parameters could be modulated according to depth, resulting in parameters optimized for specific segments of the tumor.

4.4.5 Regression Analysis for USMI, DCE-CT, and IHC Metrics

Correlations between USMI data, DCE-CT parameters, and IHC measures of microvessel density were performed to confirm USMI results. Both tumor perfusion and blood volume measured by DCE-CT were moderately associated with CD31 expression. This follows expected behavior, where upregulation of angiogenic markers corresponds to an increased blood supply to the tumor in order to support tumor maintenance and growth. This relationship was maintained between tumor perfusion and VEGFR2 expression, but no association was found between BV and VEGFR2 density. The lack of association between blood volume and VEGFR2 expression may be attributed to one case, where blood volume was high (96.42 mL/100 g) while VEGFR2 expression was low (2 VEGFR2 vessels/HPF). Removing this data point and reassessing the linear relationship between BV and VEGFR2 expression resulted in significant improvements ($\rho = 0.708$, $P = 0.015$) in the correlation between the two parameters (Supplemental Figure B.3). The strength of the association between tumor perfusion and VEGFR2 expression also improved ($\rho = 0.708$, $P = 0.015$). Comparing DCE-CT parameters and microbubble targeting, revealed positive associations between both targeted UCAs (cRGD-MBs, A7R-MBs) and peak enhancement, time to peak, and blood volume, although all were non-significant ($P > 0.05$). Tumor perfusion was weakly associated with A7R-MB targeting and had no association with cRGD-MB targeting. This relationship was maintained for tumor perfusion

measured by DCE-CT versus perfusion measured by ultrasound, which was also poorly correlated ($\rho = -0.131$, $P = 0.869$). The fact that DCE-CT tumor perfusion and microbubble targeting were poorly correlated, while there was a moderate association between DCE-CT tumor perfusion and vascular expression, suggests that microbubble targeting may not be well correlated with vascular expression. This could not be confirmed due to the low number of viable tissue samples that corresponded to ultrasound metrics. However, for the few data points available, no apparent pattern describing the relationship between microbubble targeting and vascular density emerged. Tumor volume and targeting from cRGD-MBs had a moderate negative association, while A7R-MBs had a very weak negative association. The relationship between tumor volume and DCE-CT metrics was also described by a negative linear association. In contrast, CD31 and VEGFR2 vessel density were both positively associated with tumor volume. Missing data (DCE-CT, IHC) reduced the sample size for some pairwise comparisons, but overall, regression analysis of DCE-CT, IHC, and tumor volume measures were not well correlated with USMI data. The lack of sufficient evidence to validate USMI results combined with negligible targeting in single session cases suggests that in its current state, longitudinal USMI to predict tumor response to treatment still faces many challenges before it can be successfully implemented in the clinic. Longitudinal results from a single patient (003) were promising and with further optimization, USMI may be able to reflect tumor response faster than tumor volume, but not without first significantly improving results in clinically relevant populations.

CHAPTER 5: THE PERFORMANCE OF FLASH-REPLENISHMENT CONTRAST ULTRASOUND IMAGING FOR EVALUATING KIDNEY HEALTH IN DIABETIC KIDNEY DISEASE

5.1 Overview

Previously, we discussed the benefits of flash-replenishment imaging for assessing kidney perfusion. In the kidney, tubuloglomerular feedback mechanisms and microvascular alterations work in concert to regulate and maintain kidney function. The presence of diabetes induces hypoxia, hyperglycemia, and hyperfiltration, resulting in structural and functional changes that if left untreated eventually result in permanent loss of kidney function [48,212]. However, these alterations, such as changes in renal hemodynamics and microcirculatory flow, can serve as biomarkers of diabetic kidney disease [91]. This provides an opportunity for perfusion imaging techniques, such as contrast-enhanced ultrasound, to detect developing DKD. CEUS is a portable, real-time modality that is well-tolerated by patients, less expensive than computed tomography and magnetic resonance imaging, and microbubbles are safe for compromised kidneys [39,91,213]. A study using CEUS by Ma et al. demonstrated decreased perfusion with delayed time to peak enhancement in patients with DKD [214]. Here, we use flash-replenishment imaging to assess kidney perfusion in control, insulin-resistant (IR), and diabetic nonhuman primates (NHPs).

Commercial software packages like Vuebox™, SonoPerf™ (Bracco Suisse SA, Geneva, Switzerland), and the feature CHI-Q (Canon Medical Systems, Tustin, CA, USA) are commonly used to extract blood flow parameters from reperfusion data [155,174,175,178,215].

These software apply motion correction and curve fitting to let the user quantify perfusion in selected ROIs. However, this analysis fails to comprehensively assess kidney perfusion while maintaining the spatial integrity of the distinct kidney compartments. One ROI encircling the whole kidney merges unique blood flow kinetics for the specialized subregions into a single measure. Separate ROIs isolating subsections of the cortex and medulla, relate perfusion to anatomical feature, but remain insufficient by overlooking disease-related alterations outside the analyzed region. To fully utilize microcirculation as a biomarker for DKD, blood flow parameters should correlate to anatomical features in the kidney.

The objective of this chapter was to equate perfusion parameters with kidney location to provide a more comprehensive diagnosis of kidney health. We accomplished this by segmenting the kidney into concentric layers. Flash-replenishment TICs from each layer were fit with a monoexponential model, extracting features for use in a regression model with blood pressure (BP) to distinguish kidney status in an NHP diabetic model. To our knowledge, this is the first attempt to extract CEUS features based on concentric kidney segmentation. We hypothesize that this technique will improve the ability of flash-replenishment imaging to characterize heterogeneous kidney blood flow and will aid in the identification of flash-replenishment perfusion features capable of detecting the early stages of DKD progression. Ultimately, this tool could be employed as an indicator of which patients will develop progressive DKD, an important distinction since approximately 40% of T2D patients will eventually develop DKD [48].

5.2 Materials and Methods

5.2.1 *Chlorocebus aethiops sabaeus* Diabetic Model

Nonhuman primates, specifically *Chlorocebus aethiops sabaeus* or vervets, provide a naturally occurring model for diabetic disease. Sixteen female NHPs, housed at Wake Forest

University were stratified into three cohorts, control (n = 5), IR (n = 5), or diabetic (n = 6), based on health status. Vervets were classified as control (a), IR (b), or diabetic (c), by the following criteria: a) fasting blood glucose (FBG) < 80 mg/dL and glycated hemoglobin (HbA1c) < 5%, b) FBG 80-125 mg/dL and HbA1c 5-6%, or c) FBG > 125 mg/dL and HbA1c > 6%. Blood and urine were collected at each time point to confirm the clinical presentation of disease. Average age, body weight, waist circumference, and other relevant clinical measures were collected in each vervet at the time of imaging. To evaluate potential differences in the clinical measures between cohorts, one-way ANOVA was performed, followed by Tukey's multiple comparison. Outcomes with $P < 0.05$ were considered statistically significant. P -values for post-hoc testing were reported as multiplicity adjusted values [192,193]. Prior to imaging, NHPs were sedated using ketamine and midazolam, followed by placement of a catheter into a peripheral vein by research personnel to provide access for MB injections. All vervet care was provided by skilled technicians according to Wake Forest University Institutional Animal Care and Use Committee guidelines for research involving NHPs.

5.2.2 Ultrasound Data Acquisition

CEUS imaging data was collected in triplicate for each vervet over a 6-month period, with the exception of one diabetic NHP and one IR NHP. For the diabetic NHP only one data point was collected. For the IR NHP two data points were collected. All imaging occurred at Wake Forest University using a commercial ultrasound system. Data was collected on the LOGIQ S8 scanner (General Electric, Boston, MA, USA) with a curvilinear array (C1-5). Ultrasound parameters defined prior to the start of imaging were kept constant throughout each NHP and replicate collection, including: image depth (7 cm), focal depth (5.6 cm), frequency (3 MHz), mechanical index (0.18), gain (30 dB), dynamic range (57 dB), frame rate (18 Hz), and

flash-replenishment scheme (30 s). The transducer was positioned over the left kidney and secured in a custom holder to reduce motion due to user error during data acquisition. A continuous MB infusion, containing 0.77 mL of Perflutren Lipid Microspheres (DEFINITY®, Lantheus Medical Imaging, North Billerica, MA, USA) mixed in 30 mL saline was delivered into the blood stream at 2 mL/min using an 11 Plus syringe pump (Harvard Apparatus, Holliston, MA, USA). Once MB intensity exhibited steady state behavior, a 30 second flash-replenishment video clip of the kidney along the midplane was acquired. Data was stored in DICOM format and transferred offline for analysis.

5.2.3 Data Processing and Analysis

Multi-frame image data, composed of K frames, extracted from the video captured using a flash-replenishment imaging scheme, was imported into MATLAB® (MathWorks, Natick, MA, USA) for analysis using the following workflow: kidney contouring, kidney segmentation, signal extraction, and data fitting (Figure 5.1). The process described below was applied to every flash-replenishment video collected for each vervet.

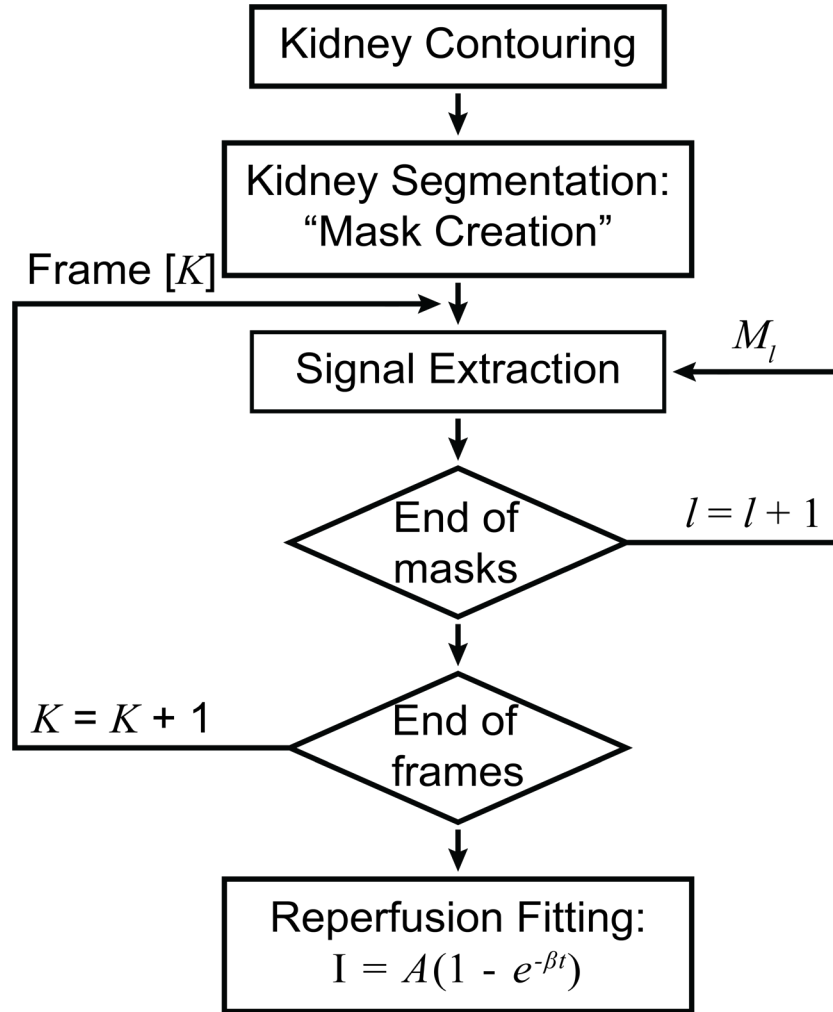


Figure 5.1 Proposed flow for flash-replenishment data analysis.

5.2.3.1 Kidney Contouring

First, a frame was extracted and MATLAB image enhancement tools used to brighten the image, including histogram equalization, image filtering, and image binarization. Next, the outer boundary of the kidney was manually delineated to generate a kidney contour (Figure 5.2a).

5.2.3.2 Kidney Segmentation

From the kidney contour a binary mask was created. The center of the mask was determined and a segmented line between the center and a point on the contour boundary was

generated (Figure 5.2b-c). The number of segments along the line were defined by the user and correspond to each concentric layer (l), created by repeating the segmentation process for all points along the kidney boundary. Ten concentric kidney layers were generated by this method (Figure 5.2d).

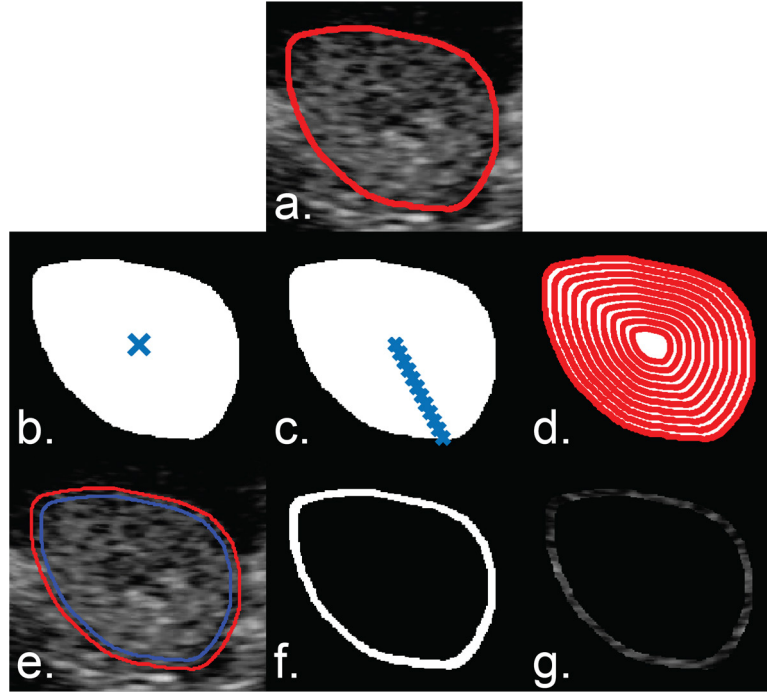


Figure 5.2 Signal extraction process. a) Kidney region boundary contouring, b) Kidney region center allocation, c) Line segmentation, based on the user-defined value of 10 segments, d) Kidney concentric layers, e) Layer l outer bounds “red” and inner bounds “blue”, f) Layer l binary mask M_l , and g) multiplication results of M_l by K^{th} frame.

5.2.3.3 Signal Extraction

A binary mask M_l was formed for each layer l using the inner and outer contours that defined the layer (Figure 5.2e-f). Next, M_l was multiplied by frame K of the CEUS image data to isolate pixel intensities in layer l (Figure 5.2g). The sum of all isolated pixel intensities was divided by the sum of all pixel intensities in M_l to calculate an intensity data point, $I_l(K)$, for a

given layer and frame. This step was repeated for all layers before moving to the next frame, $K + 1$, resulting in a plot that tracked intensity over time in each layer.

5.2.3.4 Fitting Reperfusion Data

The reperfusion TIC data for each layer was fit to a mono-exponential model (Figure 5.3a) that was first suggested in 1998 by Wei et al. [161], described by Equation (5.1):

$$I(t) = A(1 - e^{-\beta t}) \quad (5.1)$$

where, $I(t)$ is the intensity of the captured signal in the ROI, A is the steady-state intensity related to blood volume, and β is the slope of the reperfusion curve representative of blood velocity. The product $A\beta$ denoted as perfusion index (PI) provides an estimate of the flow rate [176]. Least-square fitting was applied to estimate the model parameters, A and β . This method minimized the error between the data and the target model, then returned the estimated values of A and β that resulted in the minimum difference. Using the $I_l(k)$ data, the index with minimum intensity after the flash sequence was allocated (Figure 5.3a).

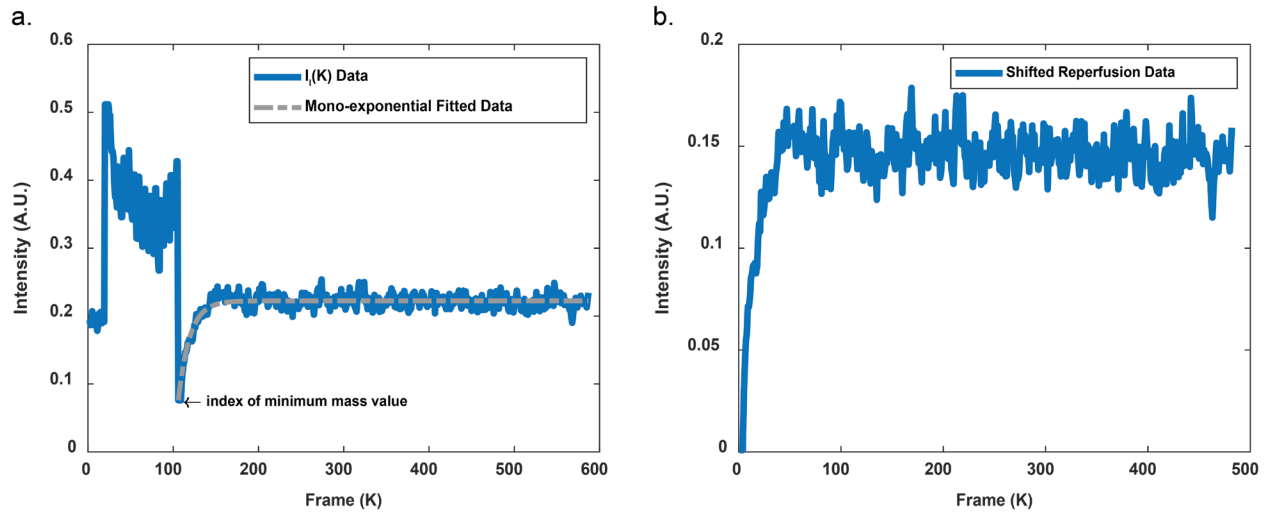


Figure 5.3 Time-intensity curve fitting process. a) $I_l(K)$ data points (blue) and reperfusion monoexponential fit (gray) for layer l , and b) Time and intensity zero-shifted reperfusion data points corresponding to all values at and beyond the allocated index of minimum mass (a).

Reperfusion data was shifted by subtracting the allocated index from its start point and all subsequent values (Figure 5.3b). Finally, using the least square method the mono-exponential parameters were deduced and fitted TIC data was computed. The process was reiterated for each kidney concentric layer (KCL) from the outer boundary (KCL 1) to the innermost region (KCL 10) (Figure 5.4). The performance of the mono-exponential fit per KCL was evaluated through the mean squared error (MSE) for each vervet cohort. The mean squared error (MSE) as a measure of the goodness of fit (GOF) considers zero-values to indicate a strong fit and large values to indicate a poor fit.

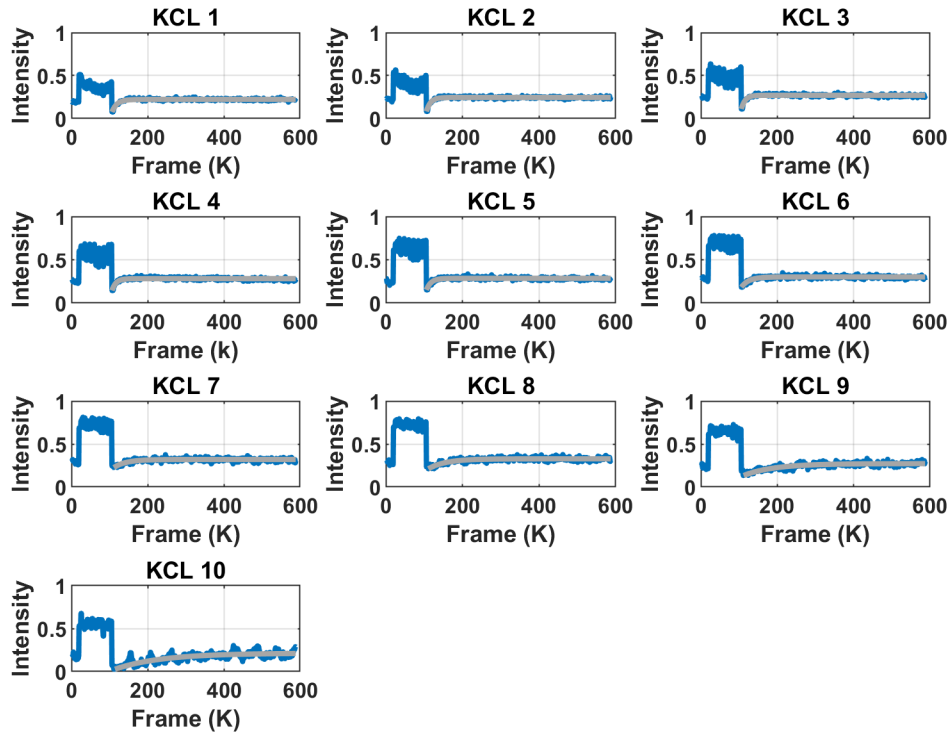


Figure 5.4 Time-intensity curve fitting of $I_l(K)$ reperfusion data per kidney concentric layer.

5.2.3.5 Estimated Parameters

The average values for the estimated parameters, A , β , and PI , for each KCL TIC were determined from the three imaging sessions for each vervet. An example of the non-normalized (Supplemental Table C. 24) and normalized (Supplemental Table C. 25) estimated parameter A

calculated for each session in a single NHP has been provided in Appendix C: Supplemental Tables. The average values were then normalized by the 5th KCL. Non-normalized (Supplemental Table C. 26, Supplemental Table C. 27, Supplemental Table C. 28) and normalized (Supplemental Table C. 29, Supplemental Table C. 30, Supplemental Table C. 31) average estimated parameters per KCL for all NHPs in the control, IR, and diabetic cohorts have been provided in Appendix C: Supplemental Tables. Normalized and non-normalized A, β , and PI were plotted against the 10 KCLs and fit with 1st and 3rd order polynomial functions (Figure 5.5). First- and third-degree polynomial fitting used Equations (5.2) and (5.3), respectively:

$$P_1 = p_{10} l + p_{11} \quad (5.2)$$

$$P_3 = p_{30} l^3 + p_{31} l^2 + p_{32} l + p_{33} \quad (5.3)$$

where p_{10} and p_{11} are 1st order coefficients, while p_{30} , p_{31} , p_{32} , and p_{33} are 3rd order polynomial coefficients.

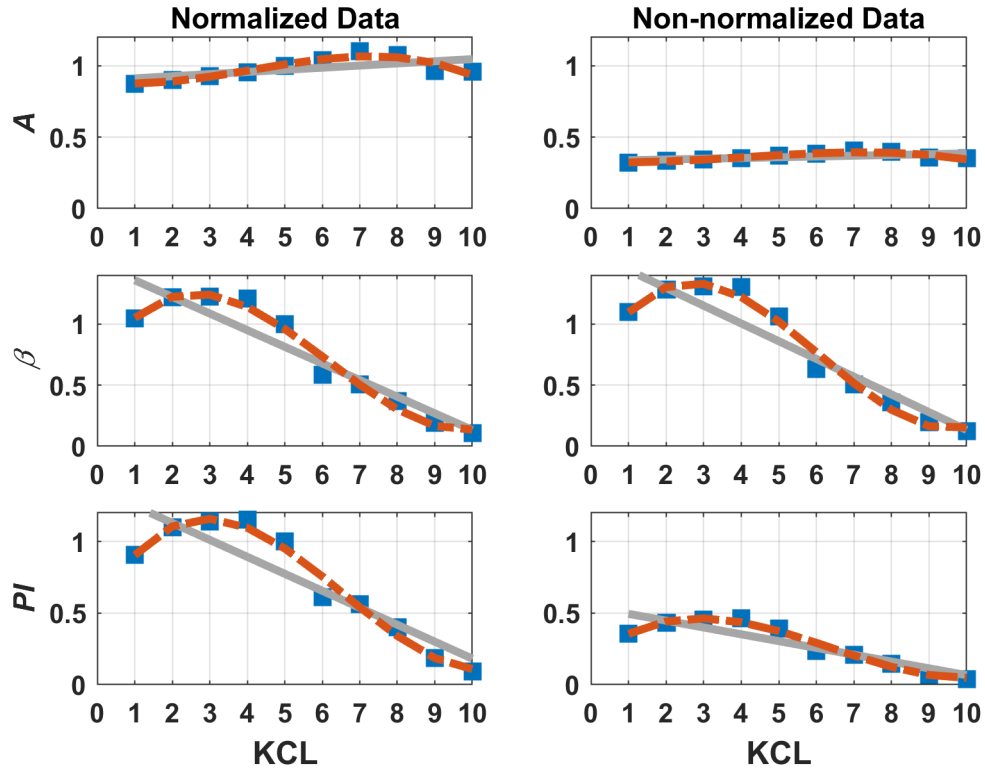


Figure 5.5 Polynomial curve fitting of the normalized and non-normalized KCL estimated parameters in a control group vervet. Left: normalized data; Right: Non-normalized data; Top row: Steady state (A); Middle row: Reperfusion rate (β); Bottom row: Perfusion index (PI). Perfusion parameters data points (blue) plotted against KCL with 1st order fitting (gray) and 3rd order fitting (orange, dashed).

5.2.3.6 Feature Extraction and Linear Regression Model

Features were extracted from both the normalized and non-normalized average A, β , and PI estimates for all KCLs in each cohort. Features included the estimated parameter KCL mean, estimated parameter KCL standard deviation (SD), area under the KCL curve (AUC), and the fitted 1st and 3rd order polynomial coefficients for the estimated parameter KCL curve. The MATLAB linear model function was used to generate a regression model from the independent variables (features) along the response variable (category ID). Control, IR, and diabetic groups were assigned category IDs of 1, 2, and 3 respectively. Available systolic and diastolic BP measurements were added to improve the model's predictive power for differentiating between study cohorts. The regression cases tested were control vs. IR, control vs. diabetic, IR vs.

diabetic, and control vs. IR vs. diabetic for both the normalized and non-normalized estimated perfusion parameters (A , β , and PI). The number of observations per case ranged from 10-16 depending on the case considered. Case comparisons with $P < 0.05$ demonstrated the potential to distinguish between NHP cohorts based on the given features.

5.3 Results

5.3.1 *Chlorocebus aethiops sabaeus* Clinical Measures

Fasting blood glucose, glycated hemoglobin, and blood pressure measurements were used to assess the health of each NHP. Average values (\pm SD) were reported for each cohort (Table 5.1). Systolic BP ranged from 88.67-145.4 mmHg, 91.33-169.4 mmHg, and 87.00-116.6 mmHg, for the control, IR, and diabetic cohorts, respectively and average systolic BP was not significantly different between groups ($P = 0.3350$). Diastolic BP ranged from 57.44-69.00 mmHg, 45.50-86.11 mmHg, and 50.00-71.22 mmHg for the three cohorts and average values were not significantly different between cohorts ($P = 0.6087$). FBG ranged from 51.33-80.67 mg/dL, 73.50-110.3 mmHg, and 249.0-577.0 mmHg for each cohort. Average FBG was found to be significantly different between groups ($P < 0.0001$). Pairwise comparisons showed that control vs. IR average FBG values were not significantly different ($P = 0.8744$), but comparing both control vs. diabetic ($P = 0.0001$) and IR vs. diabetic cohorts ($P = 0.0003$) revealed significant differences for average FBG between those populations. HbA1c ranged from 4.00-4.53%, 4.60-6.23%, and 6.83-9.67% for the control, IR, and diabetic cohorts respectively, and also revealed significant differences in the mean values between the populations ($P < 0.0001$). Pairwise comparisons found that control vs. IR average HbA1c values were not significantly different ($P = 0.0724$), but comparing control vs. diabetic ($P < 0.0001$) and IR vs. diabetic ($P < 0.0001$) revealed significant differences. Additional measures such as average age, body weight,

and waist circumference were also reported (Table 5.1). NHP age ranged from 12.77-19.87 years, 12.70-18.77 years, and 18.70-26.50 years for control, IR, and diabetic cohorts respectively. Average age was determined to be significantly different between groups ($P = 0.0315$), but only between control and diabetic cohorts ($P = 0.0429$). Average NHP age for control vs. IR ($P = 0.9489$) and IR vs. diabetic ($P = 0.0765$) was not significantly different. NHP body weight ranged from 5.27-6.77 kg, 4.07-8.17 kg, and 4.41-7.82 kg, and average body weight was not significantly different between populations ($P = 0.5181$). Waist circumference ranged from 32.37-37.03 cm, 25.67-45.25 cm, and 31.67-44.73 cm, for the control, IR, and diabetic cohorts respectively. Average waist circumference was not significantly different between cohorts ($P = 0.4814$).

Table 5.1 Average demographic and clinical measures for control, IR, and diabetic cohorts

	Average (\pm SD)		
<u>Measurement</u>	<u>Control</u>	<u>IR</u>	<u>Diabetic</u>
Age (years)	16.0 (\pm 3.13)	16.6 (\pm 2.50)	20.8 (\pm 2.92)
Body weight (kg)	5.79 (\pm 0.61)	6.53 (\pm 1.58)	5.73 (\pm 1.25)
Waist circumference (cm)	35.1 (\pm 1.80)	39.1 (\pm 7.87)	37.8 (\pm 4.42)
FBG (mg/dL)	68.5 (\pm 10.6)	91.9 (\pm 13.9)	341.6 (\pm 119.1)
HbA1c (%)	4.16 (\pm 0.23)	5.27 (\pm 0.73)	8.60 (\pm 0.94)
Systolic BP (mmHg)	115.2 (\pm 20.7)	128.9 (\pm 34.2)	107.4 (\pm 10.4)
Diastolic BP (mmHg)	64.0 (\pm 4.88)	69.4 (\pm 18.8)	62.2 (\pm 8.73)

5.3.2 Monoexponential Model Fit Performance

The mono-exponential model fit the TIC data well at each KCL. Average MSE (\pm SD) across all KCLs for the control, IR, and diabetic cohorts was 0.0254 (\pm 0.0210), 0.0321 (\pm 0.0242), and 0.0287 (\pm 0.0130), respectively. The range of average MSE values across NHP control, IR, and diabetic cohorts and KCLs was 0.0052-0.0721 (Table 5.2). The largest MSE was found in the IR cohort at KCL 7, while the smallest MSE was located in the control cohort at

KCL 2. Except for three layers (KCLs 1, 6, and 7), the control group had the smallest MSE per layer (Table 5.2). For KCL 1, the smallest MSE was found in the IR group, for KCLs 6 and 7 the smallest MSE was found in the diabetic group. Additional MSE measures by individual session for each NHP in the three cohorts are provided in the supplementary material (Supplemental Table C. 32, Supplemental Table C. 33, Supplemental Table C. 34).

Table 5.2 Monoexponential model performance by cohort per KCL

Model Performance (MSE)			
<u>KCL</u>	<u>Control</u>	<u>IR</u>	<u>Diabetic</u>
1	0.0062	0.0060	0.0096
2	0.0052	0.0059	0.0122
3	0.0086	0.0099	0.0189
4	0.0182	0.0193	0.0278
5	0.0345	0.0372	0.0356
6	0.0555	0.0569	0.0459
7	0.0618	0.0721	0.0464
8	0.0382	0.0599	0.0391
9	0.0180	0.0360	0.0277
10	0.0074	0.0175	0.0238

5.3.3 Perfusion Model Parameter Estimation

Layer-based parameter estimation resulted in noticeable changes in A, β , and PI between KCLs. Visualizing the normalized estimated parameters for a single NHP per cohort (Figure 5.6) revealed how blood volume and perfusion change across the kidney layers and with disease state. In these example NHPs, β decreased by KCL from the cortex to the renal pelvis, while A initially increased, peaked near the 7th/8th layer, and then decreased. In form, PI data resembled an asymmetric parabola across KCLs. KCLs with A, β , and PI > 1 exhibited larger blood volume, faster blood velocity, or faster flow relative to the 5th KCL. The 1st KCL includes the kidney boundary, which may influence values for that layer relative to deeper KCLs.

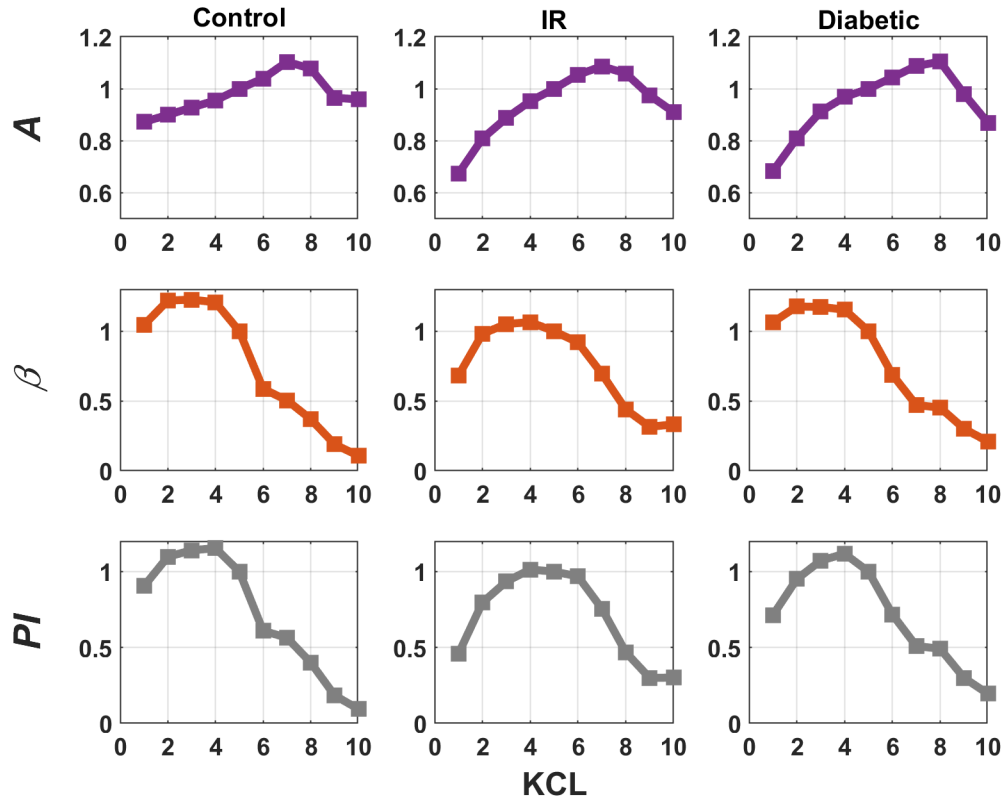


Figure 5.6 KCL curves normalized by the middle (5th) layer for representative NHPs in the control (left column), IR (center column) and diabetic (right column) groups. Each row features one of the estimated parameters: steady state (top row), reperfusion rate (middle row) and perfusion index (bottom row).

5.3.4 Linear Regression Model Fitting

Features calculated from the normalized and non-normalized KCL curves for each estimated parameter (A , β , and PI) served as inputs into the linear regression model. Calculated features from the non-normalized (Supplemental Table C. 35, Supplemental Table C. 36, Supplemental Table C. 37) and normalized (Supplemental Table C. 38, Supplemental Table C. 39, Supplemental Table C. 40) estimated parameter KCL curves for each NHP have been provided in Appendix C: Supplemental Tables. The first order linear coefficient (p_{10}), third order cubic coefficient (p_{30}), and third order quadratic coefficient (p_{31}) initial regression model estimates were zero. These terms were removed from the original model (results not shown) and the model re-assessed, but no effect on the performance of the resultant model was observed.

After removing the three zero-estimated features, the resultant model had nine contributing terms: the eight non-zero input features and the model intercept. Model performance and the significance of estimated parameters A, β , and PI varied per case (Table 5.3). Neither features extracted from A nor β non-normalized data demonstrated the ability to distinguish NHP cohorts ($P > 0.005$). The same was true for the normalized A and β features ($P > 0.005$). Features extracted from PI data demonstrated the largest influence on model performance. The non-normalized PI control vs. IR regression model resulted in a P -value of 0.0768, and the normalized PI IR vs. diabetic model resulted in a P -value of 0.0149 when the model included both the PI features and available BP measurements.

Table 5.3 Regression model P -values determined from blood pressure measurements and either non-normalized or normalized estimated parameter statistics

Case	Observations	Non-normalized			Normalized		
		A	β	PI	A	β	PI
Control vs. IR	10	0.767	0.812	0.0768	0.821	0.643	0.762
Control vs. Diabetic	11	0.138	0.958	0.475	0.186	0.844	0.853
IR vs. Diabetic	11	0.150	0.296	0.454	0.264	0.206	0.0149
Control vs. IR vs. Diabetic	16	0.213	0.733	0.597	0.205	0.646	0.516

5.4 Discussion

The aim of this chapter was to identify flash-replenishment perfusion parameters capable of monitoring kidney health. The non-human primate model *Chlorocebus aethiops sabaeus* was selected for this work given the natural development of diabetes and DKD in this population over time. NHPs were stratified into three cohorts based on health status: control, insulin-resistant, and diabetic. CEUS flash-replenishment data from the NHP kidney was evaluated to assess changes in perfusion based on health status. Several tools were developed

and reported on in this chapter to assure extraction of data that accurately represented kidney perfusion in order to monitor functional changes in the kidney.

5.4.1 Potential Confounding Factors

One significant limitation in this study was the lack of control over clinical measures and NHP health status, which introduced possible confounding variables. Many of the clinical measures were not significant between groups ($P > 0.05$) and as a result likely had little influence on the perfusion parameters for each cohort. As expected, FBG and HbA1c were significantly different between groups. However, average NHP age was determined to be significantly different between the three groups ($P = 0.0315$). Specifically, age was significantly different between control and diabetic cohorts ($P = 0.0429$), but not for control vs. IR ($P = 0.9489$) or IR vs. diabetic ($P = 0.0765$). Kidney function naturally declines with age [216], therefore differences in average age between NHP cohorts may influence the resulting perfusion parameters. Toyama et al. demonstrated that not only did kidney function, measured by eGFR, decrease with age, but that a significantly faster rate of decline occurred when risk factors such as higher blood pressure ($P < 0.01$) were considered [217]. In the same study, the authors determined that diabetes contributed to a larger decline for each age group, but without achieving significance ($P = 0.17$). Both fasting status (fasted vs. not fasted) and blood pressure status (normal vs. high) varied within and between NHPs across the three imaging sessions. Only the diabetic NHPs were consistently not fasted before every imaging session, whereas the control and IR NHPs had a combination of fasted and not fasted status for each imaging session. Each cohort also had a subset of NHPs that displayed high blood pressure for at least one of the three imaging sessions. These variations may have influenced kidney blood flow and as a result the extracted perfusion parameters. In particular, sustained hypertension has been linked to

decreased blood flow to the kidneys as well as kidney damage [218,219]. To make matters worse, diabetes impedes the kidney's ability to regulate kidney blood pressure, exposing the glomerular capillary network to dangerous fluctuations in pressure. Given the interplay between hypertension, diabetes, and developing kidney disease, it may be challenging to extract the influence of solely developing kidney disease on renal perfusion. In part, the influence of these confounding factors, or covariates, could be accounted for by increasing the complexity of the regression model. Okada et al. categorized data according to blood pressure and perfusion estimates to evaluate the association between kidney perfusion and measures of kidney disease (eGFR, urinary albumin excretion - UAE), then implemented multiple regression analyses with models adjusted by clinical measures (BMI, BP, HbA1c, etc.) and patient demographics (sex, age, smoking status, etc.) [48]. The results from Okada et al. showed that peripheral perfusion index, a marker of microcirculatory function, associated with both eGFR and UAE and could be a possible indicator of developing DKD in T2D patients. Another viable option is to use a linear mixed-effects model, which compared to a simple linear regression model, helps account for heterogeneity and variability present in analyzed data [220]. Toyama et al. incorporated a linear mixed effects model to evaluate the relationship between risk factors of kidney disease (age, sex, BP, proteinuria, hemoglobin, smoking status, etc.) and annual decline in eGFR according to baseline age [217]. Liu et al. used stepwise analysis to determine the influence of weight gain and loss on kidney function and perfusion, first evaluating body characteristics, kidney biomarkers, and CEUS measures using a linear mixed model, followed by a mixed effects model that included only the significant parameters identified by the first model [175]. These studies demonstrate how the use of more complex analysis accounting for covariates and confounding

factors helps accurately evaluate the ability of CEUS perfusion parameters to depict kidney injury and disease.

5.4.2 Kidney Segmentation and Concentric Layers

Here, the kidney was segmented into standardized KCLs to address heterogeneous blood flow within kidney compartments. KCL parameters were normalized by the 5th layer to guarantee more precise depth-independent measurements. This segmentation method offers an easy-to-implement solution to the current variability in bolus and flash-replenishment TIC analysis. From a single user-defined ROI and grid, the outlined technique automatically segments the kidney into concentric layers. The layers could be modified by reducing layer width to provide finer sampling of kidney regions or layers could be defined with variable thickness, based on the spatial extent of each kidney region. Segment orientation could also be modified to further address signal depth-dependence. Layers defined here were expected to correlate with functional aspects of the kidney, but standardizing segmentation, i.e. ROI definition, spatial patterns of functional and structural variations should be further studied. Particularly since prior studies by Ignee et al., Xie et al., and Kogan et al., have observed the influence of depth, lateral position, and transducer orientation on TIC parameters, suggesting standardized criteria to compensate [170,179,221]. Results from Ignee et al. indicated that bolus perfusion parameters were susceptible to depth and lateral position, making it important to consider ROI placement when analyzing multiple regions or comparing tissue in an image [170]. Xie et al. evaluated flash-replenishment parameter variability based on depth and perfusion rate, identifying perfusion rates and depths that resulted in the most consistent perfusion parameter measurements [179]. Kogan et al. determined the influence of transducer orientation on kidney blood flow rate measured by CEUS perfusion parameters, revealing differences in measured

reperfusion between the coronal and parasagittal views of the kidney [221]. These studies suggest that the influence of parameters such as imaging depth, ROI position, transducer orientation, and infusion rate should be considered when analyzing CEUS perfusion data.

The segmentation approach outlined in this chapter simplifies current methods used to assess kidney perfusion. For both flash-replenishment and bolus TIC analysis, common practice involves an experienced user, typically a radiologist or trained researcher, manually defining ROIs. Number and placement varies, but usually multiple ROIs are considered in the cortex and medulla [162,174,175,215,222]. The spatial distribution of key structural components contributing to underlying mechanisms of disease progression make evaluating both cortical and medullary perfusion vital for the early detection of DKD. In fact, Mannucci et al. noted significant differences in medullary peak intensity and AUC in dogs with AKI compared to healthy dogs, but noted none from cortical measurements [178]. Stock et al. found that cortical mean transit time and time to peak were significant parameters for distinguishing healthy from CKD cats, while rise time, time to peak, and fall time were significant in the medulla [174]. In the future, isolating data from regions with cortical and juxtamedullary nephrons may be informative, as glomerular and tubular mechanisms have been shown to alter surrounding microvasculature. Tubuloglomerular feedback has been linked to both dilation and constriction of glomerular arterioles [59,223–226]. Furthermore, resulting changes in vascular resistance lead to increased intraglomerular capillary pressure causing both intraglomerular and systemic hypertension and contribute to glomerular hyperfiltration [54,224,225]. This crosstalk between vascular, glomerular, and tubular systems in developing kidney disease demonstrates the need to implement imaging and analysis techniques that successfully isolate and depict the complex intersystem changes occurring due to disease progression.

The proposed flash-replenishment analysis technique could be further enhanced by fully automating segmentation. Studies using CT data have indicated that automatic kidney segmentation can be performed with high accuracy [227,228]. Sharma et al. demonstrated that accurate segmentation was possible in highly diseased kidneys [227]. Jin et al. achieved true-positive volume fractions ranging from 80-93% and false-positive volume fractions $< 1\%$ when automatically segmenting by the kidney cortex, column, medulla, and pelvis [228]. Translating these advances to US and combining the proposed KCL method with computer generated kidney contours of the outer boundary or multiple regions, could further simplify analysis for radiologists and researchers alike, providing more accurate, reproducible and easily attainable measures of kidney perfusion.

5.4.3 Model Performance

In this work, a monoexponential model was fit to flash-replenishment data, but this technique could be adapted for use with other established perfusion models. Krix's multi-vessel model [159,181], and both models proposed by Arditi [160] and Hudson [180,182] are alternatives methods of fitting flash-replenishment data, utilizing different input conditions, which could improve classification. The model proposed by Krix et al., accounted for the unknown distribution of blood vessel velocities in a given ROI to more accurately reflect heterogeneous flow throughout a tissue [159,181]. It is possible that the KCL segmentation approach, which attempted to isolate regions of differential flow may address some of the limitations of the monoexponential model that drove the formation of Krix's multi-vessel model. However, this cannot be confirmed without direct comparison between the two approaches. The models proposed by Arditi and Hudson consider the flow distribution and ultrasound field to improve perfusion estimates from flash-replenishment data, but required more knowledge about

the system to implement, specifically the beam profile and log-compression scheme [160,180,182]. The use of these models may prove particularly useful for reducing perfusion parameter variability and for accurately assessing medullary flow, given the s-shaped behavior of slower reperfusion through the medulla. Although simple, the monoexponential model still performed extremely well when fit to the flash-replenishment data. This was confirmed by the low average MSE (< 0.033) in each group. Future work should also consider how the KCL segmentation method may enhance information extracted from indicator-dilution models, such as the lognormal, Erlang, and gamma variate distributions, diffusion with drift models, or the lagged normal model, which are all applied to bolus TIC data [156,157].

The linear regression model used to classify NHP cohorts by health status based on CEUS flash-replenishment perfusion parameters found that normalized and non-normalized PI measures exceeded the other perfusion parameters (A , β) in ability to differentiate cohorts. Normalized PI distinguished IR and diabetic vervets ($P = 0.0149$), while non-normalized PI showed the potential to distinguish control from IR vervets ($P = 0.0768$). The superior performance of the normalized PI IR vs. diabetic model to classify NHP cohorts was clear from the t-statistic P -values for each model term estimated coefficient. Seven of the nine model coefficients had a t-statistic with a P -value < 0.07 , with six < 0.05 (Table 5.4). Normalized PI KCL average, KCL AUC, p_{32} , p_{33} , systolic BP, and diastolic BP were all significant features ($P < 0.05$) in distinguishing IR and diabetic vervets, while p_{11} showed potential, but failed to achieve significance ($P = 0.067$) (Table 5.4). The non-normalized PI control vs. IR model performance was similarly explained by the t-statistic P -values for each model term estimated coefficient. Seven of the nine estimated coefficients had a t-statistic with a P -value < 0.074 , but only one, the model intercept, was significant ($P = 0.048$), which explains why the model overall

did not achieve statistical significance (Table 5.5). Non-normalized PI KCL SD, p_{11} , p_{32} , p_{33} , systolic BP, and diastolic BP all displayed potential to distinguish between cohorts, but failed to achieve significance ($P > 0.05$). It is important to note that these results for the normalized and non-normalized PI parameters were only obtained after adding BP measurements to the model. Before including BP data, both cases were non-significant ($P \gg 0.05$). The small sample size (16 NHPs) likely limited the ability of the regression model to distinguish vervet cohorts based only on CEUS data. Current understanding of the complexity of developing DKD and the interaction between hypertension and altered kidney blood flow in DKD support the use of additional features in models classifying DKD. Indeed, Okada et al. found that changes in microcirculation may indicate DKD, after adjusting for blood pressure [48]. As previously mentioned, future work should consider increasing model complexity by incorporating and weighting by available clinical measures, as this has proved potentially useful for detecting changes in kidney function in both humans and animals [48,175].

Table 5.4 Model term coefficient P -values from the normalized PI perfusion data for each regression test case

Linear Regression P -values				
Model coefficients	Control vs. IR	Control vs. Diabetic	IR vs. Diabetic	Control vs. IR. vs. Diabetic
(Intercept)	0.4159	0.7308	0.6166	0.4975
P_{avg}	0.3479	0.8869	0.0189	0.8508
P_{sd}	0.4882	0.6403	0.3588	0.3493
P_{AUC}	0.3542	0.9127	0.0159	0.9290
P_{p11}	0.8700	0.8752	0.0668	0.8237
P_{p32}	0.7442	0.8782	0.0277	0.8440
P_{p33}	0.6841	0.8197	0.0498	0.6970
P_{sys}	0.6547	0.7443	0.0037	0.3885
P_{dia}	0.6226	0.9800	0.0114	0.9769

Table 5.5 Model term coefficient P -values from the non-normalized PI perfusion data for each regression test case

Linear Regression P -values				
Model coefficients	Control vs. IR	Control vs. Diabetic	IR vs. Diabetic	Control vs. IR. vs. Diabetic
(Intercept)	0.0476	0.3534	0.5200	0.8579
P_{avg}	0.5551	0.5509	0.4529	0.9437
P_{sd}	0.0574	0.3693	0.6318	0.9519
P_{AUC}	0.5875	0.5306	0.4544	0.9474
P_{p11}	0.0598	0.2878	0.1705	0.4124
P_{p32}	0.0665	0.2915	0.2016	0.5033
P_{p33}	0.0639	0.2974	0.2173	0.4963
P_{sys}	0.0735	0.8028	0.2527	0.4324
P_{dia}	0.0608	0.9507	0.4115	0.4930

Because 40% of T2D patients will potentially develop DKD, distinguishing kidneys in the diabetic milieu from those with advancing DKD is important. The CEUS flash-replenishment technique evaluated in this chapter shows promise, since it was sensitive enough to distinguish control, IR and diabetic vervets. Analysis of blood and urine samples (not shown) revealed that none of the NHPs had overt kidney disease at the time of imaging. However, this provides an opportunity for follow-up imaging to determine the prognostic capability of these methods. Additionally, future studies will implement this method in diabetic models with and without DKD. In summary, the use of a regression model demonstrated that a combination of perfusion features and clinical measures could differentiate between the phases of diabetic progression. Improving CEUS sensitivity to microvascular alterations through changes in kidney perfusion could be the key to identifying early irregularities predictive of developing disease.

CHAPTER 6: QUALITATIVE ASSESSMENT OF FLASH REPLENISHMENT CONTRAST ULTRASOUND IMAGING FOR CHARACTERIZING KIDNEY LESIONS IN PATIENTS WITH CHRONIC KIDNEY DISEASE

6.1 Overview

Early identification of chronic kidney disease, not only helps preserve loss of kidney function, but may also help reduce the risk of developing further kidney complications. For example, patients with CKD have between a twofold and threefold higher risk of kidney cancer [229,230], a risk that increases with age and as eGFR declines [231,232]. Additionally, with diabetes as one of the leading causes of CKD, the link between diabetes and cancer incidence has also been considered. A meta-analysis by Larsson et al. found a positive association between diabetes and risk of kidney cancer [233]. These risk factors have also been linked to race as there is a higher prevalence of CKD in black persons compared to white persons, resulting in a higher incidence of kidney cancer among black persons [234]. Kidney cancer management strategies in these patient populations varies, but often considers kidney sparing approaches such as partial nephrectomy or active surveillance [235,236]. Typically, kidney lesions are characterized using multiphase non-contrast and contrast enhanced CT or MRI protocols [237–239]. Solid lesions are diagnosed according to enhancement and morphology while complex cysts are typically assessed using the Bosniak criteria, which associates the presence of different lesion characteristics with potential malignancy [240–242]. CT and MRI possess high sensitivity and specificity [243–246] for the diagnosis of complex lesions, however, in patients with kidney dysfunction, like CKD, the use of these modalities may be limited due to possible contraindications from the contrast agents [247,248].

Contrast-enhanced ultrasound can be used as an alternative to contrast-enhanced CT and MRI, and has many attractive qualities including low cost, lack of ionizing radiation, real-time imaging capabilities, portability, and accessibility [249–251]. Further, UCAs are sensitive to slower microvascular perfusion and are well tolerated in patients with kidney dysfunction [252,253]. CEUS has gained traction for its ability to characterize renal lesions in strong agreement with contrast-enhanced CT, the current imaging gold standard [254–257]. Reported sensitivities are comparable to contrast-enhanced CT and MRI, with slightly lower specificity [245,258–260]. However, one study by Barr et al. achieved remarkable sensitivity (100%) and specificity (96%) using CEUS to diagnose kidney lesions [253]. Few studies have explored the use of CEUS to characterize kidney lesions in patients with impaired kidney function [260–262]. In this chapter, we assess the qualitative capabilities of flash-replenishment CEUS imaging to characterize complex kidney lesions in patients with known CKD.

6.2 Materials and Methods

6.2.1 Patient Recruitment

This was a prospective imaging study using CEUS to diagnose kidney lesions in patients with CKD. This study was performed with Institutional Review Board approval, in accordance with the ethical standards outlined in the Helsinki declaration, and written informed consent was obtained from all patients who participated. Patients were recruited primarily from Nephrology clinics at University of North Carolina (UNC) Health. Any patient who met study criteria was offered participation. Inclusion criteria were: 1) presence of kidney disease, based on an eGFR <90 mL/min/1.73 m², presence of albuminuria or proteinuria >30 mg/gm, on dialysis or with kidney transplant, or biopsy proven disease; 2) at least one kidney lesion presenting features concerning for malignancy or warranting follow-up imaging, including Bosniak IIF cystic

lesions and greater or complex cysts; and 3) able to provide consent and comply with study protocol. Exclusion criteria were: 1) any contraindications to the contrast agent, including hypersensitivity to the agent; 2) severe pulmonary hypertension or adult respiratory distress syndrome; 3) critical illness or intensive care unit status; 4) right-to-left cardiac shunt³; 5) active cardiac disease, 6) unstable neurologic disease within 3 months; 7) invasive kidney procedure between time of lesion identification and CEUS; 8) medical condition that would decrease data reliability; 9) pregnancy or lactation; and 10) obesity limiting acquisition of quality images. After obtaining written informed consent, patients underwent CEUS per a standard study protocol using a flash-replenishment imaging scheme.

6.2.2 Imaging Protocol

Flash-replenishment CEUS data were acquired with a Siemens Acuson Sequoia 512 (Siemens, Mountain View, CA, USA) using a 4C1 curvilinear abdominal transducer. For CEUS, low MI imaging was performed using CPS mode to limit MB disruption during acquisition. The following ultrasound settings were kept constant across all patients: B-mode MI, (1.9), CPS MI (0.18), dynamic range (80 dB), capture rate (10 Hz), flash duration (<1 s), and transmit frequency (1.5 MHz). Gain, depth, and infusion rate were adjusted per patient according to patient size, kidney location, and kidney size in order to optimize data acquisition. Flash MI was automatically determined and set by the Siemens ultrasound system and varied slightly (0.7-0.8) based on imaging depth. Registered sonographers with CEUS training performed all ultrasound imaging examinations. For patients with multiple lesions, the most complex lesion designated by prior imaging was chosen for CEUS imaging. If multiple complex or solid lesions were present,

³At the time the study was conducted, cardiac shunt was listed as a contraindication to Definity perflutren microspheres, but this contraindication has since been removed.

met criteria, and if consent was given, then multiple lesions were imaged and considered as separate cases. Lesions were initially located using B-mode imaging and the transducer oriented over the lesion and part of the kidney parenchyma. Out-of-plane breathing motion was reduced by imaging in the longitudinal plane whenever possible. The contrast agent, Perflutren Lipid Microspheres (DEFINITY[®], Lantheus Medical Imaging, North Billerica, MA, USA), was prepared as an infusion for flash-replenishment imaging. Lesion visibility was confirmed via CEUS and flash-replenishment imaging was performed as previously described (Chapter 2). A microbubble solution, containing 50 mL of saline mixed with 1.3 mL of Definity was infused at a variable rate based on patient body mass index (BMI), using a Medfusion[®] 4000 syringe pump (Smiths Medical, Minneapolis, MN, USA). The solution was infused at a rate of 4 mL/min, 6 mL/min, or 8 mL/min for patients with BMIs <21 kg/m², between 21 kg/m² and 30 kg/m², or >30 kg/m², respectively. Two flash-replenishment clips were collected in dual mode, viewing contrast and B-mode data side-by-side (Figure 6.1). Imaging concluded with a sweep across the whole kidney in the sagittal plane.

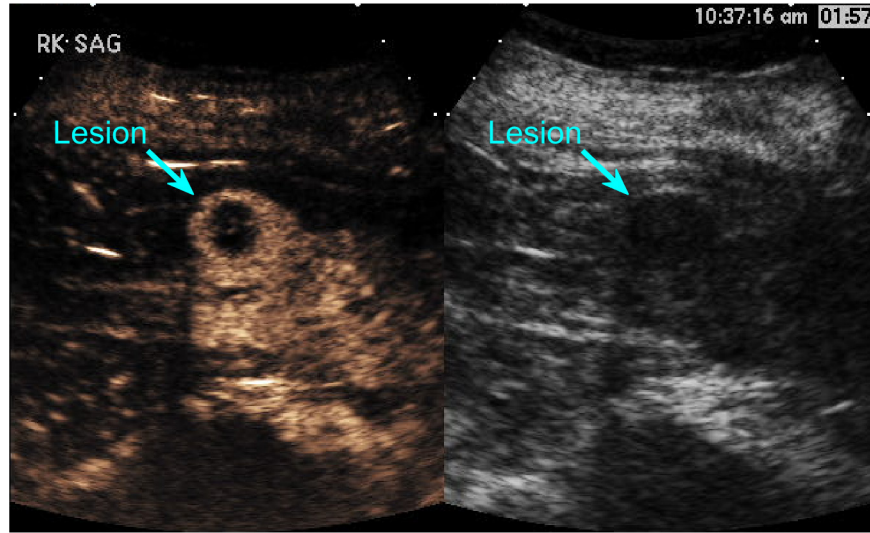


Figure 6.1 Dual mode visualization of a kidney lesion in CPS mode (left) and B-mode (right). Lesion location in each view indicated by the cyan arrow and text label.

6.2.3 Case Preparation and Interpretation

After obtaining all patient data, a custom graphical user interface (GUI) was developed in MATLAB[®] 2017a (Mathworks, Natick, MA, USA) to provide a straightforward application for image interpretation and case evaluation (Figure 6.2). The program was packaged as an external application using Matlab Compiler Runtime version 9.2 and was distributed to four readers for interpretation along with a short operational guide. Each case was de-identified, stripped of clinical information, and the case order randomized by the GUI. Readers were not involved in data acquisition, individually interpreted cases, and were blinded to true lesion diagnosis. Readers were radiologists at UNC Health with varying levels of experience interpreting ultrasound and CEUS images. Prior to image interpretation readers reviewed instructions on operating the GUI and viewed a 40-minute online lecture on CEUS of the kidneys [263]. Bosniak criteria for evaluating cystic lesions was modified for CEUS images, defined as CEUS Cystic Mass Categories I-IV (Table 6.1), and used by readers to classify lesions as benign, malignant, or indeterminate. A single flash-replenishment clip and dual mode

sweep per case were provided for assessment of lesion malignancy.

Lesion Classification
CEUS Cystic Mass Classification

Measure distance from skin to lesion
Calipers mm Recalc. distance
Measure lesion - 1st dim
Calipers mm Recalc. size
Measure lesion - 2nd dim
Calipers mm Recalc. size
Is this lesion malignant?

What adjustments would you have made regarding contrast data acquisition?

CEUS Cystic Mass Classification System

CEUS Category I
Cystic mass with no enhancement (benign)

CEUS Category II
Thin smooth septation or septations (less than 2 mm in thickness) with constant mild enhancement or occasional foci of enhancement (benign)

CEUS Category IIF
Septation(s) between 2-3 mm in thickness with enhancement (probably benign, but follow-up needed)

CEUS Category III
Cystic mass with thick (more than 3 mm in thickness) and nodular septation(s) with enhancement (indeterminate, but has potential to be malignant)

CEUS Category IV
Cystic mass with enhancing solid tissue component (malignant)

Comments Section

Choose case to view: 1 of 65
Display Marker
Hide Marker

Previous Patient
Play CEUS Clip
Clear Calipers

Next Patient
Play Sweep
Save Data

	1	2	3	4	5	6	7	8	9	10	11	12	13
Case Number													
CEUS Classification													
Dist. skin to lesion													
Lesion size - 1st dim													
Lesion size - 2nd dim													
Malignancy													
Adjustments													
Comments													

Figure 6.2 Graphical user interface layout. The user interacts with the main screen to evaluate each lesion. A B-mode image of the lesion is displayed on the left, with buttons underneath that allow the user to move between cases, change what is displayed, and externally play contrast flash-replenishment or sweep videos. The middle panel contains drop-down question menus and buttons for taking caliper measurements on the B-mode image. Definitions and a section for adding comments about the case are located on the right. The table underneath the middle and right panels populates with the responses to each field as the reader completes a case.

Table 6.1 Comparison of Modified CEUS Cystic Mass Classification to CT Bosniak Criteria

Stage	CEUS Mass Classification	Bosniak Criteria
I	Cystic mass with no enhancement	Simple cyst with hairline thin wall No septa, calcifications, or solid components Water attenuation, no enhancement
II	Thin smooth septation or septations (less than 2 mm in thickness) with constant mild enhancement or occasional foci of enhancement	Septa: few hairline-thin, but no measurable enhancement Calcifications: fine or a short segment of slightly thickened present in wall or septa High attenuation: uniform in lesions (<3cm) that are sharply marginated, no enhancement
IIIF	Septation(s) between 2-3 mm in thickness with enhancement	Septa: multiple hairline-thin, but no measurable enhancement of septum or wall Minimal thickening of wall or septa; may contain thick and nodular calcification, but no measurable contrast enhancement No enhancing soft-tissue components Intrarenal: totally intrarenal non-enhancing high-attenuating renal lesions, lesions are generally well marginated
III	Cystic mass with thick (more than 3 mm in thickness) and nodular septation(s) with enhancement	Measurable enhancement: cystic mass with thickened, irregular, or smooth walls or septa; measurable enhancement present
IV	Cystic mass with enhancing solid tissue component	Enhancing soft-tissue components: clearly malignant, cystic masses that can have all criteria from category III, but also contain distinct enhancing soft-tissue components independent of wall or septa

6.2.4 Reference Standards for Lesion Characterization

True lesion diagnosis was confirmed by tissue pathology or follow-up imaging for cases where pathology was not available. The follow-up imaging interval (≥ 12 months) and imaging modality (ultrasound, CT, MRI) were determined by the clinician providing patient care.

Contrast CT and MRI were used at the discretion of the clinical provider. The most recent exam was used when patients had multiple follow-up examinations. Diagnosis by tissue pathology was

either positive or negative for malignancy. Follow-up imaging diagnoses were either: 1) stable for lesions with no change, regression, or no concerning features, 2) suspicious for lesions with stable, but persistent concerning features, or 3) progressed for lesions with progression of concerning features. Suspicious diagnoses were primarily cases where lesions were likely malignant, but the patient and treatment team opted for active surveillance instead of surgery. Concerning characteristics included enhancing or thickened septations, calcifications, mural thickness, irregularity, nodules, or solid enhancing masses.

6.2.5 Performance Measures and Statistical Analysis

Reader interpretations were compared to true diagnoses to evaluate the ability of CEUS to characterize malignant and benign lesions. Diagnostic performance was assessed through sensitivity, specificity, positive predictive values (PPV), and negative predictive values (NPV). These metrics were computed for individual readers and for all readers combined. Combined reader measures were estimated using functions of the logistic regression parameters fitted via Generalized Estimating Equations to account for the correlation of measurements made on the same patient [264]. Reader agreement regarding malignant diagnoses was evaluated using Bowker's symmetry test. Analysis of reader performance and agreement was accomplished using the open source R statistical software environment version 4.0 and SAS version 9.4 (Cary, North Carolina, USA). A two-sided *P*-value of 0.05 was considered statistically significant.

6.2.5.1 Assessing Malignant Diagnoses

First, reader ratings and true reference values were dichotomized based on a malignancy status of either yes (malignant) or no (not malignant) (Figure 6.3). This classification scheme included reader ratings of malignant, positive pathology, and lesions labeled progressed by follow-up imaging as malignant. Reader ratings of benign or indeterminate, negative pathology,

and follow-up imaging marked stable or suspicious were classified as not malignant. For sensitivity analysis, this classification scheme was re-assessed after excluding suspicious cases and removing corresponding reader ratings (Figure 6.3).

6.2.5.2 Assessing Benign Diagnoses

Following the evaluation of malignant diagnoses, results were dichotomized based on a benign status of either yes (benign) or no (not benign) (Figure 6.3). Reader ratings of benign, negative pathology, and stable lesions identified by follow-up imaging met the criteria for benignity. Reader ratings of malignant or indeterminate, positive pathology, and lesions labeled suspicious or progressed by follow-up imaging were considered not benign.

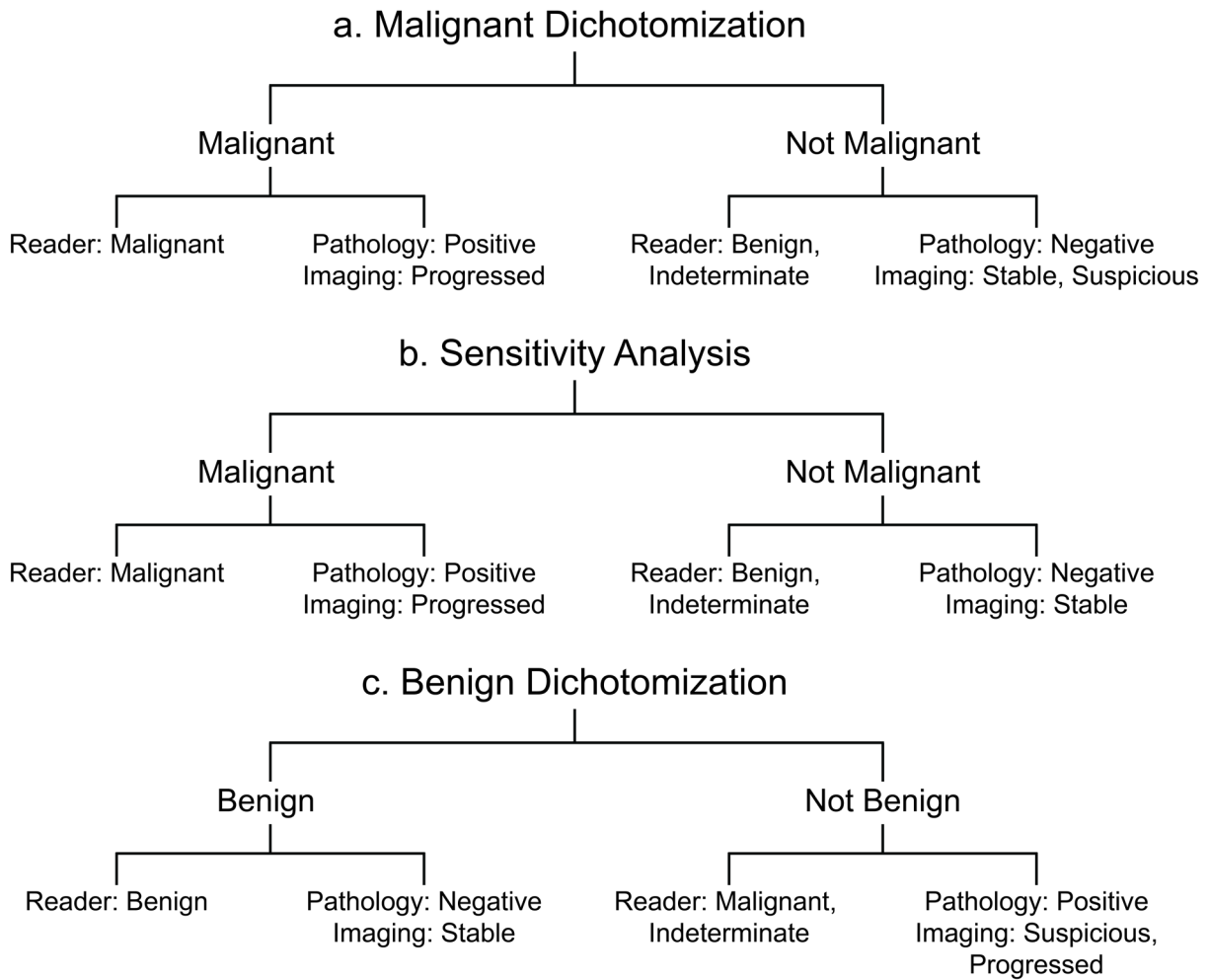


Figure 6.3 Dichotomization of reader diagnoses and true reference standards by a) malignant status, b) malignant sensitivity analysis, and c) benign status.

6.3 Results

6.3.1 Patient Enrollment, Disease Severity, and Lesion Diagnoses

Sixty patients were enrolled in the study and underwent CEUS imaging. Ten patients consented to having more than one lesion imaged, resulting in a total of 73 lesions included in the study for the 60 patients. Of that amount, 63 lesions in 53 patients were included in the final analysis. The 53 patients were comprised of 62.3% male, 37.7% female, 49.1% black, and 50.9% white, with an average age of 60 (\pm 14) years. Disease severity ranged from stage 2 CKD to ESKD, with stage 3 CKD and ESKD occurring most commonly (Table 6.2). Seventeen of the 53

patients (32.1%) had stage 3 CKD and 14 of 53 (26.4%) had ESKD. Greater detail regarding patient characteristics, CKD stage, and initial imaging study for patients included in the final analysis has been outlined in Table 6.2. For comparison, a summary of all 60 enrolled patients has been provided in Appendix C: Supplemental Tables (Supplemental Table C.41).

Table 6.2 Details on patients included in final analysis

Patient Details	N (%)
Number of Patients	53
Age (years)	
Mean \pm SD	60 \pm 14
Sex	
Male	33 (62.3%)
Female	20 (37.7%)
Race or Ethnicity	
Black	26 (49.1%)
White	27 (50.9%)
CKD Stage	
CKD II	8 (15.1%)
CKD III	17 (32.1%)
CKD IV	10 (18.9%)
CKD V	4 (7.5%)
ESKD	14 (26.4%)
Initial Imaging Study	
Non-contrast CT	3 (5.6%)
Contrast CT	2 (3.8%)
Contrast CT with renal mass protocol	10 (18.9%)
Non-contrast MRI	3 (5.6%)
Contrast MRI	3 (5.6%)
Conventional ultrasound	32 (60.4%)

Cases were excluded from analysis based on insufficient data collection, poor data quality, or lack of an adequate reference standard (Figure 6.4). Eight lesions were excluded before interpretation due to issues during data collection and two were excluded after

interpretation due to the absence of a reliable reference standard. Tissue pathology was available for 12 lesions and follow-up imaging was used to determine true lesion status for the other 51.

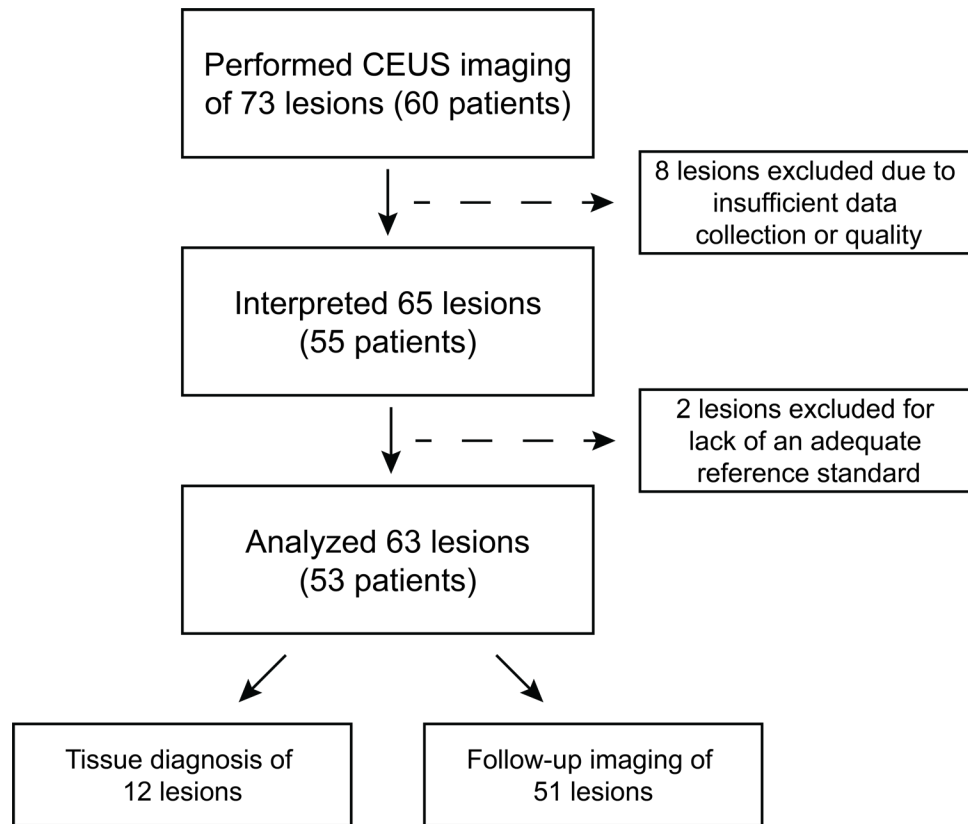


Figure 6.4 Flow diagram of patient and lesion retention from imaging through final analysis.

The lesions with pathology included one benign oncocytoma and 11 malignant subtypes of RCC (Table 6.3). For the lesions assessed by follow-up imaging, 40 were identified as stable, eight as suspicious, and three as progressed. In total, using either reference standard (tissue pathology or follow-up imaging), 22% of the lesions were malignant, 65% were benign, and 13% were suspicious/indeterminate (Figure 6.5). In comparison, readers classified between 33-38% as malignant, 48-57% as benign, and 8-19% as indeterminate (Figure 6.5). Lesion size was measured in three dimensions by ultrasound and the volume calculated for each using an ellipsoid formula. Lesion volume ranged from 0.15 cm³ to 85.4 cm³, with an average volume of 10.8 cm³ ± 14.3 cm³. Detailed information on lesion characteristics can be found in Table 6.3.

Table 6.3 Number, diagnosis, laterality, and size of analyzed lesions

Lesion Information	N (%)
Number of Lesions	63
Lesion Diagnosis	
Clear cell RCC	2 (3.2%)
Acquired cystic disease RCC	4 (6.4%)
Papillary RCC	2 (3.2%)
Clear cell papillary RCC	2 (3.2%)
Tubulocystic RCC	1 (1.6%)
Oncocytoma	1 (1.6%)
Imaging Surveillance	
Regressed/no concerning features	40 (63.5%)
Stable, but persistent concerning features	8 (12.7%)
Progressed features	3 (4.7%)
Laterality of Lesion	
Left	30 (47.6%)
Right	33 (52.4%)
Average Lesion Measurements by Imaging (cm ³ , cm)	
Volume \pm SD (range)	10.2 \pm 13.6 (0.15-85.4)
Minimum Diameter (range)	2.03 (0.6-4.4)
Maximum Diameter (range)	2.67 (0.8-6.9)

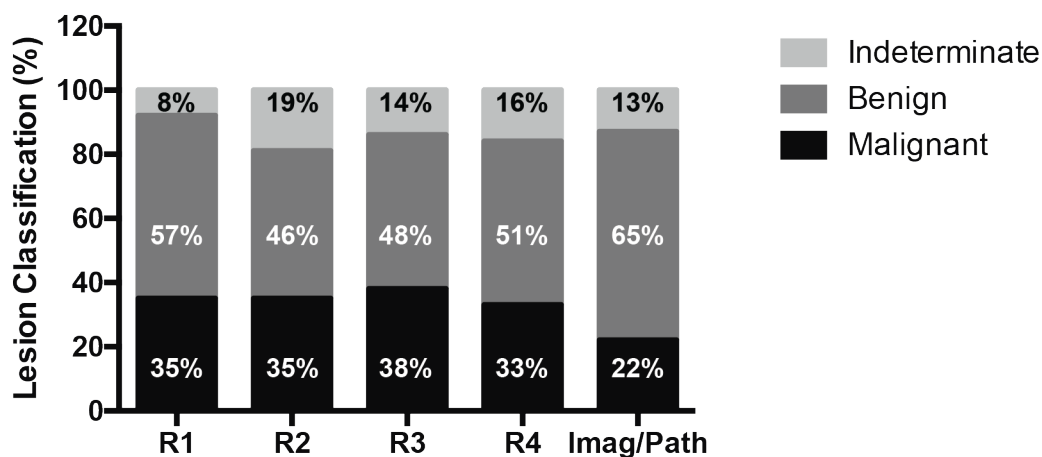


Figure 6.5 Lesion malignancy classification for each reader (R1-4) and reference standard of either imaging or pathology. Stacked column graph showing the percentage of lesions classified as malignant, benign, or suspicious/indeterminate by each reader and pathology or follow-up imaging.

6.3.2 Malignant Lesion Classification

Tissue pathology and imaging confirmed 14 lesions as malignant, 11 with positive pathology and three labeled progressed by imaging. The remaining 49 cases were considered not malignant, where one had negative pathology, 40 were stable by imaging, and eight were suspicious by imaging. Combined reader sensitivity, specificity, PPV, and NPV for diagnosing malignant lesions was 71%, 75%, 45%, and 90% (Table 6.4). Individual readers achieved between 64-79% sensitivity, 71-78% specificity, 42-50% PPVs, and 88-93% NPVs (Table 6.4). Reader 1 demonstrated the best performance across all measures. Reader 4 had the lowest sensitivity and NPV, while Reader 3 had the lowest specificity and PPV. For sensitivity analysis, suspicious cases by follow-up imaging were removed from the groupings and data re-assessed as malignant versus not malignant. The resultant combined sensitivity, specificity, PPV, and NPV were 71%, 87%, 65%, and 90% (Table 6.4). Individual readers achieved 64-79% sensitivity, 85-88% specificity, 60-69% PPVs, and 88-92% NPVs (Table 6.4). Sensitivity and NPV were not influenced by sensitivity analysis of malignant diagnoses, but specificity and PPV increased.

6.3.3 Benign Lesion Classification

Reference standards designated 41 lesions benign, where one had negative pathology and 40 stable were by imaging, and 22 not benign, where 11 had positive pathology, eight were suspicious by imaging, and three were progressed by imaging. Combined reader sensitivity, specificity, PPV, and NPV was 70%, 86%, 91% and 61%, respectively (Table 6.5). Individual readers achieved 63-80% sensitivity, 82-91% specificity, 88-93% PPVs, and 56-70% NPVs (Table 6.5). Reader 1 had the highest sensitivity and NPV. Reader 3 had the highest PPV and specificity. Reader 2 had the lowest sensitivity and NPV, while Reader 4 had the lowest specificity and PPV.

6.3.4 Reader Agreement

Individual inter-reader agreement regarding lesion status varied between 72-90% for malignant, 20-80% for indeterminate, and 75-91% for benign classification. *P*-values for reader agreement were 0.2, 0.3, and 0.4 for Reader 1 vs. Reader 2, 3, and 4, respectively (Supplemental Table C.42); 0.7 and 0.8 for Reader 2 vs. Reader 3 and 4, respectively (Supplemental Table C.43); and 0.6 for Reader 3 vs. Reader 4 (Supplemental Table C.44). Reader 2 and Reader 4 had the highest level of agreement when classifying cases, while Reader 1 and Reader 2 had the lowest agreement. Overall, Reader 1 agreed least with all other readers.

Table 6.4 Performance analysis of CEUS for diagnosing malignant kidney lesions

Diagnostic Performance	Reader 1	Reader 2	Reader 3	Reader 4	Overall
Diagnosing malignant lesions					
Sensitivity, % (CI) ⁴	79 (49, 95)	71 (42, 92)	71 (42, 92)	64 (35, 87)	71 (54, 89)
Specificity, % (CI)	78 (63, 88)	76 (61, 87)	71 (57, 83)	76 (61, 87)	75 (64, 86)
PPV, % (CI)	50 (28, 72)	45 (24, 68)	42 (22, 63)	43 (22, 66)	45 (26, 64)
NPV, % (CI)	93 (80, 98)	90 (77, 97)	90 (76, 97)	88 (74, 96)	90 (82, 98)
Sensitivity analysis					
Sensitivity, % (CI)	79 (49, 95)	71 (42, 92)	71 (42, 92)	64 (35, 87)	71 (54, 89)
Specificity, % (CI)	88 (74, 96)	88 (74, 96)	85 (71, 94)	85 (71, 94)	87 (77, 96)
PPV, % (CI)	69 (41, 89)	67 (38, 88)	62 (35, 85)	60 (32, 84)	65 (43, 86)
NPV, % (CI)	92 (79, 98)	90 (76, 97)	90 (76, 97)	88 (73, 96)	90 (82, 98)

Table 6.5 Performance analysis of CEUS for diagnosing benign kidney lesions

Diagnostic Performance	Reader 1	Reader 2	Reader 3	Reader 4	Overall
Diagnosing benign lesions					
Sensitivity, % (CI) ⁴	80 (65, 91)	63 (47, 78)	68 (52, 82)	68 (52, 82)	70 (59, 81)
Specificity, % (CI)	86 (65, 97)	86 (65, 97)	91 (71, 99)	82 (60, 95)	86 (76, 97)
PPV, % (CI)	92 (78, 98)	90 (73, 98)	93 (78, 99)	88 (71, 96)	91 (83, 99)
NPV, % (CI)	70 (50, 86)	56 (38, 73)	61 (42, 77)	58 (39, 75)	61 (45, 76)

⁴Confidence Interval (CI)

6.4 Discussion

6.4.1 Lesion Classification

This study evaluated CEUS diagnostic accuracy for complex kidney masses in patients with CKD. Analysis of 63 lesions in 53 patients, found that combined reader sensitivity for characterizing lesion malignancy (71%) was lower than reported values (86-100%), but specificity (75%) fell within the range of previously reported values (63-96%) using CEUS [245,253,258–260]. The ability of CEUS to reliably provide a true negative test result was confirmed by the high NPV (90%). Sensitivity analysis was performed to assess the influence of lesions labeled suspicious by follow-up imaging on malignant vs. not malignant lesions dichotomization. Results from this analysis revealed that incompletely characterized (suspicious) lesions mainly contributed to a larger number of false positive results when assessing malignancy, lowering specificity and PPV. These suspicious lesions appeared to influence the ability of CEUS imaging to correctly characterize complex lesions. However, the dichotomization scheme used here may have been the more likely limitation, due to readers classifying these eight suspicious lesions as malignant, when the lesions did not meet that criterion according to our dichotomization scheme (Figure 6.3). This was supported by the sensitivity analysis, where removal of the eight suspicious lesions from malignancy analysis saw an increase in both specificity (75% to 87%) and PPV (45% to 65%). In clinical practice, the true value of these eight lesions would be unknown without tissue pathology, but by other imaging modalities they would be suspicious for malignancy, albeit stable over one year. The indolent nature of these lesions is consistent with many subtypes of kidney cancer, particularly in patients with CKD. It is possible that these represent true malignancies, in line with reader interpretations; however, tissue pathology would be necessary to confirm this supposition. At a

minimum, reader interpretations of these eight lesions using CEUS would be in agreement with other imaging modalities and would not alter clinical management.

Performance metrics evaluating lesion benignity revealed similar outcomes as the malignancy analysis. Specificity for benignity was higher than for malignancy, indicative of more true negative and less false positive results using the benign criteria (Figure 6.3). PPV also increased when switching dichotomization schemes, suggesting a decrease in the number of false positive cases with the different criteria. These results again suggested that readers were more likely to classify suspicious lesions as malignant. In fact, reader 1 classified 75% (6/8) as malignant, reader 2 characterized 87.5% (7/8) as malignant, reader 3 classified 100% (8/8) as malignant, and reader 4 characterized 75% (6/8) as malignant. Studies evaluating the performance of contrast modalities (CT, MRI, ultrasound) typically assess benignity and malignancy based on lesion classification according to the Bosniak criteria or an adapted form of the criteria. Under these guidelines, Bosniak I-IIF are often considered benign, while Bosniak III and IV are considered malignant or suspected malignancies [261,265]. This distinction is based on the management of Bosniak I-IIF (non-surgical, follow-up) compared to Bosniak III and IV (surgically removed) lesions. Adapted criteria for CEUS imaging also follow a similar scheme, assigning lower class [260] or grade [258,259] lesions as benign, while higher grade lesions are considered malignant. Here, we implemented a binary classification scheme (Figure 6.3) that grouped lesions as malignant vs not malignant, with secondary analysis that grouped lesions as benign vs. not benign. This scheme compared the reader designations of malignant, benign, or indeterminate with tissue pathology of positive or negative and follow-up imaging that classified lesions as stable, suspicious, or progressed. However, use of this scheme over more conventional classification methods may have impacted CEUS performance metrics. At the very least, there

appeared to be a negative effect on the categorization of suspicious lesions, as was demonstrated by the improvements to specificity and PPV with the sensitivity analysis. This may be addressed by incorporating a different classification scheme, but, lack of standardized criteria for classifying complex lesions using CEUS imaging pose a challenge with regards to selecting the optimal classification scheme to improve CEUS performance.

6.4.2 Classification Criteria for CEUS

Bosniak criteria were first established for use with CT imaging and have since been adapted for MRI, but have not yet been established for CEUS. Studies that report on the use of CEUS imaging for characterizing kidney lesions have typically used a modified approach to the Bosniak criteria or have generated classification schemes similar to, but distinct from Bosniak criteria. Barr et al. characterized lesions primarily based on CEUS enhancement in the lesion relative to the kidney parenchyma, but also considered septal and peripheral enhancement in order to differentiate benign from malignant masses [253]. Quaia et al. used a five-point scale that ranged from definitely benign (1) to definitely malignant (5). Lesions were categorized based on the presence of individual or combined vascular characteristics including septal enhancement, peripheral wall enhancement, nodule enhancement, and thickening of the septa, wall, or nodules [258]. Others have adopted this grading scale to assess the performance of CEUS imaging [259]. Nicolau et al. have presented an alternative list of modifications to the Bosniak criteria for CEUS imaging where the features at each CEUS level can be related to CT enhancement and morphological features at the same level [265,266]. A different group reported three classes (A-C) that evaluated features including septal enhancement, nodule enhancement, or the presence of solid enhancing components to determine benignity or malignancy [260]. Lastly, Chang et al. used the Bosniak criteria with only minor adaptations that clarified internal

echogenicity [261]. Our criteria was similarly aligned to the above reported criteria and incorporated septal enhancement, nodular enhancement, solid components, and thickening as important features for determining lesion malignancy (Table 6.1). The proposed CEUS modifications in our work and prior studies suggests that Bosniak criteria alone insufficiently describe CEUS vascular features used to diagnose complex kidney masses. With CEUS characterization of complex kidney lesions on the rise, there is sufficient data to advocate for the generation of CEUS-specific Bosniak criteria. The success of CEUS-specific LI-RADS criteria for diagnosing hepatocellular carcinoma further supports the implementation of standardized CEUS-specific Bosniak criteria for diagnosing complex lesions [267–269]. Agreeing upon Bosniak criteria for CEUS would likely improve the diagnostic performance of this modality, but this conjecture would need to be validated through further study. However, evidence from the most recent Bosniak update does appear to support this conclusion. The 2019 update to the Bosniak criteria included MRI-specific criteria [270], which when compared to the old 2005 criteria by Bai et al. revealed a slight increase in sensitivity (84% to 89%) and significant increase in specificity (68% to 83%) for the new criteria compared to the old criteria [246]. Bai et al. also found that reader experience carried less weight with the updated criteria. These findings align with our assumption that standardizing CEUS criteria should improve diagnostic accuracy and may reduce the effect of other factors, such as reader experience.

6.4.3 Reader Agreement and Experience

Reader concordance was assessed using Bowker’s symmetry test to determine the level of agreement between readers, where *P*-values closer to one indicated larger agreement between two readers. The two least experienced readers had the highest inter-reader agreement, while the most experienced reader had the least agreement with all other readers. A similar trend was

observed by Quaia et al., where reader agreement decreased for increasing difference in experience [258]. Years of reader experience interpreting CEUS images may have limited the outcomes of our study. Here, reader experience with CEUS imaging ranged from 0.25-3 years at the time the reads were completed. This is lower than the range of reader experience for studies where both high sensitivity and specificity were reported [253,258,260,265]. In these studies, radiologist experience interpreting CEUS images ranged mostly from 4-10 years [253,258,260,265], with one study also including a radiologist with only 2 years experience [258]. It has been suggested that lack of reader experience could contribute to lesion upgrading compared to more familiar CT and MRI techniques [261], which would result in lower overall specificity and PPV. Reader experience was not controlled for in our study and minimal CEUS training was provided, which disadvantaged readers with less experience [263]. We would expect reader accuracy to improve with additional training and with the establishment of CEUS-specific Bosniak criteria, since for CT and MRI it has been demonstrated that accuracy was influenced by limitations within the Bosniak criteria [242,243,246,270]. Both these issues may have contributed to the lower specificity and PPV in our malignancy analysis, compared to previous reports. Interestingly, the most experienced reader for our study only labeled 5 lesions as indeterminate, while the remaining readers labeled 9 or more as indeterminate. Reader agreement and confidence making a diagnosis (number marked indeterminate) may indicate how experience influences the accurate assessment of kidney lesions by CEUS. The majority of these lesions marked indeterminate by readers were benign by pathology or follow-up imaging. For clinical decision-making reader upstaging of benign lesions may result in greater rates of intervention or additional imaging. False-positive results, from lesion upstaging or influenced by more sensitive imaging modalities (MRI, CEUS) can negatively impact case management and

result in surgical overtreatment [244,270–272]. Adapting criteria to account for the more sensitive modality of CEUS offers a partial solution. Alternatively, to reduce unnecessary intervention, recent research favors conservative management of kidney lesions, even potential malignancies since some kidney cancer subtypes are slow growing and often indolent [270,272,273]. The result is a shift towards more surveillance and less intervention, particularly with smaller lesions [273,274]. Further, some kidney masses, such as Bosniak IIF lesions, may require multiple examinations to diagnose. Reducing the cost, patient discomfort, and exposure to radiation are important considerations when repeat imaging is required [248,255]. The low cost, safety, accessibility, and portability of CEUS all favor this technology for the long-term management of kidney lesions, particularly in patients with few other imaging options.

6.4.4 Characterizing Lesions in the Presence of Kidney Disease

To our knowledge, few studies have previously assessed the use of CEUS in patients with kidney dysfunction. Studies by Zarzour et al., Sawhney et al., and Chang et al., have either included a subset of patients with renal insufficiency or have compared diagnostic performance in patients with and without CKD. The study by Sawhney et al. included lesions from many different organs (liver, kidney, pancreas, bowel, etc) and was therefore not specific to the kidney. The study population included patients with abnormal kidney function, but performance metrics were not provided according to kidney function. Overall CEUS accuracy was reported as 89% for correctly characterizing lesion pathology in the kidney [262]. The patient population by Zarzour et al. included 80 patients with $\text{eGFR} < 60 \text{ mL/min/1.73 m}^2$, and 18 that had ESKD, with undetermined overlap between the ESKD and eGFR groups. According to the authors, CEUS was able to provide a definitive (either malignant or benign) diagnosis of previously indeterminate lesions in 100% (18/18) of the patients with ESKD and 95% (76/80) of the

patients with $\text{eGFR} < 60 \text{ mL/min/1.73 m}^2$. However, the actual accuracy of these diagnoses compared to a reference standard was not provided. The reported sensitivity (100%) and specificity (85.7%) only included 41 lesions (of 94) that met the reference standard criteria of tissue pathology or follow-up imaging > 1 year, and did not include a breakdown of patient demographics for the included lesions [260]. When considering the outcomes from Zarzour et al. and Sawhney et al., our results are less pronounced, but it is difficult to make a direct and accurate comparison due to differences in study design, assessment criteria, and final reported metrics. However, Chang et al. assessed the diagnostic accuracy of CEUS in patients with and without CKD. In comparison, our work improved upon the specificity previously determined by Chang et al. in a patient population with CKD [261]. The authors reported high sensitivity (96%) and moderate specificity (50%) in CKD patients and also assessed performance metrics by CKD severity, noting a decrease in sensitivity and specificity between early ($\text{eGFR} \geq 30 \text{ mL/min/1.73 m}^2$) and advanced CKD ($\text{eGFR} < 30 \text{ mL/min/1.73 m}^2$). From early to advanced CKD, sensitivity decreased from 100% to 83% while specificity dropped from 72% to 41% for both readers combined [261]. These results suggest that the decrease in CEUS performance was influenced by disease severity and illustrate the challenge of accurately characterizing kidney lesions in the presence of disease. Further study is necessary to confirm this theory, however if true, it may help explain the lower performance outcomes reported here. For our study, patients with recorded eGFR values (39/53), averaged $37.79 \pm 17.96 \text{ mL/min/1.73 m}^2$ with 15 cases reporting $\text{eGFR} < 30 \text{ mL/min/1.73 m}^2$. The 14 remaining patients all had ESKD. Based on results from Chang et al., the presence of advanced CKD in over half of our patients may have complicated diagnostic interpretation in these patients.

For patients with advanced CKD, CEUS is emerging as a useful tool. The results discussed in this chapter point to this modality serving an important role in the management of kidney lesions in patients with kidney dysfunction. Reasonable sensitivity and specificity were achieved by readers in this study, and most promising was the high NPV (90%) when assessing malignant diagnoses and correspondingly high PPV (91%) for benign diagnoses. Factors such as reader experience, classification criteria, and disease severity present challenges to the accurate diagnosis of kidney lesions with CEUS, however these limitations could be addressed with further study. Development of CEUS-specific Bosniak criteria may improve diagnostic accuracy and continued investigation into use of flash-replenishment CEUS imaging to diagnose lesions should be considered to provide an alternative lower cost, widely available imaging modality for patients precluded from conventional CT or MRI imaging, such as those with kidney dysfunction.

CHAPTER 7: DISCUSSION AND CONCLUSIONS

7.1 Overview

The timely characterization of disease state, whether in response to therapy or in comparison to conventional measures, impacts clinical decision-making and can vastly improve patient outcomes. Ultrasound imaging offers a safe, reliable, and non-invasive method for characterizing disease. In this dissertation, disease characterization using contrast ultrasound imaging was applied to both oncology and renal health. Specifically, this work focused on furthering the clinical translation of contrast ultrasound imaging techniques that facilitate earlier assessment of response to cancer therapy and early detection of kidney disease.

7.2 Early Assessment of Response to Cancer Therapy

The first hypothesis of this work was that ultrasound molecular imaging could be used to monitor response to therapy more accurately than tumor volume. The ability of USMI to provide faster feedback on response to anti-angiogenic therapy has been well established for *in vivo* imaging [126,127,151], however its ability to evaluate response to alternate therapies has not been fully explored. In Chapter 3, we successfully demonstrated that in a rodent tumor model, USMI could identify tumor response to fractionated radiation therapy. Results showed that group changes in vascular expression in response to fractionated radiation therapy occurred on a similar timescale as group changes in tumor volume. Further, results indicated that tumor response to fractionated radiation therapy occurs in a dose-dependent manner. These insights support further study to address the challenges and limitations faced by applying USMI

techniques to RT. For example, UCAs have been shown to result in a radiosensitizing effect when delivered both prior to and following RT [185,205]. In this study, CEUS imaging ceased 24 hours before RT as well as during the 5 day treatment window, and did not commence again until at least 12 hours after RT to minimize the influence of UCA delivery on tumor response. However, to capture initial alterations in molecular expression, USMI should be performed repeatedly within the first few days following the start of treatment. Studies investigating the influence of frequent CEUS imaging on therapeutic response should be conducted to enable concurrent fractionated therapy and imaging. Ultimately, this knowledge will improve the response time and accuracy of USMI when monitoring fractionated RT. Additionally, although changes in microvascular expression have been linked to therapeutic response, further characterization of this vascular response are necessary to improve the sensitivity and efficacy of USMI. To our knowledge, the use of USMI to monitor response to fractionated radiation therapy has not been previously studied. However, this ability would greatly increase the utility of USMI. The work described in Chapter 3 serves as a proof-of-concept for using USMI to monitor and predict response to fractionated radiotherapy and supports further study into fully elucidating the vascular response to radiation therapy.

To further contribute to the clinical translation of USMI, in Chapter 4, we assessed the feasibility of using USMI to monitor anti-angiogenic treatment response in a canine patient population. The results from this study revealed that changes in molecular expression have the potential to identify tumor response prior to changes in tumor volume, but also exposed the barriers that remain before USMI becomes clinically viable. In this study, patient retention proved to be a serious challenge and the therapeutic approach a major disadvantage. Careful

consideration of the treatment regimen and a greater understanding of how USMI will best fit into the clinical decision-making tree will help tailor this technique to increase its value.

In the past, low numbers of bound microbubbles has hindered USMI. Here, acoustic radiation force, buried ligand architecture, and microbubble size-selection were all utilized to improve the sensitivity of ultrasound molecular imaging. These enhancements were previously optimized for *in vivo* imaging [138,145,148] and were modified where appropriate for use in a clinically relevant population. Previously, ARF had been optimized for imaging tumors with an average diameter around 1 cm. Here, ARF was optimized for a range of tumor sizes between 2-5 cm to prepare for clinical translation. Determining ideal ARF pushes across a range of depths was essential, not only to maximize microbubble accumulation along the vessel wall, but also to facilitate ligand-receptor interaction by exposing the shielded targeting ligand. Due to the utilization of BLA, ineffective ARF sequences would result in reduced contrast sensitivity. In practice, tumor diameter ranged from 2.5-10.8 cm and as such contrast sensitivity likely decreased with increasing size. When considering tumor characteristics, in comparison to clinically relevant populations, small rodent tumor models offer a relatively stable and homogeneous environment. Given the drastic increase and wide range of tumor sizes encountered across canine participants, further optimization of ARF parameters should be pursued before implementing USMI in the clinic.

In addition to contrast sensitivity, the lower resolution of clinical imaging systems using conventional contrast ultrasound imaging techniques, limits the amount of functional information that can be acquired. Combining USMI with imaging techniques that improve vessel visualization, such as acoustic angiography [275,276], or that by-pass system resolution limits, such as ultrasound localization microscopy (ULM) [277], should improve the sensitivity and

accuracy of USMI. Additionally, these techniques offer the advantage of superimposing functional information on anatomical features. However, to truly advance USMI for longitudinal monitoring of patient response, future work must also address accelerated blood clearance (ABC) resulting from repeated dosing. This phenomenon destabilizes USMI by interfering with the accurate representation of receptor density. USMI relies on ascribing changes in measured signal to alterations in vascular receptor expression. Unfortunately, accelerated clearance of PEGylated particles with repeated dosing, causes inconsistent MB clearance, hindering the ability to attribute signal changes to therapeutic response. For *in vivo* imaging, pre-dosing animals with PEG to generate stable MB clearance curves provides a possible solution to overcome the detrimental effects of accelerated clearance. Alternatively, the development of a microbubble formulation that does not elicit the ABC effect (i.e. a stable shell without PEG) is another potential solution. Although demonstrated in small animal models, how the ABC effect presents in larger animal models and clinical populations remains unknown. Additional questions related to the influence of dosing frequency on clearance rate, imaging interval on the magnitude and persistence of the immune response, and the exploration of possible mechanisms to recover circulation time should also be considered to understand the overall impact of accelerated clearance on the use of USMI. In spite of the present challenges, ultrasound molecular imaging has demonstrated the potential to provide faster and more accurate feedback regarding response to treatment. Future work that addresses current limitations will further the clinical translation of ultrasound molecular imaging, ultimately supplying a technique to improve patient care.

7.3 Early Detection of Kidney Disease and Characterization of Related Complications

The second hypothesis of this work was that contrast-enhanced ultrasound could be used to detect kidney disease earlier than conventional clinical markers and differentiate healthy

from disease kidneys through changes in renal perfusion. In Chapter 5, we demonstrated that CEUS perfusion parameters have the potential to classify kidney health in a non-human primate model. Features calculated from refill kinetics according to spatial location were used in a regression model to differentiate NHP cohorts by health status. Of the three perfusion parameters, PI features performed best at distinguishing between experimental groups. One setback was the lack of progression to kidney disease in the selected NHPs. DKD occurs naturally in this population, contributing to their clinical relevance, however in the small sample used in this study no DKD was present. To effectively demonstrate that CEUS perfusion imaging can identify DKD onset and progression a controlled setting with experimental cohorts composed of subjects both with and without confirmed DKD would need to be evaluated.

Another limiting factor was the variable occurrences of hypertension and differences in metabolic state for each NHP that could influence renal perfusion. Again this suggests that evaluating the current hypothesis in a more regulated environment would be beneficial and provide the ability to determine how DKD alone influences blood flow. However, it is still important to understand how components such as hypertension, other comorbidities, and metabolic state influence kidney perfusion in order to accurately attribute changes in perfusion to the onset of DKD. Combining blood flow markers with clinical measures and metabolomics or proteomics in a weighted model may offer a comprehensive method for evaluating kidney health. In fact, weighting by blood pressure enabled the ability to isolate microcirculatory changes that may indicate DKD [48]. In addition to weighting by clinical metrics, ultrasound localization microscopy may further improve the ability to isolate and detect kidney disease. Super resolution imaging not only provides detailed maps of kidney microvasculature, but may also enable the detection of previously imperceptible areas with impaired flow [278]. The superior resolution

offered using ULM imaging techniques over conventional CEUS imaging methods, may offer the ability to detect more subtle alterations in microvascular flow, which could be the key to earlier diagnosis of kidney disease.

Despite the limitations encountered in work, our pilot study demonstrated that CEUS perfusion parameters have the potential to identify changes in kidney health, specifically highlighting PI as the parameter with the most value. Early diagnosis of DKD will help inform clinical decision-making in order to offset disease progression, preserve kidney function, and tailor treatment to improve patient outcomes. This would be particularly beneficial since kidney disease increases the risk of developing additional complications, such as cardiovascular disease and cancer. Whereas CT and MRI contrast agents are contraindicated in patients with kidney dysfunction, UCAs are safe for use in compromised kidneys. Nevertheless, very few studies have validated the diagnostic accuracy of CEUS imaging for detecting malignant kidney lesions in patients with known CKD. In Chapter 6, we evaluated the ability of CEUS to accurately diagnose renal complications in the presence of chronic kidney disease. Our results demonstrated that in patients with CKD, CEUS may serve as a valuable tool for active surveillance. The necessity of preserving renal function in patients with CKD has led to an increase in the use of kidney sparing approaches to treatment. When utilizing active surveillance as a treatment option, repeated imaging with CEUS provides a safer alternative in patients with renal dysfunction, offering an advantage over other contrast imaging modalities (CT, MRI).

APPENDIX A: CONTRAST ULTRASOUND IMAGING CAPTURES LIGHT-FACILITATED DRUG RELEASE

A.1 Overview

Chemotherapeutics are commonly used to treat solid and liquid tumors, but the effectiveness of these agents is limited by the need to minimize off-target effects and systemic toxicity [279,280]. As such, delivery vehicles that facilitate localized drug release at therapeutically relevant doses while sparing healthy tissue are highly sought after [281–283]. Nanoparticles are an attractive drug carrier option and considerable work has been done to improve circulation time and develop release mechanisms to improve site specificity. External triggers, such as light, have been used to selectively release a therapeutic payload [284]. In fact, a wide variety of light responsive agents have been reported [285–287], however there is still a pressing need for long-lasting, widely-distributed phototherapeutic agents responsive to stimulation by light. RBCs are biocompatible agents with a long circulation time and high carrying capacity [288–290] that can be modified to facilitate light-specific drug release [291].

Here site-specific delivery of RBCs loaded with a taxane derivative (docetaxel) was demonstrated using light-facilitated release in a tumor model and was characterized using contrast ultrasound imaging techniques. Previously, intravital imaging was used to observe light-facilitated drug release, but was limited to a small field of viewing showing only single vessels. Ultrasound transducers have a larger footprint, the ability to acquire volumetric data, and ultrasound contrast agents are true blood pool agents, offering the ability to capture global response across the tumor volume. We hypothesized that vascular disruption caused by light-facilitated docetaxel release would be observable by contrast ultrasound imaging through increased microbubble retention at the disruption site.

A.2 Methods

The tumor microenvironment and surrounding vasculature in homozygous Nu/Nu mice bearing SVR angiosarcomas were visualized using dual-frequency imaging techniques [292]. Volumetric ultrasound data was acquired before treatment (baseline), immediately after treatment ($t = 0$), at 20 minutes post-treatment, and at 40 minutes post-treatment using microbubbles as contrast agents (Figure A.1). Animals received an injection of either drug-loaded mRBCs followed by light treatment, drug-loaded mRBCs without light treatment (dark), OH₂-loaded mRBCs (scaffold) followed by light treatment, or mock-loaded mRBCs with light treatment. Light-treated animals were exposed to a 655 nm 100 mW laser that illuminated the tumor for a total of 5 minutes. Ultrasound data was analyzed in MATLAB® (MathWorks, Natick, MA, USA) to assess microbubble retention in each treatment group. Statistically significant differences between treatment cohorts were assessed using a two-way ANOVA evaluating time and experimental group, followed by post-hoc testing using Dunnett's multiple comparison to assess differences between imaging time points within a treatment cohort.

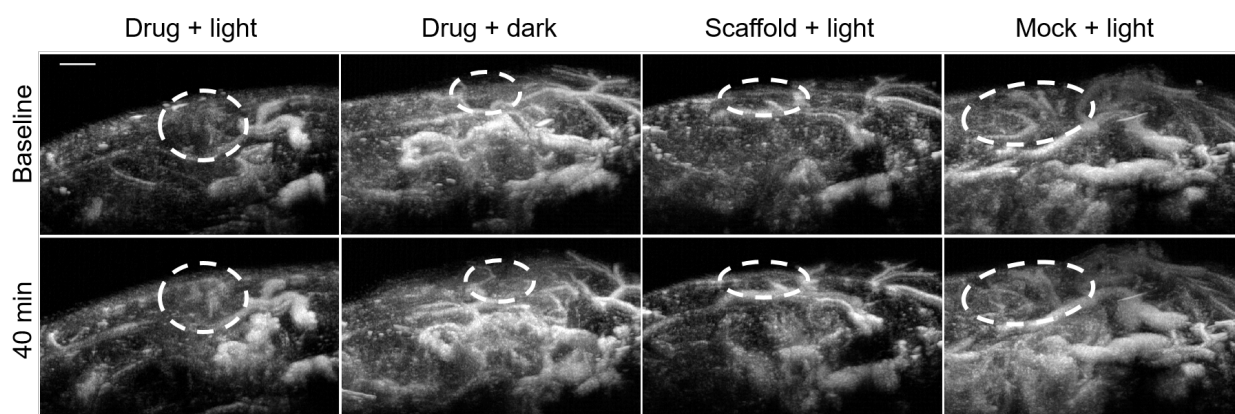


Figure A.1 Maximum intensity projection contrast ultrasound images at baseline imaging and 40 minutes following treatment in each experimental cohort; scale bar = 2.5 mm.

A.3 Results and Summary

Results obtained with drug-loaded mRBCs and light treatment found that microbubble retention (calculated as the amount of contrast agent in a region normalized to baseline measures) in the tumor was more than double the initial baseline retention 40 min after light treatment ($P < 0.01$) (Figure A.2). In contrast, mice treated in the dark with drug-loaded mRBCs, mice treated with light and scaffold-loaded mRBCs, and mice treated with light and mock-loaded mRBCs did not display any significant microbubble retention at the tumor sites ($P > 0.05$) (Figure A.2). The increase in contrast agent pooling in the tumor after treatment with drug-loaded mRBCs and light was consistent with the hypothesis that blood vessel integrity would be compromised by light-facilitated release of docetaxel.

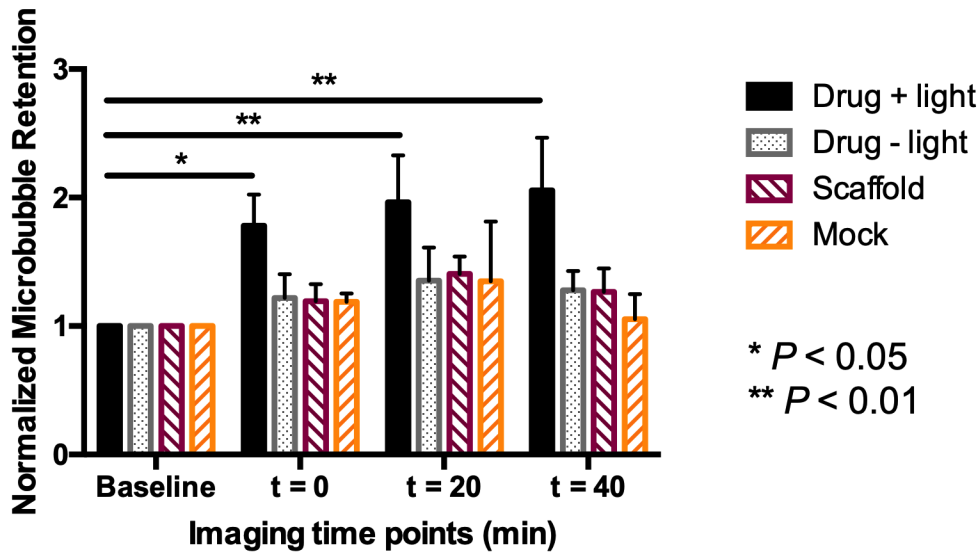
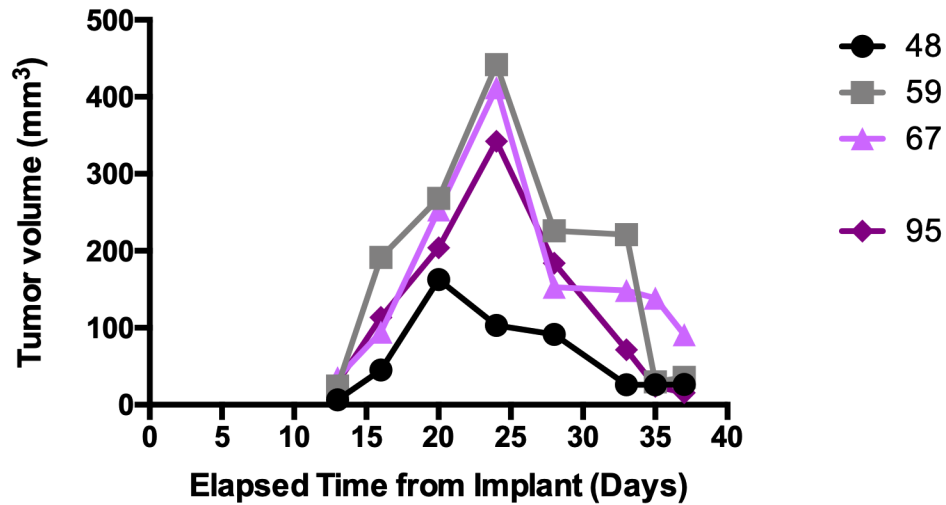


Figure A.2 Quantitative assessment of microbubble retention in the tumors of each experimental cohort normalized to baseline retention values. Significantly higher retention was observed immediately following treatment (t = 0), 20 minutes following treatment, and 40 minutes following treatment compared to baseline retention for the drug-loaded RBCs with light (n = 12). In comparison, none of the other experimental cohorts, drug-loaded RBCs without light (n = 12), scaffold-loaded RBCs with light (n = 12), and mock-loaded RBCs with light (n = 4), displayed significant retention compared to baseline values.

Here, contrast ultrasound imaging was able to validate light-facilitated drug release using RBCs as the delivery vehicle. Our collaborators went on to demonstrate that these results support the use of RBC-based phototherapeutics as a long-lasting, high payload carrier, biocompatible, localized drug delivery method with light exerting both spatial and temporal control over release mechanisms offering unique advantages for precision delivery of chemotherapeutic agents [293].

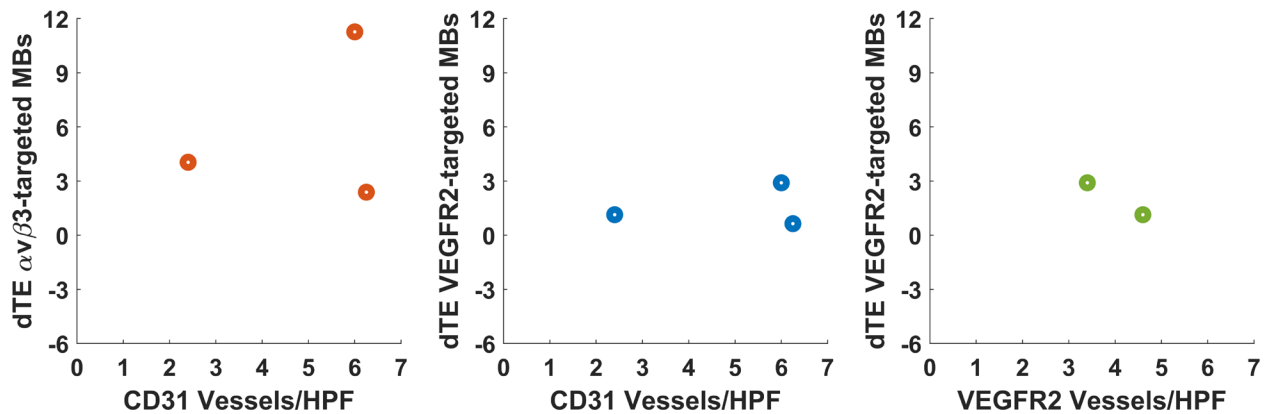
APPENDIX B: SUPPLEMENTAL FIGURES

B.1 Supplemental Figure for Chapter 3

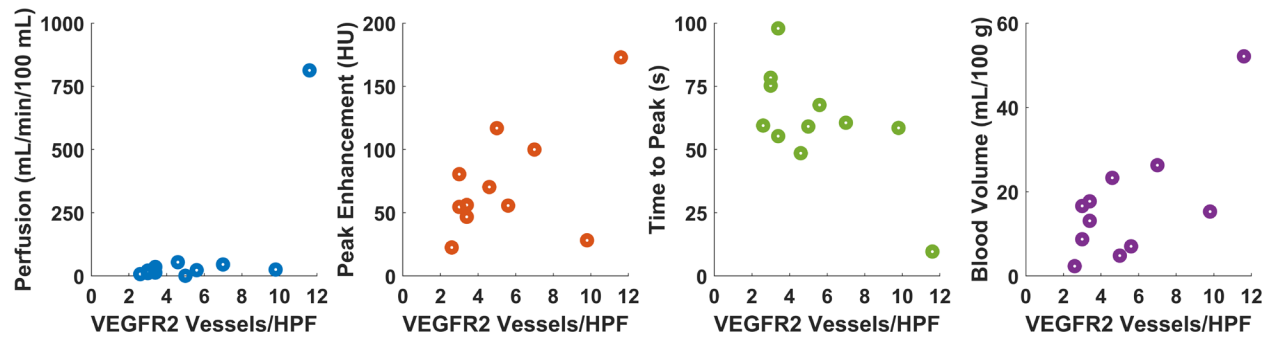


Supplemental Figure B.1 Tumor growth in the 5 Gy dosing study cohort for tumors that responded to treatment ($n = 4$). Modified from Figure 3.10 by removing the non-responding tumors ($n = 1$) for improved visualization of tumor response.

B.2 Supplemental Figures for Chapter 4



Supplemental Figure B.2 Microbubble targeting compared to available measures of CD31 and VEGFR2 expression.



Supplemental Figure B.3 Correlation between VEGFR2 expression and DCE-CT metrics after removing outlier case; n = 11.

APPENDIX C: SUPPLEMENTAL TABLES

C.1 Supplemental Tables for Chapter 3

Supplemental Table C.1 Pairwise comparisons (P -values) of background tissue AUC between imaging days for each bubble

	A7R	cRGD	cRAD	DBCO
0 vs. 3	< 0.0001	< 0.0001	< 0.0001	< 0.0001
0 vs. 7	< 0.0001	< 0.0001	< 0.0001	< 0.0001
0 vs. 10	< 0.0001	< 0.0001	< 0.0001	< 0.0001
0 vs. 14	< 0.0001	< 0.0001	< 0.0001	< 0.0001
0 vs. 17	< 0.0001	< 0.0001	< 0.0001	< 0.0001
0 vs. 21	< 0.0001	< 0.0001	< 0.0001	0.1018
0 vs. 24	< 0.0001	0.0333	0.0002	0.8532
0 vs. 28	0.0063	0.6528	0.0192	0.9466
3 vs. 7	0.9999	0.9944	0.999	0.9995
3 vs. 10	0.993	0.9356	0.9975	> 0.9999
3 vs. 14	0.9963	0.9839	0.8512	> 0.9999
3 vs. 17	0.9997	0.8365	0.8247	0.9534
3 vs. 21	0.9984	> 0.9999	0.9739	0.0345
3 vs. 24	0.9977	0.9559	0.9964	0.004
3 vs. 28	0.0625	0.0193	0.0629	< 0.0001
7 vs. 10	> 0.9999	> 0.9999	> 0.9999	> 0.9999
7 vs. 14	> 0.9999	> 0.9999	0.9998	> 0.9999
7 vs. 17	> 0.9999	> 0.9999	0.9996	0.8005
7 vs. 21	0.975	0.9884	0.8247	0.0294
7 vs. 24	0.9734	0.6899	0.9333	0.0038
7 vs. 28	0.0687	0.0085	0.0437	< 0.0001
10 vs. 14	> 0.9999	> 0.9999	0.9995	> 0.9999
10 vs. 17	> 0.9999	> 0.9999	0.9991	0.9155
10 vs. 21	0.8461	0.9104	0.7141	0.0344
10 vs. 24	0.8665	0.4031	0.8896	0.0041
10 vs. 28	0.008	0.0005	0.0121	< 0.0001
14 vs. 17	> 0.9999	0.9999	> 0.9999	0.7885
14 vs. 21	0.8631	0.9713	0.2414	0.01
14 vs. 24	0.8855	0.5247	0.5149	0.0011
14 vs. 28	0.005	0.0005	0.0004	< 0.0001
17 vs. 21	0.9444	0.8049	0.2179	0.4483
17 vs. 24	0.9504	0.2608	0.4847	0.0903

17 vs. 28	0.0117	< 0.0001	0.0003	0.0029
21 vs. 24	> 0.9999	0.9863	> 0.9999	0.9875
21 vs. 28	0.45	0.0655	0.6987	0.7844
24 vs. 28	0.696	0.76	0.7291	> 0.9999

Supplemental Table C.2 Pairwise comparisons (*P*-values) of kidney cortical AUC between imaging days for each bubble

	A7R	cRGD	cRAD	DBCO
0 vs. 3	< 0.0001	< 0.0001	< 0.0001	0.0017
0 vs. 7	< 0.0001	< 0.0001	< 0.0001	< 0.0001
0 vs. 10	< 0.0001	< 0.0001	< 0.0001	< 0.0001
0 vs. 14	< 0.0001	< 0.0001	< 0.0001	< 0.0001
0 vs. 17	< 0.0001	< 0.0001	< 0.0001	< 0.0001
0 vs. 21	< 0.0001	< 0.0001	< 0.0001	< 0.0001
0 vs. 24	< 0.0001	< 0.0001	< 0.0001	< 0.0001
0 vs. 28	0.0019	0.0078	< 0.0001	0.1093
3 vs. 7	0.28	0.2081	0.1662	0.65
3 vs. 10	0.1845	0.002	0.1275	0.1551
3 vs. 14	0.9829	0.9845	0.1224	0.332
3 vs. 17	0.3057	0.0408	< 0.0001	0.3806
3 vs. 21	0.9707	0.7245	0.1422	0.9828
3 vs. 24	0.9866	0.742	0.0944	0.7786
3 vs. 28	0.8716	0.9278	> 0.9999	0.9655
7 vs. 10	> 0.9999	0.9869	> 0.9999	0.9999
7 vs. 14	0.8149	0.721	> 0.9999	> 0.9999
7 vs. 17	> 0.9999	> 0.9999	0.9311	> 0.9999
7 vs. 21	0.9121	0.9871	> 0.9999	0.9931
7 vs. 24	0.947	0.9981	> 0.9999	> 0.9999
7 vs. 28	0.013	0.0123	0.4091	0.1357
10 vs. 14	0.7638	0.048	> 0.9999	0.9998
10 vs. 17	> 0.9999	0.9709	0.7364	0.9995
10 vs. 21	0.8949	0.4096	> 0.9999	0.8236
10 vs. 24	0.9427	0.682	> 0.9999	0.9988
10 vs. 28	0.004	< 0.0001	0.3824	0.0087
14 vs. 17	0.9166	0.413	0.5046	> 0.9999
14 vs. 21	> 0.9999	0.9968	> 0.9999	0.9698
14 vs. 24	> 0.9999	0.9937	0.9995	> 0.9999
14 vs. 28	0.2612	0.356	0.4019	0.0228
17 vs. 21	0.977	0.9481	0.7075	0.9801

17 vs. 24	0.9898	0.9921	0.9786	> 0.9999
17 vs. 28	0.007	0.0006	0.0013	0.029
21 vs. 24	> 0.9999	> 0.9999	> 0.9999	0.9987
21 vs. 28	0.2651	0.0946	0.4107	0.4985
24 vs. 28	0.4275	0.1382	0.2739	0.2119

Supplemental Table C.3 Pairwise comparisons (*P*-values) of kidney medullary AUC between imaging days for each bubble

	A7R	cRGD	cRAD	DBCO
0 vs. 3	< 0.0001	< 0.0001	< 0.0001	< 0.0001
0 vs. 7	< 0.0001	< 0.0001	< 0.0001	< 0.0001
0 vs. 10	< 0.0001	< 0.0001	< 0.0001	< 0.0001
0 vs. 14	< 0.0001	< 0.0001	< 0.0001	< 0.0001
0 vs. 17	< 0.0001	< 0.0001	< 0.0001	< 0.0001
0 vs. 21	< 0.0001	< 0.0001	< 0.0001	< 0.0001
0 vs. 24	< 0.0001	< 0.0001	< 0.0001	< 0.0001
0 vs. 28	< 0.0001	0.0006	< 0.0001	0.0295
3 vs. 7	0.9828	0.7735	0.7171	0.9558
3 vs. 10	0.9081	0.4073	0.745	0.9254
3 vs. 14	0.9998	0.9984	0.5947	0.9925
3 vs. 17	0.9897	0.7574	0.1687	0.9855
3 vs. 21	> 0.9999	> 0.9999	0.9941	0.289
3 vs. 24	> 0.9999	> 0.9999	0.9986	0.8933
3 vs. 28	0.2579	0.0138	0.4213	0.0002
7 vs. 10	> 0.9999	> 0.9999	> 0.9999	> 0.9999
7 vs. 14	0.9997	0.9788	> 0.9999	> 0.9999
7 vs. 17	> 0.9999	> 0.9999	> 0.9999	0.5338
7 vs. 21	0.9983	0.8233	0.9913	0.0484
7 vs. 24	0.9932	0.6906	0.993	0.3721
7 vs. 28	0.0663	0.0003	0.016	< 0.0001
10 vs. 14	0.9945	0.8386	> 0.9999	> 0.9999
10 vs. 17	> 0.9999	0.9993	0.9977	0.3824
10 vs. 21	0.9846	0.5071	0.9974	0.0176
10 vs. 24	0.9658	0.3888	0.998	0.2693
10 vs. 28	0.0111	< 0.0001	0.0089	< 0.0001
14 vs. 17	> 0.9999	0.9891	0.9983	0.6111
14 vs. 21	> 0.9999	0.9991	0.9921	0.037
14 vs. 24	> 0.9999	0.9854	0.9946	0.4442
14 vs. 28	0.0755	0.0011	0.0024	< 0.0001

17 vs. 21	0.9996	0.8303	0.8093	0.8658
17 vs. 24	0.9973	0.6937	0.8719	0.9996
17 vs. 28	0.0243	< 0.0001	0.0001	0.0074
21 vs. 24	> 0.9999	> 0.9999	> 0.9999	0.9991
21 vs. 28	0.2062	0.0298	0.1003	0.5165
24 vs. 28	0.5254	0.2227	0.2396	0.2362

Supplemental Table C.4 Pairwise comparisons (*P*-values) of liver AUC between imaging days for each bubble

	A7R	cRGD	cRAD	DBCO
0 vs. 3	> 0.9999	0.9884	0.9986	0.999
0 vs. 7	0.9977	0.9942	0.943	0.9971
0 vs. 10	0.1843	0.9985	0.1795	0.3191
0 vs. 14	0.1946	0.8116	0.0074	0.0024
0 vs. 17	0.2417	0.2964	< 0.0001	0.0155
0 vs. 21	0.9868	0.9109	0.1997	0.9643
0 vs. 24	> 0.9999	> 0.9999	0.6671	0.8749
0 vs. 28	> 0.9999	0.964	0.9719	> 0.9999
3 vs. 7	0.9876	> 0.9999	0.9991	> 0.9999
3 vs. 10	0.1039	0.798	0.5632	0.7363
3 vs. 14	0.1054	0.2139	0.0685	0.0252
3 vs. 17	0.1358	0.0261	0.0001	0.1122
3 vs. 21	0.9494	0.3741	0.5971	0.9999
3 vs. 24	0.9997	0.9998	0.9463	0.9929
3 vs. 28	> 0.9999	> 0.9999	> 0.9999	0.9999
7 vs. 10	0.8681	0.887	0.9842	0.9518
7 vs. 14	0.9121	0.4323	0.6849	0.2293
7 vs. 17	0.9381	0.1159	0.0436	0.4868
7 vs. 21	> 0.9999	0.5696	0.9879	> 0.9999
7 vs. 24	> 0.9999	0.9998	> 0.9999	0.9997
7 vs. 28	0.9982	> 0.9999	> 0.9999	0.9992
10 vs. 14	> 0.9999	0.9979	0.996	0.8966
10 vs. 17	> 0.9999	0.8568	0.2907	0.9923
10 vs. 21	0.84	0.9996	> 0.9999	0.9716
10 vs. 24	0.6521	0.9959	> 0.9999	0.9997
10 vs. 28	0.2213	0.7002	0.8438	0.441
14 vs. 17	> 0.9999	0.9967	0.7461	0.9998
14 vs. 21	0.8897	> 0.9999	0.9941	0.197
14 vs. 24	0.7129	0.8367	0.9496	0.6479

14 vs. 28	0.2387	0.1579	0.2397	0.0064
17 vs. 21	0.9236	0.9951	0.2647	0.4773
17 vs. 24	0.7651	0.415	0.187	0.8902
17 vs. 28	0.2902	0.0183	0.0017	0.0347
21 vs. 24	> 0.9999	0.9083	> 0.9999	> 0.9999
21 vs. 28	0.9898	0.2903	0.8659	0.9859
24 vs. 28	> 0.9999	0.9985	0.9946	0.9279

Supplemental Table C.5 Pairwise comparisons (*P*-values) of elimination rate in background tissue between imaging days for each bubble

	A7R	cRGD	cRAD	DBCO
0 vs. 3	< 0.0001	0.0001	0.0002	0.0005
0 vs. 7	< 0.0001	< 0.0001	0.0003	< 0.0001
0 vs. 10	< 0.0001	< 0.0001	0.0003	0.0007
0 vs. 14	< 0.0001	0.0012	0.0003	0.0085
0 vs. 17	< 0.0001	0.0009	0.0009	0.5054
0 vs. 21	< 0.0001	0.0436	0.0531	0.8907
0 vs. 24	0.1102	0.7829	0.6848	> 0.9999
0 vs. 28	0.0039	0.6142	0.3325	0.9974
3 vs. 7	0.1184	0.4831	0.9961	0.8483
3 vs. 10	0.1041	0.3025	> 0.9999	> 0.9999
3 vs. 14	0.9977	0.9999	> 0.9999	0.9979
3 vs. 17	0.558	> 0.9999	> 0.9999	0.2961
3 vs. 21	0.1477	0.9564	0.9635	0.1543
3 vs. 24	0.0006	0.3935	0.5622	0.0436
3 vs. 28	0.0002	0.1654	0.4507	0.0154
7 vs. 10	> 0.9999	> 0.9999	0.9998	0.9514
7 vs. 14	0.0202	0.2351	0.9946	0.4581
7 vs. 17	0.0005	0.2622	0.9739	0.0185
7 vs. 21	< 0.0001	0.0761	0.7128	0.0085
7 vs. 24	< 0.0001	0.0073	0.2769	0.0022
7 vs. 28	< 0.0001	0.0011	0.2062	0.0006
10 vs. 14	0.013	0.1079	> 0.9999	0.9893
10 vs. 17	0.0002	0.1257	0.9996	0.2533
10 vs. 21	< 0.0001	0.027	0.9136	0.1318
10 vs. 24	< 0.0001	0.0019	0.4677	0.0373
10 vs. 28	< 0.0001	0.0001	0.3682	0.0151
14 vs. 17	0.9518	> 0.9999	> 0.9999	0.7834
14 vs. 21	0.5367	0.9984	0.9708	0.5421
14 vs. 24	0.0068	0.6765	0.5885	0.2062

14 vs. 28	0.0041	0.4247	0.4809	0.1238
17 vs. 21	0.9936	0.9971	0.9951	> 0.9999
17 vs. 24	0.1321	0.6397	0.7459	0.9481
17 vs. 28	0.1459	0.383	0.6742	0.953
21 vs. 24	0.6252	0.9722	0.9926	0.9977
21 vs. 28	0.7606	0.9237	0.9946	0.9992
24 vs. 28	> 0.9999	> 0.9999	> 0.9999	> 0.9999

Supplemental Table C.6 Pairwise comparisons (*P*-values) of elimination rate in background tissue between bubbles on each imaging day

Day	A7R vs. cRGD	A7R vs. cRAD	A7R vs. DBCO	cRGD vs. cRAD	cRGD vs. DBCO	cRAD vs. DBCO
0	> 0.9999	0.8648	0.9551	0.8823	0.9643	0.9938
3	0.0003	< 0.0001	< 0.0001	0.8312	0.8718	0.9998
7	0.0025	< 0.0001	< 0.0001	0.3281	0.7275	0.9123
10	0.0004	< 0.0001	< 0.0001	0.0383	0.0439	> 0.9999
14	0.0007	0.0002	< 0.0001	0.9807	0.7482	0.9262
17	0.0463	0.0051	< 0.0001	0.8798	0.0369	0.2053
21	0.1331	0.0228	0.0002	0.8963	0.168	0.5235
24	0.7078	0.4672	0.0732	0.9808	0.5209	0.7585
28	0.1975	0.1105	0.003	0.9925	0.4188	0.5918

Supplemental Table C.7 Pairwise comparisons (*P*-values) of half-life in background tissue between imaging days for each bubble

	A7R	cRGD	cRAD	DBCO
0 vs. 3	< 0.0001	< 0.0001	< 0.0001	< 0.0001
0 vs. 7	< 0.0001	< 0.0001	< 0.0001	< 0.0001
0 vs. 10	< 0.0001	< 0.0001	< 0.0001	< 0.0001
0 vs. 14	< 0.0001	< 0.0001	< 0.0001	< 0.0001
0 vs. 17	< 0.0001	< 0.0001	< 0.0001	0.0005
0 vs. 21	< 0.0001	< 0.0001	< 0.0001	0.0169
0 vs. 24	< 0.0001	0.0017	< 0.0001	0.6838
0 vs. 28	< 0.0001	0.0002	< 0.0001	0.0141
3 vs. 7	> 0.9999	0.9989	> 0.9999	0.9995
3 vs. 10	> 0.9999	0.9974	> 0.9999	> 0.9999
3 vs. 14	> 0.9999	> 0.9999	> 0.9999	0.9994
3 vs. 17	0.9982	> 0.9999	> 0.9999	< 0.0001
3 vs. 21	0.9997	0.9996	0.9929	< 0.0001
3 vs. 24	0.8718	0.8225	0.3923	< 0.0001

3 vs. 28	0.7539	0.4787	0.2876	< 0.0001
7 vs. 10	> 0.9999	> 0.9999	> 0.9999	0.9998
7 vs. 14	> 0.9999	0.9964	> 0.9999	0.9699
7 vs. 17	0.9906	0.9827	0.998	< 0.0001
7 vs. 21	0.9967	0.9646	0.9602	< 0.0001
7 vs. 24	0.827	0.5782	0.3357	< 0.0001
7 vs. 28	0.7331	0.2871	0.2761	< 0.0001
10 vs. 14	> 0.9999	0.9919	> 0.9999	0.9995
10 vs. 17	0.9847	0.9636	0.9998	< 0.0001
10 vs. 21	0.9953	0.9342	0.9804	< 0.0001
10 vs. 24	0.7699	0.453	0.3467	< 0.0001
10 vs. 28	0.6238	0.1531	0.261	< 0.0001
14 vs. 17	0.9997	> 0.9999	> 0.9999	0.0002
14 vs. 21	> 0.9999	> 0.9999	0.9866	< 0.0001
14 vs. 24	0.9227	0.88	0.3427	< 0.0001
14 vs. 28	0.8422	0.5792	0.2389	< 0.0001
17 vs. 21	> 0.9999	> 0.9999	0.9998	0.9995
17 vs. 24	0.9947	0.9498	0.5928	0.661
17 vs. 28	0.9877	0.7486	0.5077	0.998
21 vs. 24	0.9926	0.987	0.9105	0.9523
21 vs. 28	0.9847	0.9082	0.9094	> 0.9999
24 vs. 28	> 0.9999	> 0.9999	> 0.9999	0.9617

Supplemental Table C.8 Pairwise comparisons (*P*-values) of half-life in background tissue between bubbles on each imaging day

Day	A7R vs. cRGD	A7R vs. cRAD	A7R vs. DBCO	cRGD vs. cRAD	cRGD vs. DBCO	cRAD vs. DBCO
0	0.9983	< 0.0001	0.0191	< 0.0001	0.0115	0.0121
3	0.7125	0.4463	0.5207	0.974	0.9901	0.9994
7	0.9705	0.7762	0.8857	0.9571	0.992	0.996
10	0.959	0.5103	0.4617	0.8126	0.7703	0.9998
14	0.7222	0.6125	0.2626	0.998	0.8622	0.9302
17	0.8802	0.6811	< 0.0001	0.9823	< 0.0001	< 0.0001
21	0.7829	0.3875	< 0.0001	0.9163	< 0.0001	0.0002
24	0.8347	0.3182	< 0.0001	0.8181	0.0002	0.0054
28	0.5066	0.161	< 0.0001	0.8985	0.0006	0.0067

Supplemental Table C.9 Pairwise comparisons (*P*-values) of elimination rate in the cortex between imaging days for each bubble

	A7R	cRGD	cRAD	DBCO
0 vs. 3	0.9308	0.9991	0.9998	0.9903
0 vs. 7	< 0.0001	0.177	0.8733	0.3248
0 vs. 10	< 0.0001	0.0006	0.9981	0.4274
0 vs. 14	0.2879	> 0.9999	> 0.9999	0.9829
0 vs. 17	0.2949	0.9987	> 0.9999	0.9982
0 vs. 21	0.9615	0.9995	0.9982	0.9994
0 vs. 24	0.5326	0.8439	0.9895	0.9992
0 vs. 28	0.9922	0.9681	0.9675	0.9956
3 vs. 7	0.0035	0.4829	0.9832	0.8198
3 vs. 10	< 0.0001	0.0064	> 0.9999	0.9297
3 vs. 14	0.973	> 0.9999	0.9998	> 0.9999
3 vs. 17	0.9748	> 0.9999	0.9863	> 0.9999
3 vs. 21	> 0.9999	> 0.9999	0.9498	> 0.9999
3 vs. 24	0.9891	0.9879	0.9999	> 0.9999
3 vs. 28	> 0.9999	> 0.9999	0.9995	> 0.9999
7 vs. 10	0.6562	0.9609	0.9977	> 0.9999
7 vs. 14	0.0651	0.3505	0.868	0.8545
7 vs. 17	0.0633	0.5008	0.6603	0.724
7 vs. 21	0.0066	0.5555	0.5472	0.7556
7 vs. 24	0.1992	0.9883	> 0.9999	0.8746
7 vs. 28	0.0017	0.7804	> 0.9999	0.808
10 vs. 14	< 0.0001	0.0028	0.9978	0.9506
10 vs. 17	< 0.0001	0.0072	0.9621	0.8592
10 vs. 21	< 0.0001	0.0147	0.9034	0.8826
10 vs. 24	0.0002	0.3873	> 0.9999	0.957
10 vs. 28	< 0.0001	0.04	> 0.9999	0.9212
14 vs. 17	> 0.9999	> 0.9999	> 0.9999	> 0.9999
14 vs. 21	0.9799	> 0.9999	0.9985	> 0.9999
14 vs. 24	> 0.9999	0.9605	0.9886	> 0.9999
14 vs. 28	0.8926	0.9984	0.9649	> 0.9999
17 vs. 21	0.9813	> 0.9999	> 0.9999	> 0.9999
17 vs. 24	> 0.9999	0.9899	0.9224	> 0.9999
17 vs. 28	0.8973	> 0.9999	0.8132	> 0.9999
21 vs. 24	0.9907	0.9913	0.8467	> 0.9999
21 vs. 28	> 0.9999	> 0.9999	0.7005	> 0.9999
24 vs. 28	0.9514	0.9998	> 0.9999	> 0.9999

Supplemental Table C.10 Pairwise comparisons (*P*-values) of elimination rate in cortical tissue between bubbles on each imaging day

Day	A7R vs. cRGD	A7R vs. cRAD	A7R vs. DBCO	cRGD vs. cRAD	cRGD vs. DBCO	cRAD vs. DBCO
0	0.9758	0.9924	0.7351	0.8994	0.9289	0.562
3	0.7258	0.9617	0.5114	0.9457	0.9861	0.8073
7	0.0923	0.0231	0.0144	0.9509	0.8998	0.9985
10	0.0022	< 0.0001	< 0.0001	0.0271	0.0477	0.9968
14	0.0812	0.1441	0.08	0.9941	> 0.9999	0.9937
17	0.1565	0.0526	0.0398	0.9654	0.9389	0.9996
21	0.8177	0.4147	0.509	0.9097	0.9562	0.9987
24	0.8878	0.8862	0.2302	> 0.9999	0.6403	0.6428
28	0.9982	0.9632	0.7323	0.9146	0.8262	0.4329

Supplemental Table C.11 Pairwise comparisons (*P*-values) of half-life in the kidney cortex between imaging days for each bubble

	A7R	cRGD	cRAD	DBCO
0 vs. 3	0.5128	0.9987	0.0565	0.7382
0 vs. 7	0.3908	0.8277	0.0002	0.0281
0 vs. 10	0.2782	0.632	0.0003	0.4562
0 vs. 14	0.2954	> 0.9999	0.0014	0.0897
0 vs. 17	0.3583	> 0.9999	0.002	0.9981
0 vs. 21	0.6206	0.9996	0.0437	> 0.9999
0 vs. 24	0.5618	0.937	0.001	0.9996
0 vs. 28	0.769	0.9369	0.0001	0.3389
3 vs. 7	0.9998	0.9873	0.4399	0.5928
3 vs. 10	0.9998	0.9506	0.7546	0.9998
3 vs. 14	> 0.9999	0.9998	0.9756	0.9538
3 vs. 17	> 0.9999	> 0.9999	0.9856	0.9882
3 vs. 21	> 0.9999	> 0.9999	> 0.9999	0.6597
3 vs. 24	> 0.9999	0.9987	0.7139	0.997
3 vs. 28	> 0.9999	0.9996	0.6926	0.9992
7 vs. 10	> 0.9999	> 0.9999	0.9994	0.9053
7 vs. 14	> 0.9999	0.8892	0.9396	0.9901
7 vs. 17	> 0.9999	0.9621	0.9185	0.1466
7 vs. 21	0.9998	0.9876	0.6974	0.0251
7 vs. 24	> 0.9999	> 0.9999	> 0.9999	0.3122
7 vs. 28	0.9966	> 0.9999	0.9994	0.9171
10 vs. 14	> 0.9999	0.7329	0.999	0.9997
10 vs. 17	> 0.9999	0.8823	0.9977	0.8803

10 vs. 21	> 0.9999	0.9564	0.9365	0.394
10 vs. 24	> 0.9999	> 0.9999	> 0.9999	0.954
10 vs. 28	0.9966	0.9994	> 0.9999	> 0.9999
14 vs. 17	> 0.9999	> 0.9999	> 0.9999	0.424
14 vs. 21	> 0.9999	> 0.9999	0.9989	0.0826
14 vs. 24	> 0.9999	0.9671	0.9945	0.695
14 vs. 28	0.9993	0.9711	0.9982	0.9999
17 vs. 21	> 0.9999	> 0.9999	0.9996	0.9906
17 vs. 24	> 0.9999	0.9933	0.9907	> 0.9999
17 vs. 28	0.9998	0.9962	0.9962	0.8063
21 vs. 24	> 0.9999	0.9986	0.8988	0.9973
21 vs. 28	> 0.9999	0.9995	0.9146	0.2933
24 vs. 28	0.9998	> 0.9999	> 0.9999	0.9245

Supplemental Table C.12 Pairwise comparisons (*P*-values) of half-life in cortical tissue between bubbles on each imaging day

Day	A7R vs. cRGD	A7R vs. cRAD	A7R vs. DBCO	cRGD vs. cRAD	cRGD vs. DBCO	cRAD vs. DBCO
0	0.9326	0.0049	0.2911	0.0006	0.0868	0.3796
3	0.8787	0.0956	0.1554	0.392	0.5268	0.9961
7	0.9985	0.9936	0.9907	0.9996	0.9991	> 0.9999
10	> 0.9999	0.7889	0.2738	0.7855	0.2709	0.8175
14	0.3663	0.391	0.6037	> 0.9999	0.98	0.9859
17	0.6209	0.4031	0.0061	0.9851	0.1576	0.3027
21	0.8991	0.3199	0.0028	0.7392	0.0255	0.2663
24	0.9978	0.9795	0.0732	0.9968	0.1121	0.1746
28	0.9977	0.999	0.7357	0.9876	0.6207	0.8145

Supplemental Table C.13 Pairwise comparisons (*P*-values) of medullary elimination rate between imaging days for each bubble

	A7R	cRGD	cRAD	DBCO
0 vs. 3	0.0078	0.3794	0.2204	0.2011
0 vs. 7	< 0.0001	0.0005	0.0094	0.0188
0 vs. 10	< 0.0001	< 0.0001	0.0662	0.0407
0 vs. 14	0.0036	0.8585	0.3108	0.8841
0 vs. 17	0.0988	0.9799	0.9422	> 0.9999
0 vs. 21	0.0201	0.0068	0.0022	0.643
0 vs. 24	0.0007	0.3475	0.1204	0.9995
0 vs. 28	0.6493	0.5271	0.0287	0.9411

3 vs. 7	0.0142	0.1867	0.8069	0.9145
3 vs. 10	< 0.0001	0.022	0.9989	0.9963
3 vs. 14	> 0.9999	0.9978	> 0.9999	0.9657
3 vs. 17	0.9956	0.9569	0.9359	0.4286
3 vs. 21	> 0.9999	0.7595	0.7321	0.9998
3 vs. 24	0.9289	> 0.9999	0.9983	0.8596
3 vs. 28	0.718	> 0.9999	0.9942	0.9484
7 vs. 10	0.8526	> 0.9999	0.9904	0.9996
7 vs. 14	0.0248	0.0377	0.7223	0.354
7 vs. 17	0.0012	0.0121	0.1769	0.0519
7 vs. 21	0.025	0.9768	> 0.9999	0.7301
7 vs. 24	0.5875	0.6397	0.998	0.2587
7 vs. 28	< 0.0001	0.1634	0.9955	0.3254
10 vs. 14	< 0.0001	0.0019	0.9951	0.6276
10 vs. 17	< 0.0001	0.0004	0.6339	0.114
10 vs. 21	< 0.0001	0.7934	0.9882	0.9411
10 vs. 24	0.0107	0.2838	> 0.9999	0.4789
10 vs. 28	< 0.0001	0.0197	> 0.9999	0.5873
14 vs. 17	0.9805	> 0.9999	0.973	0.9834
14 vs. 21	> 0.9999	0.3021	0.6247	0.9998
14 vs. 24	0.9688	0.9763	0.994	0.9998
14 vs. 28	0.5797	0.9997	0.9813	> 0.9999
17 vs. 21	0.9976	0.1269	0.0929	0.8642
17 vs. 24	0.5541	0.8811	0.6964	> 0.9999
17 vs. 28	0.9905	0.9847	0.4701	0.9945
21 vs. 24	0.9456	0.9887	0.998	0.9883
21 vs. 28	0.7949	0.7061	0.9946	0.9994
24 vs. 28	0.149	0.9997	> 0.9999	> 0.9999

Supplemental Table C.14 Pairwise comparisons (*P*-values) of elimination rate in the medulla between bubbles on each imaging day

Day	A7R vs. cRGD	A7R vs. cRAD	A7R vs. DBCO	cRGD vs. cRAD	cRGD vs. DBCO	cRAD vs. DBCO
0	0.9511	0.3362	0.555	0.6597	0.8627	0.983
3	0.1896	0.0238	0.0707	0.8263	0.97	0.9766
7	0.1209	0.0015	0.002	0.4445	0.493	0.9998
10	0.0005	< 0.0001	< 0.0001	0.0065	0.0276	0.9638
14	0.0173	0.0073	0.001	0.9925	0.8349	0.9429
17	0.0875	0.0061	0.0011	0.7807	0.4855	0.9635
21	0.9985	0.8243	0.047	0.8964	0.0705	0.2994

24	0.1424	0.0598	0.0003	0.982	0.1884	0.3622
28	0.9879	0.9989	0.2773	0.9979	0.4567	0.3515

Supplemental Table C.15 Pairwise comparisons (*P*-values) of half-life in the medulla between imaging days for each bubble

	A7R	cRGD	cRAD	DBCO
0 vs. 3	0.455	0.7572	< 0.0001	0.04
0 vs. 7	0.4909	0.6172	< 0.0001	0.0662
0 vs. 10	0.3468	0.4328	< 0.0001	0.061
0 vs. 14	0.418	0.9317	< 0.0001	0.3035
0 vs. 17	0.6637	0.9895	< 0.0001	0.9312
0 vs. 21	0.5355	0.6001	< 0.0001	0.7391
0 vs. 24	0.6196	0.8649	< 0.0001	> 0.9999
0 vs. 28	0.6877	0.8377	< 0.0001	0.7647
3 vs. 7	> 0.9999	0.9999	0.9992	> 0.9999
3 vs. 10	> 0.9999	0.9996	> 0.9999	> 0.9999
3 vs. 14	> 0.9999	> 0.9999	> 0.9999	0.9955
3 vs. 17	> 0.9999	0.9983	0.9553	0.0004
3 vs. 21	> 0.9999	> 0.9999	0.9998	0.9405
3 vs. 24	> 0.9999	> 0.9999	> 0.9999	0.2065
3 vs. 28	> 0.9999	> 0.9999	> 0.9999	0.8828
7 vs. 10	> 0.9999	> 0.9999	> 0.9999	> 0.9999
7 vs. 14	> 0.9999	0.9955	0.9997	0.9742
7 vs. 17	0.9997	0.9708	0.7811	0.002
7 vs. 21	> 0.9999	> 0.9999	> 0.9999	0.8774
7 vs. 24	> 0.9999	> 0.9999	> 0.9999	0.2009
7 vs. 28	0.9998	0.9997	0.9998	0.8104
10 vs. 14	> 0.9999	0.9885	> 0.9999	0.9944
10 vs. 17	0.9995	0.935	0.9358	0.001
10 vs. 21	> 0.9999	> 0.9999	> 0.9999	0.9396
10 vs. 24	> 0.9999	> 0.9999	> 0.9999	0.2319
10 vs. 28	0.9997	0.9991	> 0.9999	0.8876
14 vs. 17	> 0.9999	> 0.9999	0.9311	0.0092
14 vs. 21	> 0.9999	0.9984	> 0.9999	> 0.9999
14 vs. 24	> 0.9999	> 0.9999	> 0.9999	0.625
14 vs. 28	> 0.9999	> 0.9999	> 0.9999	0.9994
17 vs. 21	> 0.9999	0.9814	0.7766	0.092
17 vs. 24	> 0.9999	0.9987	0.9344	0.9716
17 vs. 28	> 0.9999	0.9995	0.9297	0.0896
21 vs. 24	> 0.9999	> 0.9999	> 0.9999	0.9042

21 vs. 28	> 0.9999	> 0.9999	> 0.9999	> 0.9999
24 vs. 28	> 0.9999	> 0.9999	> 0.9999	0.9229

Supplemental Table C.16 Pairwise comparisons (*P*-values) of medullary half-life between bubbles on each imaging day

Day	A7R vs. cRGD	A7R vs. cRAD	A7R vs. DBCO	cRGD vs. cRAD	cRGD vs. DBCO	cRAD vs. DBCO
0	> 0.9999	< 0.0001	0.3549	< 0.0001	0.3445	< 0.0001
3	0.9731	0.8168	0.9423	0.9703	0.9991	0.9895
7	0.9989	0.9862	0.9869	0.9973	0.9975	> 0.9999
10	0.9995	0.8005	0.8929	0.8554	0.9319	0.9973
14	0.8189	0.8366	0.4643	> 0.9999	0.9361	0.925
17	0.8269	0.2883	< 0.0001	0.7952	0.0007	0.0161
21	0.9999	0.9909	0.3214	0.9959	0.3591	0.4925
24	0.9857	0.9617	0.0321	0.999	0.0784	0.109
28	0.9957	0.9742	0.348	0.9974	0.4829	0.6055

Supplemental Table C.17 Pairwise comparisons (*P*-values) of elimination rate in the liver between imaging days for each bubble

Day	A7R	cRGD	cRAD	DBCO
0 vs. 3	> 0.9999	> 0.9999	0.0249	0.8512
0 vs. 7	> 0.9999	> 0.9999	> 0.9999	> 0.9999
0 vs. 10	> 0.9999	> 0.9999	0.0248	0.2461
0 vs. 14	0.577	> 0.9999	0.7569	0.7852
0 vs. 17	0.4928	0.7926	0.4808	0.9926
0 vs. 21	0.882	0.9492	0.9344	> 0.9999
0 vs. 24	> 0.9999	> 0.9999	> 0.9999	> 0.9999
0 vs. 28	0.9755	> 0.9999	0.9995	> 0.9999
3 vs. 7	> 0.9999	> 0.9999	0.2427	0.9946
3 vs. 10	> 0.9999	> 0.9999	> 0.9999	0.9804
3 vs. 14	0.7912	> 0.9999	0.64	> 0.9999
3 vs. 17	0.7181	0.8962	0.8688	0.9996
3 vs. 21	0.969	0.9829	0.645	0.8616
3 vs. 24	> 0.9999	> 0.9999	0.1092	0.9369
3 vs. 28	0.9976	> 0.9999	0.0987	0.8792
7 vs. 10	> 0.9999	> 0.9999	0.2173	0.7434
7 vs. 14	0.8998	> 0.9999	0.9869	0.9885
7 vs. 17	0.8585	0.9128	0.9203	> 0.9999
7 vs. 21	0.9847	0.9792	0.9984	> 0.9999

7 vs. 24	> 0.9999	> 0.9999	> 0.9999	> 0.9999
7 vs. 28	0.9988	> 0.9999	> 0.9999	> 0.9999
10 vs. 14	0.9237	> 0.9999	0.5877	0.9911
10 vs. 17	0.8831	0.8501	0.8224	0.7903
10 vs. 21	0.9934	0.964	0.5914	0.2769
10 vs. 24	> 0.9999	> 0.9999	0.0998	0.4728
10 vs. 28	0.9998	> 0.9999	0.0932	0.2979
14 vs. 17	> 0.9999	0.9393	> 0.9999	0.9983
14 vs. 21	> 0.9999	0.9926	> 0.9999	0.801
14 vs. 24	0.929	> 0.9999	0.9416	0.904
14 vs. 28	0.9967	> 0.9999	0.9727	0.8226
17 vs. 21	> 0.9999	> 0.9999	0.9997	0.9923
17 vs. 24	0.8952	0.927	0.7853	0.9972
17 vs. 28	0.9916	0.8644	0.8386	0.9943
21 vs. 24	0.9912	0.9839	0.9897	> 0.9999
21 vs. 28	> 0.9999	0.9719	0.9976	> 0.9999
24 vs. 28	0.9995	> 0.9999	> 0.9999	> 0.9999

Supplemental Table C.18 Pairwise comparisons (*P*-values) of elimination rate in the liver between bubbles on each imaging day

Day	A7R vs. cRGD	A7R vs. cRAD	A7R vs. DBCO	cRGD vs. cRAD	cRGD vs. DBCO	cRAD vs. DBCO
0	> 0.9999	0.997	0.9995	0.9976	0.9997	0.9998
3	0.9992	0.0175	0.6309	0.0122	0.5551	0.3464
7	0.9964	> 0.9999	0.9996	0.9932	0.9906	> 0.9999
10	0.9637	0.0426	0.2099	0.0115	0.0788	0.9079
14	0.3709	0.9743	0.9982	0.6314	0.5475	0.9962
17	0.9651	0.9994	0.7107	0.9849	0.9227	0.7749
21	0.9968	0.9966	0.4846	> 0.9999	0.6104	0.6513
24	0.9943	0.9973	0.9848	0.9999	0.9994	0.9976
28	0.7596	0.9057	0.7094	0.9867	0.9982	0.9629

Supplemental Table C.19 Pairwise comparisons (*P*-values) of half-life in liver tissue between imaging days for each bubble

	A7R	cRGD	cRAD	DBCO
0 vs. 3	0.9712	> 0.9999	< 0.0001	0.033
0 vs. 7	0.9311	0.9998	0.0002	0.5638
0 vs. 10	0.6749	> 0.9999	< 0.0001	0.1893
0 vs. 14	0.3264	0.9768	< 0.0001	0.0916

0 vs. 17	0.493	0.999	< 0.0001	0.8161
0 vs. 21	0.8501	> 0.9999	< 0.0001	0.9864
0 vs. 24	> 0.9999	> 0.9999	0.0004	0.9801
0 vs. 28	0.9728	> 0.9999	0.0158	> 0.9999
3 vs. 7	> 0.9999	> 0.9999	0.9997	0.9987
3 vs. 10	0.9973	> 0.9999	0.9987	0.9999
3 vs. 14	0.9512	0.9693	> 0.9999	> 0.9999
3 vs. 17	0.9889	0.9984	> 0.9999	0.7436
3 vs. 21	> 0.9999	> 0.9999	> 0.9999	0.0019
3 vs. 24	0.9999	> 0.9999	0.9796	0.0077
3 vs. 28	> 0.9999	> 0.9999	0.1545	0.045
7 vs. 10	> 0.9999	0.9988	0.9586	> 0.9999
7 vs. 14	0.9995	0.8942	0.9994	> 0.9999
7 vs. 17	> 0.9999	0.9766	0.9978	0.9989
7 vs. 21	> 0.9999	0.9942	0.9942	0.1441
7 vs. 24	0.9971	0.9998	> 0.9999	0.1859
7 vs. 28	> 0.9999	0.9997	0.6982	0.5797
10 vs. 14	> 0.9999	0.9977	0.9985	> 0.9999
10 vs. 17	> 0.9999	> 0.9999	0.9997	0.9725
10 vs. 21	> 0.9999	> 0.9999	> 0.9999	0.0197
10 vs. 24	0.9659	> 0.9999	0.7576	0.0442
10 vs. 28	0.9983	> 0.9999	0.0309	0.2176
14 vs. 17	> 0.9999	> 0.9999	> 0.9999	0.9182
14 vs. 21	0.9992	0.9998	> 0.9999	0.0067
14 vs. 24	0.8449	0.9975	0.9663	0.0207
14 vs. 28	0.9653	0.9892	0.0848	0.1143
17 vs. 21	> 0.9999	> 0.9999	> 0.9999	0.242
17 vs. 24	0.928	> 0.9999	0.9353	0.3248
17 vs. 28	0.9928	0.9997	0.0555	0.8293
21 vs. 24	0.993	> 0.9999	0.9162	> 0.9999
21 vs. 28	> 0.9999	> 0.9999	0.0883	0.9926
24 vs. 28	0.9998	> 0.9999	0.8814	0.9874

Supplemental Table C.20 Pairwise comparisons of (*P*-values) half-life in liver tissue between bubbles on each imaging day

Day	A7R vs. cRGD	A7R vs. cRAD	A7R vs. DBCO	cRGD vs. cRAD	cRGD vs. DBCO	cRAD vs. DBCO
0	> 0.9999	< 0.0001	0.4397	< 0.0001	0.405	0.008
3	0.6878	0.9966	0.7643	0.6054	0.1933	0.8923
7	0.4188	0.898	0.9928	0.8364	0.6606	0.9824

10	0.4901	0.9973	0.9862	0.4112	0.7441	0.9553
14	0.6305	0.7713	0.9478	0.9955	0.9432	0.9858
17	0.5407	0.9476	0.3082	0.8584	0.9594	0.6082
21	0.7818	0.9995	0.0018	0.7415	0.0308	0.0021
24	0.9973	0.9903	0.092	0.9997	0.1379	0.1346
28	0.7894	0.0461	0.0787	0.3452	0.4027	0.9997

C.2 Supplemental Tables for Chapter 4

Supplemental Table C.21 Multiplicity adjusted *P*-values comparing displacement results between different depths within each power output

	2 vs. 3	2 vs. 4	2 vs. 5	3 vs. 4	3 vs. 5	4 vs. 5
0	0.5165	0.3642	0.9529	0.994	0.8295	0.6851
-1	0.9637	0.7806	0.9222	0.9662	0.9987	0.9891
-2	0.7611	0.8519	0.9142	0.9981	0.3642	0.466
-3	0.9729	> 0.9999	0.8678	0.9822	0.627	0.8409
-4	> 0.9999	0.8678	0.8118	0.8409	0.7806	0.9994
-5	0.2094	0.9996	0.9787	0.2534	0.4037	0.9913
-6	0.0916	0.007	0.9708	0.7806	0.2283	0.0258
-7	0.4983	0.9543	> 0.9999	0.8118	0.502	0.9557
-8	0.1281	0.4732	0.9837	0.8729	0.2587	0.6994
-9	0.4947	0.4519	0.6635	0.9999	0.9932	0.9866
-10	0.8876	0.9057	0.5606	> 0.9999	0.9369	0.9222
-11	0.8295	0.787	0.8678	0.9998	0.9998	0.9984
-12	0.9585	0.9298	0.9932	0.9996	0.9955	0.9866
-15	> 0.9999	0.9998	0.9923	> 0.9999	0.9903	0.9837

Supplemental Table C.22 Multiplicity adjusted *P*-values comparing differences in bubble displacement results across power output

[illegible]

Supplemental Table C.23 Corresponding targeted MB, CD31, and VEGFR expression

Case	VEGFR2 MB targeting (A.U.)	$\alpha_v\beta_3$ integrin MB targeting (A.U.)	Average CD31 expression (#/HPF)	Average VEGFR2 expression (#/HPF)
003	2.90	11.26	6	3.4
005	0.64	2.38	6.25	
007	1.13	4.04	2.4	4.6

C.3 Supplemental Tables for Chapter 5

Supplemental Table C.24 Non-normalized estimated parameter, A, by KCL for each session and the average for a representative control NHP

	Non-normalized estimated parameter, A			
KCL	Session 1	Session 2	Session 3	Average
1	0.3544	0.2969	0.8388	0.3218
2	0.3776	0.2832	0.9067	0.3334
3	0.3930	0.2877	0.9417	0.3444
4	0.4011	0.2987	0.9686	0.3541
5	0.4187	0.3183	1.0000	0.3704
6	0.4420	0.3360	1.0074	0.3850
7	0.4553	0.3846	1.0157	0.4067
8	0.4427	0.3803	0.9796	0.3966
9	0.4173	0.3197	0.8961	0.3575
10	0.3993	0.3634	0.7819	0.3518

Supplemental Table C.25 Normalized estimated parameter, A, by KCL for each session and the average for a representative control NHP

	Normalized estimated parameter, A			
KCL	Session 1	Session 2	Session 3	Average
1	0.8465	0.9329	0.8388	0.8728
2	0.9019	0.8898	0.9067	0.8995
3	0.9388	0.9041	0.9417	0.9282
4	0.9581	0.9386	0.9686	0.9551
5	1.0000	1.0000	1.0000	1.0000
6	1.0557	1.0555	1.0074	1.0395
7	1.0876	1.2082	1.0157	1.1038
8	1.0574	1.1950	0.9796	1.0773
9	0.9966	1.0045	0.8961	0.9658
10	0.9537	1.1418	0.7819	0.9591

Supplemental Table C.26 Average non-normalized estimated parameters A, β , and PI per KCL for every NHP in the control cohort

Non-human primate ID															
<u>KCL</u>	<u>NHP 001</u>			<u>NHP 002</u>			<u>NHP 003</u>			<u>NHP 004</u>			<u>NHP 005</u>		
	<u>A</u>	<u>β</u>	<u>PI</u>	<u>A</u>	<u>β</u>	<u>PI</u>	<u>A</u>	<u>β</u>	<u>PI</u>	<u>A</u>	<u>β</u>	<u>PI</u>	<u>A</u>	<u>β</u>	<u>PI</u>
1	0.3218	1.0983	0.3563	0.3102	1.1243	0.3592	0.3114	1.2610	0.3917	0.2472	1.2583	0.3128	0.2925	0.8226	0.2405
2	0.3334	1.2840	0.4341	0.3698	1.0707	0.4079	0.3604	1.2716	0.4567	0.2937	1.5932	0.4783	0.3337	1.0243	0.3416
3	0.3444	1.3108	0.4567	0.4154	1.3091	0.5801	0.3881	1.3534	0.5234	0.3178	1.7000	0.5643	0.3658	1.2174	0.4459
4	0.3541	1.3016	0.4614	0.4370	1.4162	0.6583	0.3958	1.3800	0.5419	0.3404	1.6777	0.6071	0.3935	1.2238	0.4823
5	0.3704	1.0614	0.3922	0.4473	1.3628	0.6492	0.4096	1.3178	0.5349	0.3682	1.5428	0.6019	0.4159	1.1176	0.4639
6	0.3850	0.6295	0.2367	0.4523	1.0797	0.5211	0.4214	1.2741	0.5377	0.3841	1.2796	0.5250	0.4296	0.7594	0.3254
7	0.4067	0.5071	0.2081	0.4491	0.7077	0.3377	0.4213	0.8758	0.3718	0.3851	1.6370	0.6103	0.4287	0.5351	0.2297
8	0.3966	0.3572	0.1467	0.4322	0.4710	0.2125	0.4033	0.5380	0.2195	0.3802	1.0678	0.4050	0.3991	0.3716	0.1500
9	0.3575	0.1975	0.0709	0.3710	0.4219	0.1568	0.3599	0.2736	0.1010	0.3232	0.8967	0.2473	0.3377	0.4025	0.1353
10	0.3518	0.1226	0.0398	0.2725	0.3697	0.0971	0.3629	0.2324	0.0856	0.2422	0.5251	0.1109	0.2594	0.2752	0.0714

Supplemental Table C.27 Average non-normalized estimated parameters A, β , and PI per KCL for every NHP in the IR cohort

Non-human primate ID															
<u>KCL</u>	<u>NHP 006</u>			<u>NHP 007</u>			<u>NHP 008</u>			<u>NHP 009</u>			<u>NHP 010</u>		
	<u>A</u>	<u>β</u>	<u>PI</u>	<u>A</u>	<u>β</u>	<u>PI</u>	<u>A</u>	<u>β</u>	<u>PI</u>	<u>A</u>	<u>β</u>	<u>PI</u>	<u>A</u>	<u>β</u>	<u>PI</u>
1	0.2465	1.0816	0.2653	0.3177	0.9710	0.3070	0.2717	1.4838	0.4226	0.2299	1.4016	0.3498	0.3852	1.7609	0.6770
2	0.2958	1.5451	0.4551	0.3798	1.2421	0.4720	0.2740	1.4934	0.4189	0.2925	1.7511	0.5519	0.4216	2.2294	0.9391
3	0.3248	1.6635	0.5360	0.4205	1.4024	0.5912	0.2831	1.4452	0.4028	0.3241	1.7296	0.6348	0.4459	2.5978	1.1547
4	0.3483	1.6911	0.5854	0.4509	1.4299	0.6482	0.2903	1.3267	0.3764	0.3478	1.4823	0.5892	0.4604	2.7949	1.2760
5	0.3658	1.5916	0.5791	0.4768	1.2153	0.5828	0.3007	1.3067	0.3655	0.3700	1.1459	0.4705	0.4756	2.9655	1.3803
6	0.3855	1.4644	0.5620	0.5037	0.8243	0.4213	0.3138	1.0496	0.3259	0.3972	1.0298	0.4478	0.4937	2.9306	1.4017
7	0.3970	1.1261	0.4453	0.5150	0.5202	0.2719	0.3169	0.6854	0.2080	0.3995	0.8978	0.3902	0.5049	2.5602	1.2082
8	0.3863	0.7068	0.2771	0.5072	0.4780	0.2433	0.2919	0.4405	0.1232	0.3683	0.6435	0.2457	0.4931	2.8520	1.3077
9	0.3546	0.4901	0.1745	0.4792	0.4586	0.2187	0.2339	0.2449	0.0549	0.3553	0.4563	0.1727	0.4504	2.3943	1.0382
10	0.2465	1.0816	0.2653	0.3177	0.9710	0.3070	0.2717	1.4838	0.4226	0.2299	1.4016	0.3498	0.3852	1.7609	0.6770

Supplemental Table C.28 Average non-normalized estimated parameters A, β , and PI per KCL for every NHP in the diabetic cohort

Non-human primate ID																		
<u>KCL</u>	<u>NHP 011</u>			<u>NHP 012</u>			<u>NHP 013</u>			<u>NHP 014</u>			<u>NHP 015</u>			<u>NHP 016</u>		
	<u>A</u>	<u>β</u>	<u>PI</u>	<u>A</u>	<u>β</u>	<u>PI</u>	<u>A</u>	<u>β</u>	<u>PI</u>	<u>A</u>	<u>β</u>	<u>PI</u>	<u>A</u>	<u>β</u>	<u>PI</u>	<u>A</u>	<u>β</u>	<u>PI</u>
1	0.2630	1.3279	0.3484	0.2667	1.4988	0.3694	0.3335	0.8783	0.2888	0.3161	1.4449	0.4491	0.3109	1.2818	0.3984	0.2965	0.8673	0.2830
2	0.3195	1.4909	0.4639	0.3085	1.4599	0.4119	0.3860	1.0511	0.4034	0.3401	1.6342	0.5486	0.3184	1.4820	0.4718	0.3291	1.0241	0.3619
3	0.3623	1.5023	0.5202	0.3367	1.6263	0.4889	0.4152	1.2526	0.5212	0.3599	1.3195	0.4619	0.3409	1.6431	0.5601	0.3700	1.0580	0.4162
4	0.3865	1.4748	0.5444	0.3379	1.7701	0.5404	0.4333	1.3351	0.5875	0.3638	0.9681	0.3449	0.3616	1.6509	0.5970	0.4035	0.9148	0.3850
5	0.4012	1.2761	0.4888	0.3440	1.6792	0.5088	0.4540	1.2382	0.5780	0.3610	0.7156	0.2526	0.3947	1.2768	0.5039	0.4251	0.6335	0.2764
6	0.4174	0.8634	0.3556	0.3685	1.8475	0.5720	0.4640	0.9376	0.4400	0.3557	0.4381	0.1530	0.4050	0.9516	0.3854	0.4385	0.4795	0.2145
7	0.4327	0.5827	0.2545	0.3854	1.2113	0.4236	0.4655	0.5938	0.2714	0.3219	0.3229	0.0994	0.3939	0.7814	0.3078	0.4346	0.6044	0.2711
8	0.4382	0.5396	0.2528	0.3630	1.4416	0.4787	0.4557	0.3936	0.1684	0.2858	0.2099	0.0563	0.3935	0.5794	0.2280	0.4245	0.5259	0.2308
9	0.3965	0.3546	0.1569	0.3411	4.6642	1.3585	0.4097	0.3074	0.1126	0.2548	0.2018	0.0454	0.4100	0.3511	0.1439	0.4350	0.4147	0.1785
10	0.3629	0.2444	0.1032	0.3378	0.4521	0.1370	0.3681	0.3025	0.1121	0.2669	0.8544	0.1661	0.4223	0.2654	0.1121	0.4379	0.6525	0.2567

Supplemental Table C.29 Average normalized estimated parameters A, β , and PI per KCL for every NHP in the control cohort

Non-human primate ID															
<u>KCL</u>	<u>NHP 001</u>			<u>NHP 002</u>			<u>NHP 003</u>			<u>NHP 004</u>			<u>NHP 005</u>		
	<u>A</u>	<u>β</u>	<u>PI</u>	<u>A</u>	<u>β</u>	<u>PI</u>	<u>A</u>	<u>β</u>	<u>PI</u>	<u>A</u>	<u>β</u>	<u>PI</u>	<u>A</u>	<u>β</u>	<u>PI</u>
1	0.8728	1.0455	0.9048	0.7043	1.0653	0.7810	0.7576	1.0389	0.8101	0.6852	0.8682	0.6059	0.7028	0.7366	0.5177
2	0.8995	1.2194	1.0977	0.8254	0.9930	0.8057	0.8779	1.0339	0.9209	0.8014	1.0820	0.8752	0.8021	0.9318	0.7433
3	0.9282	1.2262	1.1407	0.9259	1.0103	0.9329	0.9465	1.0733	1.0190	0.8616	1.1392	0.9859	0.8798	1.1026	0.9664
4	0.9551	1.2071	1.1540	0.9760	1.0599	1.0343	0.9658	1.0644	1.0284	0.9222	1.0931	1.0095	0.9462	1.1053	1.0446
5	1.0000	1.0000	1.0000	1.0000	1.0000	1.0000	1.0000	1.0000	1.0000	1.0000	1.0000	1.0000	1.0000	1.0000	1.0000
6	1.0395	0.5866	0.6094	1.0097	0.8120	0.8196	1.0298	0.9991	1.0248	1.0452	0.8139	0.8510	1.0335	0.6773	0.7020
7	1.1038	0.5051	0.5640	1.0035	0.5635	0.5631	1.0318	0.7044	0.7133	1.0444	1.1453	1.1964	1.0327	0.4886	0.5046
8	1.0773	0.3689	0.3996	0.9675	0.3989	0.3860	0.9889	0.4361	0.4177	1.0261	0.7596	0.7723	0.9624	0.3361	0.3269
9	0.9658	0.1897	0.1838	0.8236	0.4220	0.3395	0.8813	0.2262	0.1947	0.8783	0.7200	0.6327	0.8140	0.3744	0.3038
10	0.9591	0.1065	0.0937	0.5918	0.3910	0.2021	0.8871	0.1907	0.1670	0.6663	0.4288	0.2973	0.6240	0.2539	0.1563

Supplemental Table C.30 Average normalized estimated parameters A, β , and PI per KCL for every NHP in the IR cohort

Non-human primate ID															
<u>KCL</u>	<u>NHP 006</u>			<u>NHP 007</u>			<u>NHP 008</u>			<u>NHP 009</u>			<u>NHP 010</u>		
	<u>A</u>	<u>β</u>	<u>PI</u>	<u>A</u>	<u>β</u>	<u>PI</u>	<u>A</u>	<u>β</u>	<u>PI</u>	<u>A</u>	<u>β</u>	<u>PI</u>	<u>A</u>	<u>β</u>	<u>PI</u>
1	0.6743	0.6828	0.4589	0.6699	0.8190	0.5609	0.9516	1.2126	1.0957	0.6072	1.3510	0.7822	0.8115	0.6672	0.5357
2	0.8086	0.9812	0.7959	0.7965	1.0458	0.8372	0.9385	1.2249	1.1175	0.7757	1.6768	1.2200	0.8889	0.8408	0.7372
3	0.8874	1.0515	0.9340	0.8808	1.1806	1.0397	0.9570	1.1641	1.1014	0.8593	1.5730	1.3229	0.9396	0.9581	0.8928
4	0.9521	1.0647	1.0137	0.9454	1.1918	1.1279	0.9714	1.0697	1.0344	0.9252	1.3084	1.2109	0.96955	0.9841	0.9513
5	1.0000	1.0000	1.0000	1.0000	1.0000	1.0000	1.0000	1.0000	1.0000	1.0000	1.0000	1.0000	1.0000	1.0000	1.0000
6	1.0541	0.9190	0.9685	1.0564	0.6586	0.6974	1.0449	0.8391	0.8745	1.1001	0.8450	0.9247	1.0370	0.9709	1.0060
7	1.0862	0.6953	0.7562	1.0795	0.4221	0.4561	1.0634	0.5323	0.5634	1.1068	0.7687	0.8561	1.0596	0.7345	0.7658
8	1.0592	0.4398	0.4685	1.0635	0.4022	0.4258	0.9589	0.3537	0.3427	1.0154	0.6433	0.6657	1.0353	0.7618	0.7746
9	0.9749	0.3146	0.2996	1.0075	0.3988	0.4038	0.7231	0.2036	0.1601	1.0041	0.4303	0.4315	0.9479	0.6324	0.6057
10	0.9107	0.3322	0.3006	0.9492	0.3437	0.3377	0.7442	0.0774	0.0643	0.8771	0.3360	0.3073	0.8131	0.6475	0.5112

Supplemental Table C.31 Average normalized estimated parameters A, β , and PI per KCL for every NHP in the diabetic cohort

Non-human primate ID																		
<u>KCL</u>	<u>NHP 011</u>			<u>NHP 012</u>			<u>NHP 013</u>			<u>NHP 014</u>			<u>NHP 015</u>			<u>NHP 016</u>		
	<u>A</u>	<u>β</u>	<u>PI</u>	<u>A</u>	<u>β</u>	<u>PI</u>	<u>A</u>	<u>β</u>	<u>PI</u>	<u>A</u>	<u>β</u>	<u>PI</u>	<u>A</u>	<u>β</u>	<u>PI</u>	<u>A</u>	<u>β</u>	<u>PI</u>
1	0.6830	1.0642	0.7126	0.7654	0.9902	0.7643	0.7289	0.7567	0.5435	0.8799	2.0374	1.8085	0.7876	1.0039	0.7907	0.6845	1.4373	1.0362
2	0.8102	1.1767	0.9508	0.9008	0.9169	0.8245	0.8518	0.8974	0.7650	0.9448	2.3326	2.1991	0.8067	1.1607	0.9364	0.7628	1.6194	1.2710
3	0.9127	1.1740	1.0721	0.9812	0.9860	0.9674	0.9173	1.0555	0.9703	0.9973	1.8199	1.8159	0.8638	1.2869	1.1116	0.8601	1.6456	1.4392
4	0.9683	1.1541	1.1177	0.9841	1.1073	1.0868	0.9561	1.1002	1.0526	1.0075	1.3442	1.3544	0.9163	1.2930	1.1848	0.9419	1.4405	1.3629
5	1.0000	1.0000	1.0000	1.0000	1.0000	1.0000	1.0000	1.0000	1.0000	1.0000	1.0000	1.0000	1.0000	1.0000	1.0000	1.0000	1.0000	1.0000
6	1.0439	0.6885	0.7177	1.0793	0.9619	1.0512	1.0218	0.7839	0.8013	0.9841	0.6437	0.6352	1.0262	0.7453	0.7648	1.0404	0.7787	0.8059
7	1.0877	0.4708	0.5092	1.1455	0.6799	0.7921	1.0231	0.5192	0.5294	0.8879	0.4671	0.4166	0.9981	0.6120	0.6108	1.0270	1.0025	1.0176
8	1.1043	0.4522	0.4915	1.0959	0.7130	0.8389	0.9980	0.3543	0.3472	0.7840	0.3035	0.2396	0.9970	0.4538	0.4524	0.9970	0.8829	0.8801
9	0.9800	0.3014	0.2997	1.0218	1.8296	2.1672	0.8822	0.2771	0.2257	0.6980	0.2552	0.1718	1.0388	0.2750	0.2857	1.0279	0.7219	0.7531
10	0.8692	0.2086	0.1947	0.9690	0.2931	0.2793	0.7640	0.2771	0.2130	0.7379	0.8369	0.5035	1.0699	0.2079	0.2224	1.0228	1.2321	1.2330

Supplemental Table C.32 Monoexponential model performance (MSE) in the control NHP cohort for each session per KCL

Session	Vervet ID	MSE for each kidney concentric layer									
		<u>1</u>	<u>2</u>	<u>3</u>	<u>4</u>	<u>5</u>	<u>6</u>	<u>7</u>	<u>8</u>	<u>9</u>	<u>10</u>
1	NHP 1	0.0021	0.0052	0.021	0.0404	0.0707	0.0861	0.0746	0.0409	0.0121	0.0021
	NHP 2	0.0211	0.0166	0.0116	0.0259	0.0462	0.0907	0.1135	0.0615	0.0279	0.0093
	NHP 3	0.0077	0.0082	0.0166	0.0236	0.0268	0.0354	0.0564	0.031	0.0034	0.0004
	NHP 4	0.0055	0.0053	0.0149	0.0327	0.0476	0.0566	0.0594	0.0638	0.0272	0.0121
	NHP 5	0.0079	0.0044	0.0049	0.0101	0.0174	0.0403	0.0551	0.0302	0.0051	0.0017
2	NHP 1	0.0081	0.0027	0.002	0.0058	0.0168	0.0289	0.0703	0.0287	0.0026	0.0006
	NHP 2	0.0006	0.0007	0.0037	0.0104	0.0253	0.0238	0.0123	0.0062	0.0037	0.0013
	NHP 3	0.0166	0.0168	0.0182	0.0245	0.0465	0.0601	0.0475	0.0297	0.0216	0.0134
	NHP 4	0.0008	0.0008	0.0033	0.0072	0.0108	0.0126	0.014	0.0082	0.0063	0.0018
	NHP 5	0.0048	0.0017	0.0037	0.0138	0.0318	0.0691	0.0631	0.0432	0.0164	0.0049
3	NHP 1	0.0012	0.0007	0.0041	0.0214	0.0349	0.0266	0.0231	0.0281	0.0263	0.0078
	NHP 2	0.0056	0.0079	0.0119	0.0224	0.049	0.0847	0.0622	0.0384	0.0253	0.0196
	NHP 3	0.0025	0.0011	0.0009	0.0017	0.0095	0.046	0.0719	0.0676	0.0605	0.03
	NHP 4	0.0056	0.0021	0.0045	0.0142	0.0381	0.0868	0.1438	0.0702	0.0178	0.0017
	NHP 5	0.0025	0.0034	0.00772	0.0191	0.0467	0.0854	0.0603	0.0257	0.0132	0.004

Supplemental Table C.33 Monoexponential model performance (MSE) in the IR NHPs for each session per KCL

Session	Vervet ID	MSE for each kidney concentric layer									
		<u>1</u>	<u>2</u>	<u>3</u>	<u>4</u>	<u>5</u>	<u>6</u>	<u>7</u>	<u>8</u>	<u>9</u>	<u>10</u>
1	NHP 6	0.0014	0.0033	0.0118	0.0235	0.029	0.0295	0.0241	0.0095	0.0031	0.0007
	NHP 7	0.0011	0.001	0.0031	0.0156	0.0374	0.0735	0.1438	0.1003	0.0647	0.0174
	NHP 8	0.0283	0.0289	0.0388	0.0501	0.068	0.0764	0.0697	0.041	0.0324	0.0104
	NHP 9	0.0028	0.0076	0.018	0.0346	0.0651	0.0769	0.0708	0.0397	0.0232	0.0189
2	NHP 6	0.0022	0.0018	0.0032	0.0076	0.0286	0.0754	0.1067	0.1126	0.0764	0.0355
	NHP 7	0.0056	0.0018	0.003	0.014	0.037	0.0607	0.0653	0.0639	0.0614	0.073
	NHP 8	0.014	0.0066	0.0053	0.004	0.0092	0.0184	0.0199	0.0066	0.0001	0.0001
	NHP 9	0.0003	0.0002	0.0006	0.001	0.0032	0.0103	0.0125	0.0077	0.0043	0.0013
	NHP 10	0.0093	0.009	0.0162	0.0302	0.0502	0.0631	0.0817	0.1288	0.1121	0.0376
3	NHP 6	0.0095	0.0134	0.0217	0.0229	0.0302	0.0361	0.0269	0.0273	0.0331	0.0301
	NHP 7	0.004	0.0018	0.0025	0.0117	0.0535	0.1047	0.1229	0.0938	0.0321	0.0088
	NHP 8	0.0009	0.0003	0.001	0.003	0.0047	0.0163	0.0252	0.0177	0.0025	0.0016
	NHP 9	0.0027	0.006	0.0098	0.0298	0.0499	0.0895	0.1126	0.0637	0.0184	0.0046
	NHP 10	0.0014	0.0006	0.0036	0.0218	0.0547	0.0653	0.1273	0.1263	0.0407	0.0046

Supplemental Table C.34 Monoexponential model performance (MSE) in the diabetic NHP cohort for each session per KCL

Session	Vervet ID	MSE for each kidney concentric layer									
		<u>1</u>	<u>2</u>	<u>3</u>	<u>4</u>	<u>5</u>	<u>6</u>	<u>7</u>	<u>8</u>	<u>9</u>	<u>10</u>
1	NHP 11	0.0058	0.0068	0.0123	0.0211	0.0232	0.0338	0.0512	0.0449	0.018	0.0018
	NHP 12	0.009	0.0108	0.0193	0.021	0.0244	0.019	0.0117	0.0021	0.0015	0.0045
	NHP 13	0.0011	0.003	0.0055	0.0068	0.012	0.0175	0.0147	0.0044	0.0008	0.0005
	NHP 14	0.0074	0.0129	0.0209	0.0278	0.0252	0.0116	0.0077	0.004	0.0013	0.0003
	NHP 15	0.0038	0.0036	0.0079	0.0207	0.035	0.052	0.0426	0.0279	0.0106	0.0035
	NHP 16	0.0003	0.0003	0.0012	0.0053	0.0168	0.0219	0.0081	0.0089	0.0146	0.0064
2	NHP 11	0.0005	0.0031	0.0112	0.0261	0.0446	0.0738	0.1128	0.1042	0.0728	0.0417
	NHP 12	0.0384	0.0411	0.0628	0.0696	0.0722	0.1065	0.0965	0.0619	0.054	0.0851
	NHP 13	0.0039	0.0055	0.0037	0.0077	0.0194	0.0294	0.0463	0.0605	0.0635	0.1075
	NHP 14	0.0161	0.0265	0.0328	0.0398	0.0379	0.0241	0.0045	0.0032	0.0111	0.0154
	NHP 16	0.0063	0.013	0.0296	0.0475	0.0753	0.0816	0.0834	0.0689	0.0359	0.0241
3	NHP 12	0.0121	0.0189	0.0175	0.0179	0.023	0.0476	0.0741	0.0694	0.0452	0.0191
	NHP 13	0.0173	0.0049	0.006	0.0094	0.0282	0.0593	0.0727	0.0644	0.0366	0.0235
	NHP 14	0.0118	0.0221	0.0335	0.0447	0.0337	0.0323	0.0176	0.0078	0.0103	0.0027
	NHP 16	0.0098	0.0099	0.0189	0.0513	0.0632	0.0784	0.0521	0.0533	0.0395	0.0204

Supplemental Table C.35 Regression model input features from the non-normalized A, β , and PI per KCL for control NHPs

Feature	Non-human primate ID														
	NHP 001			NHP 002			NHP 003			NHP 004			NHP 005		
	A	β	PI	A	β	PI	A	β	PI	A	β	PI	A	β	PI
μ	0.3622	0.7870	0.2803	0.3957	0.9333	0.3980	0.3834	0.9778	0.3764	0.3282	1.3178	0.4463	0.3656	0.7750	0.2886
σ	0.0273	0.4755	0.1607	0.0632	0.4054	0.2021	0.0347	0.4629	0.1801	0.0538	0.3912	0.1731	0.0586	0.3633	0.1464
AUC	3.2849	7.2595	2.6047	3.6655	8.5861	3.7518	3.4969	9.0311	3.5256	3.0374	12.2866	4.2512	3.3800	7.2006	2.7302
p_{10}	0.0053	-0.1453	-0.0476	-0.0013	-0.1087	-0.0427	0.0038	-0.1326	-0.0441	0.0038	-0.0910	-0.0260	0.0001	-0.0966	-0.0324
p_{11}	0.3331	1.5860	0.5422	0.4026	1.5311	0.6328	0.3626	1.7070	0.6188	0.3074	1.8185	0.5895	0.3651	1.3061	0.4667
p_{30}	-0.0005	0.0073	0.0024	-0.0005	0.0062	0.0033	0.0001	0.0030	0.0016	-0.0009	0.0011	0.0002	-0.0008	0.0080	0.0030
p_{31}	0.0063	-0.1335	-0.0462	0.0003	-0.1255	-0.0714	-0.0064	-0.0760	-0.0400	0.0075	-0.0492	-0.0232	0.0050	-0.1500	-0.0617
p_{32}	-0.0088	0.5566	0.2076	0.0486	0.6145	0.3979	0.0592	0.3867	0.2323	0.0104	0.3370	0.2050	0.0246	0.7146	0.3263
p_{33}	0.3264	0.6649	0.1911	0.2691	0.4986	-0.0310	0.2607	0.8679	0.1692	0.2376	1.0334	0.1423	0.2662	0.2122	-0.0492
BP_{sys}	88.67	88.67	88.67	106.6	106.6	106.6	145.4	145.4	145.4	120.4	120.4	120.4	114.8	114.8	114.8
BP_{dia}	57.44	57.44	57.44	62.33	62.33	62.33	62.67	62.67	62.67	68.78	68.78	68.78	69.00	69.00	69.00

Supplemental Table C.36 Regression model input features from the non-normalized A, β , and PI per KCL for NHPs in the IR cohort

Feature	Non-human primate ID														
	NHP 006			NHP 007			NHP 008			NHP 009			NHP 010		
	A	β	PI	A	β	PI	A	β	PI	A	β	PI	A	β	PI
μ	0.3435	1.1881	0.4054	0.4500	0.8934	0.3934	0.2813	0.9561	0.2722	0.3402	1.0883	0.3978	0.4518	2.5644	1.1290
σ	0.0463	0.4744	0.1671	0.0626	0.4129	0.1728	0.0284	0.5455	0.1559	0.0516	0.5051	0.1747	0.0428	0.3680	0.2347
AUC	3.1466	11.0796	3.8341	4.1164	8.2525	3.6917	2.5587	8.7769	2.4989	3.1286	10.0097	3.7404	4.1320	23.4844	10.4981
p_{10}	0.0099	-0.1154	-0.0274	0.0153	-0.1117	-0.0362	-0.0028	-0.1729	-0.0490	0.0099	-0.1568	-0.0439	0.0037	0.0537	0.0203
p_{11}	0.2889	1.8228	0.5560	0.3656	1.5078	0.5923	0.2965	1.9071	0.5415	0.2857	1.9507	0.6391	0.4315	2.2689	1.0173
p_{30}	-0.0002	0.0085	0.0027	-0.0002	0.0101	0.0046	-0.0004	0.0033	0.0007	-0.0001	0.0061	0.0031	-0.0007	0.0058	0.0009
p_{31}	-0.0006	-0.1756	-0.0613	-0.0015	-0.1827	-0.0892	0.0040	-0.0710	-0.0177	-0.0033	-0.1129	-0.0632	0.0064	-0.1338	-0.0440
p_{32}	0.0417	0.9211	0.3659	0.0569	0.8353	0.4555	-0.0023	0.2622	0.0669	0.0593	0.4440	0.3249	0.0066	0.9112	0.4068
p_{33}	0.2098	0.3138	-0.0537	0.2668	0.2836	-0.0828	0.2674	1.2546	0.3593	0.1783	1.1526	0.1073	0.3797	0.9410	0.3059
BP_{sys}	143.6	143.6	143.6	145.2	145.2	145.2	95.00	95.00	95.00	169.4	169.4	169.4	91.33	91.33	91.33
BP_{dia}	84.22	84.22	84.22	78.00	78.00	78.00	53.22	53.22	53.22	86.11	86.11	86.11	45.50	45.50	45.50

Supplemental Table C.37 Regression model input features from the non-normalized A, β , and PI per KCL for diabetic NHPs

Feat.	Non-human primate ID																	
	NHP 011			NHP 012			NHP 013			NHP 014			NHP 015			NHP 016		
	<u>A</u>	<u>β</u>	<u>PI</u>	<u>A</u>	<u>β</u>	<u>PI</u>	<u>A</u>	<u>β</u>	<u>PI</u>	<u>A</u>	<u>β</u>	<u>PI</u>	<u>A</u>	<u>β</u>	<u>PI</u>	<u>A</u>	<u>β</u>	<u>PI</u>
μ	0.378	0.965	0.348	0.339	1.765	0.528	0.418	0.829	0.348	0.322	0.810	0.257	0.375	1.026	0.370	0.399	0.717	0.287
σ	0.054	0.503	0.154	0.033	1.092	0.316	0.044	0.402	0.184	0.040	0.525	0.182	0.039	0.517	0.169	0.050	0.231	0.077
AUC	3.467	8.870	3.263	3.087	16.68	5.036	3.834	7.699	3.283	2.934	6.959	2.269	3.384	9.489	3.453	3.627	6.414	2.604
p_{10}	0.011	-0.155	-0.040	0.007	0.064	0.025	0.004	-0.104	-0.039	-0.009	-0.140	-0.054	0.012	-0.153	-0.045	0.014	-0.060	-0.017
p_{11}	0.312	1.819	0.572	0.300	1.412	0.389	0.392	1.402	0.564	0.374	1.581	0.555	0.308	1.870	0.621	0.319	1.049	0.382
p_{30}	-0.000	0.007	0.002	0.000	-0.013	-0.003	-0.000	0.008	0.004	0.000	0.011	0.003	0.000	0.008	0.002	0.000	0.005	0.002
p_{31}	-0.001	-0.131	-0.054	-0.002	0.206	0.057	-0.000	-0.161	-0.080	-0.013	-0.155	-0.052	-0.002	-0.152	-0.057	-0.007	-0.089	-0.040
p_{32}	0.050	0.539	0.273	0.037	-0.836	-0.200	0.043	0.793	0.425	0.072	0.398	0.155	0.032	0.684	0.285	0.070	0.318	0.174
p_{33}	0.219	0.903	0.123	0.236	2.349	0.585	0.296	0.160	-0.101	0.249	1.244	0.369	0.272	0.726	0.148	0.227	0.672	0.157
BP_{sys}	108.6	108.6	108.6	112.4	112.4	112.4	110.1	110.1	110.1	116.6	116.6	116.6	87.00	87.00	87.00	109.9	109.9	109.9
BP_{dia}	66.89	66.89	66.89	70.44	70.44	70.44	71.22	71.22	71.22	54.78	54.78	54.78	50.00	50.00	50.00	59.78	59.78	59.78

Supplemental Table C.38 Regression model input features from the normalized A, β , and PI per KCL for NHPs in the control cohort

Feature	Non-human primate ID														
	NHP 001			NHP 002			NHP 003			NHP 004			NHP 005		
	<u>A</u>	<u>β</u>	<u>PI</u>	<u>A</u>	<u>β</u>	<u>PI</u>	<u>A</u>	<u>β</u>	<u>PI</u>	<u>A</u>	<u>β</u>	<u>PI</u>	<u>A</u>	<u>β</u>	<u>PI</u>
μ	0.9801	0.7455	0.7148	0.8828	0.7716	0.6864	0.9367	0.7767	0.7296	0.8931	0.9050	0.8226	0.8797	0.7007	0.6266
σ	0.0750	0.4429	0.3999	0.1436	0.2941	0.2946	0.0859	0.3610	0.3459	0.1415	0.2310	0.2577	0.1413	0.3256	0.3146
AUC	8.8851	6.8790	6.6485	8.1797	6.9878	6.3725	8.5444	7.1521	6.8074	8.2549	8.4016	7.7747	8.1341	6.5114	5.9287
p_{10}	0.0150	-0.1362	-0.1186	-0.0044	-0.0897	-0.0776	0.0099	-0.1064	-0.0897	0.0097	-0.0510	-0.0311	0.0005	-0.0864	-0.0694
p_{11}	0.8977	1.4943	1.3669	0.9070	1.2649	1.1131	0.8823	1.3618	1.2229	0.8396	1.1856	0.9937	0.8771	1.1757	1.0080
p_{30}	-0.0015	0.0062	0.0054	-0.0014	0.0036	0.0035	0.0003	0.0018	0.0027	-0.0023	0.0001	-0.0012	-0.0018	0.0073	0.0065
p_{31}	0.0182	-0.1143	-0.1059	0.0047	-0.0674	-0.0778	-0.0149	-0.0480	-0.0691	0.0213	-0.0186	-0.0083	0.0124	-0.1363	-0.1330
p_{32}	-0.0300	0.4721	0.4808	0.0901	0.2687	0.4070	0.1430	0.2337	0.3903	0.0203	0.1435	0.1848	0.0574	0.6480	0.7038
p_{33}	0.8896	0.6869	0.5247	0.6261	0.7896	0.3777	0.6355	0.7997	0.4394	0.6641	0.8033	0.4832	0.6414	0.1887	-0.1040
BP_{sys}	88.67	88.67	88.67	106.6	106.6	106.6	145.4	145.4	145.4	120.4	120.4	120.4	114.8	114.8	114.8
BP_{dia}	57.44	57.44	57.44	62.33	62.33	62.33	62.67	62.67	62.67	68.78	68.78	68.78	69.00	69.00	69.00

Supplemental Table C.39 Regression model input features from the normalized A, β , and PI per KCL for NHPs in the IR cohort

Non-human primate ID															
Feature	NHP 006			NHP 007			NHP 008			NHP 009			NHP 010		
	<u>A</u>	<u>β</u>	<u>PI</u>	<u>A</u>	<u>β</u>	<u>PI</u>	<u>A</u>	<u>β</u>	<u>PI</u>	<u>A</u>	<u>β</u>	<u>PI</u>	<u>A</u>	<u>β</u>	<u>PI</u>
μ	0.9408	0.7482	0.6996	0.9449	0.7463	0.6887	0.9354	0.7678	0.7354	0.9271	0.9933	0.8722	0.9503	0.8198	0.7781
σ	0.1270	0.2986	0.2904	0.1305	0.3432	0.2942	0.1139	0.4392	0.4155	0.1541	0.4684	0.3370	0.0891	0.1493	0.1843
AUC	8.6154	6.9740	6.6166	8.6396	6.8816	6.4375	8.5057	7.0327	6.7744	8.5291	9.0895	8.1769	8.6904	7.5404	7.2571
p_{10}	0.0279	-0.0732	-0.0487	0.0325	-0.0930	-0.0632	-0.0185	-0.1406	-0.1292	0.0331	-0.1472	-0.0862	0.0074	-0.0206	-0.0138
p_{11}	0.7872	1.1505	0.9673	0.7662	1.2579	1.0363	1.0369	1.5408	1.4460	0.7453	1.8028	1.3462	0.9098	0.9330	0.8541
p_{30}	-0.0006	0.0055	0.0048	-0.0005	0.0086	0.0083	-0.0018	0.0026	0.0025	-0.0008	0.0050	0.0051	-0.0014	0.0033	0.0021
p_{31}	-0.0018	-0.1130	-0.1097	-0.0032	-0.1541	-0.1561	0.0191	-0.0552	-0.0568	-0.0015	-0.0888	-0.1062	0.0130	-0.0695	-0.0563
p_{32}	0.1138	0.5874	0.6467	0.1180	0.6948	0.7809	-0.0412	0.1886	0.2350	0.1343	0.2985	0.5502	0.0149	0.3949	0.3881
p_{33}	0.5741	0.1961	-0.1016	0.5635	0.2536	-0.1020	0.9643	1.0576	0.8819	0.4891	1.2460	0.4088	0.7999	0.3218	0.1874
BP_{sys}	143.6	143.6	143.6	145.2	145.2	145.2	95.00	95.00	95.00	169.4	169.4	169.4	91.33	91.33	91.33
BP_{dia}	84.22	84.22	84.22	78.00	78.00	78.00	53.22	53.22	53.22	86.11	86.11	86.11	45.50	45.50	45.50

Supplemental Table C.40 Regression model input features from the normalized A, β , and PI per KCL for NHPs in the diabetic cohort

Non-human primate ID																		
Feat.	NHP 011			NHP 012			NHP 013			NHP 014			NHP 015			NHP 016		
	<u>A</u>	<u>β</u>	<u>PI</u>	<u>A</u>	<u>β</u>	<u>PI</u>	<u>A</u>	<u>β</u>	<u>PI</u>	<u>A</u>	<u>β</u>	<u>PI</u>	<u>A</u>	<u>β</u>	<u>PI</u>	<u>A</u>	<u>β</u>	<u>PI</u>
μ	0.946	0.769	0.707	0.994	0.948	0.977	0.914	0.702	0.645	0.892	1.104	1.014	0.950	0.804	0.736	0.936	1.176	1.080
σ	0.131	0.387	0.327	0.107	0.390	0.476	0.106	0.322	0.318	0.116	0.746	0.735	0.100	0.405	0.336	0.126	0.345	0.236
AUC	8.683	7.054	6.612	9.076	8.836	9.250	8.397	6.504	6.070	8.112	9.603	8.989	8.576	7.433	6.853	8.511	10.426	9.664
p_{10}	0.026	-0.120	-0.086	0.023	-0.016	0.022	0.007	-0.086	-0.071	-0.027	-0.218	-0.224	0.031	-0.120	-0.090	0.036	-0.082	-0.036
p_{11}	0.805	1.429	1.181	0.867	1.033	0.859	0.876	1.173	1.033	1.040	2.301	2.248	0.780	1.465	1.233	0.740	1.625	1.276
p_{30}	-0.001	0.005	0.006	-0.001	-0.004	-0.005	-0.001	0.007	0.007	0.002	0.012	0.012	0.000	0.006	0.006	0.001	0.009	0.009
p_{31}	0.004	-0.095	-0.116	0.000	0.054	0.071	0.000	-0.126	-0.135	-0.038	-0.171	-0.182	-0.007	-0.120	-0.114	-0.016	-0.136	-0.151
p_{32}	0.089	0.383	0.580	0.083	-0.222	-0.223	0.093	0.615	0.715	0.204	0.371	0.499	0.083	0.536	0.566	0.161	0.456	0.635
p_{33}	0.608	0.765	0.234	0.708	1.204	1.011	0.652	0.207	-0.098	0.692	1.939	1.603	0.689	0.569	0.294	0.522	1.155	0.555
BP_{sys}	108.6	108.6	108.6	112.4	112.4	112.4	110.1	110.1	110.1	116.6	116.6	116.6	87.00	87.00	87.00	109.9	109.9	109.9
BP_{dia}	66.89	66.89	66.89	70.44	70.44	70.44	71.22	71.22	71.22	54.78	54.78	54.78	50.00	50.00	50.00	59.78	59.78	59.78

C.4 Supplemental Tables for Chapter 6

Supplemental Table C.41 Details for all enrolled patients

Patient Details	N (%)
Number of Patients	60
Age (years)	
Mean \pm SD	60 \pm 14
Sex	
Male	37 (61.7%)
Female	23 (38.3%)
Race or Ethnicity	
Black	30 (50%)
White	29 (48.3%)
Hispanic	1 (1.7%)
CKD Stage	
CKD II	9 (15%)
CKD III	18 (30%)
CKD IV	11 (18.3%)
CKD V	5 (8.3%)
ESKD	17 (28.3%)
Initial Imaging Study	
Non-contrast CT	3 (5%)
Contrast CT	2 (3.3%)
Contrast CT with renal mass protocol	12 (20%)
Non-contrast MRI	3 (5%)
Contrast MRI	3 (5%)
Conventional ultrasound	37 (61.7%)

Supplemental Table C.42 Inter-reader agreement between reader 1 and readers 2-4 regarding lesion characterization

	Reader 1	Malignant (n = 36)	Indeterminate (n = 5)	Benign (n = 22)	<i>P</i> -value
Reader 2	Malignant	26 (72%)	2 (40%)	1 (4.5%)	0.2
	Indeterminate	10 (28%)	1 (20%)	1 (4.5%)	
	Benign	0 (0%)	2 (40%)	20 (91%)	
Reader 3	Malignant	27 (75%)	1 (20%)	2 (9.1%)	0.3
	Indeterminate	6 (17%)	1 (20%)	2 (9.1%)	
	Benign	3 (8.3%)	3 (60%)	18 (82%)	
Reader 4	Malignant	27 (75%)	1 (20%)	4 (18%)	0.4
	Indeterminate	6 (17%)	4 (80%)	0 (0%)	
	Benign	3 (8.3%)	0 (0%)	18 (82%)	

Supplemental Table C.43 Inter-reader agreement between reader 2 and readers 3-4 regarding lesion characterization

	Reader 2	Malignant (n = 29)	Indeterminate (n = 12)	Benign (n = 22)	<i>P</i> -value
Reader 3	Malignant	23 (79%)	6 (50%)	1 (4.5%)	0.7
	Indeterminate	4 (14%)	4 (33%)	1 (4.5%)	
	Benign	2 (6.9%)	2 (17%)	20 (91%)	
Reader 4	Malignant	26 (90%)	4 (33%)	2 (9.1%)	0.8
	Indeterminate	2 (6.9%)	6 (50%)	2 (9.1%)	
	Benign	1 (3.4%)	2 (17%)	18 (82%)	

Supplemental Table C.44 Inter-reader agreement between reader 3 and reader 4 regarding lesion characterization

	Reader 3	Malignant (n = 30)	Indeterminate (n = 9)	Benign (n = 24)	<i>P</i> -value
Reader 4	Malignant	25 (83%)	5 (56%)	2 (8.3%)	0.6
	Indeterminate	4 (13%)	2 (22%)	4 (17%)	
	Benign	1 (3.3%)	2 (22%)	18 (75%)	

REFERENCES

- 1 The Global Cancer Observatory. Globocan 2020 Cancer Fact Sheet. World Health Organization International Agency for Research on Cancer; 2020.
- 2 Siegel RL, Miller KD, Fuchs HE, Jemal A. Cancer Statistics, 2021. *CA A Cancer J Clin*. 2021 Jan;71(1):7–33.
- 3 Division of Cancer Control and Population Sciences. Cancer Stat Facts: Cancer of Any Site. National Cancer Institute; [cited 2021 May 5]. Available from: <https://seer.cancer.gov/statfacts/html/all.html>
- 4 Siegel RL, Jemal A, Wender RC, Gansler T, Ma J, Brawley OW. An assessment of progress in cancer control: An Assessment of Progress in Cancer Control. *CA: A Cancer Journal for Clinicians*. 2018 Sep;68(5):329–39.
- 5 Zhang Y-B, Pan X-F, Chen J, Cao A, Zhang Y-G, Xia L, et al. Combined lifestyle factors, incident cancer, and cancer mortality: a systematic review and meta-analysis of prospective cohort studies. *Br J Cancer*. 2020 Mar;122(7):1085–93.
- 6 Diego Lugo, Alma L Pulido, Christos G Mihos, Omar Issa, Mike Cusnir, Sofia A Horvath, et al. The effects of physical activity on cancer prevention, treatment and prognosis: A review of the literature. *Complement Ther Med*. 2019 Jun;44:9–13.
- 7 Zielonke N, Gini A, Jansen EEL, Anttila A, Segnan N, Ponti A, et al. Evidence for reducing cancer-specific mortality due to screening for breast cancer in Europe: A systematic review. *European Journal of Cancer*. 2020 Mar;127:191–206.
- 8 Duffy SW, Field JK. Mortality Reduction with Low-Dose CT Screening for Lung Cancer. *N Engl J Med*. 2020 Feb;382(6):572–3.
- 9 Howlader N, Forjaz G, Mooradian MJ, Meza R, Kong CY, Cronin KA, et al. The Effect of Advances in Lung-Cancer Treatment on Population Mortality. *N Engl J Med*. 2020 Aug;383(7):640–9.
- 10 Howard DH, Bach PB, Berndt ER, Conti RM. Pricing in the Market for Anticancer Drugs. *Journal of Economic Perspectives*. 2015 Feb;29(1):139–62.
- 11 Yabroff KR, Lund J, Kepka D, Mariotto A. Economic Burden of Cancer in the United States: Estimates, Projections, and Future Research. *Cancer Epidemiol Biomarkers Prev*. 2011 Oct;20(10):2006–14.
- 12 Kakushadze Z, Raghubanshi R, Yu W. Estimating Cost Savings from Early Cancer Diagnosis. *Data*. 2017 Sep;2(3):30.
- 13 Papetti M, Herman IM. Mechanisms of normal and tumor-derived angiogenesis. *American Journal of Physiology-Cell Physiology*. 2002 May;282(5):C947–70.

- 14 Weis SM, Cheresh DA. Tumor angiogenesis: molecular pathways and therapeutic targets. *Nat Med*. 2011 Nov;17(11):1359–70.
- 15 Kampen KR. The mechanisms that regulate the localization and overexpression of VEGF receptor-2 are promising therapeutic targets in cancer biology. *Anti-Cancer Drugs*. 2012 Apr;23(4):347–54.
- 16 Hwang R, Varner J. The role of integrins in tumor angiogenesis. *Hematology/Oncology Clinics of North America*. 2004 Oct;18(5):991–1006.
- 17 Jin H, Varner J. Integrins: roles in cancer development and as treatment targets. *Br J Cancer*. 2004 Feb;90(3):561–5.
- 18 McCOLL BK, Stacker SA, Achen MG. Molecular regulation of the VEGF family – inducers of angiogenesis and lymphangiogenesis. *APMIS*. 112:463–80.
- 19 Holmes DI, Zachary I. The vascular endothelial growth factor (VEGF) family: angiogenic factors in health and disease. *Genome Biology*. 2005;6(2):10.
- 20 Karamysheva AF. Mechanisms of angiogenesis. *Biochemistry Moscow*. 2008 Jul;73(7):751–62.
- 21 Waldner MJ, Neurath MF. Targeting the VEGF signaling pathway in cancer therapy. *Expert Opinion on Therapeutic Targets*. 2012 Jan;16(1):5–13.
- 22 Eisenhauer EA, Therasse P, Bogaerts J, Schwartz LH, Sargent D, Ford R, et al. New response evaluation criteria in solid tumours: Revised RECIST guideline (version 1.1). *European Journal of Cancer*. 2009 Jan;45(2):228–47.
- 23 Ko C-C, Yeh L-R, Kuo Y-T, Chen J-H. Imaging biomarkers for evaluating tumor response: RECIST and beyond. *Biomark Res*. 2021 Dec;9(1):52.
- 24 Kang H, Lee HY, Lee KS, Kim J-H. Imaging-Based Tumor Treatment Response Evaluation: Review of Conventional, New, and Emerging Concepts. *Korean J Radiol*. 2012;13(4):371.
- 25 Smith AD, Lieber ML, Shah SN. Assessing Tumor Response and Detecting Recurrence in Metastatic Renal Cell Carcinoma on Targeted Therapy: Importance of Size and Attenuation on Contrast-Enhanced CT. *American Journal of Roentgenology*. 2010 Jan;194(1):157–65.
- 26 Smith AD, Shah SN, Rini BI, Lieber ML, Remer EM. Morphology, Attenuation, Size, and Structure (MASS) Criteria: Assessing Response and Predicting Clinical Outcome in Metastatic Renal Cell Carcinoma on Antiangiogenic Targeted Therapy. *American Journal of Roentgenology*. 2010 Jun;194(6):1470–8.
- 27 Fowler AM, Mankoff DA, Joe BN. Imaging Neoadjuvant Therapy Response in Breast Cancer. *Radiology*. 2017 Nov;285(2):358–75.

- 28 Stroobants S, Goeminne J, Seegers M, Dimitrijevic S, Dupont P, Nuyts J, et al. 18FDG-Positron emission tomography for the early prediction of response in advanced soft tissue sarcoma treated with imatinib mesylate (Glivec®). *European Journal of Cancer*. 2003 Sep;39(14):2012–20.
- 29 Wieder HA, Brücher BLDM, Zimmermann F, Becker K, Lordick F, Beer A, et al. Time Course of Tumor Metabolic Activity During Chemoradiotherapy of Esophageal Squamous Cell Carcinoma and Response to Treatment. *JCO*. 2004 Mar;22(5):900–8.
- 30 Zerizer I, Al-Nahhas A, Towey D, Tait P, Ariff B, Wasan H, et al. The role of early 18F-FDG PET/CT in prediction of progression-free survival after 90Y radioembolization: comparison with RECIST and tumour density criteria. *Eur J Nucl Med Mol Imaging*. 2012 Sep;39(9):1391–9.
- 31 Benjamin RS, Choi H, Macapinlac HA, Burgess MA, Patel SR, Chen LL, et al. We Should Desist Using RECIST, at Least in GIST. *JCO*. 2007 May;25(13):1760–4.
- 32 Nathan PD, Vinayan A, Stott D, Juttla J, Goh V. CT response assessment combining reduction in both size and arterial phase density correlates with time to progression in metastatic renal cancer patients treated with targeted therapies. *Cancer Biology & Therapy*. 2010 Jan;9(1):15–9.
- 33 Morgan B, Thomas AL, Dreves J, Hennig J, Buchert M, Jivan A, et al. Dynamic Contrast-Enhanced Magnetic Resonance Imaging As a Biomarker for the Pharmacological Response of PTK787/ZK 222584, an Inhibitor of the Vascular Endothelial Growth Factor Receptor Tyrosine Kinases, in Patients With Advanced Colorectal Cancer and Liver Metastases: Results From Two Phase I Studies. *JCO*. 2003 Nov;21(21):3955–64.
- 34 Tudorica A, Oh KY, Chui SY-C, Roy N, Troxell ML, Naik A, et al. Early Prediction and Evaluation of Breast Cancer Response to Neoadjuvant Chemotherapy Using Quantitative DCE-MRI. *Translational Oncology*. 2016 Feb;9(1):8–17.
- 35 Vasudev NS, Goh V, Juttla JK, Thompson VL, Larkin JMG, Gore M, et al. Changes in tumour vessel density upon treatment with anti-angiogenic agents: relationship with response and resistance to therapy. *Br J Cancer*. 2013 Sep;109(5):1230–42.
- 36 Sodickson A, Baeyens PF, Andriole KP, Prevedello LM, Nawfel RD, Hanson R, et al. Recurrent CT, Cumulative Radiation Exposure, and Associated Radiation-induced Cancer Risks from CT of Adults. *Radiology*. 2009 Apr;251(1):175–84.
- 37 Thomsen HS, Morcos SK. Risk of contrast-medium-induced nephropathy in high-risk patients undergoing MDCT – A pooled analysis of two randomized trials. *Eur Radiol*. 2009 Apr;19(4):891–7.
- 38 Marckmann P, Skov L, Rossen K, Dupont A, Damholt MB, Heaf JG, et al. Nephrogenic Systemic Fibrosis: Suspected Causative Role of Gadodiamide Used for Contrast-Enhanced Magnetic Resonance Imaging. *JASN*. 2006 Sep;17(9):2359–62.

- 39 Granata A, Zanolli L, Insalaco M, Valentino M, Pavlica P, Di Nicolò PP, et al. Contrast-enhanced ultrasound (CEUS) in nephrology: Has the time come for its widespread use? *Clin Exp Nephrol*. 2015 Aug;19(4):606–15.
- 40 Bowe B, Xie Y, Li T, Mokdad AH, Xian H, Yan Y, et al. Changes in the US Burden of Chronic Kidney Disease From 2002 to 2016: An Analysis of the Global Burden of Disease Study. *JAMA Netw Open*. 2018 Nov;1(7):e184412.
- 41 Ng JK-C, Li PK-T. Chronic kidney disease epidemic: How do we deal with it?: The global CKD epidemic. *Nephrology*. 2018 Oct;23:116–20.
- 42 Luyckx VA, Tuttle KR, Garcia-Garcia G, Gharbi MB, Heerspink HJL, Johnson DW, et al. Reducing major risk factors for chronic kidney disease. *Kidney International Supplements*. 2017 Oct;7(2):71–87.
- 43 Webster AC, Nagler EV, Morton RL, Masson P. Chronic Kidney Disease. *The Lancet*. 2017 Mar;389(10075):1238–52.
- 44 Vladu M, Clenciu D, Efrem IC, Forțofoiu M-C, Amzoloni A, Micu ST, et al. Insulin Resistance and Chronic Kidney Disease in Patients with Type 1 Diabetes Mellitus. *Journal of Nutrition and Metabolism*. 2017;2017:1–5.
- 45 National Diabetes Statistics Report 2020. Estimates of diabetes and its burden in the United States. 2020;32.
- 46 Koye DN, Magliano DJ, Nelson RG, Pavkov ME. The Global Epidemiology of Diabetes and Kidney Disease. *Advances in Chronic Kidney Disease*. 2018 Mar;25(2):121–32.
- 47 Stephens JW, Brown KE, Min T. Chronic kidney disease in type 2 diabetes: Implications for managing glycaemic control, cardiovascular and renal risk. *Diabetes Obes Metab*. 2020 Apr;22(S1):32–45.
- 48 Okada H, Tanaka M, Yasuda T, Okada Y, Norikae H, Fujita T, et al. Decreased microcirculatory function measured by perfusion index is a novel indicator of diabetic kidney disease in patients with type 2 diabetes. *J Diabetes Investig*. 2020 May;11(3):681–7.
- 49 Norton JM. Social determinants of racial and socioeconomic disparities in CKD and ESRD. *Psychosocial Aspects of Chronic Kidney Disease*. Elsevier; 2021; pp 49–88.
- 50 Zhong J, Yang H-C, Fogo AB. A perspective on chronic kidney disease progression. *American Journal of Physiology-Renal Physiology*. 2017 Mar;312(3):F375–84.
- 51 Yakush Williams JK. Management Strategies for Patients with Diabetic Kidney Disease and Chronic Kidney Disease in Diabetes. *Nursing Clinics of North America*. 2017 Dec;52(4):575–87.

- 52 Perez-Gomez MV, Bartsch L-A, Castillo-Rodriguez E, Fernandez-Prado R, Fernandez-Fernandez B, Martin-Cleary C, et al. Clarifying the concept of chronic kidney disease for non-nephrologists. *Clinical Kidney Journal*. 2019 Apr;12(2):258–61.
- 53 Lote CJ. *Principles of Renal Physiology*. New York, NY: Springer New York; 2012. DOI: 10.1007/978-1-4614-3785-7
- 54 Amorim RG, Guedes G da S, Vasconcelos SM de L, Santos JC de F. Kidney Disease in Diabetes Mellitus: Cross-Linking between Hyperglycemia, Redox Imbalance and Inflammation. *Arquivos Brasileiros de Cardiologia*. 2019 DOI: 10.5935/abc.20190077
- 55 Krishnan S, Suarez-Martinez AD, Bagher P, Gonzalez A, Liu R, Murfee WL, et al. Microvascular dysfunction and kidney disease: Challenges and opportunities? *Microcirculation*. 2021 Apr;28(3). DOI: 10.1111/micc.12661
- 56 Tanaka S, Tanaka T, Nangaku M. Hypoxia and Dysregulated Angiogenesis in Kidney Disease. *Kidney Dis*. 2015;1(1):80–9.
- 57 Hesp AC, Schaub JA, Prasad PV, Vallon V, Laverman GD, Bjornstad P, et al. The role of renal hypoxia in the pathogenesis of diabetic kidney disease: a promising target for newer renoprotective agents including SGLT2 inhibitors? *Kidney International*. 2020 Sep;98(3):579–89.
- 58 Gnudi L, Thomas SM, Viberti G. Mechanical Forces in Diabetic Kidney Disease: A Trigger for Impaired Glucose Metabolism. *JASN*. 2007 Aug;18(8):2226–32.
- 59 Hostetter TH. Hypertrophy and hyperfunction of the diabetic kidney. *J Clin Invest*. 2001 Jan;107(2):161–2.
- 60 Schoina M, Loutradis C, Theodorakopoulou M, Dimitroulas T, Triantafillidou E, Doumas M, et al. The presence of diabetes mellitus further impairs structural and functional capillary density in patients with chronic kidney disease. *Microcirculation*. 2021 Feb;28(2). DOI: 10.1111/micc.12665
- 61 Eckardt K-U, Bernhardt WW, Weidemann A, Warnecke C, Rosenberger C, Wiesener MM, et al. Role of hypoxia in the pathogenesis of renal disease. *Kidney International*. 2005 Dec;68:S46–51.
- 62 Levey AS, Becker C, Inker LA. Glomerular Filtration Rate and Albuminuria for Detection and Staging of Acute and Chronic Kidney Disease in Adults: A Systematic Review. *JAMA*. 2015 Feb;313(8):837.
- 63 Sequeira-Lopez MLS, Gomez RA. Renin Cells, the Kidney, and Hypertension. *Circ Res*. 2021 Apr;128(7):887–907.
- 64 Bakris GL. Recognition, Pathogenesis, and Treatment of Different Stages of Nephropathy in Patients With Type 2 Diabetes Mellitus. *Mayo Clinic Proceedings*. 2011 May;86(5):444–56.

- 65 Andy KH Lim. Diabetic nephropathy - complications and treatment. *Int J Nephrol Renovasc Dis.* 2014 Oct;7:361–81.
- 66 Gashti CN, Baxi PV, Whittier WL, Korbet SM. The Renal Biopsy in Chronic Kidney Disease. *Chronic Renal Disease.* Elsevier; 2020; pp 1207–22.
- 67 Gohda T, Niewczas MA, Ficociello LH, Walker WH, Skupien J, Rosetti F, et al. Circulating TNF Receptors 1 and 2 Predict Stage 3 CKD in Type 1 Diabetes. *JASN.* 2012 Mar;23(3):516–24.
- 68 Niewczas MA, Gohda T, Skupien J, Smiles AM, Walker WH, Rosetti F, et al. Circulating TNF Receptors 1 and 2 Predict ESRD in Type 2 Diabetes. *JASN.* 2012 Mar;23(3):507–15.
- 69 Lacquaniti A, Donato V, Pintaudi B, Di Vieste G, Chirico V, Buemi A, et al. “Normoalbuminuric” diabetic nephropathy: tubular damage and NGAL. *Acta Diabetol.* 2013 Dec;50(6):935–42.
- 70 Nakagawa S, Nishihara K, Miyata H, Shinke H, Tomita E, Kajiwara M, et al. Molecular Markers of Tubulointerstitial Fibrosis and Tubular Cell Damage in Patients with Chronic Kidney Disease. *PLoS ONE.* 2015 Aug;10(8):e0136994.
- 71 Gardiner L, Akintola A, Chen G, Catania JM, Vaidya V, Burghardt RC, et al. Structural Equation Modeling Highlights the Potential of Kim-1 as a Biomarker for Chronic Kidney Disease. *Am J Nephrol.* 2012;35(2):152–63.
- 72 Zhao J, Wang ZJ, Liu M, Zhu J, Zhang X, Zhang T, et al. Assessment of renal fibrosis in chronic kidney disease using diffusion-weighted MRI. *Clinical Radiology.* 2014 Nov;69(11):1117–22.
- 73 Qinghai Li, Jinning Li, Lan Zhang, Ying Chen, Minming Zhang, Fuhua Yan. Diffusion-weighted imaging in assessing renal pathology of chronic kidney disease: A preliminary clinical study. *Eur J Radiol.* 2014 May;83(7):756–62.
- 74 Hirakawa Y, Tanaka T, Nangaku M. Renal Hypoxia in CKD; Pathophysiology and Detecting Methods. *Front Physiol.* 2017 Feb;8. DOI: 10.3389/fphys.2017.00099
- 75 Inoue T, Kozawa E, Okada H, Inukai K, Watanabe S, Kikuta T, et al. Noninvasive Evaluation of Kidney Hypoxia and Fibrosis Using Magnetic Resonance Imaging. *JASN.* 2011 Aug;22(8):1429–34.
- 76 Khatir DS, Pedersen M, Jespersen B, Buus NH. Reproducibility of MRI renal artery blood flow and BOLD measurements in patients with chronic kidney disease and healthy controls: Reproducibility of RABF and BOLD in CKD. *J Magn Reson Imaging.* 2014 Nov;40(5):1091–8.
- 77 Inoue T. Morphological and functional evaluation of chronic kidney disease using magnetic resonance imaging. *WJCU.* 2014;3(3):325.

- 78 Xie L, Bennett KM, Liu C, Johnson GA, Zhang JL, Lee VS. MRI tools for assessment of microstructure and nephron function of the kidney. *American Journal of Physiology-Renal Physiology*. 2016 Dec;311(6):F1109–24.
- 79 Bennett KM, Bertram JF, Beeman SC, Gretz N. The emerging role of MRI in quantitative renal glomerular morphology. *American Journal of Physiology-Renal Physiology*. 2013 May;304(10):F1252–7.
- 80 Beeman SC, Cullen-McEwen LA, Puelles VG, Zhang M, Wu T, Baldelomar EJ, et al. MRI-based glomerular morphology and pathology in whole human kidneys. *American Journal of Physiology-Renal Physiology*. 2014 Jun;306(11):F1381–90.
- 81 Carovac A, Smajlovic F, Junuzovic D. Application of Ultrasound in Medicine. *Acta Inform Med*. 2011;19(3):168.
- 82 Jensen JA. Medical ultrasound imaging. *Progress in Biophysics and Molecular Biology*. 2007 Jan;93(1–3):153–65.
- 83 O'Brien WD. Ultrasound–biophysics mechanisms. *Progress in Biophysics and Molecular Biology*. 2007 Jan;93(1–3):212–55.
- 84 Kambe T, Nishimura K, Hibi N, Sakakibara T, Kato T, Fukui Y, et al. Clinical application of high speed B mode echocardiography. *J Clin Ultrasound*. 1977 Jun;5(3):202–7.
- 85 Sehgal CM, Weinstein SP, Arger PH, Conant EF. A Review of Breast Ultrasound. *J Mammary Gland Biol Neoplasia*. 2006 Nov;11(2):113–23.
- 86 Speets AM. Upper abdominal ultrasound in general practice: indications, diagnostic yield and consequences for patient management. *Family Practice*. 2006 Apr;23(5):507–11.
- 87 Dayton P A. Molecular ultrasound imaging using microbubble contrast agents. *Front Biosci*. 2007;12(12):5124.
- 88 Sigel B. A Brief History of Doppler Ultrasound in the Diagnosis of Peripheral Vascular Disease. *Ultrasound in Medicine & Biology*. 1998 Feb;24(2):169–76.
- 89 Evans DH, Jensen JA, Nielsen MB. Ultrasonic colour Doppler imaging. *Interface Focus*. 2011 Aug;1(4):490–502.
- 90 Gee MS, Saunders HM, Lee JC, Sanzo JF, Jenkins WT, Evans SM, et al. Doppler Ultrasound Imaging Detects Changes in Tumor Perfusion during Antivascular Therapy Associated with Vascular Anatomic Alterations. *Cancer Research*. 61:2974–82.
- 91 Erlichman DB, Weiss A, Koenigsberg M, Stein MW. Contrast enhanced ultrasound: A review of radiology applications. *Clinical Imaging*. 2020 Apr;60(2):209–15.
- 92 Cosgrove D, Lassau N. Imaging of perfusion using ultrasound. *Eur J Nucl Med Mol Imaging*. 2010 Aug;37(S1):65–85.

- 93 Yan Y, Sun X, Shen B. Contrast agents in dynamic contrast-enhanced magnetic resonance imaging. *Oncotarget*. 2017 Jun;8(26):43491–505.
- 94 Lusic H, Grinstaff MW. X-ray-Computed Tomography Contrast Agents. *Chem Rev*. 2013 Mar;113(3):1641–66.
- 95 Ignee A, Atkinson NathanSS, Schuessler G, Dietrich C. Ultrasound contrast agents. *Endosc Ultrasound*. 2016;5(6):355.
- 96 Chomas JE, Dayton P, Allen J, Morgan K, Ferrara KW. Mechanisms of contrast agent destruction. *IEEE Trans Ultrason, Ferroelect, Freq Contr*. 2001 Jan;48(1):232–48.
- 97 Lindner JR, Song J, Jayaweera AR, Sklenar J, Kaul S. Microvascular rheology of Definity microbubbles after intra-arterial and intravenous administration. *Journal of the American Society of Echocardiography*. 2002 May;15(5):396–403.
- 98 Hyvelin J-M, Tardy I, Arbogast C, Costa M, Emmel P, Helbert A, et al. Use of Ultrasound Contrast Agent Microbubbles in Preclinical Research: Recommendations for Small Animal Imaging. *Investigative Radiology*. 2013 Aug;48(8):570–83.
- 99 Sirsi SR, Borden MA. Microbubble compositions, properties and biomedical applications. *Bubble Science, Engineering & Technology*. 2009 Nov;1(1–2):3–17.
- 100 Kaya M, Feingold S, Streeter J, Hettiarachchi K, Lee AP, Dayton PA. Acoustic characterization of individual monodisperse contrast agents with an optical-acoustical system. 2009 IEEE International Ultrasonics Symposium. Rome, Italy: IEEE; 2009; pp 1813–6.
- 101 Burns PN, Wilson SR. Microbubble Contrast for Radiological Imaging: 1. Principles. *Ultrasound Quarterly*. 2006;22(1):9.
- 102 Schutt EG, Klein DH, Mattrey RM, Riess JG. Injectable Microbubbles as Contrast Agents for Diagnostic Ultrasound Imaging: The Key Role of Perfluorochemicals. *Angew Chem Int Ed*. 2003 Jul;42(28):3218–35.
- 103 Chen W-S, Matula TJ, Brayman AA, Crum LA. A comparison of the fragmentation thresholds and inertial cavitation doses of different ultrasound contrast agents. *The Journal of the Acoustical Society of America*. 2003 Jan;113(1):643–51.
- 104 Chomas JE, Dayton P, May D, Ferrara K. Threshold of fragmentation for ultrasonic contrast agents. *J Biomed Opt*. 2001;6(2):141.
- 105 Sirsi SR, Hernandez SL, Zielinski L, Blomback H, Koubaa A, Synder M, et al. Polyplex-microbubble hybrids for ultrasound-guided plasmid DNA delivery to solid tumors. *Journal of Controlled Release*. 2012 Jan;157(2):224–34.
- 106 Sugimoto K, Moriyasu F, Negishi Y, Hamano N, Oshiro H, Rognin NG, et al. Quantification in Molecular Ultrasound Imaging: A Comparative Study in Mice Between

- Healthy Liver and a Human Hepatocellular Carcinoma Xenograft. *Journal of Ultrasound in Medicine*. 2012 Dec;31(12):1909–16.
- 107 Zhao S, Kruse DE, Ferrara KW, Dayton PA. Selective imaging of adherent targeted ultrasound contrast agents. *Phys Med Biol*. 2007 Apr;52(8):2055–72.
- 108 Needles A, Couture O, Foster FS. A Method for Differentiating Targeted Microbubbles in Real Time Using Subharmonic Micro-Ultrasound and Interframe Filtering. *Ultrasound in Medicine & Biology*. 2009 Sep;35(9):1564–73.
- 109 Xiaowen Hu, Hairong Zheng, Kruse D, Sutcliffe P, Stephens D, Ferrara K. A sensitive TLRH targeted imaging technique for ultrasonic molecular imaging. *IEEE Trans Ultrason, Ferroelect, Freq Contr*. 2010 Feb;57(2):305–16.
- 110 Mauldin FW, Dhanaliwala AH, Patil AV, Hossack JA. Real-time targeted molecular imaging using singular value spectra properties to isolate the adherent microbubble signal. *Phys Med Biol*. 2012 Aug;57(16):5275–93.
- 111 Herbst EB, Unnikrishnan S, Klibanov AL, Mauldin FW, Hossack JA. Validation of Normalized Singular Spectrum Area as a Classifier for Molecularly Targeted Microbubble Adherence. *Ultrasound in Medicine & Biology*. 2019 Sep;45(9):2493–501.
- 112 Hua S. Targeting sites of inflammation: intercellular adhesion molecule-1 as a target for novel inflammatory therapies. *Front Pharmacol*. 2013 Oct;4(127):1–6.
- 113 Lindner JR, Song J, Christiansen J, Klibanov AL, Xu F, Ley K. Ultrasound Assessment of Inflammation and Renal Tissue Injury With Microbubbles Targeted to P-Selectin. *Circulation*. 2001 Oct;104(17):2107–12.
- 114 Kaufmann BA, Lewis C, Xie A, Mirza-Mohd A, Lindner JR. Detection of recent myocardial ischaemia by molecular imaging of P-selectin with targeted contrast echocardiography. *European Heart Journal*. 2007 Aug;28(16):2011–7.
- 115 Villanueva FS, Lu E, Bowry S, Kilic S, Tom E, Wang J, et al. Myocardial Ischemic Memory Imaging With Molecular Echocardiography. *Circulation*. 2007 Jan;115(3):345–52.
- 116 Weller GER, Lu E, Csikari MM, Klibanov AL, Fischer D, Wagner WR, et al. Ultrasound Imaging of Acute Cardiac Transplant Rejection With Microbubbles Targeted to Intercellular Adhesion Molecule-1. *Circulation*. 2003 Jul;108(2):218–24.
- 117 Deshpande N, Lutz AM, Ren Y, Foygel K, Tian L, Schneider M, et al. Quantification and Monitoring of Inflammation in Murine Inflammatory Bowel Disease with Targeted Contrast-enhanced US. *Radiology*. 2012 Jan;262(1):172–80.
- 118 Wang H, Hyvelin J-M, Felt SA, Guracar I, Vilches-Moure JG, Cherkaoui S, et al. US Molecular Imaging of Acute Ileitis: Anti-Inflammatory Treatment Response Monitored with Targeted Microbubbles in a Preclinical Model. *Radiology*. 2018 Oct;289(1):90–100.

- 119 Yan F, Sun Y, Mao Y, Wu M, Deng Z, Li S, et al. Ultrasound Molecular Imaging of Atherosclerosis for Early Diagnosis and Therapeutic Evaluation through Leucocyte-like Multiple Targeted Microbubbles. *Theranostics*. 2018;8(7):1879–91.
- 120 Bachawal SV, Jensen KC, Lutz AM, Gambhir SS, Tranquart F, Tian L, et al. Earlier Detection of Breast Cancer with Ultrasound Molecular Imaging in a Transgenic Mouse Model. *Cancer Research*. 2013 Mar;73(6):1689–98.
- 121 Ellegala DB, Leong-Poi H, Carpenter JE, Klibanov AL, Kaul S, Shaffrey ME, et al. Imaging Tumor Angiogenesis With Contrast Ultrasound and Microbubbles Targeted to $\alpha_v\beta_3$. *Circulation*. 2003 Jul;108(3):336–41.
- 122 Grouls C, Hatting M, Rix A, Pochon S, Lederle W, Tardy I, et al. Liver Dysplasia: US Molecular Imaging with Targeted Contrast Agent Enables Early Assessment. *Radiology*. 2013 May;267(2):487–95.
- 123 Pysz MA, Machtaler SB, Seeley ES, Lee JJ, Brentnall TA, Rosenberg J, et al. Vascular Endothelial Growth Factor Receptor Type 2–targeted Contrast-enhanced US of Pancreatic Cancer Neovasculature in a Genetically Engineered Mouse Model: Potential for Earlier Detection. *Radiology*. 2015 Mar;274(3):790–9.
- 124 Pysz MA, Foygel K, Rosenberg J, Gambhir SS, Schneider M, Willmann JK. Antiangiogenic Cancer Therapy: Monitoring with Molecular US and a Clinically Translatable Contrast Agent (BR55). *Radiology*. 2010 Aug;256(2):519–27.
- 125 Sirsi SR, Flexman ML, Vlachos F, Huang J, Hernandez SL, Kim HK, et al. Contrast Ultrasound Imaging for Identification of Early Responder Tumor Models to Anti-Angiogenic Therapy. *Ultrasound in Medicine & Biology*. 2012 Jun;38(6):1019–29.
- 126 Zhou J, Wang H, Zhang H, Lutz AM, Tian L, Hristov D, et al. VEGFR2-Targeted Three-Dimensional Ultrasound Imaging Can Predict Responses to Antiangiogenic Therapy in Preclinical Models of Colon Cancer. *Cancer Res*. 2016 Jul;76(14):4081–9.
- 127 Rojas JD, Lin F, Chiang Y-C, Chytil A, Chong DC, Bautch VL, et al. Ultrasound Molecular Imaging of VEGFR-2 in Clear-Cell Renal Cell Carcinoma Tracks Disease Response to Antiangiogenic and Notch-Inhibition Therapy. *Theranostics*. 2018;8(1):141–55.
- 128 Dayton P, Klibanov A, Brandenburger G, Ferrara K. Acoustic radiation force in vivo: a mechanism to assist targeting of microbubbles. *Ultrasound in Medicine & Biology*. 1999 Oct;25(8):1195–201.
- 129 Rychak JJ, Klibanov AL, Hossack JA. Acoustic radiation force enhances targeted delivery of ultrasound contrast microbubbles: in vitro verification. *IEEE Trans Ultrason, Ferroelect, Freq Contr*. 2005 Mar;52(3):421–33.
- 130 Dayton PA, Morgan KE, Ferrara KW. A Preliminary Evaluation of the Effects of Primary and Secondary Radiation Forces on Acoustic Contrast Agents. 1997;44(6):14.

- 131 Frinking PJA, Tardy I, Théraulaz M, Arditi M, Powers J, Pochon S, et al. Effects of Acoustic Radiation Force on the Binding Efficiency of BR55, a VEGFR2-Specific Ultrasound Contrast Agent. *Ultrasound in Medicine & Biology*. 2012 Aug;38(8):1460–9.
- 132 Leighton TG, Walton AJ, Pickworth MJW. Primary Bjerknes forces. *Eur J Phys*. 1990 Jan;11(1):47–50.
- 133 Lee CP, Wang TG. Acoustic radiation force on a bubble. *The Journal of the Acoustical Society of America*. 1993 Mar;93(3):1637–40.
- 134 Dayton PA, Morgan KE, Klibanov AL, Brandenburger GH, Ferrara KW. Optical and acoustical observations of the effects of ultrasound on contrast agents. *IEEE Trans Ultrason, Ferroelect, Freq Contr*. 1999 Jan;46(1):220–32.
- 135 Dayton PA, Allen JS, Ferrara KW. The magnitude of radiation force on ultrasound contrast agents. *The Journal of the Acoustical Society of America*. 2002 Nov;112(5):2183–92.
- 136 Rychak JJ, Klibanov AL, Ley KF, Hossack JA. Enhanced Targeting of Ultrasound Contrast Agents Using Acoustic Radiation Force. *Ultrasound in Medicine & Biology*. 2007 Jul;33(7):1132–9.
- 137 Zhao S, Borden M, Bloch SH, Kruse D, Ferrara KW, Dayton PA. Radiation-Force Assisted Targeting Facilitates Ultrasonic Molecular Imaging. *Mol Imaging*. 2004 Jul;3(3):135–48.
- 138 Gessner RC, Streeter JE, Kothadia R, Feingold S, Dayton PA. An In Vivo Validation of the Application of Acoustic Radiation Force to Enhance the Diagnostic Utility of Molecular Imaging Using 3-D Ultrasound. *Ultrasound in Medicine & Biology*. 2012 Apr;38(4):651–60.
- 139 Tartis MS, Kruse DE, Zheng H, Zhang H, Kheirrolomoom A, Marik J, et al. Dynamic microPET imaging of ultrasound contrast agents and lipid delivery. *Journal of Controlled Release*. 2008 Nov;131(3):160–6.
- 140 Willmann JK, Cheng Z, Davis C, Lutz AM, Schipper ML, Nielsen CH, et al. Targeted Microbubbles for Imaging Tumor Angiogenesis: Assessment of Whole-Body Biodistribution with Dynamic Micro-PET in Mice. *Radiology*. 2008 Oct;249(1):212–9.
- 141 Chen CC, Sirsi SR, Homma S, Borden MA. Effect of Surface Architecture on In Vivo Ultrasound Contrast Persistence of Targeted Size-Selected Microbubbles. *Ultrasound in Medicine & Biology*. 2012 Mar;38(3):492–503.
- 142 Chen CC, Borden MA. Ligand Conjugation to Bimodal Poly(ethylene glycol) Brush Layers on Microbubbles. *Langmuir*. 2010 Aug;26(16):13183–94.
- 143 Chen CC, Borden MA. The role of poly(ethylene glycol) brush architecture in complement activation on targeted microbubble surfaces. *Biomaterials*. 2011 Sep;32(27):6579–87.

- 144 Borden MA, Sarantos MR, Stieger SM, Simon SI, Ferrara KW, Dayton PA. Ultrasound Radiation Force Modulates Ligand Availability on Targeted Contrast Agents. *Mol Imaging*. 2006 Jul;5(3):7290.2006.00016.
- 145 Borden MA, Zhang H, Gillies RJ, Dayton PA, Ferrara KW. A stimulus-responsive contrast agent for ultrasound molecular imaging. *Biomaterials*. 2008 Feb;29(5):597–606.
- 146 Borden MA, Streeter JE, Sirsi SR, Dayton PA. In Vivo Demonstration of Cancer Molecular Imaging with Ultrasound Radiation Force and Buried-Ligand Microbubbles. *Mol Imaging*. 2013 Sep;12(6):7290.2013.00052.
- 147 Talu E, Hettiarachchi K, Zhao S, Powell RL, Lee AP, Longo ML, et al. Tailoring the Size Distribution of Ultrasound Contrast Agents: Possible Method for Improving Sensitivity in Molecular Imaging. *Mol Imaging*. 2007 Nov;6(6):7290.2007.00034.
- 148 Streeter JE, Gessner R, Miles I, Dayton PA. Improving Sensitivity in Ultrasound Molecular Imaging by Tailoring Contrast Agent Size Distribution: In Vivo Studies. *Mol Imaging*. 2010 Mar;9(2):7290.2010.00005.
- 149 Kabalnov A, Bradley J, Flaim S, Klein D, Pelura T, Peters B, et al. Dissolution of multicomponent microbubbles in the bloodstream: 2. experiment. *Ultrasound in Medicine & Biology*. 1998 Jun;24(5):751–60.
- 150 Borden MA, Longo ML. Dissolution Behavior of Lipid Monolayer-Coated, Air-Filled Microbubbles: Effect of Lipid Hydrophobic Chain Length. *Langmuir*. 2002 Nov;18(24):9225–33.
- 151 Wang H, Kaneko OF, Tian L, Hristov D, Willmann JK. Three-Dimensional Ultrasound Molecular Imaging of Angiogenesis in Colon Cancer Using a Clinical Matrix Array Ultrasound Transducer: Investigative Radiology. 2015 May;50(5):322–9.
- 152 Metoki R, Moriyasu F, Kamiyama N, Sugimoto K, Iijima H, Xu H, et al. Quantification of hepatic parenchymal blood flow by contrast ultrasonography with flash-replenishment imaging. *Ultrasound in Medicine & Biology*. 2006 Oct;32(10):1459–66.
- 153 Zierler K. Indicator Dilution Methods for Measuring Blood Flow, Volume, and Other Properties of Biological Systems: A Brief History and Memoir. *Annals of Biomedical Engineering*. 2000 Aug;28(8):836–48.
- 154 Bassingthwaite JB. Blood Flow and Diffusion through Mammalian Organs. *Science*. 1970 Mar;167(3923):1347–53.
- 155 Greis C. Quantitative evaluation of microvascular blood flow by contrast-enhanced ultrasound (CEUS). *Clinical Hemorheology and Microcirculation*. 2011;49(1–4):137–49.
- 156 Strouthos C, Lampaskis M, Sboros V, Mcneilly A, Averkiou M. Indicator dilution models for the quantification of microvascular blood flow with bolus administration of ultrasound contrast agents. *IEEE Trans Ultrason, Ferroelect, Freq Contr*. 2010 Jun;57(6):1296–310.

- 157 Harabis V, Kolar R, Mezl M, Jirik R. Comparison and evaluation of indicator dilution models for bolus of ultrasound contrast agents. *Physiol Meas*. 2013 Feb;34(2):151–62.
- 158 Akhbardeh A, Sagreiya H, El Kaffas A, Willmann JK, Rubin DL. A multi-model framework to estimate perfusion parameters using contrast-enhanced ultrasound imaging. *Med Phys*. 2019 Feb;46(2):590–600.
- 159 Krix M, Kiessling F, Farhan N, Schmidt K, Hoffend J, Delorme S. A multivessel model describing replenishment kinetics of ultrasound contrast agent for quantification of tissue perfusion. *Ultrasound in Medicine & Biology*. 2003 Oct;29(10):1421–30.
- 160 Arditi M, Frinking PJA, Xiang Zhou, Rognin NG. A new formalism for the quantification of tissue perfusion by the destruction-replenishment method in contrast ultrasound imaging. *IEEE Trans Ultrason, Ferroelect, Freq Contr*. 2006 Jun;53(6):1118–29.
- 161 Wei K, Jayaweera AR, Firoozan S, Linka A, Skyba DM, Kaul S. Quantification of Myocardial Blood Flow With Ultrasound-Induced Destruction of Microbubbles Administered as a Constant Venous Infusion. *Circulation*. 1998 Feb;97(5):473–83.
- 162 Schlosser T, Pohl C, Veltmann C, Lohmaier S, Goenechea J, Ehlgen A, et al. Feasibility of the flash-replenishment concept in renal tissue: which parameters affect the assessment of the contrast replenishment? *Ultrasound in Medicine & Biology*. 2001 Jul;27(7):937–44.
- 163 Emanuel AL, Meijer RI, Poelgeest E, Spoor P, Serné EH, Eringa EC. Contrast-enhanced ultrasound for quantification of tissue perfusion in humans. *Microcirculation*. 2020 Jan;27(1). DOI: 10.1111/micc.12588
- 164 Selby NM, Williams JP, Phillips BE. Application of dynamic contrast enhanced ultrasound in the assessment of kidney diseases. *Current Opinion in Nephrology & Hypertension*. 2021 Jan;30(1):138–43.
- 165 Averkiou MA, Juang EK, Gallagher MK, Cuevas MA, Wilson SR, Barr RG, et al. Evaluation of the Reproducibility of Bolus Transit Quantification With Contrast-Enhanced Ultrasound Across Multiple Scanners and Analysis Software Packages—A Quantitative Imaging Biomarker Alliance Study. *Invest Radiol*. 2020 Oct;55(10):643–56.
- 166 Gauthier TP, Chebil M, Peronneau P, Lassau N. In vitro evaluation of the impact of ultrasound scanner settings and contrast bolus volume on time–intensity curves. *Ultrasonics*. 2012 Jan;52(1):12–9.
- 167 Lassau N, Coiffier B, Faivre L, Benatsou B, Bidault S, Girard E, et al. Study of Inpatient Variability and Reproducibility of Quantitative Tumor Perfusion Parameters Evaluated With Dynamic Contrast-Enhanced Ultrasonography. *Invest Radiol*. 2017 Mar;52(3):148–54.
- 168 Gauthier M. Estimation of intra-operator variability in perfusion parameter measurements using DCE-US. *WJR*. 2011;3(3):70.

- 169 Stock E, Duchateau L, Saunders JH, Volckaert V, Polis I, Vanderperren K. Repeatability of Contrast-Enhanced Ultrasonography of the Kidneys in Healthy Cats. *Ultrasound in Medicine & Biology*. 2018 Feb;44(2):426–33.
- 170 Ignee A, Jedrejczyk M, Schuessler G, Jakubowski W, Dietrich CF. Quantitative contrast enhanced ultrasound of the liver for time intensity curves—Reliability and potential sources of errors. *European Journal of Radiology*. 2010 Jan;73(1):153–8.
- 171 Tranquart F, Mercier L, Frinking P, Gaud E, Arditi M. Perfusion Quantification in Contrast-Enhanced Ultrasound (CEUS) – Ready for Research Projects and Routine Clinical Use. *Ultraschall in Med*. 2012 Jun;33(S 01):S31–8.
- 172 Williams R, Hudson JM, Lloyd BA, Sureshkumar AR, Lueck G, Milot L, et al. Dynamic Microbubble Contrast- enhanced US to Measure Tumor Response to Targeted Therapy: 2011;260(2):10.
- 173 Bracco Suisse. VueBox Quantification Toolbox: Instructions for Use. 2018
- 174 Stock E, Paepe D, Daminet S, Vandermeulen E, Duchateau L, Saunders JH, et al. Contrast-Enhanced Ultrasound Examination for the Assessment of Renal Perfusion in Cats with Chronic Kidney Disease. *J Vet Intern Med*. 2018 Jan;32(1):260–6.
- 175 Liu DJX, Stock E, Broeckx BJG, Daminet S, Meyer E, Delanghe JR, et al. Weight-gain induced changes in renal perfusion assessed by contrast-enhanced ultrasound precede increases in urinary protein excretion suggestive of glomerular and tubular injury and normalize after weight-loss in dogs. *PLoS ONE*. 2020 Apr;15(4):e0231662.
- 176 Dietrich C, Averkiou M, Correas J-M, Lassau N, Leen E, Piscaglia F. An EFSUMB Introduction into Dynamic Contrast-Enhanced Ultrasound (DCE-US) for Quantification of Tumour Perfusion. *Ultraschall in Med*. 2012 Aug;33(04):344–51.
- 177 Nicholas Elie, Nathalie Lassau, Pierre Peronneau, Valerie Rouffiac. Method and System for Quantification of Tumoral Vascularization. 2008 May;41.
- 178 Mannucci T, Lippi I, Rota A, Citi S. Contrast enhancement ultrasound of renal perfusion in dogs with acute kidney injury. *J Small Anim Pract*. 2019 Aug;60(8):471–6.
- 179 Xie F, Wan W-B, Fei X, Zhang M-B, Zhang Y, Wang H-W, et al. Repeatability of the “flash-replenishment” method in contrast-enhanced ultrasound for the quantitative assessment of hepatic microvascular perfusion. *Braz J Med Biol Res*. 2018;51(4):e7058.
- 180 Hudson JM, Leung K, Burns PN. The Lognormal Perfusion Model for Disruption Replenishment Measurements of Blood Flow: In Vivo Validation. *Ultrasound in Medicine & Biology*. 2011 Oct;37(10):1571–8.
- 181 Krix M, Plathow C, Kiessling F, Herth F, Karcher A, Essig M, et al. Quantification of perfusion of liver tissue and metastases using a multivessel model for replenishment

- kinetics of ultrasound contrast agents. *Ultrasound in Medicine & Biology*. 2004 Oct;30(10):1355–63.
- 182 Hudson JM, Karshafian R, Burns PN. Quantification of Flow Using Ultrasound and Microbubbles: A Disruption Replenishment Model Based on Physical Principles. *Ultrasound in Medicine & Biology*. 2009 Dec;35(12):2007–20.
 - 183 Lacerda Q, Tantawi M, Leeper DB, Wheatley MA, Eisenbrey JR. Emerging Applications of Ultrasound-Contrast Agents in Radiation Therapy. *Ultrasound in Medicine & Biology*. 2021 Jun;47(6):1465–74.
 - 184 El Kaffas A, Giles A, Czarnota GJ. Dose-dependent response of tumor vasculature to radiation therapy in combination with Sunitinib depicted by three-dimensional high-frequency power Doppler ultrasound. *Angiogenesis*. 2013 Apr;16(2):443–54.
 - 185 McNabb E, Al-Mahrouki A, Law N, McKay S, Tarapacki C, Hussein F, et al. Ultrasound-stimulated microbubble radiation enhancement of tumors: Single-dose and fractionated treatment evaluation. *PLoS ONE*. 2020 Sep;15(9):e0239456.
 - 186 Korpela E, Liu SK. Endothelial perturbations and therapeutic strategies in normal tissue radiation damage. *Radiat Oncol*. 2014 Dec;9(1):266.
 - 187 Ren Y, Fleischmann D, Foygel K, Molvin L, Lutz AM, Koong AC, et al. Antiangiogenic and Radiation Therapy: Early Effects on In Vivo Computed Tomography Perfusion Parameters in Human Colon Cancer Xenografts in Mice. *Investigative Radiology*. 2012 Jan;47(1):25–32.
 - 188 Natalia Arteaga-Marrero, Jose F Mainou-Gomez, Cecilie Brekke Rygh, Nataliya Lutay, Dieter Roehrich, Rolf K Reed, et al. Radiation treatment monitoring with DCE-US in CWR22 prostate tumor xenografts. *Acta Radiol*. 2019 Jun;60(6):788–97.
 - 189 Kasoji SK, Rivera JN, Gessner RC, Chang SX, Dayton PA. Early Assessment of Tumor Response to Radiation Therapy using High-Resolution Quantitative Microvascular Ultrasound Imaging. *Theranostics*. 2018;8(1):156–68.
 - 190 Fix SM, Nyankima AG, McSweeney MD, Tsuruta JK, Lai SK, Dayton PA. Accelerated Clearance of Ultrasound Contrast Agents Containing Polyethylene Glycol is Associated with the Generation of Anti-Polyethylene Glycol Antibodies. *Ultrasound in Medicine & Biology*. 2018 Jun;44(6):1266–80.
 - 191 Streeter JE, Gessner RC, Tsuruta J, Feingold S, Dayton PA. Assessment of Molecular Imaging of Angiogenesis with Three-Dimensional Ultrasonography. *Mol Imaging*. 2011 Nov;10(6):7290.2011.00015.
 - 192 Westfall PH, Young SS, Wright SP. On Adjusting P-Values for Multiplicity. *Biometrics*. 1993 Sep;49(3):941.

- 193 S. Paul Wright. Adjusted P-values for Simultaneous Inference. *Biometrics*. 1992 Dec;48:1005–13.
- 194 Paling MR, Shawker TH, Dwyer A. Ultrasonic evaluation of therapeutic response in tumors: Its value and implications. *J Clin Ultrasound*. 1981 Jul;9(6):281–8.
- 195 Talkington A, Durrett R. Estimating Tumor Growth Rates In Vivo. *Bull Math Biol*. 2015 Oct;77(10):1934–54.
- 196 Welsh JL, Bodeker K, Fallon E, Bhatia SK, Buatti JM, Cullen JJ. Comparison of response evaluation criteria in solid tumors with volumetric measurements for estimation of tumor burden in pancreatic adenocarcinoma and hepatocellular carcinoma. *The American Journal of Surgery*. 2012 Nov;204(5):580–5.
- 197 Guo S, Jiang X, Mao B, Li Q-X. The design, analysis and application of mouse clinical trials in oncology drug development. *BMC Cancer*. 2019 Dec;19(1):718.
- 198 Feshitan JA, Chen CC, Kwan JJ, Borden MA. Microbubble size isolation by differential centrifugation. *Journal of Colloid and Interface Science*. 2009 Jan;329(2):316–24.
- 199 Agard NJ, Prescher JA, Bertozzi CR. A Strain-Promoted [3 + 2] Azide–Alkyne Cycloaddition for Covalent Modification of Biomolecules in Living Systems. *J Am Chem Soc*. 2004 Nov;126(46):15046–7.
- 200 Slagle CJ, Thamm DH, Randall EK, Borden MA. Click Conjugation of Cloaked Peptide Ligands to Microbubbles. *Bioconjugate Chem*. 2018 May;29(5):1534–43.
- 201 Yanagisawa K, Moriyasu F, Miyahara T, Yuki M, Iijima H. Phagocytosis of ultrasound contrast agent microbubbles by Kupffer cells. *Ultrasound in Medicine & Biology*. 2007 Feb;33(2):318–25.
- 202 Liu YN, Khangura J, Xie A, Belcik JT, Qi Y, Davidson BP, et al. Renal Retention of Lipid Microbubbles: A Potential Mechanism for Flank Discomfort During Ultrasound Contrast Administration. *Journal of the American Society of Echocardiography*. 2013 Dec;26(12):1474–81.
- 203 Streeter JE, Herrera-Loeza SG, Neel NF, Yeh JJ, Dayton PA. A Comparative Evaluation of Ultrasound Molecular Imaging, Perfusion Imaging, and Volume Measurements in Evaluating Response to Therapy in Patient-Derived Xenografts. *Technol Cancer Res Treat*. 2013 Aug;12(4):311–21.
- 204 Wang H, Lutz AM, Hristov D, Tian L, Willmann JK. Intra-Animal Comparison between Three-dimensional Molecularly Targeted US and Three-dimensional Dynamic Contrast-enhanced US for Early Antiangiogenic Treatment Assessment in Colon Cancer. *Radiology*. 2017 Feb;282(2):443–52.
- 205 Klein J, Tran W, Lai P, Al-Mahrouki A, Giles A, Czarnota GJ. Effect of Treatment Sequencing on the Tumor Response to Combined Treatment With ULTRASOUND-

- STIMULATED Microbubbles and Radiotherapy. *J Ultrasound Med.* 2020 Dec;39(12):2415–25.
- 206 Smeenge M, Tranquart F, Mannaerts CK, de Reijke TM, van de Vijver MJ, Laguna MP, et al. First-in-Human Ultrasound Molecular Imaging With a VEGFR2-Specific Ultrasound Molecular Contrast Agent (BR55) in Prostate Cancer: A Safety and Feasibility Pilot Study. *Investigative Radiology.* 2017 Jul;52(7):419–27.
 - 207 Willmann JK, Bonomo L, Testa AC, Rinaldi P, Rindi G, Valluru KS, et al. Ultrasound Molecular Imaging With BR55 in Patients With Breast and Ovarian Lesions: First-in-Human Results. *JCO.* 2017 Jul;35(19):2133–40.
 - 208 Lum AFH, Borden MA, Dayton PA, Kruse DE, Simon SI, Ferrara KW. Ultrasound radiation force enables targeted deposition of model drug carriers loaded on microbubbles. *Journal of Controlled Release.* 2006 Mar;111(1–2):128–34.
 - 209 Morgan KE, Allen JS, Dayton PA, Chomas JE, Klibaov AL, Ferrara KW. Experimental and theoretical evaluation of microbubble behavior: effect of transmitted phase and bubble size. *IEEE Trans Ultrason, Ferroelect, Freq Contr.* 2000 Nov;47(6):1494–509.
 - 210 van de Meer SM, Dollet B, Voormolen MM, Chin CT, Bouakaz A, de Jong N, et al. Microbubble spectroscopy of ultrasound contrast agents. *J Acoust Soc Am.* 2007;121(1):648–56.
 - 211 Qin S, Ferrara KW. The Natural Frequency of Nonlinear Oscillation of Ultrasound Contrast Agents in Microvessels. *Ultrasound in Medicine & Biology.* 2007 Jul;33(7):1140–8.
 - 212 Hostetter TH, Rennke HG, Brenner BM. The case for intrarenal hypertension in the initiation and progression of diabetic and other glomerulopathies. *The American Journal of Medicine.* 1982 Mar;72(3):375–80.
 - 213 Wymer DC, Wymer DTG. Imaging the Chronic Kidney Disease Patient. *Chronic Renal Disease.* Elsevier; 2020; pp 1321–31.
 - 214 Ma F, Cang Y, Zhao B, Liu Y, Wang C, Liu B, et al. Contrast-enhanced ultrasound with SonoVue could accurately assess the renal microvascular perfusion in diabetic kidney damage. *Nephrology Dialysis Transplantation.* 2012 Jul;27(7):2891–8.
 - 215 Schneider AG, Hofmann L, Wuerzner G, Glatz N, Maillard M, Meuwly J-Y, et al. Renal perfusion evaluation with contrast-enhanced ultrasonography. *Nephrology Dialysis Transplantation.* 2012 Feb;27(2):674–81.
 - 216 Weinstein JR, Anderson S. The Aging Kidney: Physiological Changes. *Advances in Chronic Kidney Disease.* 2010 Jul;17(4):302–7.
 - 217 Toyama T, Kitagawa K, Oshima M, Kitajima S, Hara A, Iwata Y, et al. Age differences in the relationships between risk factors and loss of kidney function: a general population cohort study. *BMC Nephrol.* 2020 Dec;21(1):477.

- 218 Blaufox MD, Fromowitz A, Lee HB, Meng C-H, Elkin M. Renal Blood Flow and Renin Activity in Renal Venous Blood in Essential Hypertension. *Circulation Research*. 1970 Dec;27(6):913–20.
- 219 Burke M, Pabbidi M, Farley J, Roman R. Molecular Mechanisms of Renal Blood Flow Autoregulation. *CVP*. 2014 Dec;12(6):845–58.
- 220 Janmaat CJ, van Diepen M, Tsonaka R, Jager KJ, Zoccali C, Dekker FW. Pitfalls of linear regression for estimating slopes over time and how to avoid them by using linear mixed-effects models. *Nephrology Dialysis Transplantation*. 2019 Apr;34(4):561–6.
- 221 Kogan P, Johnson KA, Feingold S, Garrett N, Guracar I, Arendshorst WJ, et al. Validation of Dynamic Contrast-Enhanced Ultrasound in Rodent Kidneys as an Absolute Quantitative Method for Measuring Blood Perfusion. *Ultrasound in Medicine & Biology*. 2011 Jun;37(6):900–8.
- 222 Kalantarinia K, Belcik JT, Patrie JT, Wei K. Real-time measurement of renal blood flow in healthy subjects using contrast-enhanced ultrasound. *American Journal of Physiology-Renal Physiology*. 2009 Oct;297(4):F1129–34.
- 223 Barrera-Chimal J, Jaisser F. Pathophysiologic mechanisms in diabetic kidney disease: A focus on current and future therapeutic targets. *Diabetes Obes Metab*. 2020 Apr;22(S1):16–31.
- 224 Vallon V, Thomson SC. Renal Function in Diabetic Disease Models: The Tubular System in the Pathophysiology of the Diabetic Kidney. *Annu Rev Physiol*. 2012 Mar;74(1):351–75.
- 225 Mora-Fernández C, Domínguez-Pimentel V, de Fuentes MM, Górriz JL, Martínez-Castelao A, Navarro-González JF. Diabetic kidney disease: from physiology to therapeutics: Diabetic kidney disease: from physiology to therapeutics. *The Journal of Physiology*. 2014 Sep;592(18):3997–4012.
- 226 Lin Y-C, Chang Y-H, Yang S-Y, Wu K-D, Chu T-S. Update of pathophysiology and management of diabetic kidney disease. *Journal of the Formosan Medical Association*. 2018 Aug;117(8):662–75.
- 227 Sharma K, Rupprecht C, Caroli A, Aparicio MC, Remuzzi A, Baust M, et al. Automatic Segmentation of Kidneys using Deep Learning for Total Kidney Volume Quantification in Autosomal Dominant Polycystic Kidney Disease. *Sci Rep*. 2017 Dec;7(1):2049.
- 228 Jin C, Shi F, Xiang D, Jiang X, Zhang B, Wang X, et al. 3D Fast Automatic Segmentation of Kidney Based on Modified AAM and Random Forest. *IEEE Trans Med Imaging*. 2016 Jun;35(6):1395–407.
- 229 Scelo G, Larose TL. Epidemiology and Risk Factors for Kidney Cancer. *JCO*. 2018 Dec;36(36):3574–81.

- 230 Tsuzuki T, Iwata H, Murase Y, Takahara T, Ohashi A. Renal tumors in end-stage renal disease: A comprehensive review. *Int J Urol*. 2018 Sep;25(9):780–6.
- 231 Wong G, Hayen A, Chapman JR, Webster AC, Wang JJ, Mitchell P, et al. Association of CKD and Cancer Risk in Older People. *JASN*. 2009 Jun;20(6):1341–50.
- 232 Lowrance WT, Ordoñez J, Udaltsova N, Russo P, Go AS. CKD and the Risk of Incident Cancer. *JASN*. 2014 Oct;25(10):2327–34.
- 233 Larsson SC, Wolk A. Diabetes mellitus and incidence of kidney cancer: a meta-analysis of cohort studies. *Diabetologia*. 2011 May;54(5):1013–8.
- 234 Hofmann JN, Corley DA, Zhao WK, Colt JS, Shuch B, Chow W-H, et al. Chronic Kidney Disease and Risk of Renal Cell Carcinoma: Differences by Race. *Epidemiology*. 2015 Jan;26(1):59–67.
- 235 Russo P. End Stage and Chronic Kidney Disease: Associations with Renal Cancer. *Front Oncol*. 2012;2. DOI: 10.3389/fonc.2012.00028
- 236 Ray S, Cheaib JG, Pierorazio PM. Active Surveillance for Small Renal Masses. *Rev Urol*. 2020;22(1):9–16.
- 237 Israel GM, Bosniak MA. How I Do It: Evaluating Renal Masses. *Radiology*. 2005 Aug;236(2):441–50.
- 238 Mittal M, Sureka B. Solid renal masses in adults. *Indian J Radiol Imaging*. 2016;26(4):429.
- 239 Heilbrun ME, Remer EM, Casalino DD, Beland MD, Bishoff JT, Blaufox MD, et al. ACR Appropriateness Criteria Indeterminate Renal Mass. *Journal of the American College of Radiology*. 2015 Apr;12(4):333–41.
- 240 Nicolau C, Antunes N, Paño B, Sebastia C. Imaging Characterization of Renal Masses. *Medicina*. 2021 Jan;57(1):51.
- 241 Agnello F, Albano D, Micci G, Di Buono G, Agrusa A, Salvaggio G, et al. CT and MR imaging of cystic renal lesions. *Insights Imaging*. 2020 Dec;11(1):5.
- 242 Warren KS, McFarlane J. The Bosniak classification of renal cystic masses. *BJU Int*. 2005 May;95(7):939–42.
- 243 Siegel CL, McFarland EG, Brink JA, Fisher AJ, Humphrey P, Heiken JP. CT of cystic renal masses: analysis of diagnostic performance and interobserver variation. *Am J Roentgenol*. 1997;169(3):813–8.
- 244 Sevcenco S, Spick C, Helbich TH, Heinz G, Shariat SF, Klingler HC, et al. Malignancy rates and diagnostic performance of the Bosniak classification for the diagnosis of cystic renal lesions in computed tomography – a systematic review and meta-analysis. *Eur Radiol*. 2017 Jun;27(6):2239–47.

- 245 Chen Y, Wu N, Xue T, Hao Y, Dai J. Comparison of contrast-enhanced sonography with MRI in the diagnosis of complex cystic renal masses: Comparison of CEUS and MRI. *J Clin Ultrasound*. 2015 May;43(4):203–9.
- 246 Bai X, Sun S-M, Xu W, Kang H-H, Li L, Jin Y-Q, et al. MRI-based Bosniak Classification of Cystic Renal Masses, Version 2019: Interobserver Agreement, Impact of Readers' Experience, and Diagnostic Performance. *Radiology*. 2020 Dec;297(3):597–605.
- 247 Wang ZJ, Nikolaidis P, Khatri G, Dogra VS, Ganeshan D, Goldfarb S, et al. ACR Appropriateness Criteria® Indeterminate Renal Mass. *Journal of the American College of Radiology*. 2020 Nov;17(11):S415–28.
- 248 Chang EH, Chong WK, Kasoji SK, Dayton PA, Rathmell WK. Management of Indeterminate Cystic Kidney Lesions: Review of Contrast-enhanced Ultrasound as a Diagnostic Tool. *Urology*. 2016 Jan;87:1–10.
- 249 Harvey CJ, Alsafi A, Kuzmich S, Ngo A, Papadopoulou I, Lakhani A, et al. Role of US Contrast Agents in the Assessment of Indeterminate Solid and Cystic Lesions in Native and Transplant Kidneys. *RadioGraphics*. 2015 Sep;35(5):1419–30.
- 250 Schwarze V, Rübenthaler J, Čečátka S, Marschner C, Froelich MF, Sabel BO, et al. Contrast-Enhanced Ultrasound (CEUS) for the Evaluation of Bosniak III Complex Renal Cystic Lesions—A 10-Year Specialized European Single-Center Experience with Histopathological Validation. *Medicina*. 2020 Dec;56(12):692.
- 251 Bertolotto M, Bucci S, Valentino M, Currò F, Sachs C, Cova MA. Contrast-enhanced ultrasound for characterizing renal masses. *European Journal of Radiology*. 2018 Aug;105:41–8.
- 252 Correas J-M, Claudon M. The Kidney: Imaging with Microbubble Contrast Agents. *Ultrasound Quarterly*. 2006;22(1):14.
- 253 Barr RG, Peterson C, Hindi A. Evaluation of Indeterminate Renal Masses with Contrast-enhanced US: A Diagnostic Performance Study. *Radiology*. 2014 Apr;271(1):133–42.
- 254 Lan D, Qu H-C, Li N, Zhu X-W, Liu Y-L, Liu C-L. The Value of Contrast-Enhanced Ultrasonography and Contrast-Enhanced CT in the Diagnosis of Malignant Renal Cystic Lesions: A Meta-Analysis. *PLoS ONE*. 2016 May;11(5):e0155857.
- 255 Graumann O, Osther SS, Karstoft J, Hørlyck A, Osther PJS. Bosniak classification system: a prospective comparison of CT, contrast-enhanced US, and MR for categorizing complex renal cystic masses. *Acta Radiol*. 2016 Nov;57(11):1409–17.
- 256 Sanz E, Hevia V, Gómez V, Álvarez S, Fabuel J-J, Martínez L, et al. Renal Complex Cystic Masses: Usefulness of Contrast-Enhanced Ultrasound (CEUS) in Their Assessment and Its Agreement with Computed Tomography. *Curr Urol Rep*. 2016 Dec;17(12):89.

- 257 Park BK, Kim B, Kim SH, Ko K, Lee HM, Choi HY. Assessment of cystic renal masses based on Bosniak classification: Comparison of CT and contrast-enhanced US. *European Journal of Radiology*. 2007 Feb;61(2):310–4.
- 258 Quaia E, Bertolotto M, Cioffi V, Rossi A, Baratella E, Pizzolato R, et al. Comparison of Contrast-Enhanced Sonography with Unenhanced Sonography and Contrast-Enhanced CT in the Diagnosis of Malignancy in Complex Cystic Renal Masses. *American Journal of Roentgenology*. 2008 Oct;191(4):1239–49.
- 259 Xue L-Y, Lu Q, Huang B-J, Ma J-J, Yan L-X, Wen J-X, et al. Contrast-enhanced ultrasonography for evaluation of cystic renal mass: in comparison to contrast-enhanced CT and conventional ultrasound. *Abdom Imaging*. 2014 Dec;39(6):1274–83.
- 260 Zarzour JG, Lockhart ME, West J, Turner E, Jackson BE, Thomas JV, et al. Contrast-Enhanced Ultrasound Classification of Previously Indeterminate Renal Lesions: Contrast-Enhanced US Classification of Indeterminate Renal Lesions. *J Ultrasound Med*. 2017 Sep;36(9):1819–27.
- 261 Chang EH, Chong WK, Kasoji SK, Fielding JR, Altun E, Mullin LB, et al. Diagnostic accuracy of contrast-enhanced ultrasound for characterization of kidney lesions in patients with and without chronic kidney disease. *BMC Nephrol*. 2017 Dec;18(1):266.
- 262 Sawhney S, Wilson SR. Can Ultrasound With Contrast Enhancement Replace Nonenhanced Computed Tomography Scans in Patients With Contraindication to Computed Tomography Contrast Agents? *Ultrasound Quarterly*. 2017 Jun;33(2):125–32.
- 263 Edward G. Grant. Contrast Enhanced Ultrasound of the Kidneys. 2017 Dec Available from: https://sonoworld.com/LectureDetails/Contrast_Enhanced_Ultrasound_of_the_Kidneys.aspx?Id=2455&Sequence=1
- 264 Lim Y. A GEE approach to estimating accuracy and its confidence intervals for correlated data. *Pharmaceutical Statistics*. 2020 Jan;19(1):59–70.
- 265 Nicolau C, Buñesch L, Paño B, Salvador R, Ribal MJ, Mallofré C, et al. Prospective evaluation of CT indeterminate renal masses using US and contrast-enhanced ultrasound. *Abdom Imaging*. 2015 Mar;40(3):542–51.
- 266 Nicolau C, Bunesch L, Sebastia C. Renal complex cysts in adults: contrast-enhanced ultrasound. *Abdom Imaging*. 2011 Dec;36(6):742–52.
- 267 Wilson SR, Lyshchik A, Piscaglia F, Cosgrove D, Jang H-J, Sirlin C, et al. CEUS LI-RADS: algorithm, implementation, and key differences from CT/MRI. *Abdom Radiol*. 2018 Jan;43(1):127–42.
- 268 Huang J-Y, Li J-W, Lu Q, Luo Y, Lin L, Shi Y-J, et al. Diagnostic Accuracy of CEUS LI-RADS for the Characterization of Liver Nodules 20 mm or Smaller in Patients at Risk for Hepatocellular Carcinoma. *Radiology*. 2020 Feb;294(2):329–39.

- 269 Makoyeva A, Kim TK, Jang H-J, Medellin A, Wilson SR. Use of CEUS LI-RADS for the Accurate Diagnosis of Nodules in Patients at Risk for Hepatocellular Carcinoma: A Validation Study. *Radiology: Imaging Cancer*. 2020 Mar;2(2):e190014.
- 270 Silverman SG, Pedrosa I, Ellis JH, Hindman NM, Schieda N, Smith AD, et al. Bosniak Classification of Cystic Renal Masses, Version 2019: An Update Proposal and Needs Assessment. *Radiology*. 2019 Aug;292(2):475–88.
- 271 Israel GM, Hindman N, Bosniak MA. Evaluation of Cystic Renal Masses: Comparison of CT and MR Imaging by Using the Bosniak Classification System. *Radiology*. 2004 May;231(2):365–71.
- 272 Schoots IG, Zaccai K, Hunink MG, Verhagen PCMS. Bosniak Classification for Complex Renal Cysts Reevaluated: A Systematic Review. *Journal of Urology*. 2017 Jul;198(1):12–21.
- 273 Silverman SG, Israel GM, Trinh Q-D. Incompletely Characterized Incidental Renal Masses: Emerging Data Support Conservative Management. *Radiology*. 2015 Apr;275(1):28–42.
- 274 Chang EH, Tan H-J, Nielsen M. Management of small renal masses in patients with chronic kidney disease: Perspectives from a nephrologist. *Urologic Oncology: Seminars and Original Investigations*. 2020 May;38(5):533–6.
- 275 Shelton SE, Lindsey BD, Tsuruta JK, Foster FS, Dayton PA. Molecular Acoustic Angiography: A New Technique for High-resolution Superharmonic Ultrasound Molecular Imaging. *Ultrasound in Medicine & Biology*. 2016 Mar;42(3):769–81.
- 276 Lindsey BD, Shelton SE, Foster FS, Dayton PA. Assessment of Molecular Acoustic Angiography for Combined Microvascular and Molecular Imaging in Preclinical Tumor Models. *Mol Imaging Biol*. 2017 Apr;19(2):194–202.
- 277 Zhao F, Unnikrishnan S, Herbst EB, Klibanov AL, Mauldin FW, Hossack JA. A Targeted Molecular Localization Imaging Method Applied to Tumor Microvasculature. *Invest Radiol*. 2021 Apr;56(4):197–206.
- 278 Andersen SB, Taghavi I, Hoyos CAV, Søgaaard SB, Gran F, Lönn L, et al. Super-Resolution Imaging with Ultrasound for Visualization of the Renal Microvasculature in Rats Before and After Renal Ischemia: A Pilot Study. *Diagnostics*. 2020 Oct;10(11):862.
- 279 Ai D, Banchs J, Owusu-Agyemang P, Cata JP. Chemotherapy-induced cardiovascular toxicity: beyond anthracyclines. *MINERVA ANESTESIOLOGICA*. 2014;80(5):9.
- 280 Raucher D, Dragojevic S, Ryu J. Macromolecular Drug Carriers for Targeted Glioblastoma Therapy: Preclinical Studies, Challenges, and Future Perspectives. *Front Oncol*. 2018 Dec;8:624.
- 281 Ding S, O'Banion CP, Welfare JG, Lawrence DS. Cellular Cyborgs: On the Precipice of a Drug Delivery Revolution. *Cell Chemical Biology*. 2018 Jun;25(6):648–58.

- 282 Nam L, Coll C, Erthal L, de la Torre C, Serrano D, Martínez-Máñez R, et al. Drug Delivery Nanosystems for the Localized Treatment of Glioblastoma Multiforme. *Materials*. 2018 May;11(5):779.
- 283 Zhang J, Tang H, Liu Z, Chen B. Effects of major parameters of nanoparticles on their physical and chemical properties and recent application of nanodrug delivery system in targeted chemotherapy. *IJN*. 2017 Nov;Volume 12:8483–93.
- 284 Karimi M, Sahandi Zangabad P, Baghaee-Ravari S, Ghazadeh M, Mirshekari H, Hamblin MR. Smart Nanostructures for Cargo Delivery: Uncaging and Activating by Light. *J Am Chem Soc*. 2017 Apr;139(13):4584–610.
- 285 Yang Y, Mu J, Xing B. Photoactivated drug delivery and bioimaging: Photoactivated drug delivery and bioimaging. *WIREs Nanomed Nanobiotechnol*. 2017 Mar;9(2):e1408.
- 286 O'Banion CP, Lawrence DS. Optogenetics: A Primer for Chemists. *ChemBioChem*. 2018 Jun;19(12):1201–16.
- 287 Ankenbruck N, Courtney T, Naro Y, Deiters A. Optochemical Control of Biological Processes in Cells and Animals. *Angew Chem Int Ed*. 2018 Mar;57(11):2768–98.
- 288 Yan J, Yu J, Wang C, Gu Z. Red Blood Cells for Drug Delivery. *Small Methods*. 2017 Dec;1(12):1700270.
- 289 Pierigè F, Bigini N, Rossi L, Magnani M. Reengineering red blood cells for cellular therapeutics and diagnostics: Biomedical applications of reengineered erythrocytes. *WIREs Nanomed Nanobiotechnol*. 2017 Sep;9(5):e1454.
- 290 Villa CH, Anselmo AC, Mitragotri S, Muzykantov V. Red blood cells: Supercarriers for drugs, biologicals, and nanoparticles and inspiration for advanced delivery systems. *Advanced Drug Delivery Reviews*. 2016 Nov;106:88–103.
- 291 Shell TA, Shell JR, Rodgers ZL, Lawrence DS. Tunable Visible and Near-IR Photoactivation of Light-Responsive Compounds by Using Fluorophores as Light-Capturing Antennas. *Angew Chem Int Ed*. 2014 Jan;53(3):875–8.
- 292 Gessner RC, Frederick CB, Foster FS, Dayton PA. Acoustic Angiography: A New Imaging Modality for Assessing Microvasculature Architecture. *International Journal of Biomedical Imaging*. 2013;2013:1–9.
- 293 Marvin CM, Ding S, White RE, Orlova N, Wang Q, Zywoot EM, et al. On Command Drug Delivery via Cell-Conveyed Phototherapeutics. *Small*. 2019 Sep;15(37):1901442.